

Study on the Mechanical Properties of Carbon Nanotube CoatedFiber Multi-Scale (CCFM) Hybrid Composites

Original

Study on the Mechanical Properties of Carbon Nanotube CoatedFiber Multi-Scale (CCFM) Hybrid Composites / Malekimoghadam, Reza. - (2022 Jul 28), pp. 1-241.

Availability:

This version is available at: 11583/2970995 since: 2022-09-06T15:14:02Z

Publisher:

Politecnico di Torino

Published

DOI:

Terms of use:

Altro tipo di accesso

This article is made available under terms and conditions as specified in the corresponding bibliographic description in the repository

Publisher copyright

(Article begins on next page)



ScuDo
Scuola di Dottorato ~ Doctoral School
WHAT YOU ARE, TAKES YOU FAR



Doctoral Dissertation
Doctoral Program in Energy Engineering (34th Cycle)

Study on the Mechanical Properties of Carbon Nanotube Coated–Fiber Multi-Scale (CCFM) Hybrid Composites

Reza Malekimoghadam

Supervisor
Prof. Marco Gherlone

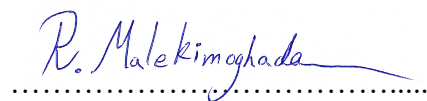
Doctoral Examination Committee:

Prof. Stepan Lomov, Referee, KU Leuven University
Prof. Nicholas Fantuzzi, Referee, University of Bologna

Politecnico di Torino
June 28, 2022

This thesis is licensed under a Creative Commons License, Attribution - Noncommercial - NoDerivative Works 4.0 International: see www.creativecommons.org. The text may be reproduced for non-commercial purposes, provided that credit is given to the original author.

I hereby declare that, the contents and organisation of this dissertation constitute my own original work and does not compromise in any way the rights of third parties, including those relating to the security of personal data.



Reza Malekimoghadam
Turin, June 28, 2022

Summary/ Abstract

The aim of this thesis is to scrutinize the mechanical properties and stress analysis of carbon nanotube (CNT) coated-fiber multi-scale hybrid composites, which is henceforth referred to as CCFM hybrid composites, through proposing analytical and numerical methods. Firstly, the mechanical properties of the CNT coating region have been calculated at the lower scales, nano, and micro scales. The models comprise a core fiber, CNT coating region (CCR) and surrounding matrix, in which the coating region around the core fiber encompasses CNTs and matrix.

In addition, different types of coating regions in terms of configurations of the grown CNTs on the fiber surface are constructed consisting of axially, radially, and randomly oriented CNTs. The mechanical properties of various coating regions are calculated employing the Eshelby–Mori–Tanaka method in conjunction with an equivalent continuum approach. Having obtained the properties of the CNT structure and the coating regions at the lower scale, the models are then established at macro scale and the multi-scale modeling is conducted covering various effective parameters from nano-to macro-scale.

In the next step, interfacial radial and axial stresses of CCFM hybrid composites are acquired through multi-scale finite element analysis. The results reveal that: (I) a remarkable influence of CNT coating on the fiber-matrix interfacial properties, particularly in the composites containing axially and randomly oriented CNTs, (II) considering two hybrid systems, composites with CNTs coated-fibers demonstrate notable improvements in the interfacial behaviors than those with CNTs in matrix, (III) the pronounced effect of non-bonded interphase region on the interfacial properties, while less significant influence on the Young's moduli is observed.

Moreover, the influence of carbon nanotube coated-carbon fibers on thermal residual stresses of multi-scale hybrid composites is investigated through analytical approach. Utilizing the total energy minimization method, the closed-form solution of the thermal residual stresses of hybrid composite is obtained. The results disclose a noteworthy influence of CNT-coating on the reduction of interfacial stresses which precludes debonding at interface and attenuates the effect of thermal expansions mismatch between the carbon fiber and matrix. Furthermore, the results demonstrate that unlike radially oriented CNTs, the existence of axially and randomly oriented CNTs at the coating region has a remarkable diminishing effect on residual interfacial stresses. It is also shown that increasing the coating thickness leads to reduction of maximum interfacial stresses even at a constant CNT volume fraction.

With the aim of investigating the bending analysis of CCFM hybrid composite beam, the Refined Zigzag Theory (RZT) is utilized and developed for both laminated and sandwich carbon nanotube coated-fiber multi-scale composite (CFMC) beams. Having implemented the multi-scale modeling, the results are

then fed into the RZT. Considering two types of CNT coating around the core fiber consisting of axially aligned' and 'randomly oriented' CCRs (hereafter referred to as ACCR and RNCCR, respectively), the bending stress analysis is carried out through the RZT taking into account simply-supported beam with transverse sinusoidal loading. The results reveal a pronounced reduction in transverse displacement in laminated and sandwich CCFM composite beams with respect to conventional composite beams. Moreover, by employing a combination of ACCR and RNCCR for the layers in the sandwich CFMC beams, a pronounced decrease in the transverse shear stress of the core medium is demonstrated which can postpone the core shear failure in the sandwich structures. In addition, effect of CCR types, CNT volume fraction, core fiber material and orientation, and CNT coating thickness are entirely assessed on the bending analysis of CCFM composite beams.

By way of conclusion, it should be stated that the proposed techniques in this thesis could be utilized as an effective, accurate and viable tools for future design and analysis of CCFM hybrid composite structures.

Acknowledgment

First and foremost, I would like to express my deep gratitude to my former supervisor Prof. Ugo Icardi for the continuous support of my PhD study and related research. My utmost and sincere thanks also go to my supervisor, Prof. Marco Gherlone, for his immense support and guidance. Without his precious support, it would not have been possible to continue and accomplish my PhD program perfectly.

My appreciation also extends to Politecnico di Torino and Department of Mechanical and Aerospace Engineering (DIMEAS) that provided me an excellent environment to carry out my education and research activities. I would also like to acknowledge my colleagues at DIMEAS for their assistance during PhD program.

Last but not the least, my endless gratitude is devoted to my family: my father, my mother, and my wife, for their kind encouragement, unequivocal sacrifice, and support throughout my PhD study and my life in general.

Contents

Chapter 1: Introduction	5
1.1 Background.....	5
1.2 Motivations and Steps.....	6
1.2.1 Motivations	6
1.2.2 Steps of Research.....	7
1.3 Objectives and Major Achievements.....	9
1.3.1 Objectives	9
1.3.2 Major Achievements.....	10
1.4 Outline of the Thesis.....	11
Chapter 2: Principles of Nanocomposite Materials.....	13
2.1 Fundamentals of Carbon Nanotubes (CNTs)	13
2.1.1 CNT Structure and Physical Properties.....	14
2.1.2 Engineering Applications of CNTs	19
2.1.3 Processing and Fabrication.....	23
2.1.4 Mechanical Properties of Isolated CNT	24
2.1.5 Modeling Techniques and Stress Analysis of CNTs	28
2.2 Full-Scale Investigation into CNT–Polymer Nanocomposites.....	37
2.2.1 Processing and Fabrication	37
2.2.2 Mechanical Properties	41
2.2.3 Nonlinear Multi-Scale Modeling Technique.....	46
2.2.4 Challenges and Concluding Remarks.....	55
Chapter 3: A Study on Fracture Behavior of Clay-Polymer Nanocomposites ...	58
3.1 Introduction.....	58
3.2 Nano-Clay Structure and Mechanical Properties	60
3.3 Constitutive multi-scale modeling of clay-epoxy nanocomposites	63
3.3.1 FEM of Nano-Clay	64
3.3.2 FEM of Surrounding epoxy matrix	64
3.3.3 FEM of Interphase region and interactions of clay/epoxy.....	65
3.4 Stress Analysis of Semi-Elliptical 3D Crack.....	69
3.5 Results and Discussion	73
3.6 Conclusion	80

Chapter 4: Fundamentals of Nano-Engineered Multi-Scale Hybrid Composites (NMHCs).....	82
4.1 Introduction.....	82
4.2 Processing and Fabrication Methods of NMHCs	84
4.3 Properties and Remarkable Engineering Advantages of NMHCs.....	89
4.3.1 Properties	89
4.3.2 Remarkable Engineering Advantages	91
4.4 Conclusion and future trends	101
Chapter 5: Investigation of Interfacial Shear & Radial stresses of Carbon Nanotube Coated–Carbon Fiber Hybrid Composites.....	103
5.1 Introduction.....	103
5.2 Framework of Multi-Scale Modeling	105
5.3 Nano-Scale Modeling	107
5.4 Interface region between Carbon Nanotube and Matrix (Cohesive zone formulation)	108
5.5 Numerical Modeling of CNT-coated Fiber Hybrid Composites	112
5.6 Results and Discussion	118
5.7 Conclusion	127
Chapter 6: Effect of Carbon Nanotubes Coated–Carbon Fibers on Interfacial Residual Thermal Stresses	128
6.1 Introduction.....	128
6.2 Constitutive Modeling of CNT– Coated Carbon Fiber Hybrid Composite.....	130
6.2.1 Analytical Modelling of Carbon Nanotube Structure.....	132
6.2.2 Effective Elastic Properties of CNT– Coating Region (CCR)	134
6.3 Problem Formulation and Analytical Implementation	140
6.3.1 Constructing the Stress Functions	141
6.3.2 Stress components in the fiber	143
6.3.3 Stress components in the CNT- coating region (CCR)	144
6.3.4 Stress components in the matrix	144
6.3.5 Boundary Conditions	144
6.3.6 Thermo- elastic equations.....	146
6.3.7 Energy minimization	147
6.4 Result and Discussion.....	149
6.5 Conclusion	156
Chapter 7: Bending Analysis of CNT Coated–Fiber Multi-Scale Composite (CFMC) Beams Using the Refined Zigzag Theory (RZT)	157
7.1 Introduction.....	157

7.2 Framework of Modeling Procedure of CNT Coated–Fiber Multi-Scale Composites	159
7.2.1 Simulating of Carbon Nanotube (CNTs) with Surrounding Interphase.....	162
7.2.2 Effective Elastic Properties of the CNT Coating Region (CCR)	165
7.2.3 Modelling of the Core Fiber with Surrounding CCR	169
7.2.4 Macro-Scale Modeling of CNT Coated–Fiber Multi-Scale Composites	173
7.3 Formulation of the Refined Zigzag Theory (RZT).....	177
7.4 Results and Discussion	183
7.5 Conclusion	194
Conclusion/ Major Contributions/ Perspectives.....	195
References	198
Appendix A	219
Appendix B	219
Appendix C	219
Appendix D	220
Appendix E.....	224

List of Tables

Table 1.1 Published article during PhD degree	11
Table 2.1 Mechanical Properties of Carbon Nanotubes Compared with Some Engineering Materials [44]	18
Table 2.2 General Categorization of CNTs [49].....	19
Table 2.3 Comparison of different CNT processing methods [63]	24
Table 2.4 Experimentally Obtained Young's Modulus of SWCNTs & MWCNTs [64].	25
Table 2.5 Experimentally Obtained Tensile Strength of SWCNTs & MWCNTs [64] ...	28
Table 2.6 Computationally Determined Tensile Strength of CNTs [64].....	28
Table. 2.7. Calculated mechanical properties of isolated SWCNT using FEM	36
Table 2.8 Mechanical Properties of CNT-Based Polymer Composites [105]	46
Table 2.9 Effective Parameters of Each Scale in Multiscale Modeling [126].....	53
Table 3.1: Experimental characterization and MD simulation of clay modulus [145].	62
Table 3.2 Experimental characterization of nanoclay/polymer [145]	63
Table 5.1: Mechanical properties of Carbon Nanotube [94] [212] [213] [214]	108
Table 5.2: The input values of Cohesive Model for finite element modeling [178] [217] [219].....	112
Table 5.3: Elastic Properties of Carbon Fiber [220]	113
Table 6.1: Mechanical Properties of Equivalent Nanofiber [122] [205]	134
Table 6.2: Elastic Properties of Carbon Fiber and Polymer Matrix [220] [221] [264] .	149
Table 7.1: Mechanical Properties of Equivalent Nanofiber [122] [205]	165
Table 7.2: Elastic Properties of IM7 Carbon Fiber, Glass Fiber and Polymer Matrix [14] [296] [297]	170
Table 7.3 : Mechanical properties of composite beam [267] [285].....	173
Table 7.4: Obtained Mechanical properties of CCFMC & CGFMC beams versus CNT coating thicknesses [267]	176
Table 7.5: Obtained Mechanical properties of CCFMC & CGFMC beams with respect to CNT contents [267]	177
Table 7.6: Laminate stacking sequences used for sandwich/ laminated composite beams and sandwich/laminated CFMC beams (from bottom to top direction) [267].....	184

List of Figures

Figure 1.1: A single fuzzy fiber with predominantly radially oriented CNT's (left) [19], SEM of fibers with densely coated CNTs on the surface (right) [20]	6
Figure 1.2: Schematic diagram of (a) withered tree (representing pure fiber) and (b) thriving tree being pulled out [21]	7
Figure 2.1: Schematic diagram of (A) SWCNT. (B) MWCNT [27]	14
Figure 2.2: Schematic representation of the relation between nanotubes and graphene [28].....	15
Figure 2.3: HRTEM images of bent CNTs under mechanical duress [46].....	18
Figure 2.4: A) Micrograph showing the cross-section of a CF laminate with CNTs dispersed in the epoxy resin; (B) a lightweight CNT-fiber composite boat hull (C) CNT-reinforced polyurethane blade obtained by vacuum bag technique [55].....	20
Figure 2.5: Cylinder-shaped multiwalled nanotube (MWNT) towers grown by thermal CVD [32]	23
Figure 2.6: Variation of SWCNT Young's modulus with diameter and chirality through different computational modeling techniques [45]	26
Figure 2.7: Effect of number of concentric tubes on the Young's modulus of MWCNT [75].....	27
Figure 2.8: Formation and coalescence of Stone–Wales defect through different stages under the axial tensile loading [76].....	27
Figure 2.9: Constructed models of CNT using: (a) Nano-scale continuum mechanics, (b) continuum modeling using shell model and (c) atomistic modeling techniques [77]	29
Figure 2.10: Potential energy terms of Carbon-Carbon bond [43]	34
Figure 2.11: Representation of single-walled carbon nanotube modeling [43].....	35
Figure 2.12: Finite element model of intact single walled carbon nanotube [43]	36
Figure 2.13: Natural frequencies of intact CNT [43].....	37
Figure 2.14: Schematic diagram of solution mixing technique for CNT/PNCs [101]	38
Figure 2.15: (A) Twin screw extruder, (B) view of micro-compounder showing different valves and channels, and (C) twin-screw extruder for melt mixing of CNTs & polymer matrix [102]	39
Figure 2.16: Schematic representation of in situ polymerization process [100]	40
Figure 2.17: Schematic diagram for CNT–phenolic resin paper composite preparation [104].....	41
Figure 2.18: Stress–strain curves. (A) PE/PE-g-MWCNTs composites; (B) PE/MWCNTs composites [107]	42
Figure 2.19: Stress–strain curves for neat PMMA, PMMA/MWCNT, and PMMA/MWCNT/P3HT-g-PMMA with various MWCNT contents [109]	43

Figure 2.20: (A) Tensile modulus and (B) tensile strength of CNTs/epoxy composites versus CNTs loading [110]	44
Figure 2.21: Schematic description of crack propagation; (a) crack bridging mechanism of CNTs; (b) rupture of CNTs and pull-out of CNTs and inner tubes [112]	45
Figure 2.22: SEM images of the CNT/Epoxy nanocomposite. A crack is bridged by CNTs. (a) rupture of CNT; (b) crack-bridging of CNT by forming pull-out of the inner tubes [112]	45
Figure 2.23: Snapshots of CNT pull-out simulations from polyethylene matrix at (A) $x = 0$ nm, (B) $x = 2$ nm, (C) $x = 4$ nm, (D) $x = 6.4$ nm [115]	47
Figure 2.24: A 3D unit cell of the PNCs [117]	47
Figure 2.25: Variation of vdW force vs. interatomic distance for C–C bonds [97] [94]	49
Figure 2.26: Finite element model of RVE and its constituents [97]	50
Figure 2.27: Plot of the elastic modulus as a function of RVE size [114]	52
Figure 2.28: Convergence of the average elastic modulus over the number of realizations [125]	52
Figure 2.29: Length scales spectrum of carbon nanotube–reinforced polymers (CNTRP) for the multiscale modeling [126]	53
Figure 2.30: Schematic representation of (A) hierarchical or sequential, (B) concurrent, and (C) semi-concurrent multiscale methods [129]	54
Figure 3.1: Nanoclay morphologies in polymers [145]	61
Figure 3.2: Schematic view of a RVE model with two types of periodic cells (a) Short RVE (b) Long RVE [149]	64
Figure 3.3: Modeling procedure of four-phase clay/epoxy nanocomposite [149]	65
Figure 3.4: Elastic modulus distribution at interphase region [166] [134]	66
Figure 3.5: Cohesive zone material (a) Mixed-mode traction-separation behavior (b) INTER204 element geometry [118]	68
Figure 3.6: Finite element model of intact half RVE (a) Long RVE (b) Short RVE (c) multi-scale finite element procedure of four-phase clay/ polymer nanocomposite [134]	69
Figure 3.7: (a) Finite Element model of short RVE with 3D crack (b) Enlarged view of crack face, (c) Spider web shape of singular elements (d) Cut- view at crack face [134]	70
Figure 3.8: (a) Finite Element model of Long RVE with 3D crack, (b) Enlarged view of crack structure, (c) Spider web shape of singular elements (d) Cut–view at crack face [134]	70
Figure 3.9: Normalized mesh density versus normal stress [134]	71
Figure 3.10: Total Strain Contour/Semi-elliptical crack propagation in Short RVE (a) $a/w = 0.25$ (b) $a/w = 0.5$ (c) $a/w = 0.7$ [134]	73

Figure 3.11: Total Strain Contour/Semi-elliptical crack propagation in Long RVE (a) $a/w = 0.15$ (b) $a/w = 0.2$ (c) $a/w = 0.25$ [134].....	74
Figure 3.12: Short RVE with CZM -Total elastic/plastic strain (a) Debonding damage left side (b) Right side [134]	74
Figure 3.13: Variation of normalized J along crack front for several crack sizes in the short RVE; propagation along Z direction [134]	75
Figure 3.14: Variation of normalized J along crack front for several crack sizes in the short RVE; propagation along Y direction [134].....	76
Figure 3.15: Variation of normalized J versus clay content at different crack locations the in the short RVE [134]	77
Figure 3.16: J_0/J versus longitudinal crack positions for several points along the crack front in the short RVE [134]	78
Figure 3.17: Influence of CZM on normalized J along crack front in the short RVE: (a) wt = 8%, (b) wt = 5%, (c) wt = 3% [134]	79
Figure 3.18: Influence of long/short RVE type on normalized J along crack front in: (a) wt = 8%, (b) wt = 5%, (c) wt = 3% [134]	79
Figure 3.19: Normalized J_n versus interphase thickness with respect to different interfacial enhancement indices [134]	80
Figure 4.1: Schematic of crack bifurcation, deflection mechanisms owing to multi-scale CNT-coated fibers [170]	84
Figure 4.2: Schematics of typical surface coating techniques of fibers/ fabrics: (a) CVD process (b) electrophoresis process (c) sizing process and (d) spray coating process [169].....	87
Figure 4.3: Scheme of ‘sacrificial’ interleaving with an epoxy resin soluble CNT-containing thermoplastic polymer [177].....	87
Figure 4.4: Schematic representation of the electrospraying of CNTs onto carbon fiber [18].....	88
Figure 4.5: Concept of the self-healing process using carbon nanotubes [185]	90
Figure 4.6: SEM images of the (a) desized CF, (b) CNTs/CF, and (c) GO/CF [186].92	92
Figure 4.7: (a) Interfacial shear strength results of the composites (b) Interlaminar shear strength of the composites [186]	92
Figure 4.8: Schema illustration for the preparation of CF absorbed with EG [173] ...	93
Figure 4.9: Schema for the differences between pristine, hierarchical, and sonicated composites [173].....	93
Figure 4.10: ILSS of (a) hierarchical composite with graded interphase, (b) sonicated composite [173]	94
Figure 4.11: Fracture morphology of single fiber composite fragmentation tests: (a) CF, (b) 10 min CNT-coated CF by 20 kV/10 cm, 25 °C, (c) 10 min CNT-coated CF using 10 kV/5 cm, 100 °C , (d) 20 min CNT-coated CF by 20 kV/10 cm, 100 °C [187]	94

Figure 4.12: Interlaminar shear strengths of CF/EP, CF/EP-CNTs, and CF-CNTs/EP [188].....	95
Figure 4.13: a) Macroscale view of MWNT sheet scrolled on carbon fiber, b) Schematic of nanoscale RVE of the interface region between epoxy-MWNT-carbon fiber, c) AFM Image of Epon 862, carbon fiber, MWNT interface [189].....	96
Figure 4.14: A schematic diagram showing a nano-micro-macro multiscale approach to calculate the improvement in the Compressive Strength in MWNT scrolled Fiber/ Epoxy Composite (Boeing 787 Dreamliner) [189].....	96
Figure 4.15: Electrical conductivity for CFRP and FCFRP in (a) in-plane, (b) the out-of- plane direction (thickness) and (c) the out-of-plane (volume) direction [190].....	97
Figure 4.16: Resistivity measurement result with respect to wt% of CNT [191].....	98
Figure 4.17: (a) SEM micrograph of CNT growth on glass fiber (sensor), (b) Composite panel with embedded strain sensors [19].....	99
Figure 4.18: (a) VACNTs placed in between two plies of a laminated composite (b) Illustration of the ‘transfer-printing’ process [192]	99
Figure 4.19: (a) spray coating process and (b) electrical in-situ damage sensing test set-up for DCB specimen [175]	100
Figure 4.20: Comparison of Mode-I interlaminar fracture toughness for reference, 0.02 wt.% and 0.047 wt.% CNT concentration [175].....	100
Figure 5.1: Randomly oriented CNTs on the surface of the carbon fiber [201].....	106
Figure 5.2: The multi-scale modeling framework of multi-scale hybrid composite and effective parameters at each scale [178]	107
Figure 5.3: Equivalence molecular, finite element and continuum models [178]	108
Figure 5.4: The cohesive law for a carbon nanotube and polymer matrix established from the van der Waals interactions at the CNT/matrix interface [217]	110
Figure 5.5: Cohesive zone material (a) Mixed-mode traction-separation behavior (b) INTER204 3D element geometry (c) Defining tangential and normal directions through the element [118].....	111
Figure 5.6: Schematic illustration of carbon nanotube configuration around core fiber (a) radially aligned CNTs (b) axially aligned CNTs (c) randomly distributed CNTs [178].....	112
Figure 5.7: Schematic illustration of fuzzy fiber reinforced composite RVE with corresponding global and local coordinate systems [178]	114
Figure 5.8: Finite element model of CF–CNT hybrid composite (a) with axially aligned CNTs, (b) with randomly oriented CNTs (c) with radially aligned CNTs [178]	115
Figure 5.9: 8-nodes brick elements with relevant degrees of freedom [178]	117
Figure 5.10: Stress contour of the hybrid composite (a) quarter of the RVE model (b) cut view at coating region (c) partial view, debonding damage between CNTs & matrix [178]	119
Figure 5.11: Normalized mesh density versus maximum interfacial shear stress [178]	120

Figure 5.12: (a) The longitudinal and (b) transverse elastic moduli of CNT–CF reinforced hybrid composite versus CNT volume fraction [178].....	120
Figure 5.13: The normalized interfacial stress distribution, (a) Interfacial shear stress, (b) Interfacial radial stress [178].....	121
Figure 5.14: The normalized interfacial stress distribution for different CNT's configurations, (a) Interfacial shear stress, (b) Interfacial radial stress [178]	122
Figure 5.15: Schematic illustration of two systems of multi-scale hybrid composites; (a) Mixed CNT/ matrix system, (b) Hybrid fiber system [178].....	123
Figure 5.16: The interfacial stress distribution for different hybrid system (a) Interfacial shear stress (b) Interfacial radial stress [178]	123
Figure 5.17: The normalized maximum interfacial shear stress versus CNT weight percentage [178]	124
Figure 5.18: The maximum interfacial shear stress ratio considering perfect bond and debonding condition [178].....	125
Figure 5.19: The maximum interfacial radial stress ratio considering perfect bond and debonding condition [178].....	126
Figure 5.20: The normalized maximum interfacial radial stress versus CNT weight percentage [178]	126
Figure 6.1: Carbon fiber coated with CNTs forest (a) randomly oriented CNTs on the surface of the carbon fiber [201] (b) Growth of CNTs with uniform distribution on the fiber surface [202].....	130
Figure 6.2: (a) CNT-coated CF Multi-scale hybrid composite (b) RVE with radially aligned CNTs (c) RVE with axially aligned CNTs (d) RVE with randomly oriented CNTs [179]	131
Figure 6.3: Flowchart of obtaining residual stress in CNT–coated CF hybrid composite [179]	132
Figure 6.4: Description of CNT equivalent modeling (a) FE multi-scale model (b) Equivalent nanofiber [179]	133
Figure 6.5: RVE model of CNT- Coated fiber hybrid composite and corresponding coordinate system [179].....	141
Figure 6.6: Multi-scale Finite element model (a) CNT–Carbon Fiber hybrid composite (b) Cut-view [179]	149
Figure 6.7: Distribution of thermal residual interfacial stresses of hybrid composite, with coating thickness of 900 nm and $\Delta T = 50$ K (a) Shear stress (b) Radial stress [179].....	151
Figure 6.8: Distribution of thermal residual interfacial stresses of hybrid composite considering different CNT's orientations at coating region and $\Delta T = 50$ K (a) Shear stress (b) Radial stress [179].....	152
Figure 6.9: Distribution of thermal residual interfacial stresses of hybrid composite at different coating thickness and $\Delta T = 100$ K (a) Shear stress (b) Radial stress (c) Fiber axial stress [179]	153

Figure 6.10: Distribution of thermal residual interfacial stresses of hybrid composite at different temperature variations (a) Shear stress (b) Radial stress (c) Fiber axial stress with coating thickness of 1 μm [179].....	154
Figure 6.11: Normalized maximum stresses versus different coating thicknesses & CNTs orientations (a) Interfacial shear stress (b) Interfacial radial stress (c) Fiber axial stress [179].....	155
Figure 6.12: Normalized maximum stresses versus different CNT volume fractions& CNTs orientations (a) Interfacial Shear stress (b) Interfacial radial stress (c) Fiber axial stress [179]	155
7.1: (a) Top-down description of plain weave CNT coated–carbon fabric with randomly oriented CNTs on the fiber [290] (b) Carbon fiber with axially aligned CNT coating; the red arrows indicate the axial direction of the carbon fiber [291]	160
Figure 7.2: The procedure of hierarchical multi-scale modeling of CNT coated–fiber hybrid composites [267]	161
Figure 7.3: Flowchart of stress analysis of CNT coated–fiber composite beam through RZT method [267]	162
Figure 7.4: Description of equivalent nanofiber (a) Finite element model–Cut view of the RVE, (b) Finite element model–Cross section of the RVE, (c) Schematic of equivalent nanofiber [267].....	164
Figure 7.5: RVE representation consisting of two CNT coating regions (a) RNCCR, (b) ACCR [267]	166
Figure 7.6: Schematic description: (a) CFMC beam geometry and Coordinate System, (b) layers numbering, (c) applied loads [267].....	178
Figure 7.7: Zigzag functions and layer notation of the Refined Zigzag Theory for a three-layered laminate [283]	180
Figure 7.8: Through-thickness distributions for the laminated beams L5 and L [*] 5; L [*] 5 comprises RNCCR with coating thickness of 1.4 μm (a) transverse shear stress, (b) axial stress, (c) axial displacement and (d) maximum transverse displacement [267]	185
Figure 7.9: Finite element model of the laminated CFMC beam (L [*] 5) (a) geometry and sinusoidal loading (b) partial view exhibiting mesh density (c) normalized mesh density versus maximum axial stress [267]	187
Figure 7.10: FEA contours of the laminated CCFMC beam (L [*] 5) (a) transverse displacement (b) axial stress [267]	187
Figure 7.11: Through-thickness distributions for the sandwich beams L4 and L [*] 4; L [*] 4 comprises RNCCR with coating thickness of 1.4 μm (a) transverse shear stress, (b) axial stress, (c) axial displacement and (d) maximum transverse displacement [267]	188
Figure 7.12: Finite element model of the sandwich CFMC beam (L [*] 4) (a) geometry and sinusoidal loading (b) partial view exhibiting mesh density (c) normalized mesh density versus maximum axial stress [267]	189
Figure 7.13: FEA contours of the sandwich CCFMC beam (L [*] 4) (a) transverse displacement (b) axial stress [267]	190

Figure 7.14: Through-thickness distributions for the sandwich beams L3 and L*3; L*3 contains CNT volume fraction of 0.08 (a) transverse shear stress, (b) axial stress, (c) axial displacement and (d) transverse displacement along x-direction [267]..... 191

Figure 7.15: Through-thickness distributions versus CNT volume fraction for the laminated beams L7 and L*7; L*7 consists of CNT coating thickness of 1.4 μm (a) transverse shear stress, (b) axial stress, (c) axial displacement and (d) transverse displacement along x-direction [267] 192

Figure 7.16: Through-thickness distributions versus CNT volume fraction for the sandwich beams L4 and L*4; L*4 includes CNT coating thickness of 1.4 μm (a) transverse shear stress, (b) axial stress, (c) axial displacement and (d) transverse displacement along x-direction [267] 193

Nomenclature

Symbol

C_h	CNT Chiral Vector
T	CNT Translation Vector
n, m	CNT indices
a_1, a_2	Basis vectors of graphene lattice
d_{CNT}	CNT diameter
a_{C-C}	Carbon–Carbon bond length
θ	CNT Chiral angle
U_{Total}	Interatomic potential energy
U_r	Bond stretching
U_θ	Bond angle variation
U_ϕ	Bond dihedral torsion
U_ω	Bond out of plane torsion
U_{vdW}	Van der Waals interactions
E	Young's modulus of equivalent beam of CNT structure
A	Cross section area of equivalent beam of CNT structure
I	Moment of inertia of equivalent beam of CNT structure
G	Shear modulus of equivalent beam of CNT structure
J	Polar moment of equivalent beam of CNT structure
F_{vdw}	Non-linear van der Waals force
T_n	Normal component of cohesive tractions
T_t	Tangential component of cohesive tractions
δ_n	Normal separation of cohesive zone model (CZM)
δ_t	Tangential separation of cohesive zone model (CZM)
D_m	Damage parameter
K_I	Stress intensity factor for mode I
J	J- Integral for a line contour surrounding the crack tip
a	Crack radius
C_{ENF}	Stiffness matrix of Equivalent Nanofiber
C_{CCR}	Stiffness tensor of coating region
$K_{ACCR/RNCCR}$	Bulk modulus of different coating regions
$G_{ACCR/RNCCR}$	Shear modulus of different coating regions
$(\alpha_{CCR})_L$	Longitudinal coefficient of thermal expansion (CTE) of CCR
$(\alpha_{ACCR/RCCR})_T$	Transverse CTE of CCR region

$\sigma_{zz}, \sigma_{rr}, \sigma_{\theta\theta}, \tau_{rz}$	Axial, radial, hoop and shear stresses
$\phi_j(r, z)$	Airy stress function
V_m	Volume fraction of matrix
V_f	Volume fraction of fiber
V_{CCR}	Volume fraction of CNT coating region (CCR)
$\varepsilon_{zz}, \varepsilon_{rr}, \varepsilon_{\theta\theta}, \gamma_{rz}$	Axial, radial, hoop and shear strains
Π_{HC}	Total complementary energy of hybrid composite
U_{HC}, V_{HC}	Strain energy and potential/external work energy of hybrid composite
$(E_x)_{FC ACCR/RNCCR}$	Axial Young's modulus of fiber with surrounding coating (FC) with ACCR or RNCCR types
$(\nu_{xz})_{FC ACCR/RNCCR}$	Axial Poisson's ratio of fiber with surrounding coating (FC) with ACCR or RNCCR types
$K_{FC ACCR/RNCCR}$	Bulk modulus of fiber with surrounding coating (FC) with ACCR or RNCCR types
$(G_{xz})_{FC ACCR/RNCCR}$	Axial shear modulus of fiber with surrounding coating (FC) with ACCR or RNCCR types
$(E_x)_{CFMC ACCR/RNCCR}$	Longitudinal Young's modulus of Carbon Nanotube Coated–Fiber Multi-Scale (CCFM) Hybrid Composite beam
$(E_z)_{CFMC ACCR/RNCCR}$	Transverse Young's modulus of Carbon Nanotube Coated–Fiber Multi-Scale (CCFM) Hybrid Composite beam
$(G_{xz})_{CFMC ACCR/RNCCR}$	Longitudinal shear modulus of Carbon Nanotube Coated–Fiber Multi-Scale (CCFM) Hybrid Composite beam
$(G_{zy})_{CFMC ACCR/RNCCR}$	Transverse shear modulus of Carbon Nanotube Coated–Fiber Multi-Scale (CCFM) Hybrid Composite beam
$u(x), \theta(x), w(x), \psi(x)$	Four kinematic variables of RZT: axial displacement, bending rotation, transverse deflection, and zigzag rotation (amplitude of the zigzag)
$\phi^{(k)}_{CFMC}(z)$	Zigzag function of CCFM Hybrid Composite beam
$u_x^{(k)}, u_z^{(k)}$	Displacement field of RZT
γ	Average shear strain (or shearing angle)
$(\sigma_x)_{CFMC}^{(k)}$	Axial stress of CCFM Hybrid Composite beam in the kth layer
$(\tau_{xz})_{CFMC}^{(k)}$	Transverse shear stress of CCFM Hybrid Composite beam in the kth layer
$(N_x)_{CFMC}, (M_x)_{CFMC}, (V_x)_{CFMC}$	Conventional axial force, bending moment, and shear force of CCFM composite beam
$(M_\phi)_{CFMC}, (V_\phi)_{CFMC}$	Bending moment and shear force due to the zigzag distortion of CCFM composite beam

Acronyms and Abbreviations

Symbol	Explanation
CNT	Carbon nanotubes
SWCNT	Single-walled carbon nanotube
MWCNT	Multi-walled carbon nanotube
CCFM Hybrid Composites	Carbon Nanotube Coated–Fiber Multi-Scale (CCFM) Hybrid Composites
CNTRP	Carbon nanotube reinforced polymer
FEA	Finite element analysis
CF	Carbon Fiber
FF	Fuzzy fiber
CF-CNT	Carbon fiber coated with carbon nanotubes
NMHC	Nano-engineered multi-scale hybrid composites
FEM	Finite element modeling
RZT	Refined Zigzag Theory
IFSS	Interfacial Shear Strength
ILSS	Interlaminar Shear Strength
FFRC	Fuzzy-fiber reinforced composites
TPa	Tera-Pascal (10e12 Pa)
CVD	Chemical Vapor Deposition
PECVD	Plasma-Enhanced CVD
EPD	Electrophoretic deposition
C–C	Carbon- Carbon bond
APDL	ANSYS Parametric Design Language
TEM	Transmission electron microscope
AFM	Atomic force microscope
SEM	Scanning electron microscopy
EMA	Electro-magnetic actuation
MD	Molecular dynamics
ABC	Atomistic-based continuum method
MM	Molecular mechanics
NCM	Nano-scale continuum modeling
TBT	Timoshenko beam theory
PNCs	polymer nanocomposites
RVE	Representative Volume Element
SVE	Statistical volume element
vdW Interactions	van der Waals Interactions

L-J (LJ)	Lennard–Jones potential
CNRPs	Carbon nanotube–reinforced polymers
CZM	Cohesive Zone Model
GO	Graphene Oxide
IEI	Interfacial enhancement index
CTE	Coefficient of thermal expansion
CCR	CNT coating region
ENF	Equivalent nanofiber
RCCR	CCR with radially aligned CNTs
ACCR	CCR with axially aligned CNTs
RNCCR	CCR with randomly oriented CNTs
CFMC	CNT coated–fiber multi-scale composite
CCA	Composite cylinder assemblage
COF	Core fiber
FC	Fiber with surrounding coating

Chapter 1: Introduction

1.1 Background

By making a breakthrough of nanomaterials such as carbon nanotubes (CNTs), graphene, nano-clays, etc., many attentions in composite research have been shifted to the relatively new class of composite materials called nanocomposites. More recently, advanced composite materials called Carbon Nanotube Coated–Fiber Multi-Scale (CCFM) Hybrid Composites have received great attraction more than nanocomposites and conventional composite materials, covering all dimension scales from nano to macro scale. The main reason for that shift is the improvement of mechanical, physical, chemical, and electrical properties of CCFM hybrid composites which are remarkably enhanced with negligible additional weight on the final structures. Thus, CCFM hybrid composites possess improved characteristics which can be considered as conventional composite materials plus nanomaterials in which the latter could be CNT, nano-clay, etc. As a fundamental issue, fiber-matrix interfacial properties significantly influence on the mechanical behavior and load transferring phenomenon of composite structures [1], [2], [3], [4], [5]. CNTs can be utilized to hierarchically reinforce carbon fibers (CFs) in order to acquire the benefits of enhanced interfacial/ interlaminar shear and impact strength since more energy is required to separate the CNTs from CF as well as pulling CNTs out from the matrix [6], [7].

Multifarious experimental, computational and analytical investigations have been carried out in order to characterize and ameliorate the interfacial and interlaminar properties of composite structures [8], [9], [10]. Thus, improvement of fiber-matrix interfacial properties plays a momentous role which augments the overall mechanical behaviors, however, with poor interfacial strength, debonding occurs, resulting in a weaker composite structure [11]. Different approaches such as experimental investigation, analytical method and numerical/ finite element analysis can be used to investigate the mechanical properties of CCFM hybrid composites.

Owing to the exceptional characteristics of CNTs, by incorporating them into conventional composites, multi-scale hybrid composites are being developed due to their outstanding behaviors in obviating cardinal drawbacks of conventional composites regarding interfacial and interlaminar properties, by altering the fiber-matrix interface region [12]. In the aerospace, automotive and wind-turbine industries, the carbon nanotube coated–fiber multi-scale (CCFM) hybrid composites can promisingly fulfill structural, thermal, and environmental demands for the

long-term structural and environmental durability, reduction of fuel consumption and efficient energy generation, remarkably better than conventional composites and nanocomposite materials. Hence, CCFM hybrid composites are considered as a new era of composite materials which can be employed in different industries. So, due to time-consuming and expensive experimental methods of such materials, obtaining the mechanical properties of such materials through analytical and numerical approaches is of crucial importance.

1.2 Motivations and Steps

1.2.1 Motivations

Carbon nanotubes have been proved to be a promising candidate material for augmenting the mechanical and physical properties of the traditional fiber-reinforced polymer composites, particularly for improving the interfacial and transverse mechanical properties [13], [14]. This scientific interest is motivated by the fact that CNTs have an axial young's modulus ranging between 300-1000GPa depending on CNT's lattice structure and CNT's walls, while their theoretical elongation to break reaches 30-40% [15], [16]. Specifically, grafting or depositing CNTs on the fiber surfaces through the chemical vapor deposition (CVD) [17] and electrospray technique [18], etc., to form the fuzzy fiber (FF), is one of the most desirable and efficient techniques for fabricating multi-scale hybrid composites. In essence, composites with enhanced fibers are hierarchical reinforcing structures, in which the glass or carbon fibers are coated with CNTs, and the latter is embedded in the polymer matrix, as described in Figure 1.1.

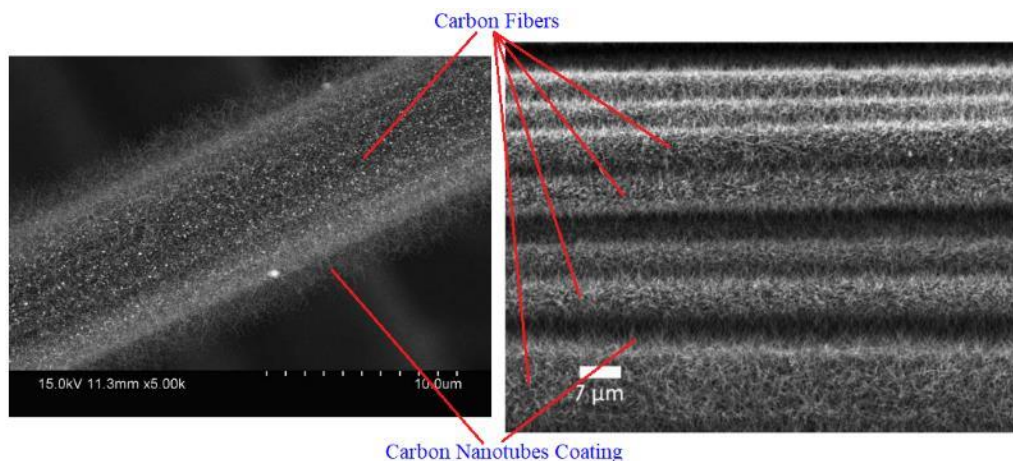


Figure 1.1: A single fuzzy fiber with predominantly radially oriented CNT's (left) [19], SEM of fibers with densely coated CNTs on the surface (right) [20]

To explain this well, Figure 1.2 [21] delineates a schematic diagram of the enhancement of a multiscale CF-CNT hybrid composite. As it is well known, the “withered tree” is easily pulled out from soil due to poor combination between its

main root and soil (Figure 1.2 (a)). However, for the thriving tree, there are many fibrous roots spreading into the soil, which greatly augments the interaction between the main root and soil, making the tree difficult to draw out from the soil (Figure 1.2 (b)). In CF-CNT polymer composite, the CNT acts as the fibrous root, CF is main root, and polymer matrix is like of soil (images inset in Figure 1.2). CNT with high mechanical strength has a reinforcing effect to ameliorate the load-carrying capacity of polymer matrix. More importantly, CNT can enhance the interfacial effect between CF and surrounding matrix, which makes the load transfer from matrix to CF efficiently, and also carry a part of the applied load to decrease the stress concentration around core fiber [21].

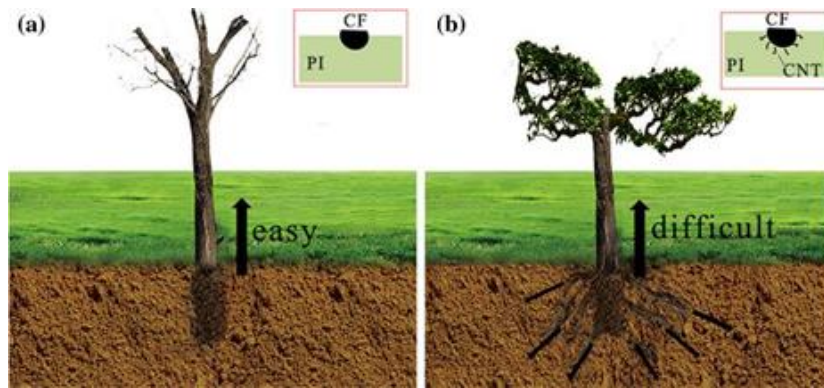


Figure 1.2: Schematic diagram of (a) withered tree (representing pure fiber) and (b) thriving tree being pulled out [21]

Apart from the experimental methods which is time consuming and expensive tasks for investigating CCFM hybrid composites, the increasing application and development of new fuzzy fiber (coated fibers) composites and their structural components have also flourished a novel research sphere from the simulation communities aiming at identifying the nano/microstructure properties of such composites. Hence, this thesis is devoted to proposing and developing new analytical method and novel multi-scale finite element analysis for investigating the mechanical properties and stress analysis of such composites which can be utilized in designing of nano-engineered multi-scale hybrid composites (NMHC).

1.2.2 Steps of Research

Following steps are pursued in this thesis:

1. Firstly, at the lowest scale, nanoscale, a thorough assessment is carried out regarding mechanical properties of various nanomaterials such as carbon nanotubes and nan-clay. The mechanical properties of nanomaterials are then acquired using multi-scale finite element analysis and different analytical approaches.

2. To provide a bottom-top computational modeling framework, at the next step (micro/meso scale), the interaction between nanomaterials and surrounding polymer are entirely investigated. For instance, the non-bonded interphase (weak Van der Waals interactions) between CNT and polymer or nan-clay and polymer is simulated through Cohesive Zone Theory (CZT), or nonlinear spring/beam elements and the mechanical properties and elastic moduli of final nanocomposite materials are obtained. Employing accurate numerical and theoretical methods and obtaining precise results at this section are of utmost importance since the constructed nanocomposite in this section will be later utilized as a coating region on fiber surface or inter-ply medium in the nano-engineered multi-scale hybrid composites. The novelty at this step encompasses the multi-scale modeling and non-bonded interactions simulation between CNT and surrounding matrix through non-linear finite element analysis.
3. Then, the nanocomposite medium is incorporated into composite materials. Various types of coating regions (nanocomposite materials) encompassing axially, radially, and randomly oriented CNTs are utilized on the core fiber surface in the laminated composites. At this step, two approaches are followed in this thesis, (1) numerical analysis through FEM and, (2) analytical method. Regarding the developed/proposed analytical method, the Eshelby–Mori–Tanaka method in conjunction with equivalent continuum approach is utilized to obtain the mechanical properties of nanocomposite/ coating region at micro/ meso scale. Regarding the developed FEA, a multi-scale FEM framework is proposed, and the subroutine codes are written to simulate and obtain the mechanical properties of nanocomposite and CCFM hybrid composites.
4. In the next step, a 3D multi-scale finite element analysis is performed to investigate the interfacial shear and radial stresses of CCFM hybrid composites which is the subject of Chapter 5. In accordance with the published articles, majority of studies were dedicated to the elastic moduli of hybrid composites. Furthermore, a detailed 3D multi-phase model which is capable of capturing all length-scale parameters and considering CNTs' orientations and debonding is lacking. Hence, to scrutinize the interfacial strength of CF–CNT hybrid composite, this chapter proposes a 3D multiscale finite element model of carbon fiber-carbon nanotube reinforced hybrid composites, taking into account all the parameters covering from nano-to macro-scale and considering debonding damage between CNTs and surrounding matrix.
5. On the other hand, 3D stress analysis is carried out to analyze the thermal residual stresses of CCFM hybrid composites employing energy minimization method, and remarkable improvement is observed with respect to conventional composite structures. This issue is the subject of Chapter 6. It should be mentioned that majority of studies in this subject was devoted to residual stress analysis of conventional composite materials. Owing to the lack of a straight and efficient method for interfacial stress analysis of multi- scale hybrid composites, a micromechanics modeling approach in conjunction with energy

minimization method is developed in this chapter, capable of obtaining a closed form solution for such materials and remarkably decreasing the computation time with respect to finite element analysis. To this end, a CNT-coating region with different configurations including axial, radial, and random oriented CNT is considered around the carbon fiber. Utilizing the proposed method, the influence of CNT-coating on the fiber–matrix thermal residual stresses is parametrically assessed. It should be noted that the axial, hoop, and radial stresses are considered in the energy formulation, for sake of achieving more accurate outcomes of the residual stress distributions.

6. Once the methods are developed and the targets are achieved, parametric study is performed considering different variables such as CNT volume fraction, fiber volume fraction, matrices materials, core fibers materials, coating thicknesses, etc.
7. In the last chapter, a novel technique is proposed regarding bending stress analysis of CCFM composite beam. To this end, this chapter furnishes a thorough analytical technique encompassing multi-scale modeling and bending stress analysis in which the former comprises the effective parameters of all length scales from nano- to macro-scale whereas the latter is conducted through the Refined Zigzag Theory (RZT). The hierarchical multi-scale modeling is performed utilizing the Eshelby–Mori–Tanaka method and composite cylinder assemblage (CCA) in conjunction with an equivalent continuum approach. Finally, the four RZT kinematic variables are acquired for CNT coated- fiber multiscale composite beam which is capable of applying parametric study in terms of CNT volume fraction, coating thickness, CNT orientation in the coating region and material and volume fraction of the core fiber.
8. All the methods provided in this thesis can be used as viable tools for future analysis and design of CCFM composite structures and are validated by published experimental data or obtained finite elements results.

1.3 Objectives and Major Achievements

1.3.1 Objectives

The chief purpose of this thesis is to propose and develop both multi-scale computational and analytical methods to predict the mechanical properties, stress distribution and interfacial strength of CCFM hybrid composites. Both proposed methods possess their own features regarding analysis time, advantages, limitations, accuracy, etc. It is worth mentioning that the proposed techniques in this thesis can be utilized for any types of the loading conditions and capable of considering different nanomaterials, different core fibers and different matrices within CCFM

hybrid composites. The following issues have been exploited and combined to achieve the goals in this research:

1. Determining the mechanical properties of nanomaterials at nanoscale; defining the non-bonded interactions between nanomaterials and surrounding matrix and simulating through Cohesive Zone Theory (CZT) or nonlinear spring elements.
2. Constructing Representative Volume Element (RVE) consisting of core fiber, coating region (nanomaterials) and surrounding matrix capable of considering various materials properties and loading conditions.
3. To make a comprehensive assessment, various coating regions (i.e., nanocomposite materials encompassing CNT and matrix), namely axially, radially and randomly oriented CNTs have been determined. The Eshelby–Mori–Tanaka method in conjunction with equivalent continuum approach are employed to attain the mechanical properties of various coating regions.
4. Employing different methods such as energy minimization method, multi-scale finite element analysis and RZT method, the interfacial and bending stresses analyses of CCFM composite are thoroughly conducted.

1.3.2 Major Achievements

This thesis investigates novel advanced laminated composites so-called ‘Carbon Nanotube Coated–Fiber Multi-Scale (CCFM) Hybrid Composites’ which demonstrate remarkable mechanical, thermal, and electrical properties. Specifically, this research is devoted to investigating the mechanical properties and stress analysis of CCFM hybrid composites and representing major improvements on the various critical parameters that are significant in designing of these materials. The proposed methods in this thesis introduce parametric study analysis (i.e., effect of volume fraction/ material of the core fiber, core fiber orientation, CNT volume fraction, CNT coating thickness around core fiber, etc.) covering all effective parameters at each scale from nano to macro which can be used as a viable tool for future designing of CCFM hybrid composite structures in different industries such as aerospace, automotive, high-speed boats, etc. The major achievements have been provided as ISI papers and are listed in Table 1.1 Published article during PhD degree, published during PhD program.

Authors	Title	Journal	Year	Chapter
Reza Malekimoghadam, Marco Gherlone	Bending Analysis of CNT Coated-Fiber Multi-Scale Composite Beams Using the Refined Zigzag Theory, 2022	is being Submitted	2022	7
R. Malekimoghadam, U. Icardi, Seyyed Ahmad Hosseini	The Influence of Carbon Nanotube Coated-Carbon Fibers on Thermal Residual Stresses of Multi-Scale Hybrid Composites: Analytical Approach”, <i>International Journal of Solids and Structures</i> , 233 (2021) 111212 https://doi.org/10.1016/j.ijsolstr.2021.111212	Elsevier/ International Journal of Solids and Structures	2021	6
R. Malekimoghadam, S. Krause, S. Czichon	A Critical Review on the Structural Health Monitoring Methods of the Composite Wind Turbine Blades”, <i>Lecture Notes in Civil Engineering</i> , 2021, 110, pp. 409–438, Springer Books Series https://doi.org/10.1007/978-981-15-9121-1_29	Springer/ Lecture Notes in Civil Engineering	2020	Internship in Germany
R. Malekimoghadam, U. Icardi	Prediction of Mechanical Properties of Carbon Nanotube-Carbon Fiber Reinforced Hybrid Composites Using Multi-Scale Finite Element Modelling”, <i>Composites Part B: Engineering</i> , 177 (2019) 107405 https://doi.org/10.1016/j.compositesb.2019.107405	Elsevier/ Composites Part B: Engineering	2019	5
M. Zahedi, R. Malekimoghadam, R. Rafiee, U. Icardi	A Study on Fracture Behavior of Semi-Elliptical 3D Crack in Clay-Polymer Nanocomposites Considering Interfacial Debonding”, <i>Engineering Fracture Mechanics</i> , 209 (2019) 245–259 https://doi.org/10.1016/j.engframech.2019.01.031	Elsevier/ Engineering Fracture Mechanics	2019	3

Table 1.1 Published article during PhD degree

1.4 Outline of the Thesis

Firstly, it should be mentioned that the arrangement of the chapters in the thesis are made in a manner of following the bottom-top multi-scale modeling of the composite structures from nano (CNT), micro (nanocomposite RVE) to macro scale (hybrid composite with coated fiber). Hence, chapters 2 and 4 represent a literature review regarding CNT/ nanocomposites and multi-scale hybrid composites, respectively, while chapters 3, 5, 6 and 7 are based on the author’s papers during PhD program.

In Chapter 2, a literature review is performed regarding CNTs and CNT reinforced nanocomposites at nano/ micro scales and some principles and fundamental issues associated with the modeling procedure, processing and analysis methods are presented. Firstly, the mechanical and physical properties of CNT are reviewed. Then, the CNT fabrication & processing, modeling and analytical approaches are presented to obtain the mechanical properties of CNT as a fundamental constituent in CCFM hybrid composites for fiber coating or inter-ply applications in laminated composites. In the following, a full-scale investigation into CNT-polymer nanocomposite is carried out encompassing CNT/ Polymer interactions, different types of multi-scale modeling (such as hierarchical, concurrent, continuum modeling, etc.), fabrication & processing of nano-composite materials.

Chapter 3 is based on the author's paper during PhD program which elaborates a study on fracture behavior of clay-polymer nanocomposites. The nano-clay structure and mechanical properties are assessed as another significant nanomaterials that can be utilized in CCFM hybrid composites as a coating region or inter-ply medium in laminated composites. Having determined the nano-clay/ polymer interactions, the multi-scale modeling of whole nanocomposites is then represented. In the next step, the presence of semi-elliptical 3D crack is assessed, and the J-Integral/ energy released rate for this structure is acquired in comparison with the matrix without reinforcing agent.

In Chapter 4, a literature review is carried out regarding fundamentals of carbon nanotube coated-fiber multi-scale (CCFM) hybrid composites. The fabrication process and remarkable engineering advantages and outcomes are provided considering different engineering applications such as ILSS, IFSS, (structural health monitoring (SHM), thermal and electrical conductivities.

Chapter 5 is based on the author's paper during PhD program in which an important investigation is conducted on the interfacial shear and radial stresses in CCFM hybrid composites. A framework of multi-scale modeling of CCFM hybrid composites is proposed which is capable of parametric study and simulating wide range of such materials with different mechanical properties. Moreover, two hybrid systems in multi-scale composites are introduced and a crucial result regarding interfacial strength is disclosed for the mentioned systems. The obtained outcomes are then compared with conventional composites to demonstrate the benefits of using CCFM hybrid composites in which the increasing of the structure's weight due to adding nanomaterials is negligible.

Chapter 6 is based on the author's paper during PhD program that reveals the effect of CNT coated-carbon fiber, on residual thermal stresses in multi-scale hybrid composites and the results are compared with conventional composites. Employing energy minimization method and Eshelby-Mori-Tanaka method in conjunction with equivalent continuum approach, a novel technique is proposed for determining the interfacial residual stress in CCFM hybrid composites. Finally, the improvements in interfacial strength are outlined and highlighted.

Chapter 7 is based on the author's paper during PhD program that furnishes a thorough analytical technique encompassing multi-scale modeling and bending stress analysis in which the former comprises the effective parameters of all length scales from nano- to macro-scale whereas the latter is conducted through the Refined Zigzag Theory (RZT). The hierarchical multi-scale modeling is performed utilizing the Eshelby-Mori-Tanaka method and composite cylinder assemblage (CCA) in conjunction with an equivalent continuum approach. Developing a Maple code for both modeling and stress analysis, therefore, the RZT kinematic variables are acquired for CNT coated- fiber multiscale composite beam which is capable of applying parametric study in terms of CNT volume fraction, coating thickness, CNT orientation in the coating region and material/ volume fraction of the core fiber.

Chapter 2: Principles of Nanocomposite Materials

Abstract: This chapter provides some principles, fundamental issues, and review regarding nano-composite materials. Firstly, the mechanical and physical properties of CNT are reviewed. Then, the fabrication process, finite element modeling and analytical approaches are presented to obtain the mechanical properties of isolated CNT as a fundamental constituent in CCFM hybrid composites for fiber coating or inter-ply applications. In the following, a full-scale investigation into CNT-polymer nanocomposite is carried out encompassing CNT/ Polymer interactions, different types of multi-scale modeling (such as hierarchical, concurrent, continuum modeling), fabrication and processing of nano-composite materials.

2.1 Fundamentals of Carbon Nanotubes (CNTs)

As the most important constituent in carbon nanotube coated–fiber multi-scale (CCFM) hybrid composites, carbon nanotubes can be used as a coating region of core fiber or as an inter-ply medium. Thus, different aspects and features of CNTs are discussed in this section. Carbon’s outstanding capability to bond with many elements makes it the most versatile element in the periodic table. The existence of different structural and geometric isomers, and enantiomers, found in multifarious structures, is a direct consequence of the diverse bonds and their corresponding geometries that carbon can form [22]. The possible configurations of the electronic states of an atom, known as hybridization, are responsible for the geometry of carbon allotropes and their properties [22]. Graphite, diamond, buckminsterfullerene, and nanotubes are four allotropic forms of carbon in the solid phase.

The discovery of CNTs has stimulated major controversy among the scientific communities over recent years as “who should be given credit for the discovery of multiwalled carbon nanotubes (MWCNTs)?” [23]. A review of the literature on the history of CNTs indicates that most scientists had cited Iijima as the discoverer of MWCNTs because he provided the first unequivocal evidence of MWCNTs in 1991 [24], while recent investigations have traced the discovery of MWCNTs back to the early 1950s. In contrast with MWCNTs, the discovery history of single-walled carbon nanotubes (SWCNTs) is perfectly clear. The first reports on the formation of SWCNTs were submitted to the June 17th issue of *Nature* in 1993 by two independent groups, one by Iijima and Ichihashi [25], the other by Bethune et al. [26]. The significant aspect of the discovery of SWCNTs is that they are more

fundamental than MWCNTs, so they have supported a large body of theoretical studies and predictions [23].

2.1.1 CNT Structure and Physical Properties

CNT Structures: CNTs can be considered as rolled-up graphene sheets forming hollow seamless cylinders. CNTs usually exist in two forms, namely (a) SWCNTs, comprising a single graphene layer, and (b) MWCNTs, encompassing two or more concentrically rolled graphene sheets separated from each other by approximately 0.34 nm due to van der Waals forces between adjacent layers [23]. A schematic representation SWCNT and MWCNT are depicted in Figure 2.1 [27], in which typical dimensions of length, diameter, and separation distance between two graphene layers in MWCNTs are shown. CNTs might be considered as a one-dimensional (1D) nanostructure owing to their high aspect ratio, which can be greater than 1000.

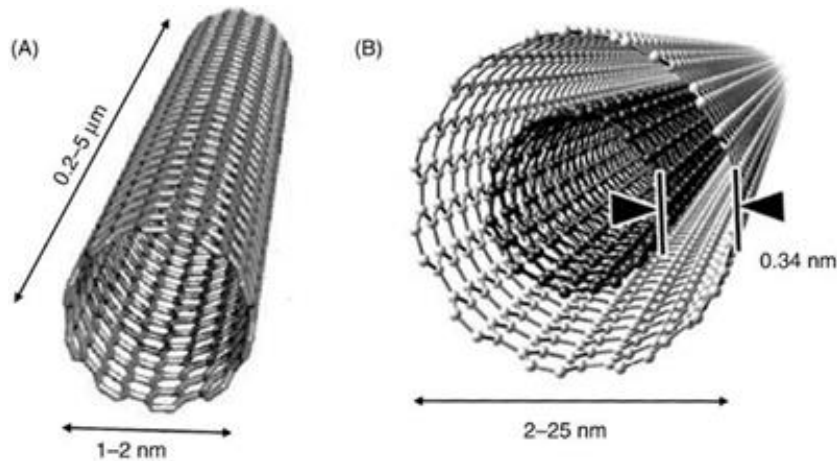


Figure 2.1: Schematic diagram of (A) SWCNT. (B) MWCNT [27]

The chemical bonds in CNTs are essentially sp^2 bonds, similar to those of graphite. The curvature, however, results in quantum confinement and σ - π rehybridization; that is, forcing three σ bonds to be placed slightly out of plane and, for compensation, delocalizing the π orbital more outside the tube. This makes CNTs mechanically stronger, thermally, and electrically more conductive, and chemically and biologically more active than graphite [23]. The wall of CNT can be imaginary generated by rolling up a graphene sheet into seamless tube with a constant radius. An SWCNT is a hollow cylinder of a graphene sheet, so the hexagonal honeycomb lattice of the graphene is used to describe the structure of the SWCNT which is exhibited in Figure 2.2 [28]. For this purpose, the chiral vector of the CNT, C_h , and translation vector, T , are introduced. The vector C_h determines the circumference on the surface of the tube connecting two crystallographically equivalent sites on a 2D

graphene sheet. Vector T is parallel to the CNT axis, but perpendicular to the chiral vector.

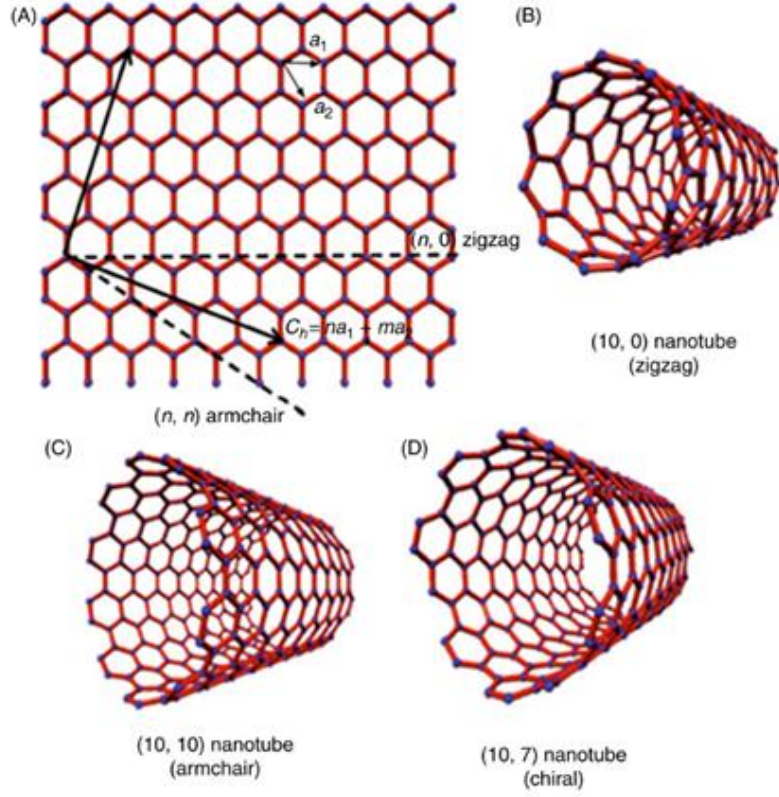


Figure 2.2: Schematic representation of the relation between nanotubes and graphene [28]

C_h can be uniquely characterized by a pair of integers (n, m) , known as indices, corresponding to basis vectors a_1 and a_2 of the graphene lattice:

$$C_h = na_1 + ma_2 \quad (2.1)$$

The nanotube diameter, d_{CNT} , can be calculated by:

$$d_{CNT} = \frac{a}{\pi} \sqrt{m^2 + mn + n^2} \quad (2.2)$$

where C_h is the length of the chiral vector, $a = |a_1| = |a_2| = \sqrt{3} a_{C-C}$ is the lattice constant of graphene, and $a_{C-C} = 0.142$ nm is the C–C bond length. The chiral angle θ , the angle between the vector C_h and the basis vector a_1 , is given by:

$$\theta = \tan^{-1} \left(\frac{\sqrt{3} m}{m + 2n} \right) \quad (2.3)$$

Depending on how the graphene sheet is rolled up, three individual types of CNTs are distinguishable: (1) armchair, (2) zigzag, and (3) chiral. The (n, m) CNTs with m= n correspond to armchair CNTs and m= 0 to zigzag CNTs. The zigzag and armchair CNTs are also recognized, by chiral angles of $\theta = 0$ and $\theta = 30$ degree, respectively. These two types of CNTs are named from the shape of the cross-sectional ring, as displayed at the edge of the nanotubes in Figure 2.2 B-C, respectively. All other (n, m) CNTs with $n \neq m \neq 0$ are commonly referred to as chiral CNTs, which correspond to chiral angle of $0 < \theta < 30$ degree (Figure 2.2 D).

MWCNTs are a group of coaxial SWCNTs, possibly with different chiralities, so the investigation of their physical properties is more complicated than that of SWCNTs. Combining different diameters and chiralities, which plays an important role in the transport properties of CNTs, noticeably the electronic ones, leads to many individual nanotubes, each with its own distinct electronic, mechanical, and thermal properties [23].

Physical Properties- Electronic: The unique structure of CNTs yields many exceptional properties such as high electrical and thermal conductivities, high tensile strength, high ductility, and high thermal stability, which make them suitable for various applications, such as gas sensors [29], energy storage systems and electrodes of batteries and capacitors [30], catalyst supports [30], used alone or in composite forms [31], and thin film. This section provides brief overviews on some of the unique electronic, mechanical, and thermal properties of CNTs. The superior electronic properties of CNTs have drawn the greatest attention in CNT research and applications [32]. The nanometer dimensions and the highly symmetric structure of CNTs as well as the unique electronic structure of a 2D graphene sheet are listed as the main reasons for the outstanding electronic properties of 1D CNT structures [33]. Earlier theoretical calculations [34] and later experimental measurements [35] have introduced many peculiar electronic properties of CNTs, for example, the metallic and semiconducting characteristics of an SWCNT and the quantum wire feature of an SWCNT, SWCNT bundles, and an MWCNT [32]. As previously stated, the SWCNT can geometrically be viewed as a graphene sheet rolled up to form a hollow cylinder; so, the physics behind the electronic properties of CNTs can be traced back to the electronic structure of graphene. Graphene is a zero-gap semiconductor while early theoretical calculations [35] [36] have predicted that SWCNTs can be either metals or semiconductors with different-sized energy gaps. The theory has proved that the electronic properties of SWCNTs depend sensitively on the diameter and helicity of the tubes (indices (n, m)). Concisely, it can be stated that by solving the periodic boundary condition [37], for varieties of (n, m) SWCNTs led to the following general rules: (n, n) SWCNTs, also known as armchair SWCNTs, are

always metallic, independent of SWCNT curvature due to their symmetry; (n, m) SWCNTs with $n - m = 3q$, where q is a nonzero integer, are very tiny-gap semiconductors; and all SWCNTs with $n - m = 3q \pm 1$ are large-gap (~ 1.0 eV for $d_t \sim 0.7$ nm) semiconductors [23]. Experiments have verified that, at low temperatures, a single metallic SWCNT [38], a SWCNT rope [39], or a MWCNT [40] inherently behave like a quantum wire, in which the conduction appears to occur through well-separated discrete electron states that are quantum-mechanically coherent over distances exceeding many hundreds of nanometers, due to the confinement effect on the tube circumference. The system acts like an elongated quantum dot at adequately low temperatures [32]. The unmarked and easily predictable electronic properties and simple structure of CNTs have attracted remarkable attention in applications of nanotubes in nanoelectronics. The diameter-dependent energy gap has put a spotlight on the semiconducting SWCNTs [23]. The simple geometry of SWCNT-based field-effect transistor (FET) imparts them a huge advantage over other types of FETs. Semiconducting SWCNTs can be the key component in a single-electron transistor because of their 1D nature. The high conductance sensitivity of SWCNTs to the electrostatic environment, emanating from their considerable surface-to-volume ratio, makes the semiconducting SWCNT a promising candidate for memory applications. Moreover, SWCNTs have also been used for constructing diodes [27].

Physical Properties- Mechanical: The mechanical properties of CNTs are a direct consequence of the nature of the chemical bonds between the carbon atoms and of the particular geometrical arrangement of such bonds in CNTs. Majority of the remarkable mechanical properties of CNTs were first predicted theoretically [41] and then confirmed through experimental investigation [42]. Most theoretical calculations were conducted on defect-free CNTs and have provided consistent results. Some other investigations were devoted to evaluating the influence of different types of defects, such as Stone–Thrower–Wales (STW) defect, vacancy defects, etc., on the CNTs’ mechanical properties [43]. Young’s modulus and the elastic response to deformation are two important parameters that characterize the mechanical properties of CNTs. In the elastic region, experimental measurements and theoretical calculations demonstrated that a CNT is as stiff as diamond with the highest Young’s modulus and tensile strength [44]. It is worth mentioning that Young’s modulus of CNT is independent of tube chirality [45], but dependent on tube diameter. The SWCNTs with diameters between 1 and 2 nm are expected to have the highest value of Young’s modulus, approximately 1 TPa. The Young’s modulus for MWCNTs is higher than SWCNTs, typically 1.1–1.3 TPa, because the Young’s modulus of an MWCNT takes the highest Young’s modulus of the SWCNTs contributed in the MWCNT plus contributions from coaxial inter-tube coupling or van der Waals forces [32].

The superior elastic response of a CNT to deformation has also attracted special attention. Atomic force microscopy (AFM) measurements [45] have divulged that CNTs can be bent to form sharp U-tubes and loops with small curvatures, testifying

to their flexibility, toughness, and capacity for reversible deformations [33]. Although most hard materials fail with a strain of 1% or less owing to propagation of dislocations and defects, CNTs can sustain up to 15% tensile strain before fracture [23]. Thus, assuming 1 TPa for Young's modulus of an SWCNT, its tensile strength can be as high as 150 GPa, which is an order of magnitude higher than any other material. Such a high strain is ascribed to an elastic buckling through which high stress gets released [44]. A figure of CNT resilience is exhibited in Figure 2.3 [46], in which the bends seem fully reversible up to very large bending angles. As it can be seen, Figure 2.3 A and B show single kinks in the middle of single-walled nanotubes with diameters of 0.8 and 1.2 nm, respectively, while Figure 2.3 C and D depict a multiwalled tube (with diameter of ~ 8 nm) showing a single kink and a two-kink complex.

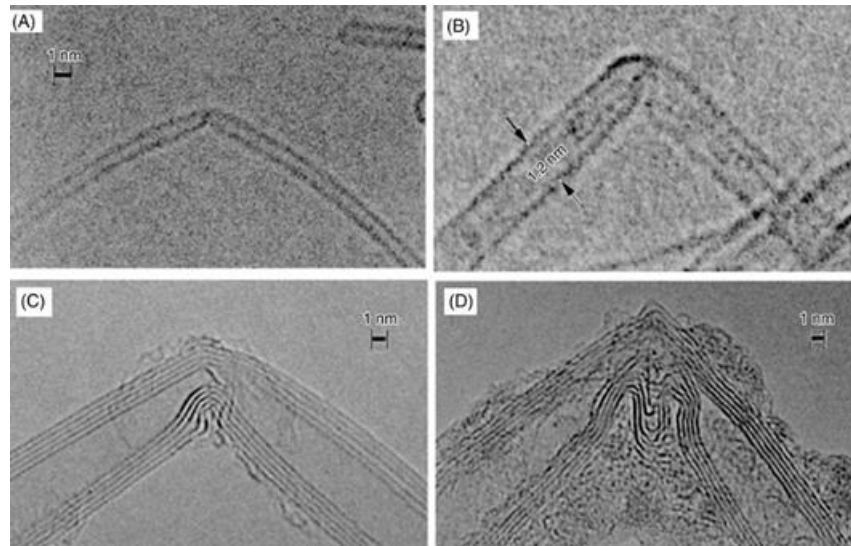


Figure 2.3: HRTEM images of bent CNTs under mechanical duress [46]

Table 2.1 [44] shows the calculated Young's modulus and tensile strength for a (10, 10) SWCNT and an MWCNT in comparison with other materials.

Materials	Young's Modulus (GPa)	Tensile Strength (GPa)	Density (g/cm ³)
MWCNT	1200	~ 150	2.6
SWCNT	1054	~ 150	1.3
Graphite (in-plane)	350	2.5	2.6
Steel	208	0.4	7.8
Wood	16	0.08	0.6

Table 2.1 Mechanical Properties of Carbon Nanotubes Compared with Some Engineering Materials [44]

The high stiffness, large tensile strength, and the capability to sustain large deformation without fracture make CNTs attractive for various applications

including high-performance composites, high-energy-absorbing materials, hydrogen and VOC absorbers for the environmental applications [31], and nanoelectromechanical systems.

Physical Properties- Thermal: the exceptional heat capacity and thermal conductivity of diamond and graphite have raised researchers' expectations that CNTs might display similar thermal properties at room and elevated temperatures. The thermal properties of CNTs, nonetheless, have not been as extensively studied as their electronic and mechanical properties, in part because the required techniques for such studies are still under development. The CNTs show a broad range of thermal properties stemming from their relation to the corresponding 2D graphene sheet and from their unique structure and nanometer dimensions [33]. Thermal conductivity, the same as electrical conductivity, is 1D for CNTs. Therefore, measurements provide a wide range of 200–6000 W/(m·K), implying a great dependence upon the sample quality and alignment [32]. Experimental measurements and theoretical calculations demonstrated that the thermal conductivity of SWCNT ropes and of MWCNTs at room temperature could be in the range of 1800–6000 W/(m·K) [47]. In addition to the superb thermal conductivity, CNTs also exhibits excellent thermal stability. The thermogravimetric analysis of different carbon materials under air flow has proved that CNTs are much more resistant to oxidation than either graphite or C60, indicated by the onset temperature for weight loss and the peak temperature corresponding to maximum oxidation rate. The analysis showed a peak temperature of 695°C for CNTs, which was higher than that of C60 (420°C), diamond (630°C), and graphite (645°C) [48].

2.1.2 Engineering Applications of CNTs

Owing to their notable thermal conductivity, mechanical, and electrical properties, the literature is replete with various engineering applications of CNTs which shown in Table 2.2 [49]. These applications are discussed in this section under the following topics: structural reinforcement, coatings and films, electromagnetics, sensors, and actuators.

CNT Type	SWCNTs	MWCNTs
Manufacturing technique	<ul style="list-style-type: none"> • Arc discharge • Laser ablation method (Catalyst is required for synthesis) 	<ul style="list-style-type: none"> • CVD (can be produced without catalyst)
Young's modulus (GPa)	1054	1200
Diameter range (ID) nm	1.5–15	20-50
Most important applications	<ul style="list-style-type: none"> • Sensors • Electrodes • Nanodevices 	<ul style="list-style-type: none"> • Metal composites for polymers

Table 2.2 General Categorization of CNTs [49]

The applications of CNTs are not limited to the above-mentioned fields, and this section provides only the most important engineering applications of CNTs concisely. Worldwide commercial interest in CNTs is reflected in a production capacity that at present exceeds several thousand tons per year [49].

Structural Reinforcement: Currently, the most popular use for CNTs is in structural reinforcement. Many structures have been proposed ranging from everyday items (e.g., clothes and sports gear) to combat jackets and space elevators with respect to the CNT's superior mechanical properties [50]. The composite reinforcing is probably the most demanding application of CNTs. CNTs are a promising material as building blocks in hierarchical composite materials given their exceptional mechanical properties which is exclusively discussed and assessed in this thesis. In fact, this application range is widespread, ranging from expensive tennis rackets to aircraft body parts and spacecraft. NASA has invested large amounts of money in developing CNT-based composites for applications, such as the futuristic Mars mission, because experiments have confirmed that nanotubes are one of the stiffest structures ever made [51] [52].

As one the significant benefits, CNTs are also mixed with polymers and resins to increase their stiffness, strength, and toughness, e.g., adding ~1 wt.% multiwalled nanotubes (MWNT) to epoxy resin augments stiffness and fracture toughness by 6 and 23%, respectively, without compromising other mechanical properties [53]. However, this application has some limitations due to the improper/non-bonded interface between the CNTs and the polymer matrix [54]. Some applications of CNT-enhanced resin carbon fiber composites in wind turbine blades and hulls for maritime security boats are delineated in Figure 2.4 [55].

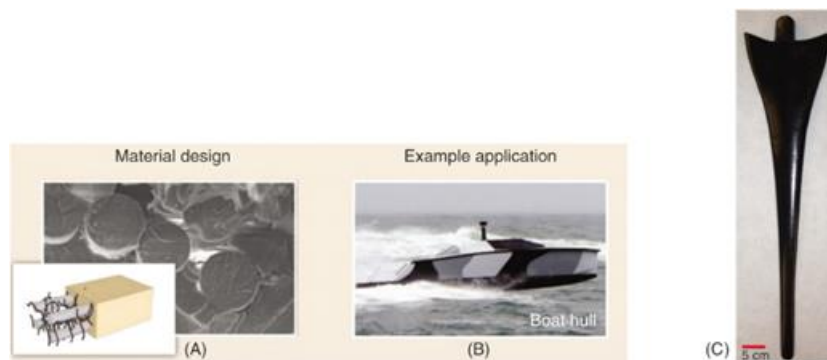


Figure 2.4: A) Micrograph showing the cross-section of a CF laminate with CNTs dispersed in the epoxy resin; (B) a lightweight CNT-fiber composite boat hull (C) CNT-reinforced polyurethane blade obtained by vacuum bag technique [55]

CNT-rich composites have many applications in automotive and aerospace engineering. CNT plastics have been utilized to enable electrostatically assisted painting of mirror housings, and fuel lines to dissipate electrostatic charge in the automotive industry [56]. Substituting carbon black cathodes with CNTs may have a significant impact on the development of lithium-ion batteries for electric and

hybrid vehicles due to an increase in energy density by prevention of electrode degradation, lower impedance, higher discharge capacity, and improved charging cycling [49].

Importantly, adding CNTs to aerospace materials could protect them against lightning strikes. As a novel, surprising and promising material in a recent research study, MIT experts have strengthened these advanced aerospace materials with what they call “nano-stitching.” Rows of CNTs perpendicular to the carbon microfibers fill the spaces between them, reinforcing the fiber layers without piercing them. The researchers demonstrated that these materials are not only 10 times stronger than those that don’t contain nanotubes, but they are also more than 1 million times more electrically conductive, which could provide a great protective medium for aircrafts from lightning strikes [57].

Moreover, high tensile strength and electrical conductivity of CNTs are exploited in developing CNT–metal matrix composites (MMCs). This material is still in the research phase, but the potential areas of application are nanonetworks, nanorobotics, and future soldiers. Some of the other significant structural applications of the CNTs are listed below [49]:

- CNTs can be used in reinforcement of turbine blades to enhance the strength of marine current turbines that must survive in the ocean [58].
- CNTs in concrete increase its tensile strength and halt crack propagation.
- CNTs may be able to replace steel in suspension bridges.
- The high strength-to-weight ratios of CNTs enable very high rotational speeds.
- Composites that use CNTs as secondary fillers are already commercialized (e.g., cranks, handlebars, front forks, etc., of road racing bikes from various manufacturers).
- Secondary filler CNT composites are also used in ice hockey sticks for durability and controllability.

Coatings and Films Applications of CNTs: CNTs are employed widely in marine current turbine coatings to reduce the effect of biofouling due to their nanostructure and hydrophobic nature [42]. Since they can discourage attachment of algae and barnacles, they are a possible alternative to environmentally hazardous biocide-containing paints [58]. Other coating applications of the CNTs (e.g., thin-film heaters, flame-retardant coating, transparent conductors, and electrostatic dissipative windows) are being followed industrially [49].

CNTs in Electromagnetics: Another appealing area of CNT applications is use as electrical conductors, semiconductors, and insulators. The light weight and remarkable electrical conductivity of CNTs enable them to be used as heat sinks for chipboards, as LCD screen backlights, and even as electrical protection in Faraday cages [59]. The electromagnetic parameters of a high CNT loading film have been characterized in recent years by analyzing the layer number of CNT laminate, CNT

alignment, and resin impregnation effects. The outcomes of experiments demonstrate [49]:

- The anisotropic electromagnetic characteristic of CNT film
- Increase of complex permittivity and decrease of shielding effectiveness with increasing layer number
- Decrease of conductivity and shielding effectiveness with resin impregnation into CNT film.

Taking the aforementioned characteristics into account, the possibility of using CNTs in several ways was discussed, such as [60]:

- as an alternative to tungsten filaments
- in magnetic fields development using coated MWCNTs
- as antennae for electromagnetic devices

In 2009, Park et al. [61] reported on a new assessment yielding enhanced electromagnetic shielding, utilizing CNT integrated with a reactive ethylene terpolymer (RET) with the luxury of incorporating reasonable dispersion with low electrical percolation volume fractions (~ 0.1 vol.%), yielding outstanding microwave shielding efficiency for electromagnetic interference (EMI) applications. They showed experimentally that both single-walled CNTs (SWCNT) and multiwalled CNT (MWCNT) based composites could be used for this purpose.

Sensors and Actuators Applications of CNTs: Thanks to their excellent thermal and electrical conductivity, CNTs are widely utilized in sensors and actuators development. Since the electrical conductivity of SWNTs changes when it encounters oxygen, NH₃, and nitrogen, they could be used in the manufacturing of chemical sensors with fast response time and small dimensions. CNTs are also used in nanoprobe application for different purposes, such as drug delivery, nanoelectrodes, high-resolution imaging, sensors, field-emitting devices, electrostatic force microscopes, etc. [49]. In 2013, Technical University of Munich (TUM) researchers in Germany reported on their new findings to demonstrate the way toward low-cost, industrial-scale sensors using CNTs. A new gas sensor was introduced for indicating the freshness level of food packages and for use in wireless air-quality monitors as their leading examples. Furthermore, new types of solar cells, and pressure and temperature sensors that could be built into electronic skin for robotic or bionic applications [49].

The most recent progress in this field was reported by IBM in 2015 regarding a breakthrough on CNT transistors. IBM researchers say they have overcome the major manufacturing challenge of how to combine nanotubes with the metal contacts that deliver electric current, which has been standing in the way of commercially viable nanotube devices [62]. They addressed the issue by altering the interface between a nanotube and the two metal contacts.

There are many other applications of CNTs in the engineering field such as Acoustic and Electroacoustic Applications, Biotechnological and Biomedical

Applications, Hydrogen Storage, Water Treatment, etc. which are excluded in this thesis for sake of brevity.

2.1.3 Processing and Fabrication

Although the growth mechanism of CNTs is not exactly known, new synthesis methods for higher yield, higher purity, and low defects of the produced CNTs are the main points of investigation being pushed forward by the burgeoning fields of nanotechnology and nanoscience, which have many ideas of possible applications. The most common synthesis techniques of CNTs are arc discharge, laser ablation, CVD (chemical vapor deposition), and PECVD (Plasma-Enhanced CVD) [63]. The mechanism of the SWNT synthesis in the arc discharge and laser ablation processes appears to be fairly simple. It is governed mainly by the dynamics of hot vapor cooling and carbon diffusion through the bulk metal catalyst particle. It allows intentional control of the arc and laser processes and is the basis for the successful scaling-up efforts of the arc process. Semiquantitative treatment of the arc and laser processes is possible, which prepares a basis for a detailed mathematical modeling of arc and laser ablation reactors. This is necessary to design practical processes for maximum productivity, yield, and quality of SWNTs. Scaling up the arc discharge processes of SWNT, double-walled carbon nanotubes, and MWNT production is possible and can be realized in practice on an industrial scale [63].

Significant advances have been achieved during the last years including the development of new CVD methods for mass production and for aligned growth on surfaces, both vertically and horizontally. Mass production and vertically aligned growth by CVD have been significantly boosted by the discovery of “super-growth,” adding small amounts of water to the CVD precursor or utilizing alcohol as the carbon feedstock, to proscribe the formation of amorphous carbon, and thus to enhance the formation of clean carbon nanotubes [63]. Figure 2.5 [32] displays MWNTs grown by thermal CVD at 750°C with ethylene feedstock and exploiting a catalyst preparation recipe. As it can be seen, a series of cylinder-shaped towers composed of MWNTs is produced, which are fairly uniform, about 200 μm in diameter and 400- μm tall.

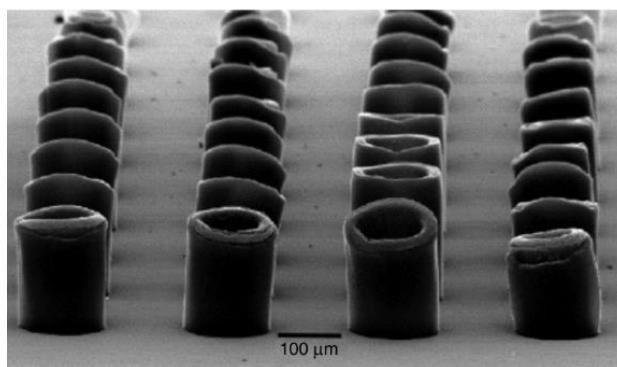


Figure 2.5: Cylinder-shaped multiwalled nanotube (MWNT) towers grown by thermal CVD [32]

It can be inferred that, among the foregoing techniques, the CVD-based methods appear to be the most suitable for large-scale CNT production because of their scalability. However, arc discharge and laser ablation suffer from many disadvantages for being expensive and uneconomical for large-scale production of CNTs, despite their high quality and yield of CNT produced. Admittedly, a fundamental key to further increase the control of carbon nanotube synthesis is the proper understanding of the different mechanisms of carbon nanotube formation, which determines its structure, electronic properties, and arrangement [63].

A comparison of the mentioned techniques considering different parameters such as synthesis temperature, nanotube graphitization, yield, and relative CNT quantity, etc., is represented in Table 2.3 [63].

Process	Laser ablation	Arc-discharge	CVD
Reaction Temperature	3000°C	3000- 4000°C	500- 1100°C
Per unit design cost	High	High	Low
Nanotube selectivity	Low	Low	High
Source of Carbon	Difficult	Difficult	Easy Available
Purification of CNT	High	High	Low
CNTs yield	70%	<30%	95-99%
Process nature	Batch	Batch	Continuous
Process parameter control	Difficult	Difficult	Easy to control
Energy requirement	High	High	Low
Reactor design	Difficult	Difficult	Easy to design reactor
Nanotube graphitization	High	High	Middle

Table 2.3 Comparison of different CNT processing methods [63]

2.1.4 Mechanical Properties of Isolated CNT

Experimentally Determined Young's Modulus of CNTs: Elastic modulus, or Young's modulus, is a primary material property required for mechanical and structural design. For continuum level, the elastic or Young's modulus is defined as the following [64]:

$$Y = \frac{1}{V} \frac{\partial^2 \varepsilon}{\partial E^2} \quad (2.4)$$

where Y is the Young's modulus, E is the direct uniform strain, and ε is the total strain energy. Due to the nanoscale size of CNTs, the difficulties associated with their handling in experiments give rise to uncertainty in the measurements. Most of

the experimental approaches to measure the elastic properties of CNTs involve the bending or vibrational response of the cantilever or fixed beam configuration of isolated CNTs. Treacy et al. [52] attached the bundles of carbon nanotubes to a 3-mm nickel ring and studied the vibrating free end of the CNTs using transmission electron microscope (TEM) at 300 and 600 K [52]. CNTs on the ring are treated as cantilever beams vibrating due to thermal loading. The vibration energy of the CNT is given in as following:

$$W_n = \frac{1}{2} C_u U_n^2 \quad (2.5)$$

where U_n represents the vibration amplitude of CNT in nth mode. The term, C_u , defined as effective spring constant, is obtained as follows:

$$C_u = \frac{\pi \beta_n^4 Y (a^4 b^4)}{16 L^3} \quad (2.6)$$

where β_n represent a constant related to the mode of vibration, Y is the Young's modulus, a , b , and L are the inner diameter, outer diameter, and the length of CNTs, respectively. Krishnan et al. used similar approach involving stochastically driven oscillator and reported the average Young's modulus equal to 1.3–0.4/+0.6 TPa [64].

Another experimental technique to define the Young's modulus of CNTs involves the application of atomic force microscope (AFM). Wong et al. [42] used AFM to calculate the Young's modulus and tensile strength of CNTs that they plotted the bending force-displacement response of cantilever (rod-like) CNTs using AFM tip of known spring constant. Table 2.4 shows the records of experimentally determined values of CNT Young's modulus [64].

Types of CNTs	Experimental Approaches	Young's Modulus (TPa)	References	Years
MWCNT	TEM	1.8	Treacy et al. [52]	1996
MWCNT	AFM	1.28	Wong et al. [42]	1997
MWCNT	SEM	1.0	Muster et al. [65]	1998
SWCNT	TEM	1.25	Krishnan et al. [66]	1998
MWCNT	AFM	0.81	Selvetatet al. [67]	1999
SWCNT	AFM	1.002	Yu et al. [68]	2000
MWCNT	AFM	1.2	Tombler et al. [69]	2000
MWCNT	TEM	1.25	Demczyk et al. [70]	2002
MWCNT	TEM	0.35	Guhados et al. [71]	2007
MWCNT	TEM	0.62	Ding et al. [72]	2007
SWCNT	EMA	0.97	Wu et al. [73]	2008

Table 2.4 Experimentally Obtained Young's Modulus of SWCNTs & MWCNTs [64]

Computationally Evaluated Young's Modulus of CNTs: Several computational approaches, ranging from highly sophisticated quantum mechanics–based density functional theory (DFT) and tight binding (TB) methods, molecular dynamics to molecular-mechanics (MM) supported quasi-continuum and equivalent continuum methods, have been applied to study the mechanical behavior of CNTs. Due to its well-defined and translational structural invariance along the length, the structural equivalency between SWCNTs and engineering structures, where C–C chemical bonds are simulated by truss or beam elements, has enabled researchers to apply the aforementioned continuum level approaches with acceptable level of success in studying the mechanical properties of CNTs [64]. This subject will be thoroughly addressed in the next section. Figure 2.6, shows the effect of chirality, CNT diameter and modeling approaches of CNT lattice structure (linear or nonlinear) on the Young's modulus of SWCNT. It is evident from the information provided that the Young's modulus of SWCNT is independent from chirality and diameter in nonlinear modeling approach.

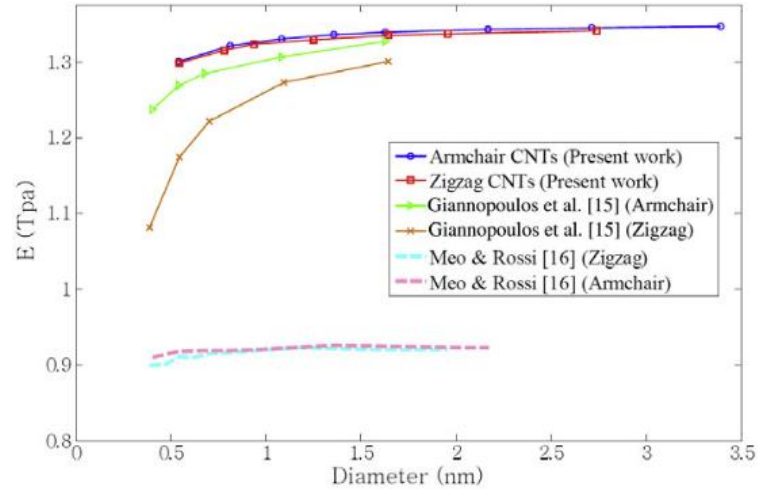


Figure 2.6: Variation of SWCNT Young's modulus with diameter and chirality through different computational modeling techniques [45]

Regarding radial elastic modulus, from the atomistic point of view, the out-of-plane bending behavior of local C–C covalent bonds can be directly related to bond inversion energy [74]. Significantly, for both SWCNTs and MWCNTs, the radial elastic modulus is much lower than their axial Young's modulus. Chen et al. [74] utilized modified molecular structural mechanics (MSM) to show that the depending upon the diameter (0.39–2.35 nm) of zigzag SWCNTs, the radial modulus of elasticity varies between 60 and 0.4 GPa, and for armchair SWCNTs (0.48 nm < SWCNT diameter < 2.38 nm) varies between 30 and 0.3 GPa.

Effect of Number of Concentric Sleeves: Ganji et al. [75] carried out a DFT-based study to show the effect of number of walls on the Young's and shear moduli of SWCNT, double-walled CNTs (DWCNTs), and triple-walled CNTs (TWCNTs). According to their calculations, for a fixed outer diameter, the CNT mechanical

properties decrease as the number of walls increase which the results are depicted in Figure 2.7.

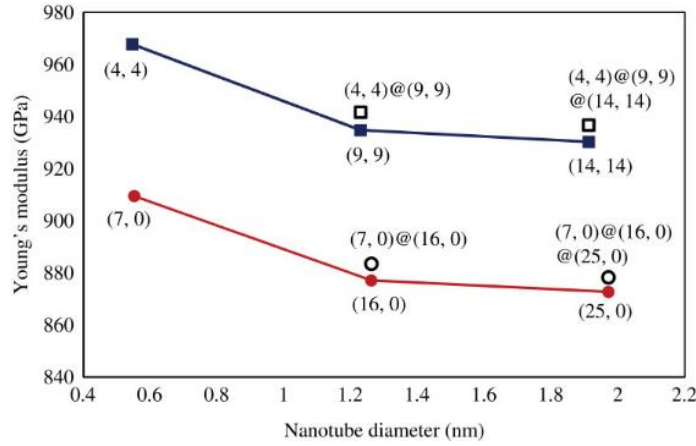


Figure 2.7: Effect of number of concentric tubes on the Young's modulus of MWCNT [75]

Tensile Strength of CNTs: In general, fracture is a dynamic process where strain or loading rate affect the material behavior and strength. The inelastic failure or fracture of CNTs is an interesting area of contemporary research. The fracture of CNTs involves energy relaxations by bond breaking, formation of defects, and propagation of defects by coalescence [64]. During the low strain rate loading, 90-degree rotation of C–C bond to form a “5–7–7–5” Stone–Wales defect is the preferred mechanism of defect formation. As the loading continues, the more such defects are nucleated and promote plastic flow of the CNTs by coalescing resulting in CNT fracture which is represented schematically in Figure 2.8 [76]. As a crucial issue, it can be seen that the formation of these defects along the length of CNTs takes place in a helical fashion and the overall movement of the “Stone–Wales slip” is chirality dependent [64].

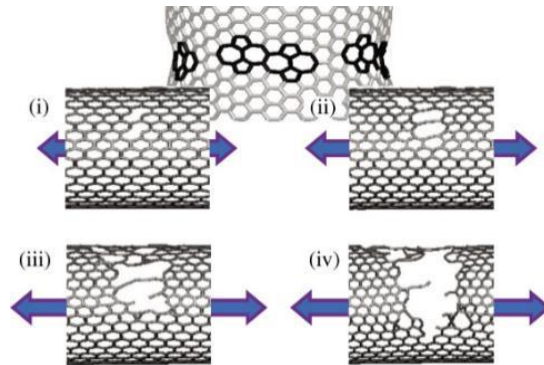


Figure 2.8: Formation and coalescence of Stone–Wales defect through different stages under the axial tensile loading [76]

Different research groups have carried out extensive investigations into obtaining the tensile strength of CNTs through experimental or computational methods. For sake of brevity, some results of experimentally and computationally

determined tensile strength of CNTs are listed in Table 2.5 and Table 2.6 [64], respectively.

References	Types of CNTs	$\sigma_{t, \max}$ (GPa)	Years
Falvo et al.	MWCNT	100-150	1997
Wagner et al.	MWCNT	55	1998
Walters et al.	MWCNT	45 \pm 7	1999
Demczyk et al.	MWCNT	150	2000
Yu et al.	MWCNT	11-63	2000
Ding et al.	MWCNT	10-66	2007
Khandoker et al.	MWCNT	48	2011

Table 2.5 Experimentally Obtained Tensile Strength of SWCNTs & MWCNTs [64]

References	Methods	Types of CNTs	$\sigma_{t, \max}$ (GPa)	$\epsilon_{t, \max}$	Years
Belytschko et al.	MD	(20,0) (8,8)	84	0.16	2002
Ogata and Shibutani	TB	(8,0) (8,8)	112 86.8	0.187 0.211	2003
Tserpes and Papanikos	ABC	(20,0) (12,12)	98 122	0.16 0.19	2007
Duan et al.	MM	(10,0) (10,10)	105.6 134	0.333 0.435	2007
Khare et al.	QM/MM	(10,0) (5,5)	106 147	0.181 0.247	2007
Baykasoglu et al.	MM/FEA	(10,0) (5,5)	95 122	0.16 0.21	2007
Jhon et al.	MD	(9,0) (5,5)	94 123	0.164 0.216	2016
Zhu et al.	MD	(8,0) (7,7)	101.8 105.9	0.273 0.235	2016

Table 2.6 Computationally Determined Tensile Strength of CNTs [64]

2.1.5 Modeling Techniques and Stress Analysis of CNTs

The theoretical efforts in modeling CNT behavior can be categorized in three categories as atomistic modeling, continuum modeling and nano-scale continuum modeling which are elaborated subsequently. Constructed models for CNT employing aforementioned approaches are shown in Figure 2.9 [77].

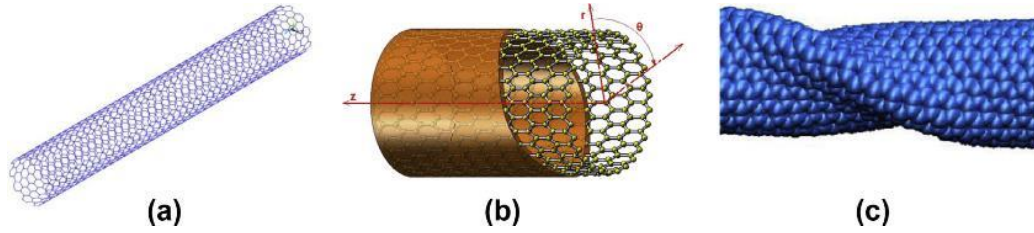


Figure 2.9: Constructed models of CNT using: (a) Nano-scale continuum mechanics, (b) continuum modeling using shell model and (c) atomistic modeling techniques [77]

Atomistic modeling: Atomistic modeling predicts the positions of atoms based on interactive forces and boundary conditions. This information is required to solve Schrodinger wave equation for obtaining chemical information on materials. Atomistic modeling techniques can be classified into three main categories, namely the molecular dynamics (MD), Monte Carlo (MC) and ab initio approaches. Other atomistic modeling techniques such as tight bonding molecular dynamics (TBMD), local density (LD), density functional theory (DFT), Morse potential function model, and modified Morse potential function model were also applied later on [77]. The first technique used for simulating the behaviors of CNTs and CNT's allotropes was molecular dynamic (MD) method [46]. This method uses realistic many-body inter-atomic potential functions (force fields) to calculate the total energy of a system of particles. When the total potential energy and force fields of a system are obtained, the realistic calculations of the behavior and subsequently, the properties of a system of atoms and molecules can be acquired. Although the main aspect of both MD simulations and MC methods is geared down to second Newton's law, MD methods are deterministic approaches, while MC methods are stochastic ones. Meanwhile, the ab initio techniques are accurate methods which are based on an accurate solution of the Schrödinger equation. Furthermore, the ab initio techniques are potential-free methods wherein the atoms forces are determined by electronic structure calculations progressively. In contrast, the MD and MC methods depend on the potentials that the forces acting on atoms are acquired by differentiating interatomic potential functions [77].

Continuum modeling (CM): Continuum mechanics-based models are utilized by many engineers to investigate properties of CNTs. The basic assumption in these theories is that a CNT can be modeled as a continuum structure which has continuous distributions of mass, stiffness, etc. The lattice structure of CNT is simply neglected in continuum modeling, and it is replaced with a continuum medium. It is important to carefully investigate the validity of continuum mechanics approaches for modeling CNTs which the real discrete nanostructure of CNT is replaced with a continuum one (see Figure 2.9b). The continuum modeling can be either accomplished analytical or numerically representing FEM. Different researchers applied continuum shell models to study the CNT properties. Yakobson et al. [78] showed similarities between MD simulation of CNTs and macroscopic shell model.

It has shown that mechanical properties of CNTs were strongly dependent on helicity and atomic structure of the tubes and obviously the curvature and chirality effects on the mechanical behavior of CNTs cannot be captured in an isotropic shell model, due to neglecting the discrete nature of the CNT geometry in this method.

Silvestre and co-workers [79] have shown that shallow shell theories (e.g., Donnell theory [80]) are not accurate for CNT analysis due to CNT non-shallow structure. Only more complex shell theories (e.g., Sanders theory [81]) are capable of reproducing the results of MD simulations. On the other hand, some parameters, such as wall thickness of CNTs are not well defined in the continuum mechanics. For instance, while a value of 0.34 nm which is interplanar spacing between graphene sheets in a graphite is widely used for tube thickness in many continuum models, Yakobson et al. [78] compared the molecular dynamics simulation results with the continuum shell model and fitted an effective thickness of carbon nanotubes to be 0.066 nm. Therefore, definition of wall thickness in modeling CNT using shell is a key parameter in the analytical simulation procedure. Using continuum approach, Tserpes et al. [82] employed 3D beam element in ANSYS to model the CNT in the RVE with surrounding polymer, in which the material properties of the 3D beam was adopted from the modeling of the CNT lattice structure at lower (nano) scale.

Nano-scale continuum modeling (NCM): In contrast to continuum modeling (CM) of CNTs where the whole nanostructure is replaced with a continuum medium, nano-scale continuum modeling (NCM) provides a rationally acceptable compromise in the modeling process by replacing C–C bond with a continuum element [77]. In other word, in nano-scale continuum modeling the molecular interactions between C–C bonds are captured using structural members whose properties are obtained by atomistic modeling. Development of nano-scale continuum theories has excited more enthusiasm by incorporating continuum mechanics theories at the scale of nano.

A comparison between the presented methods: atomistic modeling techniques are suffering from some shortcomings which can be summarized as: (I) inapplicability of modeling large number of atoms (II) huge amount of computational tasks (III) complex formulations. Other atomistic methods such as tight bonding molecular dynamic, local density, density functional theory, Morse potential model and modified Morse potential model are also available which are in need of intensive calculations [77].

On the other hand, continuum modeling originated from continuum mechanics are also applied to study mechanical behavior of CNTs. Comprising of analytical and numerical approaches, the validity of continuum modeling has to be carefully observed wherein lattice structure of CNT is replaced with a continuum medium. Numerical continuum modeling is accomplished through finite element modeling using shell or curved plate elements. The degree to which this strategy, i.e., neglecting lattice structure of CNT, will lead us to sufficiently accurate results is under question. Moreover, it was extensively observed that almost all properties of

CNTs (mechanical, buckling, vibrations and thermal properties) depend on the chirality of CNT; thus, continuum modeling cannot address this important issue [77].

Recently, nano-scale continuum mechanics methods are developed as an efficient way of modeling CNT. These modeling techniques are not computationally intensive like atomistic modeling and thus they are able to be applied to more complex system without limitation of short time and/or length scales. Moreover, the discrete nature of the CNT lattice structure is kept in the modeling by replacing C–C bonds with a continuum element. Since the continuum modeling is employed at the scale of nano, therefore the modeling is called as nano-scale continuum modeling [77].

The performed investigations in literature addressing mechanical properties, buckling, vibrations and thermal behavior of CNT were reviewed and classified on the basis of three aforementioned modeling techniques by Rafiee and Malekimoghadam [77].

Concerning CNTs buckling properties, many researchers have conducted the simulation using MD methods. The shell theories and molecular mechanic structure simulation are also applied to assess the CNTs buckling in order to avoid time consuming simulations. But, for the specific case of buckling behavior, it is not recommended to scarify the lattice structure of CNT for less time-consuming computations. But instead, nano-scale continuum modeling is preferred. Comparing the results with the obtained results of MD simulation, it can be inferred from literature that for large aspect ratios (i.e., length to diameter ratio $L/d > 10$) the simple Euler–Bernoulli beam is reliable to predict the buckling strains of CNTs while the Timoshenko’s beam model or their non-local counterpart’s theory is needed for CNTs with intermediate aspect ratios (i.e., $8 < L/d < 10$) [77]. The Donnell thin shell theory [83] is incapable to capture the length dependent critical strains for CNTs with small aspect ratios (i.e., $L/d < 8$). On the other hand, Sanders shell theory [81] is accurate in predicting buckling strains and mode shapes of axially compressed CNTs with small aspect ratios.

From the dynamic analysis point of view, the replacement of CNT with a hollow cylinder has to be extremely avoided, despite the widely employed method. In other words, replacing CNT with a hollow cylinder will not only lead us to inaccurate results, but also there will not be any difference between and nano-structure in the form of tube with continuum level of modeling. It is a great importance to keep the lattice structure of the CNT in the modeling since the discrete structure of CNT play an important role in the dynamic analysis. From the vibration point of view, MD simulations are more reliable and NCM approaches are preferred to CM techniques using beam elements [77].

Finally, exploring thermal properties of carbon nanotubes is the field which is still under development and is an ongoing field of study in contrast to other moderate maturity which can be realized in above-mentioned areas of study. Generally, Boltzmann equation (BE) and fluctuation–dissipation relation are the two approaches

which have been utilized to calculate transport properties of materials based on phenomenological and linear response theory, respectively. The BE is in need of experimental data, but the fluctuation–dissipation relation with MD can be applied directly to calculate the transport coefficients in the linear response regime. Thus, the later has been received more attention among researchers, since performing experiments at the scale of nano is a challenging task. Hence, for novel materials and materials which are confronted to some difficulties in implementing experiments, molecular dynamics simulation has a unique advantage in predicting their thermal transport properties. From the investigations, it can be concluded the CNTs thermal conductivity strongly depends on chirality, diameter, and temperature [77].

Generally, it can be stated that while MD techniques are reliable and the most widely used techniques to investigate mechanical properties of nanostructures, their intensive computations are encouraged researchers to seek more appropriate tools such as continuum or nano-scale continuum modeling. While the replacement of CNT with a totally continuum medium in the form of either hollow or solid cylinder at the scale of nano is seriously vulnerable to capture the real behavior of CNT nanostructure, nano-scale continuum modeling can be considered as an acceptable approach overcoming the shortcomings of atomistic simulations. In other words, MD techniques can present more accurate results while they are suffering from huge computational efforts. Although, continuum and nano-scale continuum modeling significantly reduce required runtime for modeling, the degree to which they are able to capture the real behavior of nano-structure has to be carefully investigated. In contrast to continuum modeling wherein lattice structure of CNT is simply neglected, nano-scale continuum modeling simulates the lattice structure of CNT in the form of discrete structure. Despite the fact that nano-scale continuum modeling provides a powerful tool for characterizing mechanical behavior (mechanical properties, vibrations and buckling) of CNTs, they are still suffering from addressing the thermal characteristics of nano-structure, while MD simulations are reliable in this field. The development of nano-scale continuum mechanics is still developing and the ongoing subject of study. The fundamentals of these techniques are constructed at the scale of nano using atomistic modeling. Subsequently, the bridging between these two spaces is the most important issue which should be resolved prior to their application and can also pave their successful establishment [77].

Although the classical local elasticity models are able to analyze the wave propagation behaviors of CNTs in low wave numbers, they fail to estimate the wave propagation properties of CNTs in relatively high wave numbers since the material microstructure shows an important scale effect on relatively high wave numbers and the small-scaled parameters are absent in their constitutive relations [84]. To assess the size-dependent effect, the CNTs are usually modelled by using the nonlocal elasticity theory [85], whose stress at a reference point are assumed to depend not only on the strains at the reference point but also on the strains at all other points in the body. Nonetheless, nonlocal continuum theory cannot always predict the

behavior of nanostructures well, and therefore the capability of nonlocal continuum theory for predicting the physical behavior is questionable for some special cases [86]. To list a few examples, its capability of identifying size-dependent stiffness may exist some limited problems [87]. There is a serious unresolved paradox that these bending solutions of nonlocal nanobeams in some cases were found to be identical to the classical local solution, i.e., the small scale effects cannot be observed at all [86] [88]. The gradient elasticity theory [89] is also a size-dependent method and considers additional higher-order strain gradient terms by using the assumption that the materials must be considered as atoms with higher-order deformation mechanism at small scale rather than modelled as collections of points [86]. Li and Hu [86] carried out an investigation of wave propagation in fluid-conveying viscoelastic SWCNTs (single-walled carbon nanotubes). Furthermore, due to the less accuracy of the classical elasticity theorems, the modified couple stress theory could also be applied to capture the size-dependent properties of the carbon nanotubes. The size-dependent behaviors of the carbon nanotubes under electrostatic actuation using the modified couple stress theory and homotopy perturbation method was presented by Fakhraadi [90].

Employing FEM as a computationally powerful tool in nano-scale continuum modeling, the influence of CNT chirality, diameter, thickness, and other involved parameters can be evaluated conveniently in comparison with other methods.

In accordance with the above conclusion/ comparison regarding different CNT modeling techniques, NCM is selected in this chapter for conducting CNT and RVE multi-scale simulations at nano and micro scales.

According to molecular dynamics field, the total steric interatomic potential energy is expressed as bonded and non-bonded interactions [91] defined as below:

$$U_{total} = \sum U_r + \sum U_\theta + \sum U_\phi + \sum U_\omega + \sum U_{vdW} \quad (2.7)$$

A schematic representation of energy terms for linear method of CNT modeling is described in Figure 2.10.

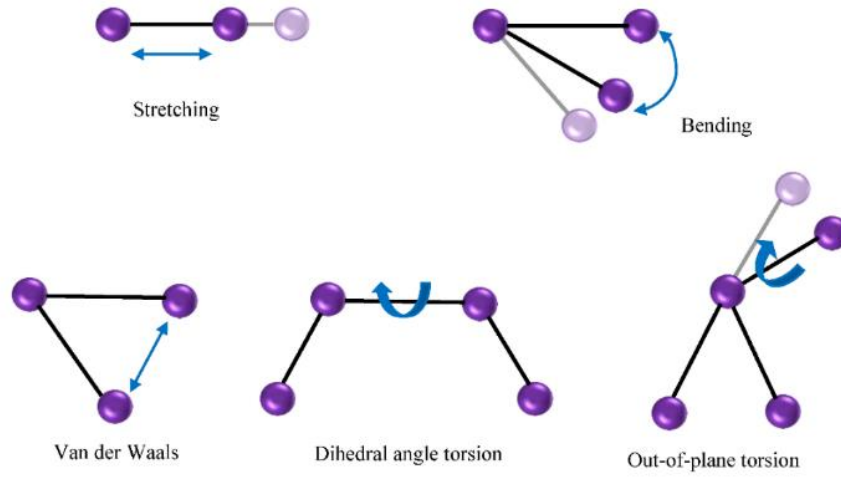


Figure 2.10: Potential energy terms of Carbon-Carbon bond [43]

Disregarding the electrostatic interactions dealing with weak and non-bonded energy, the U_r , U_θ , U_φ and U_ω are energies associated with bond stretching, bond angle variation, dihedral torsion, and inversion (out of plane torsion), respectively. U_{vdW} indicates Van der Waals interactions implying on non-bonded energy which is negligible in comparison with bonded energies. Considering small deformations and merging dihedral torsion with inversion as U_τ , the covalent energy of C–C bond can be expressed accordingly [91]:

$$U_r = \frac{1}{2} k_r \Delta r^2 \quad (2.8)$$

$$U_\theta = \frac{1}{2} k_\theta \Delta \theta^2 \quad (2.9)$$

$$U_\tau = \frac{1}{2} k_\tau \Delta \varphi^2 \quad (2.10)$$

Where k_r , k_θ and k_τ are bond stretching, bond bending and torsional resistance force field constant, respectively, while Δr , $\Delta \theta$ and $\Delta \varphi$ indicate the bond stretching increment, bond angle variation and angle variation of bond twisting, respectively. The CNT lattice structure is established, replacing the Carbon- Carbon bond with a 3D Timoshenko's beam element. The linear modeling procedure which has been also utilized in this thesis is described in Figure 2.11 [43].

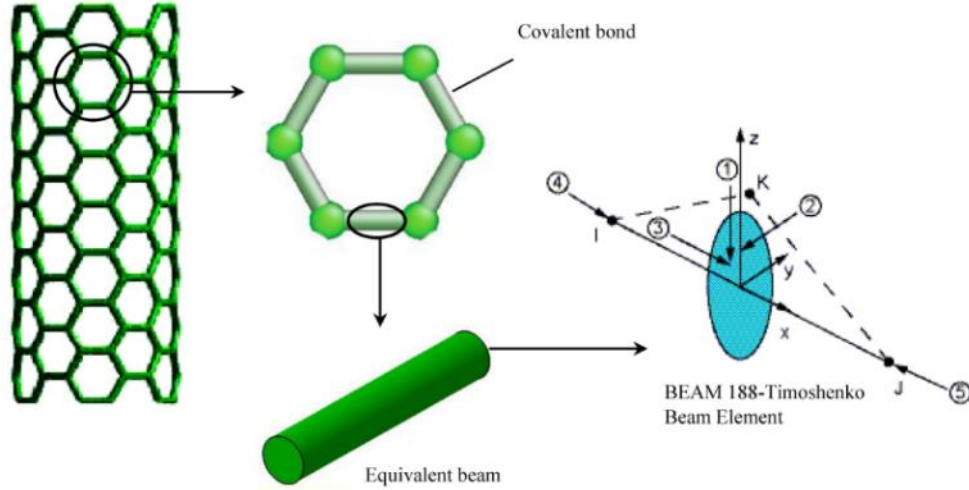


Figure 2.11: Representation of single-walled carbon nanotube modeling [43]

Based on the equivalence of energy [91], by correlating between inter-atomic molecular potential energy and strain energy of structural mechanics, the following relationships can be acquired:

$$\frac{EA}{L} = k_r, \quad \frac{EI}{L} = k_\theta, \quad \frac{GJ}{L} = k_\tau \quad (2.11)$$

Where E, A, I, G and J represent Young's modulus, cross section area, moment of inertia, shear modulus and polar moment inertia of equivalent beam, respectively. Supposing circular beam section with diameter d, the elastic modulus of equivalent beam element at nanoscale is given by:

$$E = \frac{k_r^2 L}{4\pi k_\theta} \quad (2.12)$$

$$G = \frac{k_r^2 k_\tau L}{8\pi k_\theta^2} \quad (2.13)$$

Where L indicates covalent bond length as 0.1421nm which is introduced as beam element length in C–C modeling procedure. The force field constants k_r , k_θ and k_τ are considered as $6.52 \times 10^{-7} \text{ N nm}^{-1}$, $8.76 \times 10^{-10} \text{ N nm rad}^{-2}$ and $2.78 \times 10^{-10} \text{ N nm rad}^{-2}$, respectively [92].

Subsequently an APDL macro-file is written and executed to construct CNT structure employing BEAM 188 element. The mentioned element is suitable for analyzing slender to stubby beam structure which is based on Timoshenko beam theory (TBT) including shear deformation impressions. BEAM 188 is a linear, quadratic or cubic two-node beam element with six degrees of freedom comprising translations in x, y and z directions and rotations about x, y and z directions. In this

thesis, the cubic option is used for the Beam188 which effectively makes it a beam element based on cubic shape functions. The intact CNT finite element model is exhibited in Figure 2.12 [43].

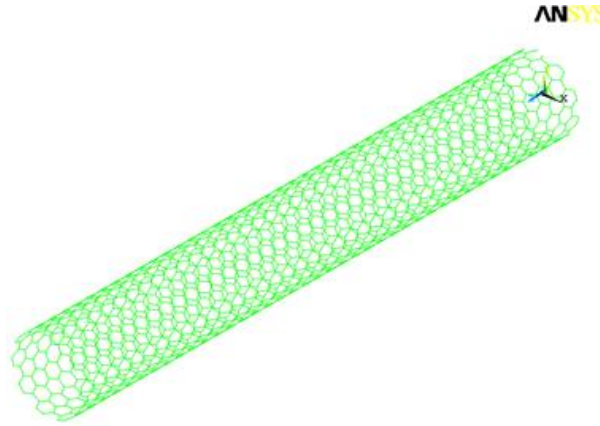


Figure 2.12: Finite element model of intact single walled carbon nanotube [43]

The obtained Young's modulus of CNT shown in above figure is represented in Table. 2.7 in comparison with previous published data.

Researchers	Tube Thickness [nm]	Employed element	Young's modulus [TPa]
Li and Chou [91]	0.34	Beam	1.010
Tserpes and Papakinos [93]	0.34	Beam	1.028
Kalamkarov et al. [94]	0.68	Beam	0.980
Giannopoulos et al. [95]	0.34	Spring	1.307
Shokrieh and Rafiee [96]	0.34	Beam	1.042
Malekimoghadam et al. [43] [97] (present chapter)	0.34	Beam	1.045

Table. 2.7. Calculated mechanical properties of isolated SWCNT using FEM

As a crucial issue, prior to continuation of this thesis, a briefly comparison was fulfilled on the influence of exploiting Timoshenko (present work) and Euler–Bernoulli (Ref. [98]) beam to simulate Carbon–Carbon bond on the natural frequencies of perfect CNT. Considering CNT with diameter 0.814 nm (Chiral index (6,6)), the results revealed that the model using Euler–Bernoulli beam exhibits 12%, 15% and 20% greater natural frequencies in first bending, third bending and axial vibration modes, respectively, than those of Timoshenko's beam, stemming from neglecting shear deformation effects in Euler–Bernoulli beam, especially in higher mode shapes. Regarding the Carbon–Carbon bond shape with length of 0.142 nm and diameter of 0.147 nm, it behaves as a stubby beam in which the influence of shear deformation is more pronounced. Therefore, employing Timoshenko beam element plays a crucial role in modeling C–C bond. The natural frequencies versus the CNT length of two nanotube models encompassing TBT and Euler–Bernoulli

beams are shown in Figure 2.13 [43] for axial vibration mode exposed to cantilever boundary condition.

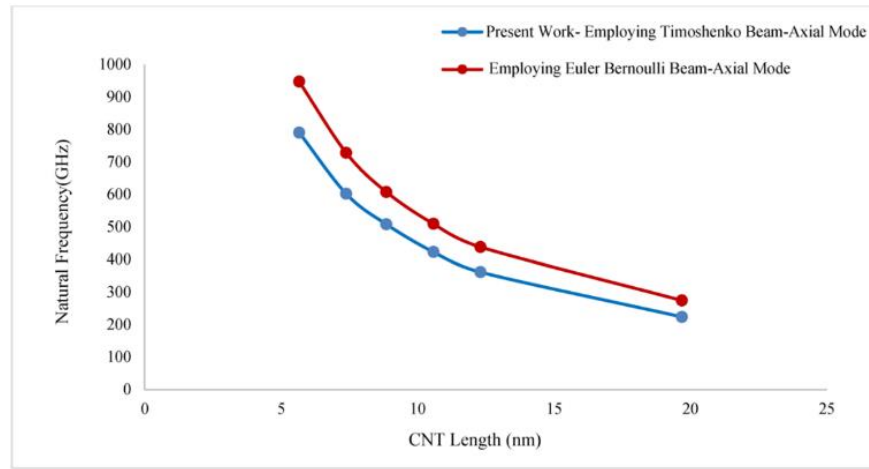


Figure 2.13: Natural frequencies of intact CNT [43]

Utilizing nonlinear approach for CNT modeling, Meo and Rossi [99] proposed a SWCNT finite element model, based on the use of nonlinear and torsional spring elements, to evaluate its mechanical properties. The behaviors of the C–C bond stretching and bending follow the Morse potential.

Hence, while atomistic modeling is a reasonable simulation technique for CNT modeling, its applicability is limited to the small systems. On the other hand, the continuum modeling neglects the discrete structure of CNT leading to inaccurate results. Nano-scale continuum modeling can be considered as an acceptable compromise in the CNT modeling, presenting result in a close agreement with than that of atomistic modeling.

2.2 Full-Scale Investigation into CNT–Polymer Nanocomposites

A variety of techniques for the fabrication of PNCs are in practice for incorporation of CNTs into various polymer matrices. The main objective is to debundle the CNTs and to achieve their uniform dispersion in the polymer matrix. At present, there is no single technique that is universally applicable to all situations. Thus, both traditional approaches and new approaches used for the fabrication of CNT/PNCs are discussed here briefly [100].

2.2.1 Processing and Fabrication

Traditional Approaches: Solution mixing, melt blending, and in situ polymerization are three traditional approaches for the fabrication of CNT/PNCs.

The solution mixing method is one of the most useful methods for the fabrication of CNT/ PNCs on a laboratory scale. This method is also useful to make nanocomposites without losing properties of nanosized fillers [100] because dispersion and interfacial bonding of nanofillers is important to achieve good mechanical and electrical properties. In this process, the CNTs and polymer are mixed separately in a suitable solvent. The choice of solvent is mainly governed by solubility of the polymer matrix. The solvent for CNTs and polymer matrix may be same or different but should have good miscibility. The dispersed CNTs and polymer are mixed, and finally a composite film is produced with and without vacuum-assisted solvent evaporation. During the whole process, ultrasonication, magnetic stirring, and high-speed homogenization techniques are utilized to disperse and mix CNTs properly into the polymer matrix and are schematically displayed in Figure 2.14 [101].

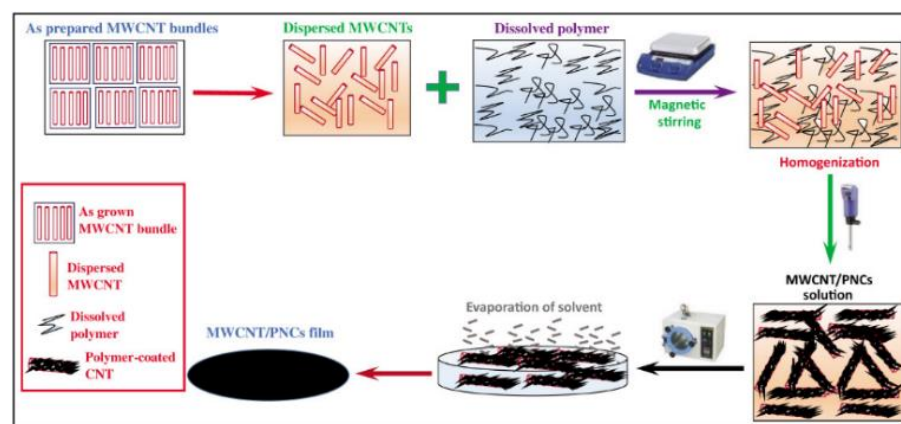


Figure 2.14: Schematic diagram of solution mixing technique for CNT/PNCs [101]

In some cases, CNTs are not separately dispersed; rather, they are directly mixed to the polymer solution using high-power ultrasonication or shear mixing. It should be mentioned, the main disadvantage related to the use of ultrasonication and shear mixer for a long time is that it can shorten the length of CNTs leads to decrease of the properties of PNCs.

Melt processing technique is the most promising approach for the fabrication of thermoplastic PNCs on an industrial scale due to its low cost. This technique is also suitable to insoluble polymers, especially for thermoplastic polymers that cannot be processed with solution techniques due to their insolubility in common solvents. In general, melt processing involves blending of polymer matrix with CNTs by the application of intense shear forces at elevated temperatures, which contributes in partial deagglomeration of CNT bundles and their dispersion into the matrix. The melt blending can be carried out in batch or continuous operation using high shear mixer and twin-screw extruder, respectively [100]. A typical twin-screw extruder comprising of two rotating screws is depicted in Figure 2.15 [102].

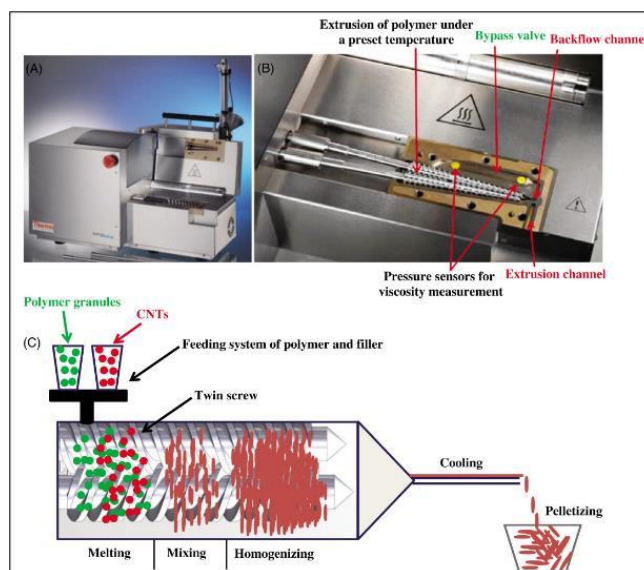


Figure 2.15: (A) Twin screw extruder, (B) view of micro-compounder showing different valves and channels, and (C) twin-screw extruder for melt mixing of CNTs & polymer matrix [102]

Having loaded the polymer granules via hopper into the extruder, they are then caught and pushed forward by rotating screw. These polymer granules are melted inside the heated melting zone and shearing of material between the two screws is also taking place. The CNTs are also loaded into the extruder via a separate hopper, and the mixing takes place in the melting zone due to the shearing action and then reaches to homogenization zone [102]. Finally, the mixture passes to die before becoming semisolid and cooled by air drying or by passing through a water bath and being chopped into granules for further use, or composites of desired size and shape can be made using an injection molding machine. This is a simple, fast, environmentally friendly, and industrially viable technique for large production, and no solvent is required during the preparation of nanocomposites; but it is not very effective in the breaking of bundles of CNTs compared to solution mixing [100].

In situ polymerization is a very effective method to improve the dispersion and interaction of CNTs in polymer matrix and a viable option for the preparation of insoluble and thermally unstable polymer-based composites. This is a very convenient method for preparation of polymer nanocomposites with high CNT loading and good miscibility with almost all polymer matrices. In this process, dispersed CNTs are mixed with a monomer solution and then polymerization takes place in the presence of an initiator under certain conditions [55]. Figure 2.16 [100] exhibits all the steps of in situ polymerization for CNT/PNCs.

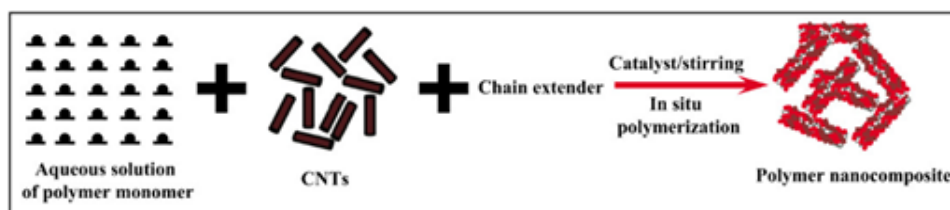


Figure 2.16: Schematic representation of in situ polymerization process [100]

It is worthwhile to mention that this method provides good dispersion and compatibility between polymer chains and CNTs as compared to solvent mixing and melt blending techniques. This method also provides a stronger and more active interface between polymer and CNTs, but it is less applicable as it requires a large amount of solvent for processing.

New Approaches: The layer-by-layer (LBL) approach involves building a layered composite film on the substrate by dipping the substrate alternately in a CNT-dispersed polyelectrolyte solution [103]. Initially, substrate is dipped in positively charged polyelectrolyte solution; after that the substrate is rinsed with pure water to remove loosely attached polyelectrolytes. To grow the LBL further, the substrate is dipped in negatively charged polyelectrolyte solution; as a result, a double layer of polyelectrolyte is attached on the substrate [100].

Bucky paper approach is a thin, porous sheet of CNTs usually formed by filtration of CNT dispersion. Infusing the bucky paper with polymer is a simple way to create PNCs with high loading of CNTs and with improved mechanical and electrical properties. It is noteworthy to mention that the bucky paper sheet can also be inserted between laminates to enhance the mechanical properties and fabricate the nano-engineered multiscale hybrid composites. Teotia et al. [104] reported an approach to make bucky paper-based phenolic resin composites as depicted in Figure 2.17. In the foregoing method, CNTs were dispersed in some solvent and added to the dissolved phenolic resin. The suspension was then mixed and homogenized employing a high-speed homogenizer at 30,000 rpm. The dispersed CNTs and phenolic resin mixture were then filtered in a specially designed filtration system, and a film of CNT impregnated polymer resin was acquired, which was then dried to get a CNT-phenolic resin prepreg. The prepreg is compression molded utilizing a hydraulic press.

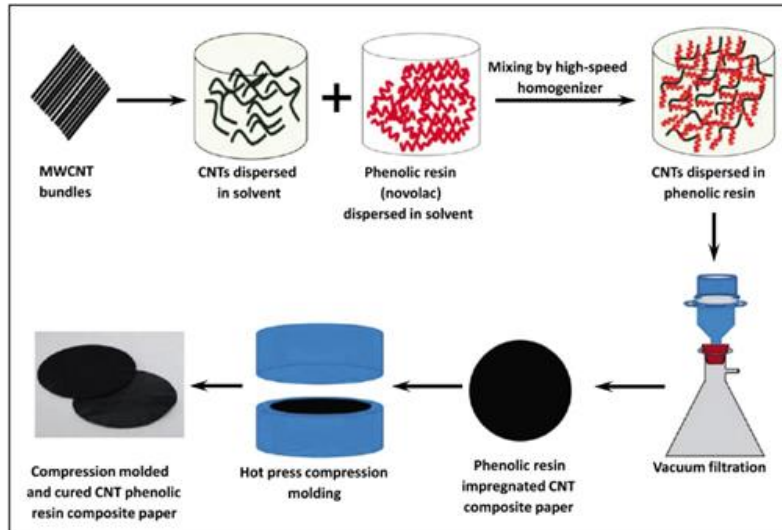


Figure 2.17: Schematic diagram for CNT–phenolic resin paper composite preparation [104]

Finally, it should be emphasized that the interface between CNTs and polymer matrix should be carefully engineered; otherwise, it will lead to poor load transfer between CNTs when in bundles and may result in interfacial slippage between CNTs and polymer chains. Hence, to resolve these problems, two major approaches including covalent and noncovalent functionalization are used as interactions between active materials and CNTs. In-detail investigations regarding this issue can be found in literature [100].

2.2.2 Mechanical Properties

In order to demonstrate the influence of CNTs on the mechanical properties of neat materials, this section discusses the mechanical properties of CNTs reinforced composites concisely made with different polymer matrixes. One way to take advantage of the marvelous properties of the carbon nanotubes (CNTs) consists in incorporating them into a matrix to build composite materials. The best candidates for this task are undoubtedly polymers, which thanks to their strength, toughness, low weight, and easy processing have been used in a broad variety of industrial application [105].

Polyethylene–Carbon Nanotube Composites: Achaby et al. [106] synthesized high-density polyethylene (HDPE)/MWCNT nanocomposites by the melt mixing method and measured their mechanical properties. In the HDPE/ MWCNTs nanocomposite the tensile strength and modulus were improved, with respect to neat HDPE, by 57% and 58%, respectively. Yang et al. [107] created a composite adding MWCNTs to a polyethylene (PE) polymer matrix. A small amount of maleic anhydride group has been grafted to MWCNT-NH₂ by a simple melt blending process. PE-g-MWCNTs are well dispersed in the PE matrix, leading to a highly

effective reinforcement effect. The stress–strain curves of composites of PE reinforced with PE-g-MWCNTs are delineated in Figure 2.18.

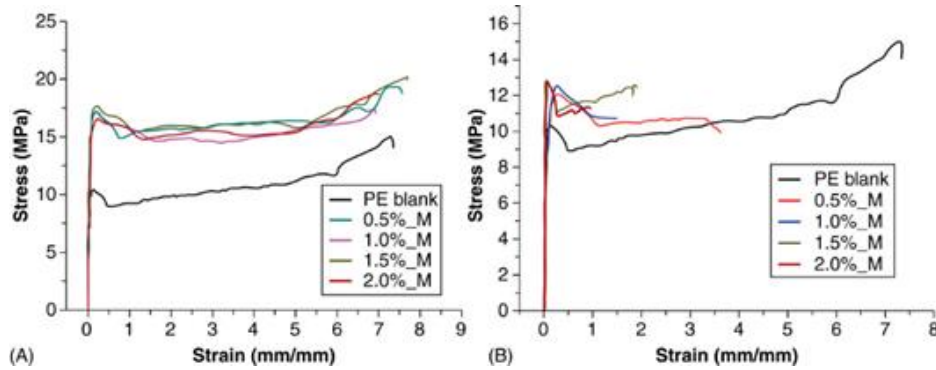


Figure 2.18: Stress–strain curves. (A) PE/PE-g-MWCNTs composites; (B) PE/MWCNTs composites [107]

Polymethyl Methacrylate–Carbon Nanotube Composites: Using melt-mixed, Gorga and coworkers [108] fabricated SWCNT/PMMA (Polymethyl methacrylate) nanocomposites. The orientation of MWCNTs in PMMA proved to be the only way to substantially toughen the nanocomposite. The mechanical properties of MWCNT/PMMA nanocomposites were assessed as a function of nanotube orientation, length, concentration, and type. A level of 1 wt.% MWCNTs in PMMA (oriented nanocomposite) exhibited the largest increase in tensile toughness with a 170% improvement over oriented PMMA. Growths in the modulus and yield strength were notable only at a high loading of 10 wt.% with increases of 38% and 25%, respectively.

Kim and coworkers [109] added MWCNTs to PMMA utilizing poly(3-hexylthiophene) (P3HT)–graft–PMMA as a compatibilizer. P3HT-g-PMMA proved to be very effective for dispersing MWCNT in PMMA matrix and in improving mechanical properties of the resultant composite. The fluorescence emission and Raman spectra pinpoint the strong π – π interaction between P3HT-g-PMMA and MWCNT in the composite. The resulting composite has increased both Young's modulus and tensile strength of PMMA matrix without sacrifice of elongation at break. Figure 2.19 demonstrates stress–strain curves for neat PMMA, PMMA/MWCNT, and PMMA/MWCNT/P3HT-g-PMMA with various MWCNT contents.

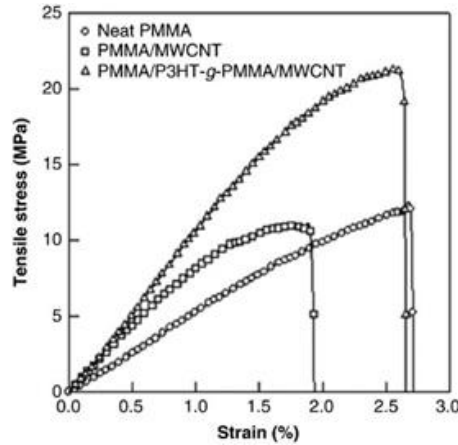


Figure 2.19: Stress–strain curves for neat PMMA, PMMA/MWCNT, and PMMA/MWCNT/P3HT-g-PMMA with various MWCNT contents [109]

Epoxy–Carbon Nanotube Composites: Song et al. [110] found that the epoxy composites embedded with poorly dispersed CNTs have higher tensile modulus. However, as the CNTs loading increases, tensile strength of the composite filled with well-dispersed CNTs increases but that of the composite filled with poorly dispersed CNTs decreases. The agglomerates present in poorly dispersed composite cause cracks to initiate and propagate easily. They found a 17% increase in tensile modulus of the composite for 1.5 wt.% MWCNTs. The limited improvements were attributed to the weak bonding between the CNTs and the surrounding matrix. It has been reported that the interfacial bonding between the CNTs and the polymer resin is weak and the load transfer from the polymer to the CNTs is not large enough for the CNTs to be broken under tensile loading; Instead, the CNTs tend to be pulled out. Figure 2.20 [110] plots the graphs of the tensile modulus and tensile strength of CNTs/epoxy composites with respect to CNTs content.

Rajoria and coworkers [111] investigated damping properties of CNT–epoxy composites for use in structural vibration applications. Both single-walled and multiwalled nanotube-epoxy composites were prepared with different proportion of nanotubes. Free and forced vibration tests were conducted on cantilevered beams. Multiwalled nanotubes were observed to be a better reinforcement than single-walled nanotubes. Up to a 700% increase in damping ratio was observed for a multiwalled nanotube–epoxy beam as compared to the plain epoxy beam.

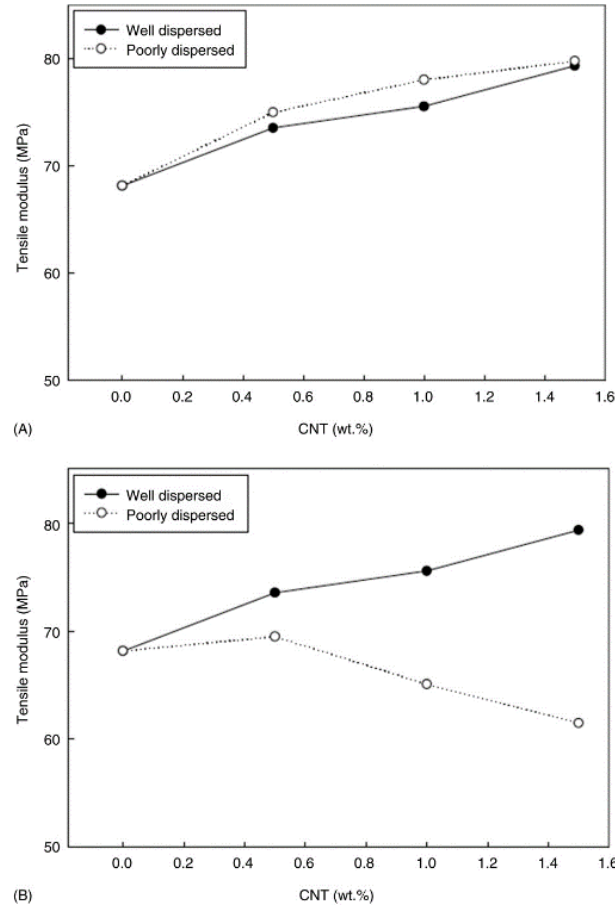


Figure 2.20: (A) Tensile modulus and (B) tensile strength of CNTs/epoxy composites versus CNTs loading [110]

Cha et al. [112] carried out an investigation in which the CNTs are functionalized by attaching melamine to improve the dispersibility in epoxy matrix and to augment the interfacial bonding between CNTs and matrix. The tensile tests and single edge notch bending (SENB) tests were conducted for CNT/Epoxy and M-CNT/ Epoxy nanocomposites at various weight fraction of functionalized CNTs. The M-CNT/Epoxy nanocomposites with addition of 2wt% functionalized CNTs demonstrated enhancements of Young's modulus by 64% and ultimate tensile strength by 22%. Furthermore, a remarkable increase of fracture toughness by 95% was observed for 2wt% M-CNT/Epoxy nanocomposite.

Figure 2.21 schematically exhibits possible mechanisms for explaining the deformation and failure of CNTs bridging a crack. As crack opens, processes depicted in (a) and (b) can occur, depending on the interfacial bonding and the mechanical properties of CNTs. As shown in (a), the bridging CNTs should hinder the growth of crack opening, as well as contributes positively to the measured fracture toughness. Depending on the progress of the crack propagation, the CNTs can be either pulled-out or broken. It is worth mentioning that in case of a weak interfacial bonding using pristine CNTs, the pull-out of CNTs from the epoxy matrix takes place, whereas, in case of a strong interfacial bonding between M-CNT and epoxy matrix, a complete rupture of CNTs or forming pull-out of the inner tubes can occur (Figure 2.21 b).

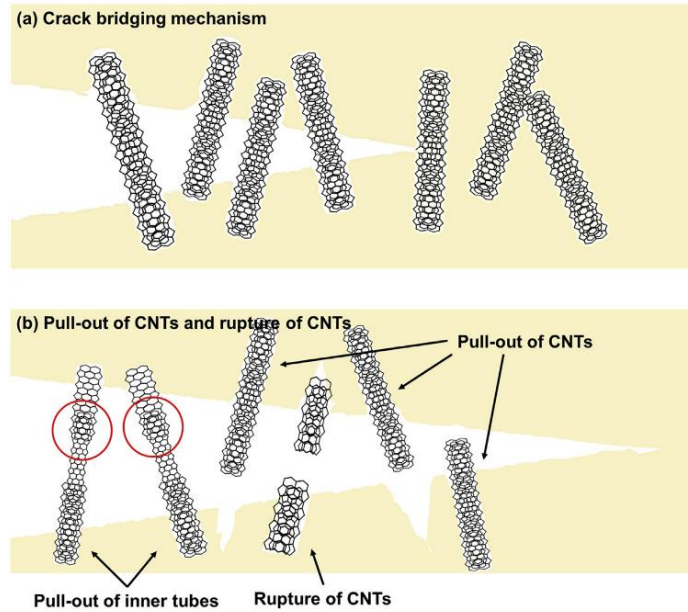


Figure 2.21: Schematic description of crack propagation; (a) crack bridging mechanism of CNTs; (b) rupture of CNTs and pull-out of CNTs and inner tubes [112]

To evaluate whether the crack bridging mechanisms lead to an improvement of fracture toughness, Cha et al. implemented SEM measurement of etched samples. It should be indicated the investigations were carried out without any additional surface coating. The observed surfaces had crack bridging of CNTs as depicted in Figure 2.22. The rupture of M-CNTs was observed in Figure 2.22 (a) and the bridging M-CNTs were also discovered by forming pull-out of the inner tubes in Figure 2.22 (b). The mentioned investigation can be considered as further evidence for strong interfacial bonding between the M-CNTs and the epoxy matrix.

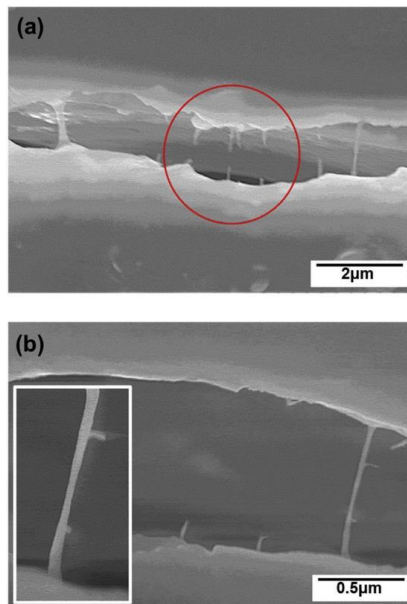


Figure 2.22: SEM images of the CNT/Epoxy nanocomposite. A crack is bridged by CNTs. (a) rupture of CNT; (b) crack-bridging of CNT by forming pull-out of the inner tubes [112]

As a conclusion, Table 2.8 [105] demonstrates the improvement achieved by adding CNTs to neat polymers on the mechanical properties of final composites.

Polymer Matrix	Nanotube Type	Sample Type	CNT Weight Fraction (%)	Composite Modulus Improvement (%)	Composite Tensile Strength Increase (%)	Composite Elongation at Break ϵ (%)	Toughness Improvement (%)
HDPE	MWNTs	Melt mixing	5	10	12	-	5
PMMA	MWNTs	Polymer grafting	0.10	103	85	3.8	-
PMMA	MWNTs	Melt mixing	1	0	0	-	170
PP	MWNTs	Pan milling–melt mixing	1	36	0	6.7	-
PP	MWNTs	Shear mixing	0.75	38	15	-	-
PP	MWNTs	Ultrasonication and stir	2.1	37	-	-	-
PS	MWNTs	Solution mixing	0.26	55	44	-	-
PS	MWNTs	Melt mixing	25	236	113	-	-
PVC	MWNTs	Bath sonication	0.5	696	-10	-60	-
PVC	MWNTs	Solution mixing	0.2	40	74	-	145
Epoxy	MWNTs	Solution mixing	0.5	20	14	16	-
Epoxy	MWNTs	Solution mixing	1.5	17	16	-23	-
Epoxy	MWNTs	Solution mixing	2	26	50	-	-
Nylon-6	MWNTs	Melt extrusion	1	15	46	-	-
Nylon-6	MWNTs	Melt blending	2	213	161	-27	-
PI	SWNTs	In situ polymerization	0.4	27	47	-	-

Table 2.8 Mechanical Properties of CNT-Based Polymer Composites [105]

2.2.3 Nonlinear Multi-Scale Modeling Technique

At nanoscale, the adopted method as linear FE modeling of CNTs was elaborated in the previous sections. At microscale, the multi-scale modeling deals with interphase interactions between CNTs and surrounding polymer, therefore, it is required to characterize the properties of this region. The properties of CNRPs strongly depend on the interface/interphase behavior between the polymer matrix and the CNT [113]. Therefore, the load transfer mechanism through the interfacial region is crucial in enhancing the mechanical and thermal properties of the PNCs. MD simulations of pulling out single fibers of the polymer matrix are commonly utilized to study the interfacial shear strength of conventional fiber–reinforced polymer composites [114].

The CNT pull-out process is depicted in Figure 2.23. During the pull-out process, the potential mean force (PMF)—the pull-out energy—and the total potential energy are computed and plotted. The total potential energy and the PMF of the system increases with increasing displacement of the CNT and levels off after it has been completely pulled out of the Polyethylene (PE) matrix [115]. Moreover, the United Atom (UA) Model and Parameters of the Force Field can be found in Ref [115].

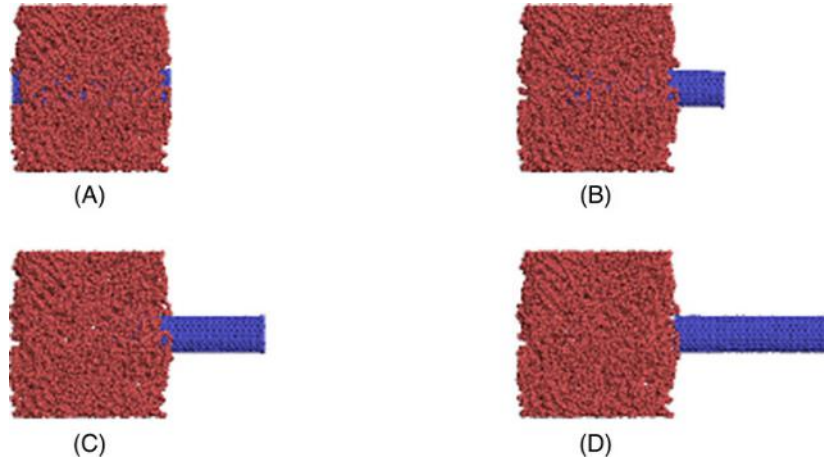


Figure 2.23: Snapshots of CNT pull-out simulations from polyethylene matrix at (A) $x = 0$ nm, (B) $x = 2$ nm, (C) $x = 4$ nm, (D) $x = 6.4$ nm [115]

Based on the potential mean force (PMF), the Interfacial Shear Strength (ISS) is acquired as below:

$$E_{pullout} = \int_0^L 2\pi r (L - x) \tau_i dx = \pi r \tau_i L^2 \quad (2.14)$$

$$\tau_i = \frac{E_{pullout}}{\pi r L^2} \quad (2.15)$$

where r and L denote the respective radius and length of the CNT inside the PE matrix, x is the displacement of the CNT, and τ_i represents the ISS.

Once the interphase region is characterized, it can be simulated via finite element modeling. Employing truss or nonlinear spring element, the non-bonded interphase between CNT and matrix is modeled based on Lennard–Jones (LJ) potential [116]. Wernik and Meguid [117] used truss rod elements to simulate the vdWs interactions which connect a node on the CNT to a node of the solid element of the polymer which is described in Figure 2.24.

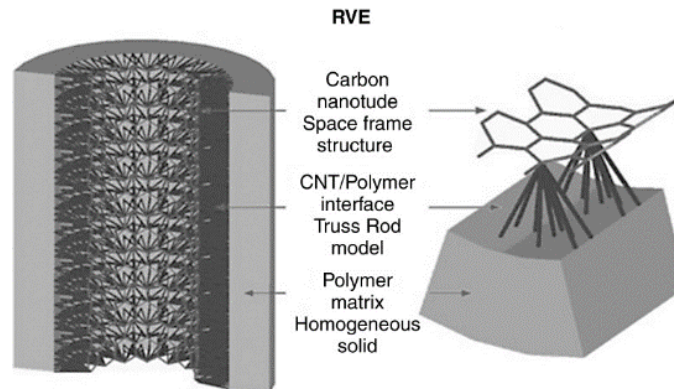


Figure 2.24: A 3D unit cell of the PNCs [117]

The finite element modeling of CNT employed in this thesis has been already elaborated in previous section. The FEM of interphase region and surrounding polymer used in this thesis is expounded as following [43] [77] [97].

FEM of Polymer matrix: Considering the volume fraction of 5% for CNT in a Representative Volume Element (RVE), polymer volume is much higher than that of CNT. Therefore, simulating chain of polymers at molecular scale requires a massive amount of elements and calculations. Since molecular chains of polymer are significantly tighter than atomistic structure of CNT, it can be modeled as a continuum medium as an acceptable simplification in modeling procedure. Subsequently, multi-scale finite element modeling is utilized wherein carbon nanotube is simulated at nanoscale, while polymer is modeled at micro-scale. A 3D SOLID 95 element with 20 nodes was used for modeling polymer resin. This element has three degrees of freedom per each node which are: translational in x, y and z directions. This element can tolerate irregular shapes without loss of accuracy. Also due to usage of intermediate nodes on each edge of the element, it has higher order shape function and consequently well-suited to model curved boundaries [118]. The simulated resin is treated as an isotropic material with Young's modulus of 10 GPa, 0.3 as Poisson's ratio and 890 kg/m³ as density.

FEM of Interphase region between CNT and polymer: The key issue defining the efficiency of CNTs in improving properties of polymers at micro-scale is load transferring phenomenon from matrix to CNT which is accomplished through the interphase region between CNT and matrix. Thus, accounting for load transferring mechanism from host matrix to CNT, simulation of interphase region plays a crucial role in proper understanding of CNTRP behavior [97]. From atomistic point of view, the governing interactions between CNT and surrounding polymer are weakly non-bonded van der Waals (vdW) interactions in absence of chemical functionalization [119]. Introducing covalent cross links between carbon atoms of CNTs and molecules of polymer, functionalization process can enhance the load transferring capability from matrix to CNT [97]. But this process has a negative aspect in causing defects in the structure of CNTs in order to form the cross covalent links. As a subsequent, the interphase region is treated as non-bonded interactions, and it is modeled using vdW interactions. From structural point of view, two different approaches can be found in literature for simulating interphase either as a continuum or as a discrete region. In continuum modeling of interphase, both CNT and polymer are simulated as continuum hollow/solid cylinders and interphase region is also modeled as intermediate solid cylinder between CNT and interphase. Since performing experimental studies at nanoscale is a challenging task, both mechanical properties and thickness of the interphase region in this approach have not been unambiguously characterized, yet. For instance, different mechanical properties have been suggested by researchers for this region ranging from the ten times the Young's modulus of the resin to one-tenth of that reflecting hard to soft interphase [120]. Inconsistent data can be also found in literature for the outer radii of this region

varying from 1 to 9 times of the SWCNT radius [97]. In discrete modeling of the interphase, which has been employed in this thesis, CNT is simulated as a discrete structure using beam/spring elements, while resin is modeled using solid elements. The interphase region is constructed using truss/spring elements connecting the carbon atoms of the discrete structure of CNT to the nodes of the inner surface of matrix elements. The properties of these truss/spring elements are obtained using Lennard–Jones (L–J) “6–12” potential resulting in vdW forces. This approach was firstly proposed by Li and Chou [121] to study compressive and tensile properties of CNTRP. Shokrieh and Rafiee developed an adaptive vdW interaction (AVI) model [122] to capture instantaneously non-linear behavior of vdW interactions using non-linear spring elements. AVI model is a progressive model rearranging the whole vdW interactions in the FEM according to their new position during the analysis. In other words, as the FEA evolves some vdW interactions will be deactivated as their length exceeds the cut-off distance dictated by L–J potential. In the meantime, some new vdW links will be generated and activated in adaptation with instantaneous situation of the model. Georgantzinos et al. [123] used joint elements with variable stiffness interconnecting CNT and matrix to simulate discrete interphase. In this thesis, discrete interphase region based on vdW interactions is simulated. The vdW forces are modeled using L–J “6–12” which is a non-linear force [94]:

$$F_{vdw} = 4 \frac{\varepsilon}{r} \left[-12 \left(\frac{\sigma}{r} \right)^{12} + 6 \left(\frac{\sigma}{r} \right)^6 \right] \quad (2.16)$$

where ε and σ are the Lennard–Jones parameters and 0.4492 kJ/mol and 0.3825 nm, respectively [94]. The vdW interaction can be neglected when the inter-atomic distance is equal or greater than 0.85 nm as depicted in Figure 2.25.

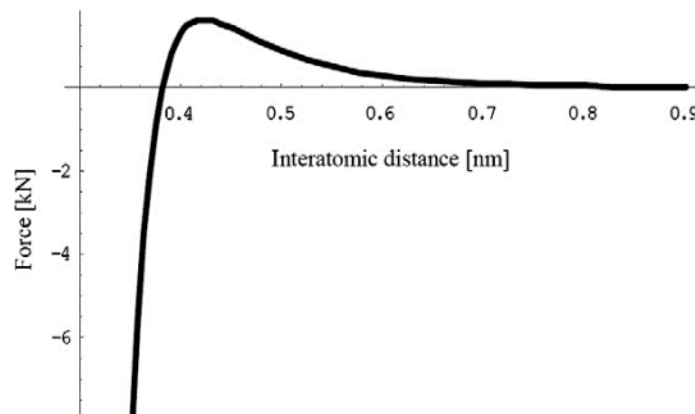


Figure 2.25: Variation of vdW force vs. interatomic distance for C–C bonds [97] [94]

In this paper [97], the vdW interactions between carbon atoms of CNT and the nodes of inner surface of the surrounding resin, is modeled using a 3D non-linear

spring. COMBIN39 element is used in ANSYS software for this purpose. A macro file has been written via Ansys Parametric Design Language (APDL) to model interphase region which creates non-linear spring elements between CNT atoms and inner surface atoms of the polymer which their distances are less than 0.85 nm. The properties of non-linear spring elements follow L-J equation (5.16). By executing the APDL code, the distance of each carbon atom with inner surface atoms of polymer is checked, if it is lower than 0.85 nm, the nonlinear spring is generated. Finally, thousands of nonlinear springs are constructed, and the input data as REAL CONSTANT (force-displacement) is individually inserted in ANSYS for each spring. Therefore, the model has thousands of nonlinear springs with their corresponding real constants, force-displacement curves, based on L-J potential formula. The thickness of CNT is selected as 0.34 nm and center of the carbon atoms in the CNT are placed at the midsection of the tube thickness. Due to the high repulsion force between two atoms in small distances, locating atoms in less than a definite distance is impossible. This equilibrium distance between carbon atoms and polymer atoms is 0.28 nm [97]. All three parts of multi-scale finite element model consisting of CNT, interphase and surrounding polymer are displayed in Figure 2.26 [97].

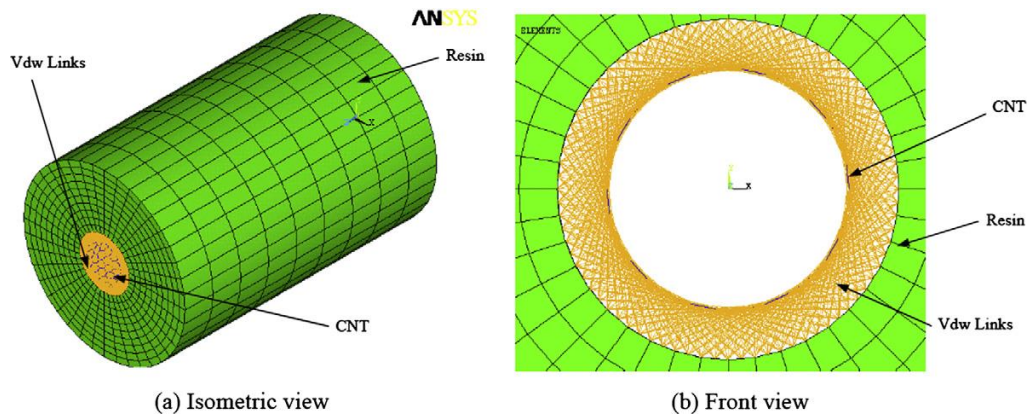


Figure 2.26: Finite element model of RVE and its constituents [97]

Points Regarding RVE Definition: According to Hill [124], an RVE is “structurally entirely typical of the whole mixture on average.” An RVE must include enough information to represent a model of heterogeneous material. By using the RVE approach, the heterogeneous material is substituted by an equivalent homogeneous material and the original properties are homogenized (averaged) by different methods. In this way, simulating an infinite medium is avoided, but still the average properties of the heterogeneous material should be obtained [114]. To ensure the characteristic of the RVE from its definition, an adequate RVE size must be determined based on the so-called “sample enlargement” approach. Thus, a statistical volume element (SVE) should be firstly generated on which sensitivity of the overall properties to the size of the SVE (and spatially random components within the SVE) is then estimated. If the sensitivity is insignificant, the SVE can be considered as an

RVE, and the acquired properties over the SVE is representative for the material properties [114]. As the SVE is randomly generated, the overall properties of an ensemble can be determined as [114]:

$$\langle R \rangle = \frac{1}{M} \sum_{k=1}^M R^{(k)} \quad (2.17)$$

where $R^{(k)}$ denotes the properties obtained from the k^{th} RVE, $k = (1, 2, \dots, M)$, and M is the number of realizations in the ensemble.

Points Regarding RVE Size: At first, a number of realizations (ensemble of RVEs) of the material model whose size is l are generated randomly in which the same volume fraction of fiber is utilized for these realizations. The mechanical properties (e.g., Young's modulus) of each realization are then obtained. These properties over realizations exhibit statistical scatter values when their sizes ' l ' are still small. Therefore, averaging on a set of realizations of the same size will be required to obtain the ensemble average of the properties of the RVE. The same steps are repeated for a set of realizations whose size is $l' > l$. By gradually increasing the size of realizations until the following criteria (below equation) is satisfied [114]; l' is considered as a sufficiently large size of the RVE.

$$\frac{|\langle E \rangle_{l'}^{(l)} - \langle E \rangle_l^{(l)}|}{(l' - l) \cdot \langle E \rangle_{l'}^{(l)}} < Tol^a \quad (2.18)$$

where $\langle E \rangle_l^{(l)}$ and $\langle E \rangle_{l'}^{(l)}$ represent to the first realization of the ensemble of RVEs, whose sizes are l and l' , respectively. Tol^a denotes the stopping criteria. For example, the resultant of the elastic modulus in Figure 2.27 is converged when the REV size is beyond 15,000 nm [114].

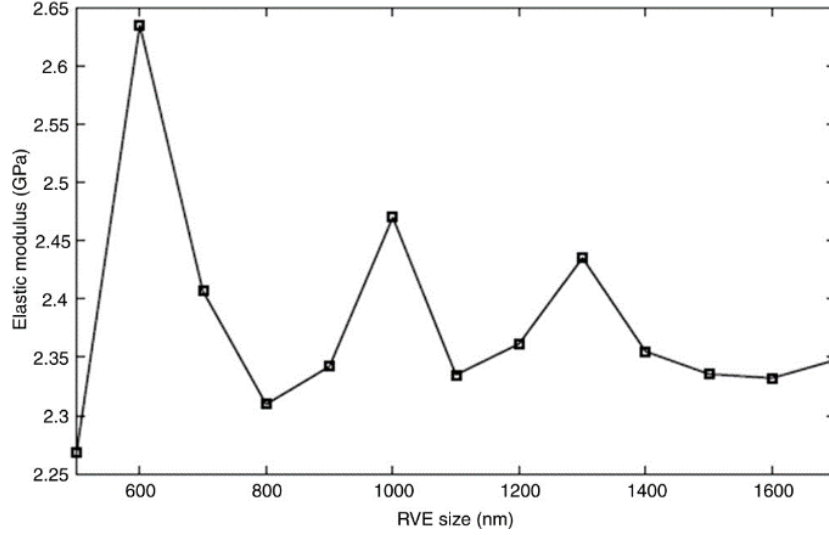


Figure 2.27: Plot of the elastic modulus as a function of RVE size [114]

Ensemble Averaging: As the fibers are randomly generated within the RVE, it is necessary that the ensemble of realizations be a good statistical representation of the PNC. To determine a proper number of realizations, the ensemble averages must be evaluated as:

$$\left| \frac{\langle E \rangle^{(2J)} - \langle E \rangle^{(J)}}{\langle E \rangle^{(2J)}} \right| < Tol^b \quad (2.19)$$

Where $\langle \bullet \rangle^{(J)}$ and $\langle \bullet \rangle^{(2J)}$ refer to the properties obtained from an ensemble average using the J realization and the 2J realizations, respectively. For example, the average elastic over the number of realizations is displayed in Figure 2.28 for PNCs. It can be seen that the convergence is achieved after 100 realizations.

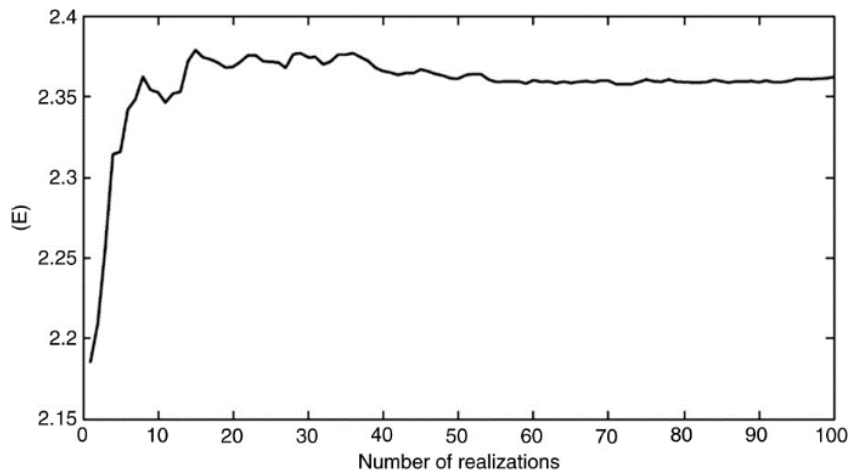


Figure 2.28: Convergence of the average elastic modulus over the number of realizations [125]

Stochastic Multi-Scale Modeling: Some investigations has conducted a hierarchical multiscale modeling procedure for predicting the mechanical properties of CNTRPs capturing all involved scales starting from the nanoscale and lasting to the macroscale passing in-between the micro- and mesoscales [126] [127]. Hence, in the mentioned approach, processing-induced inconsistencies are also treated as random parameters addressing associated uncertainties, and thus stochastic implementation of the developed modeling is carried out. The involved scales and associated phenomena are schematically delineated in Figure 2.29 for the specific case of CNTRPs wherein CNT appears at nanoscale as the reinforcing agent and the mechanical properties of CNTRP are intended to be extracted at bulk material level known as the scale of macro.

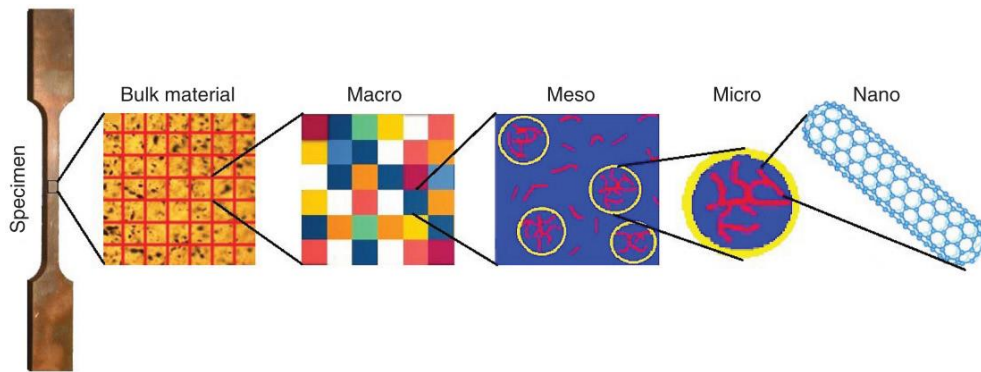


Figure 2.29: Length scales spectrum of carbon nanotube–reinforced polymers (CNTRP) for the multiscale modeling [126]

Following the general procedure of hierarchical modeling, the outputs of each scale are fed into the next upper scale as input data. An appropriate multiscale modeling of CNTRP demands the definition of separate representative volume elements (RVE) at each scale to facilitate the recognition of corresponding effective parameters. Considering the introduced scales in above figure, the effective parameters of each scale are given in Table 2.9 [126] in conjunction with the output of each level of simulation.

Scale	Effective Length	Parameters	Output
Nano	nm	Covalent carbon–carbon bond configurations	Young’s modulus of isolated CNT
Micro	nm/ μ m	Interaction between CNT and polymer, stress transfer in interphase	Young’s modulus of CNT and interphase
Meso	μ m	CNT orientations, agglomeration, and curvature	Mechanical properties of constitutive blocks
Macro	mm	Nonuniform dispersion of CNTs	Mechanical properties of CNTRP

Table 2.9 Effective Parameters of Each Scale in Multiscale Modeling [126]

As it is illustrated in Figure 2.29, the material region is partitioned into different constitutive blocks with different properties. This partitioning strategy simulates material in-homogeneity caused by uncertainties in processing method of CNTRP. The properties of each constitutive block are calculated on the basis of modeling process at meso-scale and are used here as input data. The overall properties of investigated material region can be calculated using FEA [127]. FEA of the partitioned material region is practically a time-consuming procedure, especially when it is utilized numerous times in a random analysis. As another alternative, Voigt model [128] can be used to determine the overall properties of the material region. Voigt model is defined in below equation:

$$\overline{X} = \frac{\sum_i X_i p_i}{\sum_i p_i} \quad (2.20)$$

where X_i represents corresponding mechanical property (Young's modulus or Poisson's Ratio) of i^{th} block and p_i is volume fraction of that block. Overhead line denotes the calculated average value.

Generally, all multiscale methods can be divided to hierarchical or sequential multiscale methods, semi-concurrent multiscale methods, and concurrent multiscale methods which are described in Figure 2.30. It is worthwhile to mention that hierarchical and concurrent multiscale modeling methods have been utilized in this thesis.

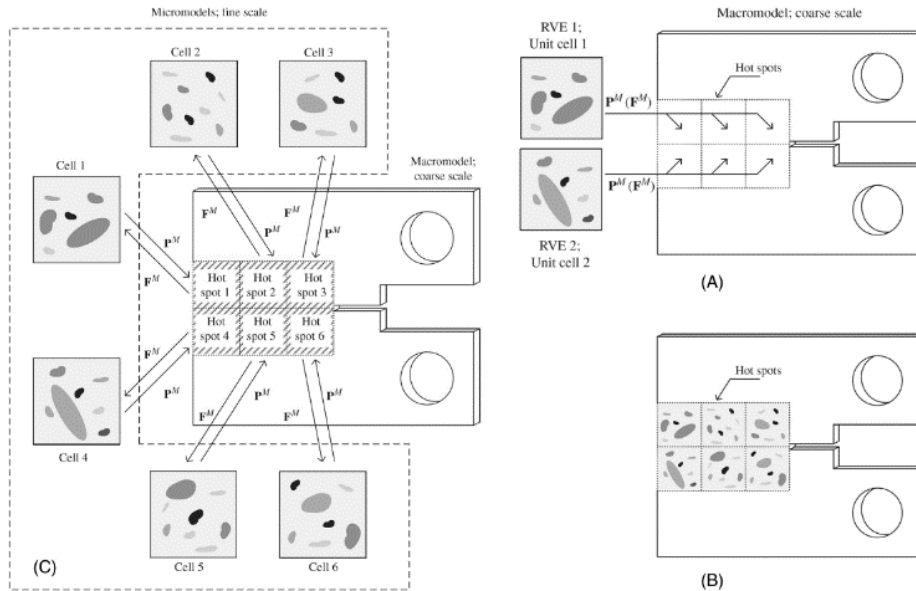


Figure 2.30: Schematic representation of (A) hierarchical or sequential, (B) concurrent, and (C) semi-concurrent multiscale methods [129]

Hierarchical Multiscale Methods: CNRPs are often considered homogeneous at the macroscopic level. To obtain macroscopic or “homogenized” or “effective”

material properties for CNRPs with a fine-scale microscopic structure, the homogenization theory can be utilized. The aim of the homogenization theory is to study the thermomechanical behavior of heterogeneous materials, such as CNRPs. The behaviors of CNRPs are usually the outcome of phenomena that occur at one to several length scales below the macroscale. Practically, it is not feasible to consider all length scales in a unified framework and hence, a two-scale framework is suggested [130].

Semi-concurrent multiscale methods utilize a reciprocal information passing technique between the fine scale and the coarse scale. At the coarse scale, strain measures (such as deformation gradient) are known, and stress measures must be calculated. Therefore, and in most cases, the deformation gradient of the coarse scale is passed to the fine scale and the stress tensor is sent back using homogenization theory. The numerical scheme of semi-concurrent multiscale method for CNRPs can be described as follows: in every integration point of the macro model of CNRPs, an RVE (fine scale model) is attached. The RVE contains the details of carbon nanotubes, as well as interfaces and interphases (when needed) [130].

In concurrent multiscale methods, both scales are considered simultaneously, and the fine scale is directly embedded into the coarse scale. Several concurrent multiscale methods, such as the Arlequin method [131], bridging domain method (BDM), and quasi-continuum method, have been proposed that can be used to predict intact CNRP's behaviors. Concurrent multiscale methods can be employed to couple continuum–continuum, as well as continuum–atomistic domains [130].

2.2.4 Challenges and Concluding Remarks

CNT–polymer nanocomposites are among the most appealing materials discovered during the last 20 years. These nanocomposites possess many exceptional features due to their excellent processability characteristics of the polymer and superior magnetic, electrical, and mechanical properties of the CNTs. Incorporation of CNTs in polymer matrices provides materials that could be utilized for many high-performance engineering applications. Investigations on CNT/PNCs suggest that CNTs have great potential in altering the properties of PNCs. The quality of CNT-reinforced PNCs depends on several factors, such as type of CNTs, chirality, dispersion, alignment, purity, aspect ratio, functionalization, and interfacial interaction between CNTs and polymer matrix. The most significant challenge is to achieve homogeneous dispersion and interfacial adhesion of CNTs with polymer matrix so that maximum filler surface area will be available for load transfer between filler and matrix. The functionalization of CNTs provides a convenient way to improve the dispersion and stress transfer between CNTs and polymer matrix, but much improvement is required in this area. Currently, CNTs are widely employed in nanocomposites for electronic applications, such as protection from unwanted electromagnetic radiation and for electrostatic discharge components. The

microwave-absorbing capability of CNTs could be exploited to heat temporary housing structures and may have applications in space exploration. Thin layers of CNTs on polymer sheets might also be utilized in transparent conducting composites. The high mechanical strength of these PNCs could be used to make some high-end sporting goods, such as tennis rackets, baseball bats, and bicycle frames and therefore deliver superior performance. Hence, the biggest markets for CNT nanocomposites will undoubtedly be for high-value applications that can absorb the added costs; these include commercial sectors, such as electronics, as well as aerospace industries that require lightweight, high-strength, high-temperature-resistant composites [100].

From the experimental point of view, since the interfacial interaction is principally dominated by the atomistic scale phenomena, it has been proven arduous to achieve reliable experimental data on CNT–polymer interactions. Furthermore, experimental studies usually suffer from several limitations such as the inability to measure load transfer at the interface, the nanometer size of the specimen, and the high cost of experiments. Thus, numerical modeling techniques can furnish helpful insights into interactions behavior that are not directly accessible to the experiment [132].

As previously mentioned, nanostructured are lightweight and cost effective, they are widely utilized in the industry. However, the challenge remains of coupling physical description at the molecular level to component design at the continuum level. From modeling techniques point of view, a predictive physics-based model is therefore essential for a comprehensive understanding of material behavior. The macroscopic properties of the CNRPs are acquired from continuum models whose parameters are known from molecular level. Atomic details of nanostructured materials are hence inserted into continuum constitutive models by using the homogenization technique. These models can be extensively applied to a wide range of materials whose systems are so complex that multiscale modeling is required to predict their behavior. It is believed that these models will provide an efficient and effective tool for the design of PNCs [114].

By employing FEM and taking into account the CNT waviness, agglomeration, and CNT/polymer interphase, several studies were conducted which reveal some remarkable issues:

- CNT's wavy shape mostly affects the effective axial elastic modulus.
- With increasing the multitude of CNTs in the agglomerate, the elastic properties decrease.
- With increasing the waviness of CNTs, the elastic properties increase, as curling of CNTs results in the alignment of larger parts of the CNTs.
- The effect of CNT topology is balanced between the different directions; the largest elastic modulus appears in the direction with the more aligned CNTs, and the shear moduli and Poisson's ratios are rather independent of CNT topology.

The thermomechanical properties of CNRPs come from phenomena at lower scales. Therefore, it is of crucial importance to adopt efficient and appropriate multiscale techniques for modeling polymeric nanocomposites. These methods should account for all important mechanisms, such as defects, cracks, and voids. Different multiscale methods have been developed that can be divided into hierarchical, semi-concurrent, and concurrent multiscale methods. It is believed that semi-concurrent multiscale methods are more suitable for nonlinear cases, as they account only for deformation states that really take place in a simulation. It is also more convenient to couple different packages specially for different scales utilizing semi-concurrent methods. For instance, semi-concurrent methods can exploit molecular dynamic packages at the fine scale and finite element packages at the coarse scale. Nonetheless, the application of these methods for modeling damage and fracture is still challenging. The existence of disparate length scale and application of the periodic boundary conditions (PBC) when the cracks touch the boundaries of RVE should be assessed in more detail. Concurrent multiscale methods are more suitable for modeling fracture phenomena in CNRPs. They can easily couple a molecular domain directly to a continuum one using (bridging domain method) BDM, though numerous challenges in dynamic applications remain, i.e., bridging the disparate time scales and avoiding spurious wave reflections are just two of them [130].

Last but not the least, utilizing CNTs for coating fibers or inserting as inter-ply medium in laminated composites has recently attracted the utmost attentions of research groups as the latest and most novel application of CNTs which is also the topic of this thesis. Engineering fibers can be utilized for the modern uses of carbon fibers for structural reinforcement in different industries, aircrafts, such as the landmark Boeing 787 jet airliner. As for many other materials, the new trends in textiles, fibers, and polymer composites require that, besides fulfilling a primary purpose, the properties of the material allow delivery of one or more secondary functions—in other words, multifunctionality. One approach to reach multifunctionality for the case of engineering fibers, such as glass, carbon, or aramid fibers is to deposit carbon nanotubes (CNTs) on their surface, or to directly grow them on the fiber surface [133]. Depositing CNTs on the surface of fibers may greatly modify their surface properties, electrical conductivity, and thermal conductivity, among many other properties. If this CNT deposit/growth is achieved without altering the mechanical and other volumetric properties of the fibers, a multifunctional fiber with improved capabilities and a host with variety of applications may be acquired [133]. As well as fibers coating with CNTs, CNTs can be utilized as inter-ply medium to improve the adhesion between layers in laminated composites and enhance the interlaminar shear strength (ILSS) by decreasing delamination phenomenon which is one of the most significant drawbacks in conventional composites.

Chapter 3: A Study on Fracture Behavior of Clay-Polymer Nanocomposites

Abstract: This chapter provides a novel approach regarding a study on fracture behavior of clay-nanocomposites and is based on the author's paper during PhD program [134]. In the current chapter, the influence of clay platelet on crack characteristics of fully exfoliated clay-polymer composite is scrutinized. A multi-scale 3-D finite element model comprising of four phases as clay platelet, non-perfect bond interactions, interphase region and surrounding matrix is constructed to investigate semi-elliptical matrix crack properties, as a nano-notch, subjected to fracture mode I. Subsequently, the strain energy release rate is acquired in terms of J-integral parameter considering the location and dimension, geometrical variables, and modeling strategy. The results imply on the pronounced effect of clay debonding on crack behavior which leads to local stiffness reduction. Furthermore, interphase characteristics such as thickness and elastic modulus, have significant influences on the critical energy release rate. The results are consistent with published literature and the model can be invoked as a viable tool to investigate the fracture behaviors of clay-polymer nanocomposites.

3.1 Introduction

Regarding the virtues of nanoparticle-reinforced polymeric composites, application of these materials pervades the state-of-the-art technologies in the aerospace, marine, automotive and other similar thriving industries. Owing to the superior mechanical, physical and thermal properties of polymeric nanocomposites with addition of carbon nanotube, nanoclay or nanoparticles, against pristine polymers, wide-range of investigations have been conducted in order to characterize of such materials [135] [136] [137] [138] [139]. Due to striking properties of nanoclay, the variation of elastic modulus and tensile strength pursuant to its content ratio in epoxy was vastly examined in some studies [140] [141] [142] [143] considering various procedures. Among different clay types, Montmorillonite (MMT) is extensively exploited as nano-reinforcing agent in constructing nanocomposite materials due to its high aspect ratio and moderate cost [144]. A comprehensive review on nanoclay and nanoclay reinforced polymers, meanwhile, was accomplished by Rafiee and Shahzadi [145]. A profound investigation was carried out by Boo et al. [146] to identify the impact of clay dispersion on the mechanical properties and the results disclosed inevitable effect of material

preparation process technique besides the amount of clay on fracture toughness and other attributes. In addition to elastic modulus, many experimental studies have been conducted to obtain fracture parameters including several matrix materials [147]. The increase in epoxy toughness after mixing both nanoclay and thermoplastic materials was reported by Rostamiyan et al. [148], in which, the obtained results indicated that the tensile, compressive and impact strength of the new ternary nanocomposites were ameliorated as opposed to those of neat resin. Considering debonding damage between interphase and nanoclay, the mechanical properties of nanoclay reinforced nanocomposite were acquired by Malekimoghdam et al. through finite element multi-scale modeling [149]. Notwithstanding the comprehensive experimental macro-scale clay/epoxy studies, a relatively infrequent number of researches could be found focused on the numerical 3D fracture behavior of nanocomposites in nano/micro scale. Furthermore, most researches put forward a 2D finite element representative volume element to investigate the mechanical behavior of exfoliated and intercalated clay-nanocomposites [150] [151]. Silani et al. [152] conducted the experimental and numerical investigations in macro-scale exploring the effect of clay on the brittleness of the nanocomposite and damage initiation simulation in dog-bone sample by means of XEFM. Dai et al. [153] elucidated damage behavior of nanoclay/polymers in a FEM analysis employing disk-shape inclusion as nanoparticle reinforcing material without considering stress singularities by means of singular elements. It was observed that the rise in aspect ratio leads to an increase in Young's modulus, yet a decrease in strength. A semi- concurrent modeling approach on 2D fully exfoliated clay/ epoxy nanocomposite materials was utilized by Silani et al. [154] in order to find out the damage initiation and propagation through the material. Invoking phase field model, the fracture parameters of fully exfoliated clay/ polymer nanocomposites were obtained in some other literatures [155]. Various novel approaches are defined and developed in order to model the multi-scale modeling of fracture, coupling molecular dynamics to extended finite element as well as proposing coarse-graining techniques [156] [157].

Considering the cumbersome procedure of performing experimental tests and the existing of limited computational investigations in this scope, the main aim of this chapter is to propose a novel approach for studying the interaction between an epoxy matrix weakened by a semi-elliptical crack as a built-in nano-cleavage, and clay platelet via 3-D finite element method. For this purpose, a new Representative Volume Element (RVE) which is realistically capable of capturing clay debonding effect at nano/ micro scale is developed. The current study investigates the influence of clay on fracture behavior of cracked epoxy by conducting a comparative study between nanocomposite and neat resin. Unlike 2-D analysis and with the aid of semi-elliptical crack model, representing nonlinear crack front, the influence of interphase thickness on fracture behavior of RVE is also revealed.

3.2 Nano-Clay Structure and Mechanical Properties

A class of material containing layered silicates or clay minerals with traces of metal oxides and organic matter is known as “Clay” [145]. Forming from the weathering and erosion of feldspar rocks over a period of time, they are usually constituted of variable amounts of iron, magnesium, alkali metals, alkaline earth and other cations. Various types of clays exist in terms of chemical composition and crystal structure. Natural clays are classified into three groups in terms of ratios of 1:1 (kaolinite), 2:1 (montmorillonite and vermiculite), and 2:2 (chlorite) associated with constitutive alternating sheets of “SiO₂” and “AlO₆” units. Among various types of smectite clays, Montmorillonite (MMT) is extensively utilized in materials applications because of its high aspect ratio and high swelling property in polar spaces. Called hereinafter “nanoclays”, these layered crystals have aspect ratios ranging from 100 to 1000 and the thickness in the order of nanometer. These nanoplatelets are bonded parallel together by weak van der Waals (vdW) and electrostatic interactions and corresponding interlayer gap is referred to as “Gallery” or “Interlayer” [145] [149]. In general, three morphologies of nanoclay can coexist in polymer matrix depending on the nanoclay dispersion state, separation degree of silicate layers and polymer penetration between them: (1) Aggregated, (2) Intercalated, and (3) Exfoliated [158] which are schematically delineated in Figure 3.1. Several factors account for the morphologies of nano clay including processing method, type of clay, clay modification, type of polymer matrix, the weight fraction of clay incorporated into polymer and the interaction between clay and polymer. Aggregated morphology encompasses a conventional micro-particulate composite that the clay particles are available in their original stacked status with no insertion of polymer matrix between the layers. It should be mentioned, this situation is not considered as nanocomposites and thus limited improvement is achieved in mechanical properties. Penetration of a single polymer chain into the gallery space between parallel silicate nanolayers will engender the intercalated morphology. In this state, the interaction between nanoclay layers and filled polymer results in formation of a modified polymer at molecular level. Consequently, an interphase with a thickness of few nanometers appears. For in situ polymerized clay/polymer nanocomposites, applying surfactant to nanoclay enables the monomer to penetrate the gallery space and polymerize. Exfoliated morphology implies on fully separated nanoclays in the polymer matrix. In this morphology, separated nanoplatelets of silicates are individually dispersed in a polymer [145]. This morphology introduces the best performance from mechanical viewpoint because of the very thin and, in the meantime, very large aspect ratios of particles. The dispersion of nanoclay in polymer matrix is of crucial importance for successful processing of nanocomposites. The reinforcement efficiency of nanoclay seriously depends on the intensity of its interaction with surrounding polymer matrix.

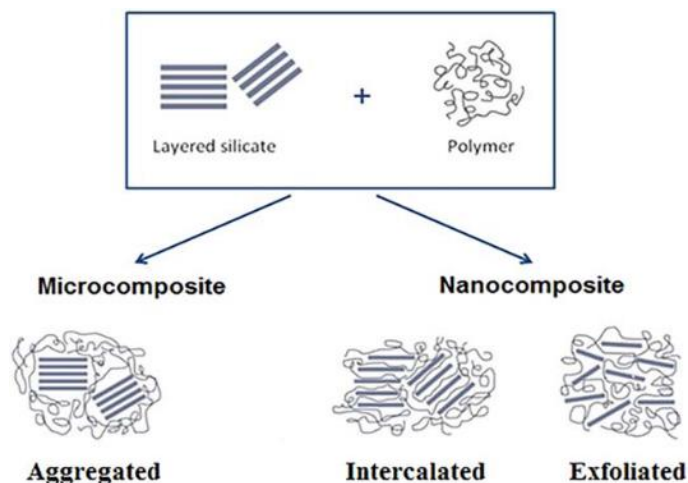


Figure 3.1: Nanoclay morphologies in polymers [145]

An exfoliated polymer-clay nanocomposite (PCN) was developed by the Toyota group by synthesizing a nylon 6/clay nanocomposite [159]. Extracting mechanical properties of isolated nanoclays is primarily essential in order to predict the mechanical properties of nanoclay reinforced polymers. Characterizing mechanical properties of clay platelets is categorized into two main groups as experimental and computational methods. Getting access to a single clay platelet without the intermediate medium between clay and polymer is almost impossible. Subsequently, different experimental methods have been utilized to extract mechanical properties of aggregated nanoclay. These methods comprise direct compressibility measurement, acoustic measurement, optical measurement such as Brillouin scattering, ultrasonic measurement, and inelastic neutron scattering. In these direct methods, mechanical properties of aggregated nanoclays are measured and then the same properties are assumed for a single nanoclay platelet [160]. As an indirect technique, mechanical properties of nanoclay/ polymer composites are measured using simple tensile tests. Then, the measured properties and mechanical properties of neat resin are fed into micromechanics equations and mechanical properties of aggregated nanoclay are theoretically calculated [145]. Some of the experimental outcomes and conducted MD simulations for predicting mechanical properties of nanoclays are represented in Table 3.1. Reflected E_{11} and E_{22} in Table 3.1 are in-plane moduli while E_{33} denotes the modulus in the direction perpendicular to clay sheets. A notable difference between E_{33} and E_{11} or E_{22} is believed to be originated from the influence of gallery in experimental measurement. Thus, it is expected that E_{33} is equal to the in-plane modulus for the case of isolated nanoclay.

Researcher(s)	Year	Type of clay	Reported Young's modulus [GPa]	Method
Aleksandrov and Ryzhova	1961	muscovite	$E_{11}=178$ $E_{22}=178$ $E_{33}=55$	Experimental, Ultrasonic measurement
McNeil and Grimsditch	1993	muscovite	$E_{11}=176.5$ $E_{22}=179.5$ $E_{33}=61$	Experimental, Brillouin scattering
Mazu et al.	2008	MMT	$E_{11}=216$ $E_{22}=233$ $E_{33}=165$	MD
Xu et al.	2012	MMT	$E_{11}=277$ $E_{22}=277.8$ $E_{33}=271.4$	MD
Suter et al.	2007	MMT	Thickness: 0.669 nm $E_{11}=320$ $E_{22}=344$ Thickness: 0.937 nm $E_{11}=233$ $E_{22}=247$	MD
Zhang et al.	2009	muscovite	79.36 ± 6.9	Experimental, Nanoindentation test

Table 3.1: Experimental characterization and MD simulation of clay modulus [145]

The experimental characterizations of nanoclay/polymer have revealed that mechanical properties of the neat polymer can be improved by adding small portions of nanoclay [145] [149] [161]. Various thermosetting and thermoplastic resin systems are used by researchers for processing nanoclay/polymers. Among them, Nylon-6 and Epoxy systems have received much more attentions than Polyester, Polyimide, PU and PP. An overall outcome of implemented experimental studies on nanoclay/polymer is shown in Table 3.2. It is evident from Table 3.2, the level of enhancement in mechanical properties of neat polymer with addition of nanoclay is highly fluctuating even at the same nanoclay weight fraction depending noticeably on the dispersion of nanoclay in polymer. The dispersion quality of nanoclay in polymer plays a crucial role in defining the degree of nanoclay capability in reinforcing polymers.

Researcher(s)	Year	Polymer Type	Neat polymer modulus [GPa]	Nanoclay weight fraction [%]	Nanocomposite modulus [GPa]	Level of improvement in properties [E_{NC}/E_{Resin}]
Kornman et al.	1998	Polyester	2.87	5	3.79	1.32
Tyan et al.	1999	Polyimide	2.45	7	3.46	1.41
Shelly et al.	2001	Nylon6	1.2	5	2.43	2.025
Wang et al.	2005	Epoxy	1.96	5	2.74	1.39
Dong Y et al.	2009	Polypropylene	1.76	10	2.1	1.19
Jumahat et al.	2012	Epoxy	3.02	5	3.6	1.19
Zappalaroto et al.	2015	Epoxy	3.1	8	3.5	1.13
Uhrig et al.	2015	Nylon6	2.4	2.76	4.8	2
Ji et al.	2002	Nylon6	0.5	4	1.35	2.7
Kaushik et al.	2009	Polyurethane	0.025	13	0.45	18

Table 3.2 Experimental characterization of nanoclay/polymer [145]

3.3 Constitutive multi-scale modeling of clay-epoxy nanocomposites

High exfoliation is desirable for enhancing the functional properties of nanocomposites; however complete exfoliation is never achieved. In this work, the proposed FE model of a representative volume element (RVE) consisting of a clay platelet, the surrounding matrix and an interphase region considering interfacial debonding is established via writing macro code through ANSYS commercial package [118] [149]. According to substantial material behavior on a macro scale, the load transfer occurs from the surrounding matrix to the clay platelets. Thus, a short-clay model is adopted which is entirely embedded in an epoxy matrix and hereinafter is called “Short RVE” to investigate the load transferring phenomena on the nano/micro scale. It should be mentioned, “long RVE” nanocomposites model, the homogenization method excluding debonding damage and 2D FE modeling cannot substantially capture the tensile behavior and load transferring phenomena of clay-polymer nanocomposites. The aforementioned models are shown in Figure 3.2 [149].

A four-phase short RVE model including a clay platelet, an interphase region, clay-epoxy interactions, and an encircling epoxy polymer that is capable of capturing interphase debonding, elasto-plastic behavior of a polymer, load transferring phenomena and interphase parameters influences on the tensile behavior of clay-polymer nanocomposites is constructed. The proposed modeling technique of the RVE is depicted in Figure 3.3.

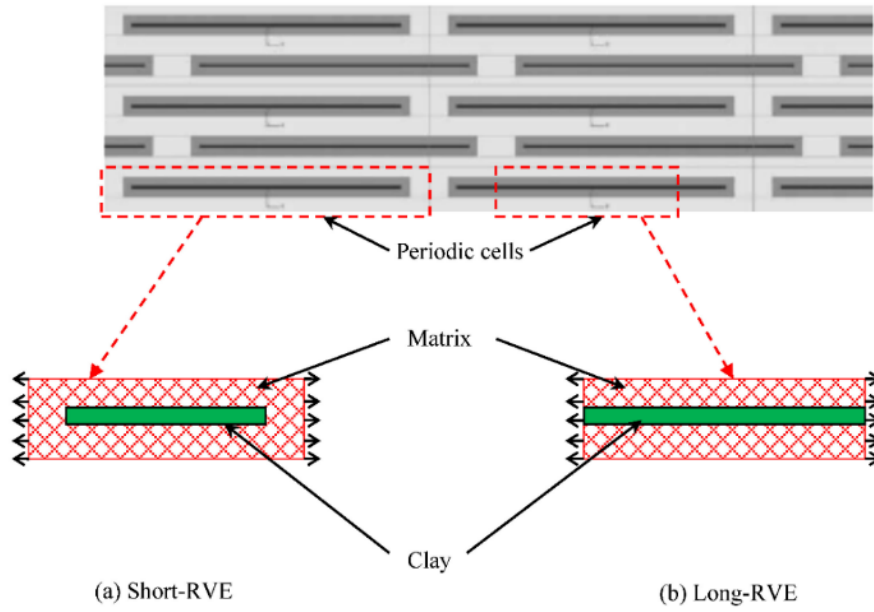


Figure 3.2: Schematic view of a RVE model with two types of periodic cells (a) Short RVE (b) Long RVE [149]

3.3.1 FEM of Nano-Clay

The clay platelet is simulated as an elastic isotropic material with the same material properties as Montmorillonite, a well-known clay platelet. The thickness of each platelet is assumed to be 1nm [162] [149] with Young's modulus of 200 GPa and Poisson's ratio of 0.3 [163]. The SOLID 186 element has been employed to construct the finite element of the clay model. This element possesses 20 nodes with three degrees of freedom per node which are translational in x, y and z directions [118]. Additionally, because of the usage of an intermediate node on each edge of the element, it has higher order shape function and thus results in a higher accuracy.

3.3.2 FEM of Surrounding epoxy matrix

Considering various weight percentages of clay, the epoxy resin has been simulated with the SOLID 186 element. The constructed resin is treated as an isotropic material with elasto-plastic and failure properties capable of exhibiting plastic behavior in the matrix during tensile analysis. The multi-linear isotropic hardening plasticity is adopted to simulate a finite element model which may be preferred for cycling where the kinematic hardening could exaggerate the Bauehinger effect. Furthermore, a maximum of 100 stress-strain points can be defined to explain polymer behavior [118]. Hence the stress-strain parameters and failure criteria of epoxy have been extracted from datasheets.

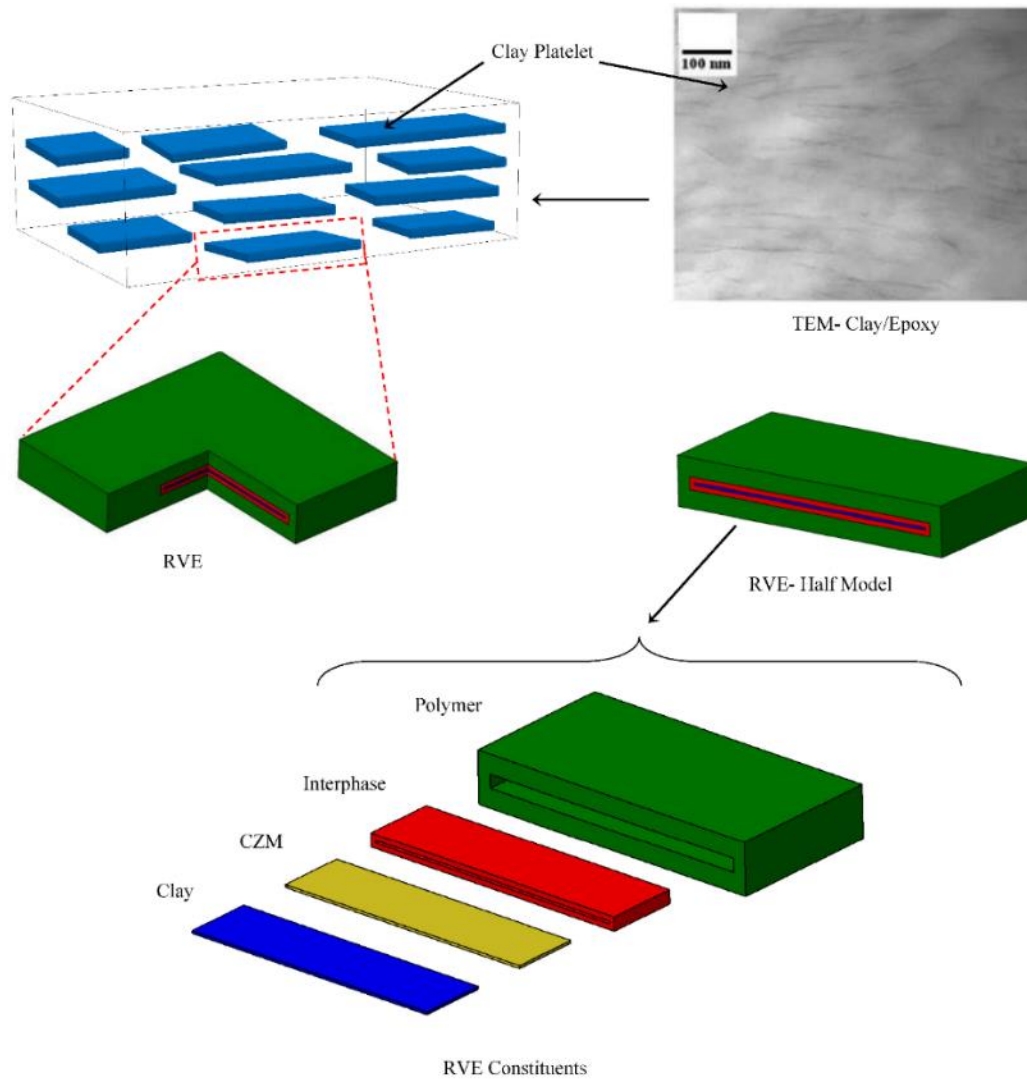


Figure 3.3: Modeling procedure of four-phase clay/epoxy nanocomposite [149]

3.3.3 FEM of Interphase region and interactions of clay/epoxy

The key issue defining the efficiency of improving the properties of clay-polymer nanocomposites at micro-scale is the load transferring phenomenon from the resin to the clay platelet through the interphase-interactions between the clay and the matrix. Thus, accounting for the load transferring mechanism from the matrix to the clay, modeling the interphase region plays a crucial role in a proper understanding of the polymer clay nanocomposites (PCN). Consequently, the aforementioned region is broken down into two segments comprising the mobility region and the interactions between epoxy and clay which are simulated by the interphase and the CZM model, respectively, according to Figure 3.3.

Interphase region: For both intercalated and exfoliated clay particles, the outer surface of the clay is in contact with the matrix which is defined as interphase in this region. The interphase region between the surrounding matrix and the clay can exhibit as a mobility region [164] for which the mechanical properties vary from the clay to the matrix with different values reported for the thickness magnitude. By

considering r as a variable within the interphase region the following condition should be satisfied [165]:

$$\begin{aligned} E_i(r) &= E_f & \text{at } r &= r_f \\ E_i(r) &= E_m & \text{at } r &= r_i \end{aligned} \quad (3.1)$$

Where $E_i(r)$ indicates elastic modulus of the interphase at r , and r_f and r_i are half of the clay and interphase length and E_m and E_f are the matrix and clay elastic modulus, respectively. Relying on foregoing conditions, the elastic modulus of the interphase region is reachable by [165]:

$$E_i(r) = E_m \left(\frac{r_i}{r} \right) + \left[\frac{(r_i - r)}{(r_i - r_f)} \right]^{n/2} \left[E_f - E_m \left(\frac{r_i}{r_f} \right) \right] \quad (3.2)$$

Where n is interfacial enhancement index (IEI). The value of n depends on the properties of the matrix and the inclusion, surface treatment of nanoclay as well as the degree of intercalation/exfoliation occurred in the nanocomposite. The average elastic modulus of interphase can be acquired by the following equation:

$$E_i = \frac{1}{r_i - r_f} \int_{r_f}^{r_i} E_i(r) dr \quad (3.3)$$

The interphase region is simulated via SOLID 186 element utilizing the elastic modulus extracted from Eq. (3.2) for various IEIs of 6, 40 and 100. Figure 3.4 displays the elastic modulus distribution at the interphase region from r_f to r_i in which the difference between r_f and r_i , indicates the interphase thickness.

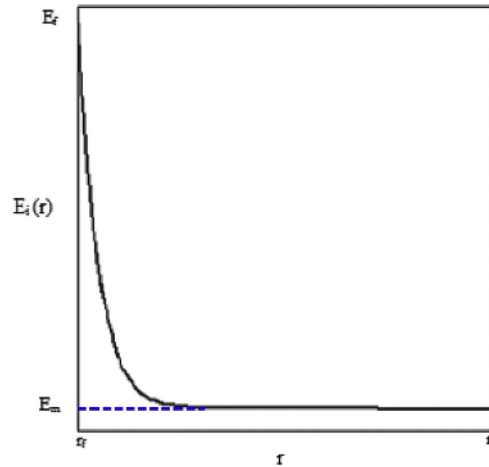


Figure 3.4: Elastic modulus distribution at interphase region [166] [134]

Cohesive zone material model: The cohesive zone material is introduced as a non-perfect bond at the interphase region, employing the zero thickness INTER204

3D element to simulate interactions and debonding between clay and epoxy. This element is defined by 16 nodes having three degrees of freedom at each node in the x, y, z directions as shown in Figure 3.5. Likewise, it is capable of simulating an interface between two surfaces and the subsequent delamination process, where the separation is represented by an increasing displacement between initially coincident nodes, within the interface element itself. Because the CZM encircles the entire clay platelet, the mixed-mode type including mode I and mode II is adopted to simulate interfacial debonding and fracture phenomena in both normal and tangential directions based on the bilinear traction-separation law. The CZM model consists of a constitutive relation between the traction “T” acting on the interface and the corresponding interfacial separation “ δ ” (displacement jump across the interface). The bilinear cohesive law is exploited under mixed-mode fracture in which the separation of material interfaces depends on both the normal and tangential components of displacement jumps which are displayed in Figure 3.5. To take into account the difference in the normal and tangential jumps contributions to the separation of material interfaces, a non-dimensional effective displacement jump λ for mixed-mode fracture is defined.

The normal and tangential components of cohesive tractions and corresponding relations in mixed-mode type are expressed as [118] [149]:

$$T_n = K_n \delta_n (1 - D_m) \quad (3.4)$$

$$T_t = K_t \delta_t (1 - D_m) \quad (3.5)$$

$$\lambda = \sqrt{\left(\frac{\delta_n}{\delta_n^c}\right)^2 + \beta^2 \left(\frac{\delta_t}{\delta_n^c}\right)^2} \quad (3.6)$$

T_n , T_t , δ_n , δ_t , D_m describe normal traction, tangential traction, normal separation, tangential separation and damage parameter, respectively. The β is the non-dimensional parameters which assigns different weights to tangential and normal displacement jumps. The damage parameter associated with mixed-mode bilinear cohesive law is illustrated as:

$$Dm = \begin{cases} 0 & \lambda_{\max} = \lambda_\alpha \\ \text{Min}(1, d_m) & \lambda_{\max} > \lambda_\alpha \end{cases} \quad (3.7)$$

Where

$$\lambda_{cr} = \frac{\delta_n^*}{\delta_n^c} = \beta \frac{\delta_t^*}{\delta_t^c} \quad (3.8)$$

$$d_m = \eta \left[\frac{\lambda_{\max} - \lambda_{cr}}{\lambda_{\max}} \right] \quad (3.9)$$

$$\eta = \frac{\delta_n^c}{\delta_n^c - \delta_n^*} = \frac{\delta_t^c}{\delta_t^c - \delta_t^*} \quad (3.10)$$

Where δ_n^c / δ_t^c and δ_n^* / δ_t^* , indicate normal/tangential displacement jump at the completion of debonding and normal/tangential displacement jump at maximum normal cohesive traction, respectively. There are six basic parameters to define the bilinear mixed-mode cohesive law in ANSYS [118] provided by the molecular dynamics (MD) simulation for the Van der Waals interactions between surfactants adhered to the clay surface and the surrounding matrix [164].

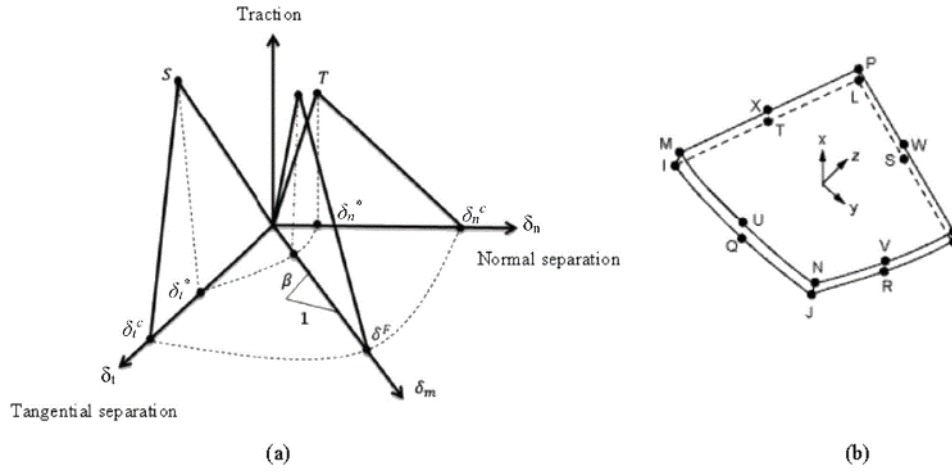


Figure 3.5: Cohesive zone material (a) Mixed-mode traction-separation behavior (b) INTER204 element geometry [118]

Furthermore, both long and short RVEs and their constituents are constructed via FEM in accordance with the technique illustrated in Figure 3.3. Hence, firstly, the multi-scale finite element model of clay-epoxy without crack is constructed as described in Figure 3.6 [134]. It is worthwhile to emphasize that in the ‘Short RVE’ model, the clay platelet is surrounded by polymer matrix and load transfer phenomenon is accomplished via non-bonded interphase region. Employing RVE with the aid of mixed-mode CZM, therefore, both normal and tangential clay debonding processes can be captured. It is worth mentioning that interphase is modeled as mobility region considering the variation of mechanical properties between matrix and clay, while interface is invoked for the purpose of simulating vdW interactions and debonding between clay and surrounding medium.

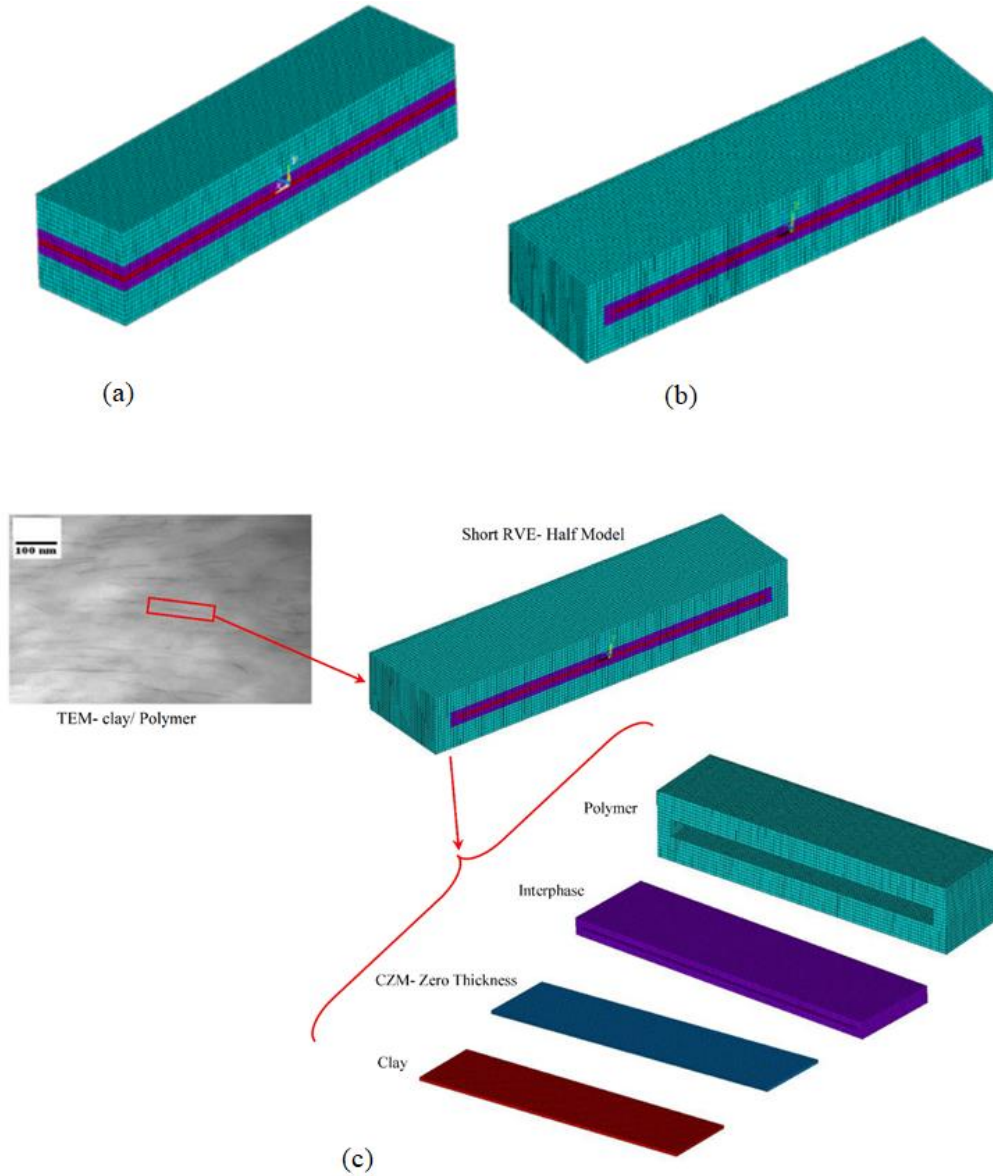


Figure 3.6: Finite element model of intact half RVE (a) Long RVE (b) Short RVE (c) multi-scale finite element procedure of four-phase clay/ polymer nanocomposite [134]

3.4 Stress Analysis of Semi-Elliptical 3D Crack

Generally speaking, stress and deformation fields around the crack tip have high gradients. The precise nature of these fields depends on the material, geometry, and other factors such as loading conditions. Additionally, convergence considerations would entail using higher order elements with higher order shape functions. As it can be seen in Figure 3.7 and Figure 3.8 [134], in order to capture the rapidly varying stress and deformation fields, a refined mesh pattern is constructed in the region adjacent to crack front, utilizing hexahedral 20-node solid element (SOLID186). In these figures, crack location is indicated by x_c and RVE length, width and height are defined by l , w and $2t$, respectively. Producing singularity in stress field, the crack

front mesh (i.e., possessing elements next to the crack front) is chosen as a wedge-shape quadratic, with the mid-side nodes placed at the quarter point [58].

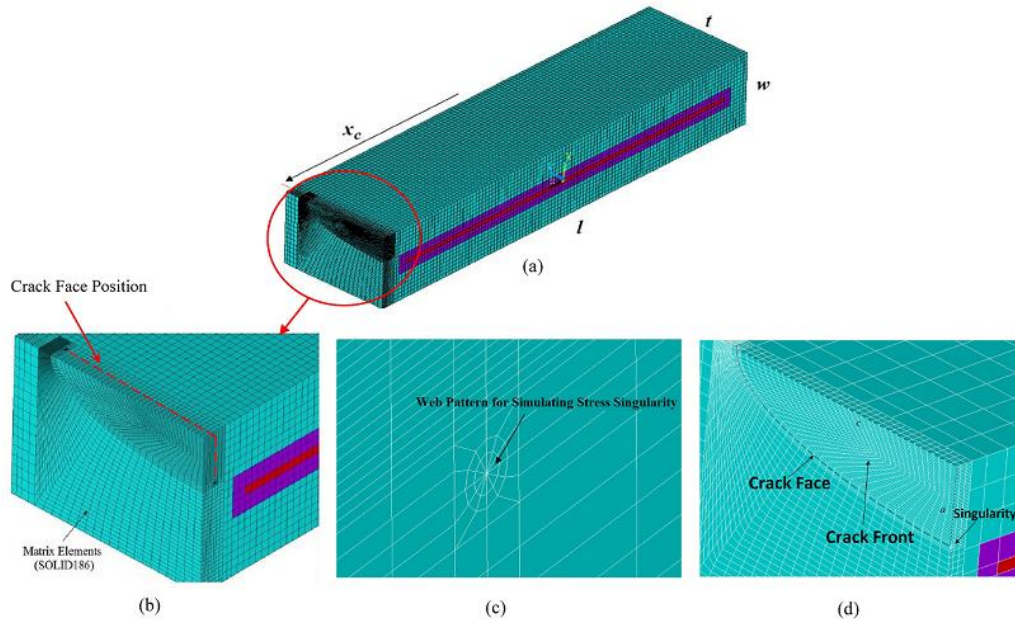


Figure 3.7: (a) Finite Element model of short RVE with 3D crack (b) Enlarged view of crack face, (c) Spider web shape of singular elements (d) Cut- view at crack face [134]

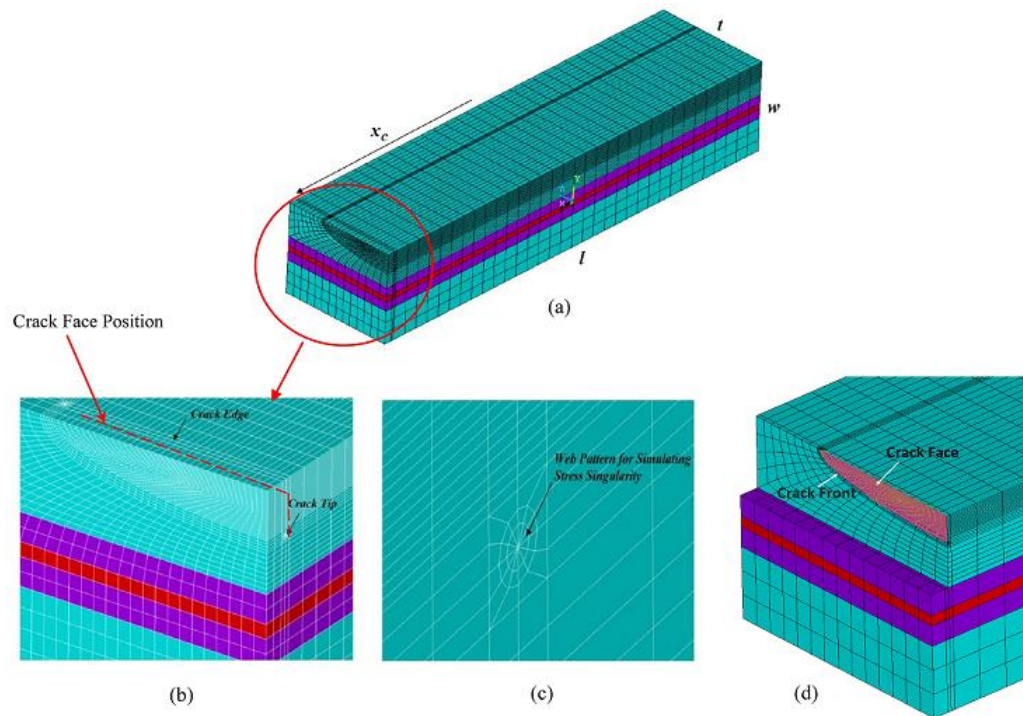


Figure 3.8: (a) Finite Element model of Long RVE with 3D crack, (b) Enlarged view of crack structure, (c) Spider web shape of singular elements (d) Cut-view at crack face [134]

Prior to the elaboration of the outcomes, in order to verify the accuracy of the constructed FE model, a comparison is performed between the tensile stress-strain behavior of experimental study and also finite element model [149] in the absence of any cracks. A very good agreement for the small strains (less than 2%) is observed signifying the RVE accuracy. Regarding the loading process, a monotonic displacement in longitudinal direction was exerted to the end side of the model, while for the nodes belonging to the opposite side, the rotational and translational degrees of freedom are totally constrained.

Extracting proper mesh density in the crack front, a neat resin block is employed under pure tension with semi-circular crack ($a=c$) embedded in mid-plane section that is highly related to the typical closed form solution for mode I stress intensity factor given by [167]:

$$K_I = \frac{2}{\pi} \sigma \sqrt{\pi a} \quad (3.11)$$

where a is the crack radius and σ is the nominal remote tensile stress. In comparison with crack dimension, the resin block is large enough implying a valid analogy between infinite domain and aforesaid simulation. As a criterion for verifying the model, the computed stress intensity factor in finite element analysis based on contour-integral determination has deviation 1.2–1.6% from the exact values of above formulation showing reasonable accuracy. These results were attained by a crack front element size of $c/50$ where c stands for half of a crack's longer diameter [168]. It is worth mentioning the path independency of J-integral has been already checked by calculating it on two contours adjacent the crack tip, which the discrepancy of the values is less than 4%. The mesh convergence study has been carried out in terms of stress using refined mesh which is depicted in Fig. 7 where $R = 1$ denotes 12,000 elements.

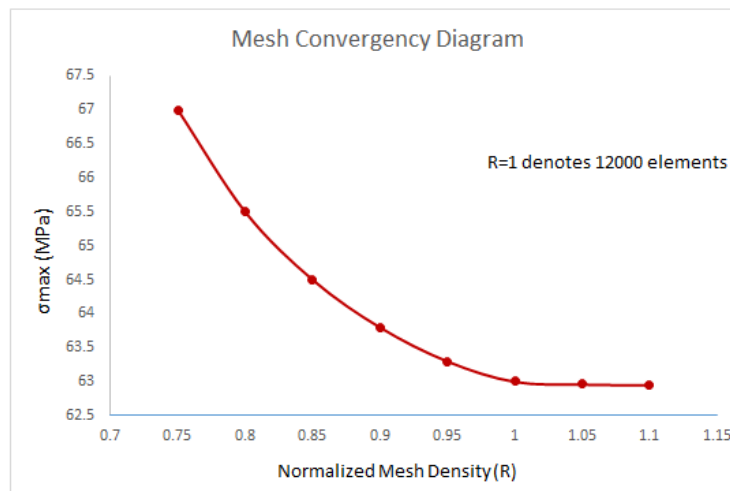


Figure 3.9: Normalized mesh density versus normal stress [134]

Due to the intrinsic non-linear behavior of CZM interaction, full Newton-Raphson iterative method was employed, and the model was subjected to 1.5% of nominal strain. As an energy-based criterion for determining the onset of crack growth, J-integral is implemented to specify energy release rate in the current model. The original form of the J- Integral for a line contour surrounding the crack tip(Γ) could be written as [167]:

$$J = \int_{\Gamma} \left(w dy - T_i \frac{\partial u_i}{\partial x} \right) ds \quad (3.12)$$

In which,

$$w = \int \sigma_{ij} d\epsilon_{ij} \quad (3.13)$$

whereby w denotes the strain energy density (σ_{ij} and ϵ_{ij} as stress and strain tensor components),

$$T_i = \sigma_{ij} n_j \quad (3.14)$$

where T_i is the component of the traction vector which acts on the contour, u_i is the displacement component, and ds is a length increment along the contour Γ . Moreover, it should be noted that J-Integral is nothing but non-linear energy release rate defined by:

$$J = \frac{1}{V} \frac{-d\Pi}{da} \quad (3.15)$$

Where

$$\Pi = U - V \quad (3.16)$$

where, Π is the total potential energy. U and V stand for strain energy and external work, respectively. Pursuant to path-independency nature of J-integral and in the absence of any restrictions for plastic region size, this integral is an appropriate tool for assessing the fracture behavior based on numerical methods, hence, it is applied in the present work.

3.5 Results and Discussion

The total elastic-plastic strain contours of short and long RVE models are illustrated in Figure 3.10 and Figure 3.11 [134], respectively. As expected, the maximum strain value is observed in the vicinity of deepest crack tip and in this case debonding damage phenomenon occurs at about 1.1% of strain. It is apparent from the contours supplied, in the short RVE that the total strain is greater than long RVE, since in the former the loading is transferred from matrix to clay via interphase, whereas in the latter, the load is directly imposed to clay platelet. Under longitudinal stress, strain concentration at the interphase-epoxy boundary also initiates after the detachment of clay along X direction due to the heterogeneous material properties of this region as delineated in Figure 3.10 (a), (b). The mentioned area is subjected to sharp elastic modulus variation and according to Hook's law, the magnitude of strain in this zone increases drastically.

In accordance with the Figure 3.12 [134], the total strain of short RVE is described, emphasizing the debonding damage between clay and interphase region as well as crack opening. The dominant factors that have significant effects on J-integral at any point belonging to crack front are categorized as: crack dimensions (a, c), angular position of intended point on crack front (ϕ), crack location with respect to RVE's length (l), clay content percentage, RVE properties e.g., long/short type modeling, with and without CZM mode and interphase stiffness, which are elaborated subsequently.

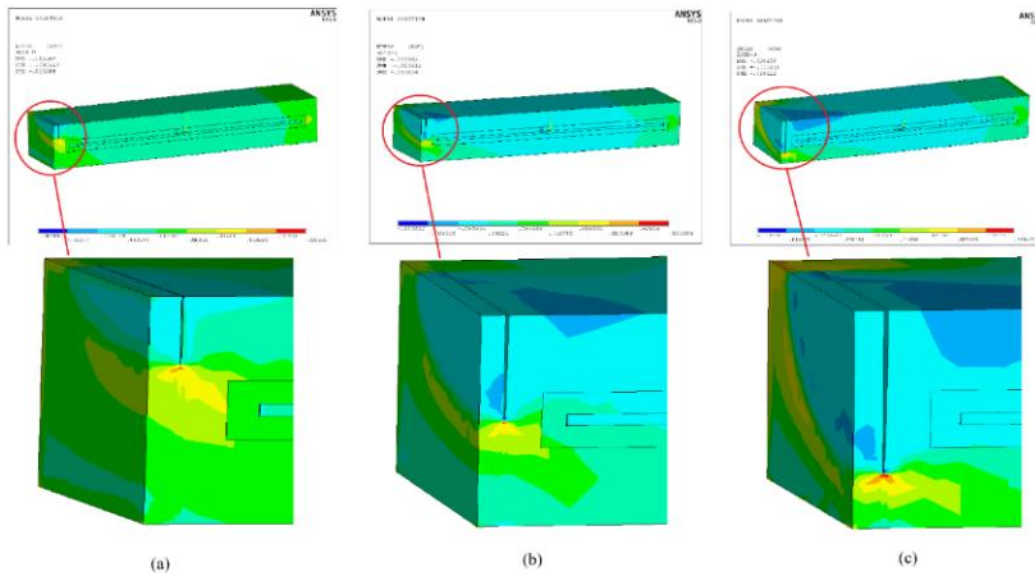


Figure 3.10: Total Strain Contour/Semi-elliptical crack propagation in Short RVE (a) $a/w = 0.25$ (b) $a/w = 0.5$ (c) $a/w = 0.7$ [134]

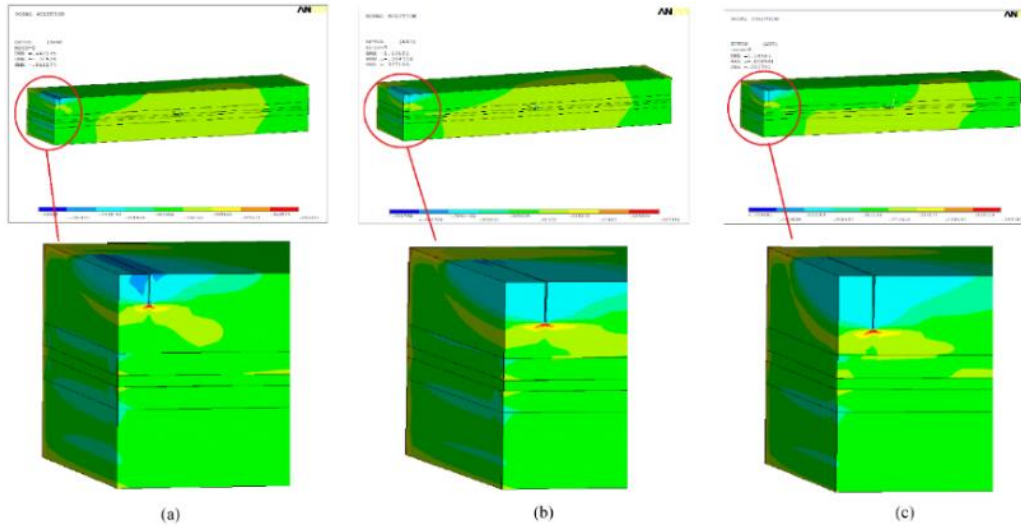


Figure 3.11: Total Strain Contour/Semi-elliptical crack propagation in Long RVE (a) $a/w = 0.15$ (b) $a/w = 0.2$ (c) $a/w = 0.25$ [134]

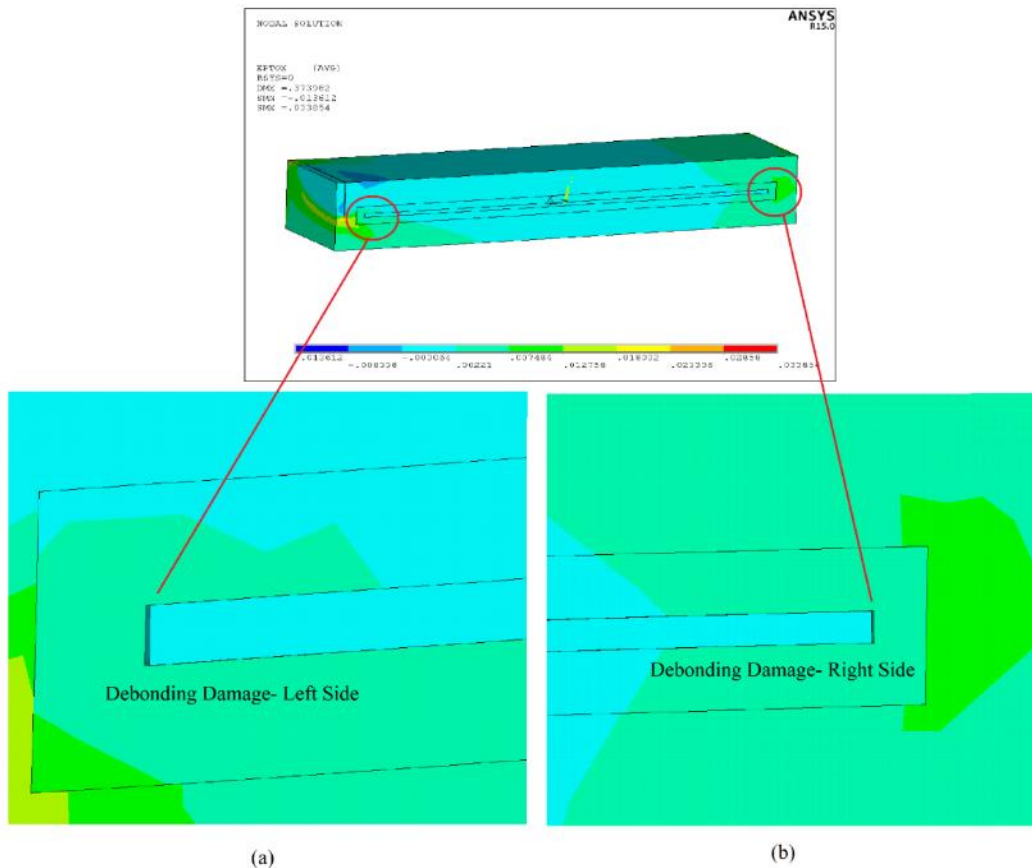


Figure 3.12: Short RVE with CZM -Total elastic/plastic strain (a) Debonding damage left side (b) Right side [134]

Figure 3.13 and Figure 3.14 [134] exhibit the influence of crack dimensions on dimensionless energy release rate, J_0/J . The values of this ratio demonstrate the significant effect of nanoclay on the fracture behavior of neat epoxy even at the outermost points of crack front. It should be expressed that the horizontal and vertical

axes imply the non-dimensional position angle on crack front and normalized J integral, respectively. Normalizing factor (J_0) denotes the contour integral for a crack with the same size in neat epoxy without any inclusion. Moreover, it should be indicated that in the nanocomposite models, the interfacial enhancement index was adopted as 40.

As shown in the Figure 3.13, normalized J increases during the crack propagates along its longer diameter c . In such 3D configuration, the middle region of crack front ($\frac{\pi}{4} < \varphi < \frac{3\pi}{4}$ approximately) in the vicinity of clay and interphase, is subjected to a high increase in normalized J rate than the other zones. Thus, it is worth noting that all contours reach their apexes at the deepest point ($\varphi = \pi/2$) which is in close proximity to the clay platelet.

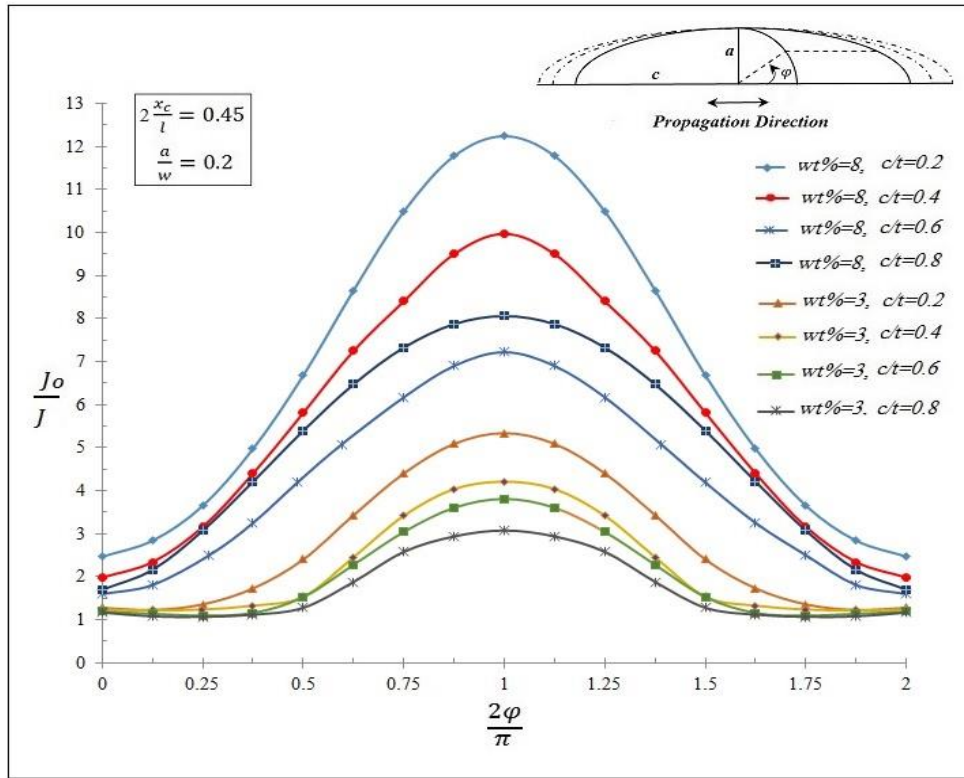


Figure 3.13: Variation of normalized J along crack front for several crack sizes in the short RVE; propagation along Z direction [134]

On the contrary, the tendency of crack propagation improves towards the end regions of crack ($\varphi = 0, \pi$) in 'c' direction. The impediment effect of nanoclay on crack propagation in 'a' direction (towards platelet thickness), is stronger than that of transverse direction (along 'c' diameter) on the crack edge. Furthermore, the amount of clay content has a remarkable influence on the crack characteristics. As a matter of fact, once local stiffness goes up, the crack tendency to growth decreases. In accordance with Figure 3.14, at crack endpoints ($0 < \varphi < \frac{\pi}{8}, \frac{15\pi}{8} < \varphi < 2\pi$ approximately) by increasing clay content (%), J_0/J decreases. This

anomalous phenomenon is observed through 3D nature of existing model [134]. In a RVE with a higher percentage of nanoclay, J_0/J for deepest point is almost 5 times greater (at maximum condition) than crack endpoints. Therefore, by moving away from deepest point on the crack front of short RVE model, normalized energy reduces, owing to the decline in clay influence on crack characteristics. Comparing the crack propagation between Y and Z direction, the convexity of curves in-plane (XY) successive crack positions is more than to out-of-plane ones.

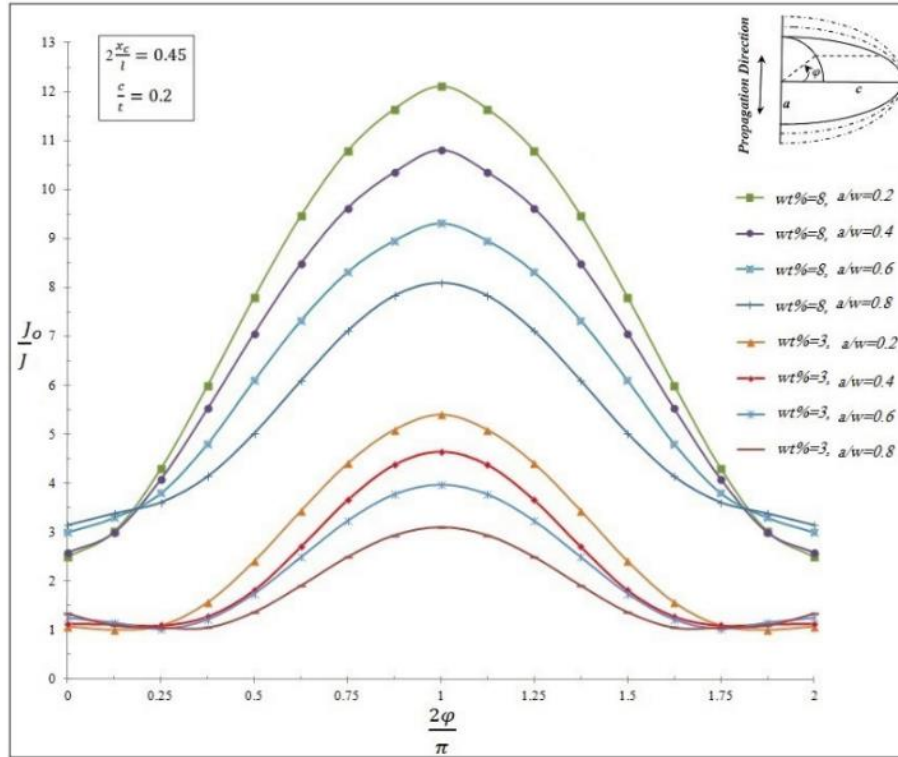


Figure 3.14: Variation of normalized J along crack front for several crack sizes in the short RVE; propagation along Y direction [134]

The variation trend in normalized J at the deepest point of crack front versus clay content considering various crack locations is depicted in Figure 3.15 [134]. As previously mentioned, the inclusion volume fraction plays a significant role on toughening. It should be noted, a and c have been chosen as one-fifth of w and t , respectively. Considering aforementioned crack size, there is a continuous enhancement in dimensionless J as the value of clay content increases. However, this noticeable improvement observed by increasing clay volume fraction up to about 8%, is at least 4 times in comparison with the lowest clay content.

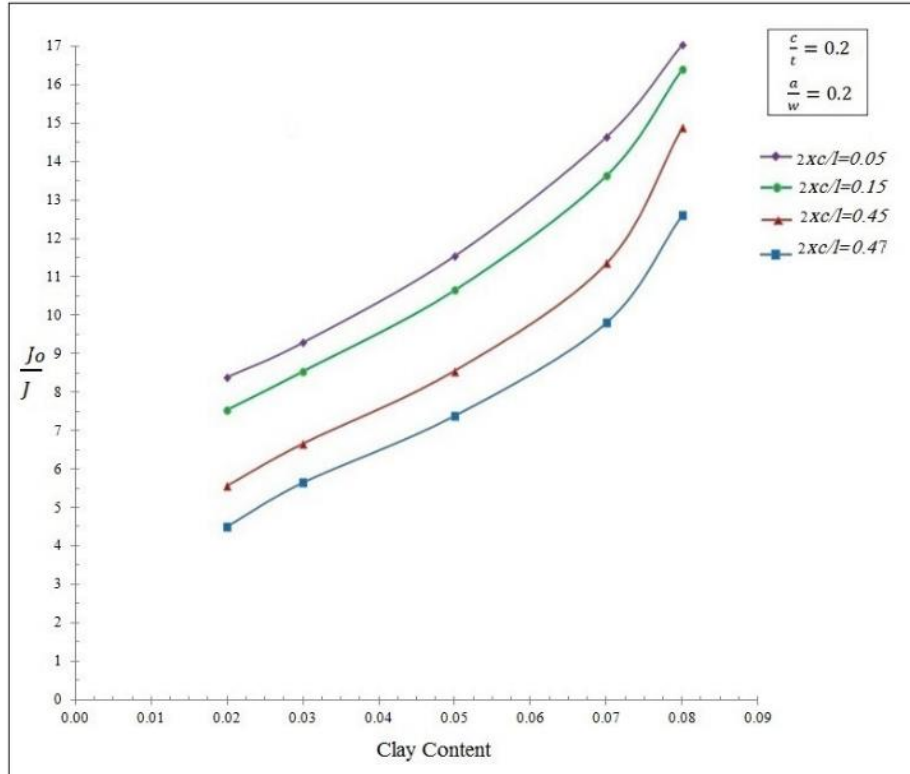


Figure 3.15: Variation of normalized J versus clay content at different crack locations the in the short RVE [134]

In order to evaluate the effect of crack location on contour integrals, twelve positions are defined and their corresponding results are reflected in Figure 3.16 along the crack front [134]. Significant observed drop in normalized J factor is attributed to dwindling effect of nanoclay presence on crack driving force at the end of RVE since toughening factor of nanocomposite diminishes with a high gradient in the region which is far from nanoclay ($2x_c/l = 1$). Adversely, crack propagation is highly hindered when the crack is located at the mid-plane of short RVE model ($2x_c/l = 0$). It is worthwhile to indicate that, in the nanocomposite model with higher clay contents, the influence of crack position is more tangible than the model with lower inclusion contents. As described in the Figure 3.16, due to the three-dimensional clay geometry which embedded in epoxy, the normalized J at crack end points ($\theta = 0, \pi$) approximately dropped by 20% more than the deepest point ($\varphi = \pi/2$) in clay content of 8 wt%. Unequivocally, this result is inferred from the presence of nanoclay which is thoroughly embedded in the surrounding matrix.

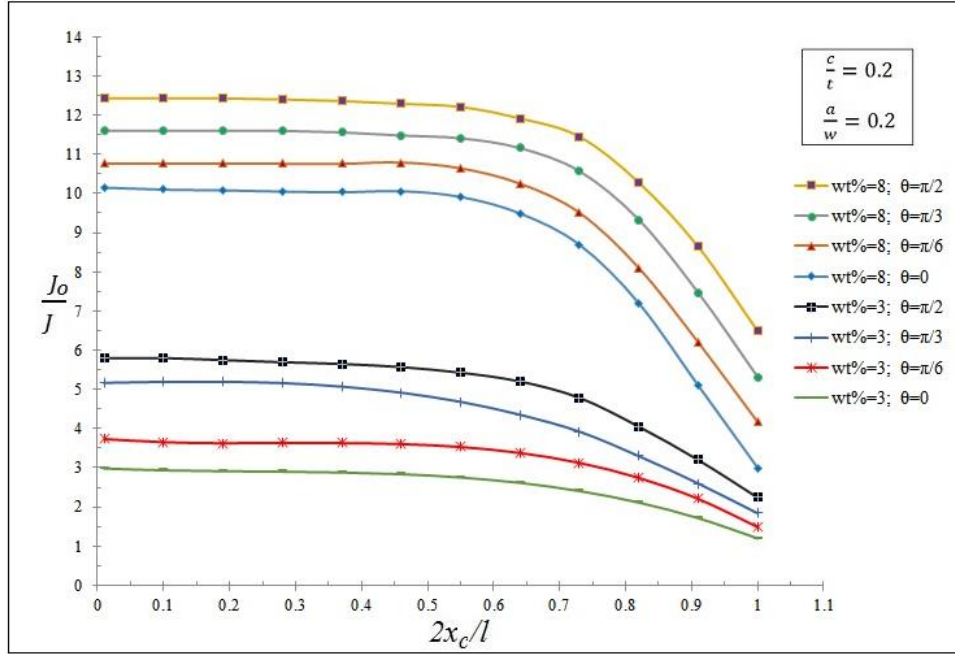


Figure 3.16: J_0/J versus longitudinal crack positions for several points along the crack front in the short RVE [134]

Figure 3.17 [134], the influence of CZM on dimensionless energy release rate is scrutinized for both long and short RVE models. It is evident from the graph that incorporating CZM between clay and interphase decreases the elastic modulus of nanocomposite leading to an increase in the normalized J .

In the short RVE model, the maximum value of J_0/J taking place at the deepest point of semi-elliptical crack decreases about 26% in 8 wt% of clay content in the model possessing CZM compared to the short model without CZM. By reducing the percentage of clay contents, the obvious effect of CZM on energy release rate diminishes. For instance, in 3% of clay content, exploiting of CZM results in 18% reduction in J_0/J . Recalling from previous section, the type of load transferring to clay has an undeniable influence on the mechanical behavior of RVE. Indeed, in the long type model, load is directly transferred to inclusion and as a consequence of this modeling approach, the elastic modulus of such RVE is considerably higher than short RVE model. In contrast, in the latter, load is transferred from clay through the medium via non-perfect bonding and the main outcome of such modeling approach is lower stiffness which is consistent with published experimental data.

The influence of long/short type RVE on crack toughening factor is demonstrated in Figure 3.18 [134]. As it can be seen, RVE selection strategy can intensify the crack energetic; long type RVE results in the amplification of J_0/J up to about 35% in comparison with the short one at $\theta = \pi/2$. The most affected zones belong to crack deepest point indicating the significant effect of load transfer type on local stiffness in vicinity of clay platelet.

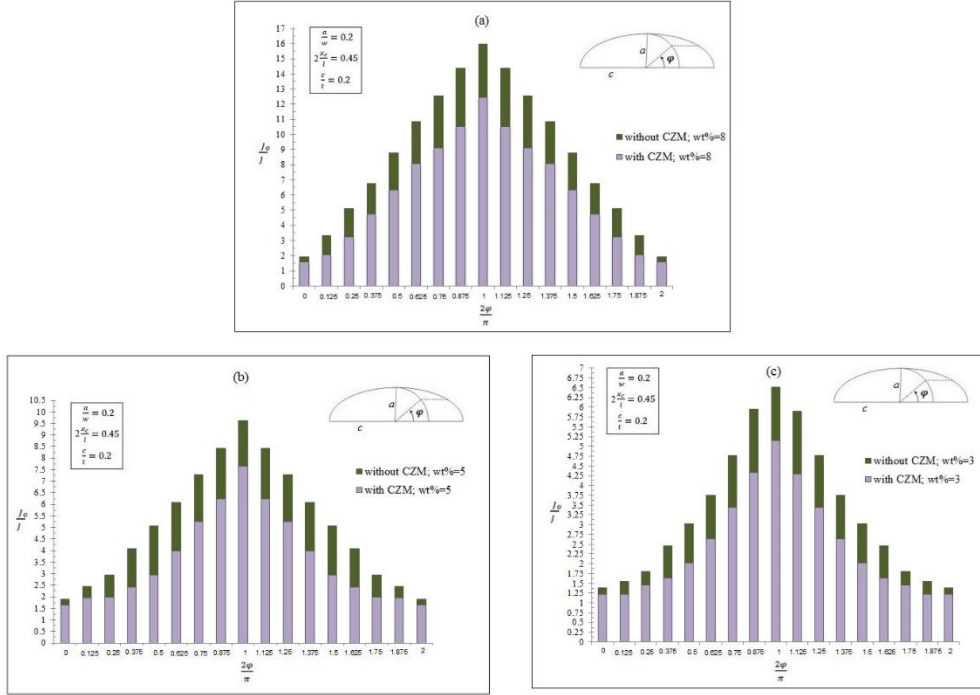


Figure 3.17: Influence of CZM on normalized J along crack front in the short RVE: (a) wt = 8%, (b) wt = 5%, (c) wt = 3% [134]

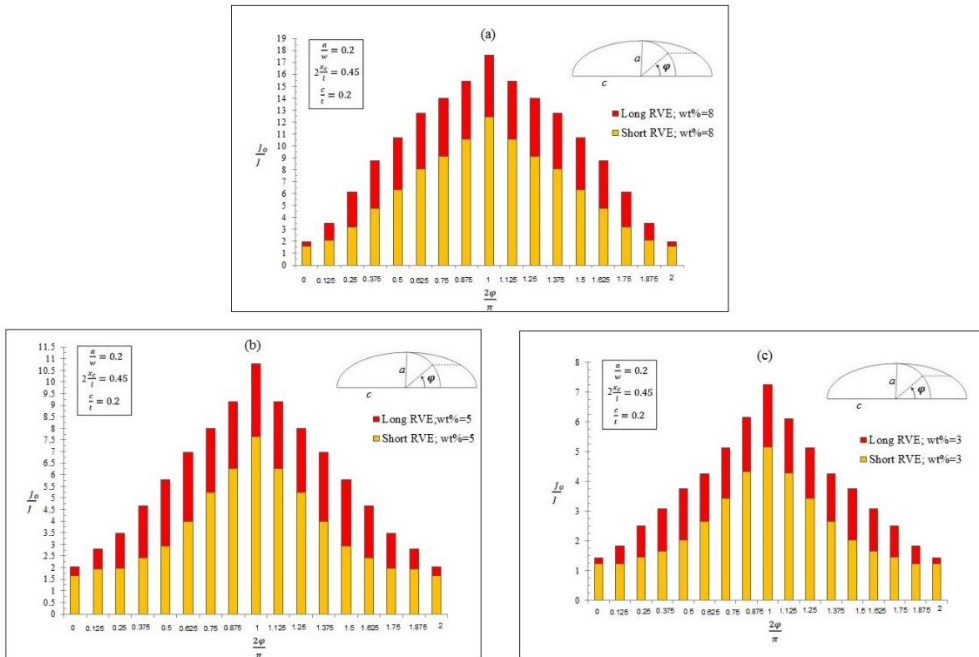


Figure 3.18: Influence of long/short RVE type on normalized J along crack front in: (a) wt = 8%, (b) wt = 5%, (c) wt = 3% [134]

Thanks to the remarkable influence of interfacial enhancement index on interphase elastic moduli, IEI variation effect on the crack behavior should also be investigated. The variation of normalized J versus interphase thickness in different n values at the deepest crack tip is shown in Figure 3.19 [134]. The normalizing factor

utilized herein, is J computed with $n = 40$. Remarkably, the magnitude of dimensionless J is augmented by decreasing of IEI. Furthermore, for higher amounts of IEI than selected IEI ($n = 40$), as interphase thickness increases, J_n diminishes. On contrary, by decreasing IEI (lower than $n = 40$), non-dimensional factor (J_n/J_{40}) becomes smaller than unit because of elastic modulus increment emanating from lower IEI values.

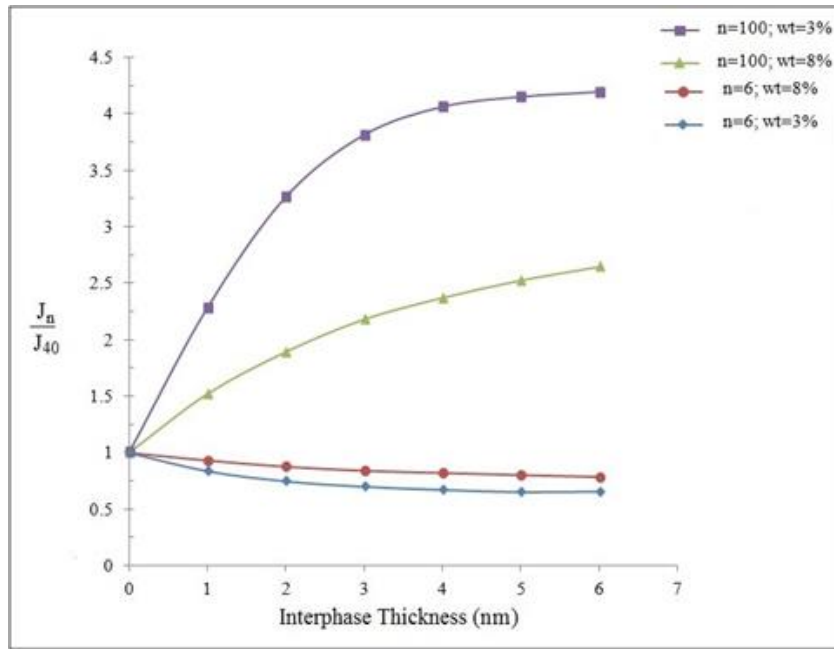


Figure 3.19: Normalized J_n versus interphase thickness with respect to different interfacial enhancement indices [134]

3.6 Conclusion

This chapter is devoted to investigating the role of non-bonded interaction between clay and polymer on fracture behavior of nanoclay reinforced polymers. For this purpose, a 3-D multi-scale FE model is constructed. Normalized J contour integral is defined and computed as a toughening criterion for monitoring the influence of crack existence and its characteristics. The variation of this factor as a function of crack geometry, crack location and RVE aspects such as clay debonding damage are examined thoroughly. The mix-mode CZM model is implemented accounting for non-perfect bonding between clay and epoxy. The results reveal the pronounced effect of clay debonding on crack behavior which leads to local stiffness reduction. Therefore, in the short RVE model, the maximum value of J_0/J taking place at the deepest point of semi-elliptical crack decreases about 26% in 8 wt% of clay content in the model possessing CZM compared to the short model without CZM. The influence of long/short type RVE on crack toughening factor is demonstrated in Figure 3.18. As it can be seen, RVE selection strategy can

remarkably intensify the crack energetic; long type RVE results in the amplification of J_0/J up to about 35% in comparison with the short one at $\varphi = \pi/2$.

Likewise, the influence of interphase thickness on crack energetic pertaining to 3D crack front is studied (as shown in Figure 3.19) and the results of which disclose that the deepest crack point is subject to higher toughening effects in presence of nanoclay. Finally, the outcomes disclose that nanocomposite modeling strategy encompassing long/short model and with/without CZM plays a critical role in toughening factor and therefore should not be neglected in numerical investigations. The remarkable results are listed as following:

- The crucial role of considering interface region and clay debonding on crack behavior.
- The considerable effect of interphase thickness on crack behavior.
- The remarkable difference of crack properties between ‘Short RVE’ and ‘Long RVE’ models.
- The noticeable improvement of toughening factor in clay/epoxy nanocomposite than neat resin, in presence of non-bonded interaction between clay and surrounding matrix.

Chapter 4: Fundamentals of Nano-Engineered Multi-Scale Hybrid Composites (NMHCs)

Abstract: This chapter represents a review and fundamentals regarding carbon nanotube coated-fiber multi-scale (CCFM) hybrid composites. The fabrication process and remarkable engineering advantages and outcomes are provided considering different engineering applications such as ILSS, IFSS, (structural health monitoring (SHM) and thermal and electrical conductivities.

4.1 Introduction

Smart and novel materials require the replacement of conventional composites with superior ones, which needs an advanced class of composites with multi-functionality. Composites structures utilizing reinforcing fibers (carbon, basalt, glass, aramid, natural fibers) together with nano-dimensional filler materials (graphene, carbon nanotube, nanoclay, metal nanoparticles) are known as multi-scale composites. These kinds of composites are also known as multifunctional composites due to their conventional load-sharing properties of the reinforced fibers as well as the additional functional properties (conductivity, sensing, thermal resistivity) associated with the particular nanomaterial [169].

Hence, multi-scale hybrid composites are advanced composites that are reinforced with nanoscale materials along with macroscale fibers, and these materials have attracted the attention of researchers as well as various industries. Multi-scale composites have potential applications in almost every field due to their pronounced features such as exceptional mechanical, electrical, and optical properties; extremely high aspect ratios of the nanomaterial constituents; and the uniformity, flexibility, and stability of the fibers. To optimize the performance of these kinds of composites, it is crucial to understand the selection of appropriate reinforcements, processing, and utilization of these advanced materials [169].

Mechanical properties, processing, and fabricating of CNT-coated multi-scale fibers are reviewed in this chapter as an overall perspective on this topic. A multi-scale or hierarchical structure is the result of a combination of micro-scaled fibers and nano-scaled fillers which inherently depends on physical or chemical interactions. Carbon nanotubes and nanofibers, graphene, and its oxidized derivatives, can be deposited on CFs by different techniques. Multi-scale structuring of the interlaminar region is conducted via various deposition strategies and employing CNTs as inter-ply medium in laminated composite. Assessment of multi-

scale fibers/ multi-scale structures is the core content and purpose of this thesis exploring the improvement in load transferring between the fibers and surrounding matrix. Moreover, the use of NMHCs to add new functionalities (e.g., electric conductivities, sensing, thermal conductivities) to structural composites is introduced as the momentous advantages and engineering applications of NMHCs' [170].

Once the load is applied, the matrix transfers the load to the fibers and distributes the stress among the fibers. Significantly, prerequisite for an efficient and perfect shear transfer under load is therefore the presence of a proper fiber-matrix bonding [170]. It should be indicated that interphase denotes a finite interlayer between the fiber and matrix with distinct physico-chemical properties which was introduced in the 1970s [171]. The load transfer capability of the interphase depends on the fiber-matrix adhesion which can be physico-chemical, frictional, or both, in nature [170]. In polymer-based composites, physico-chemical contributions are generally assumed to be more important than the frictional ones. In most cases, both chemical and frictional components are operative, like in the case of multi-scale fibers and related composites. The term "multi-scale" implies the presence of a structure arranged in a multiscale morphology spanning over different length scales from nano to macro. In fact, in case of multi-scale all-carbon fibers the surface of the micro-scaled CFs (typical diameter $\sim 7\ \mu\text{m}$) is covered by nano-scaled carbon nanoparticles, such as carbon black, CNT, carbon nanofiber (CNF), graphene and its derivatives. It is worth noting that such reinforcements, also terms "hierarchical", "hybrid" and "fuzzy", have remarkable analogies with nature-based multi-scale structures which perfectly 'engineered' to fit with the dominant loading situation [172]. Consequently, these materials are nominated as nano-engineered multiscale hybrid composites in this thesis.

Another type of multi-scale fibers is assembled by combining individual units of CNT or graphene. Such fibers, if free of defects and sufficiently long and highly aligned, are expected to generate extreme mechanical and transport properties as well as to possess multifunctional properties for applications in energy harvesting, capacitors, or flexible batteries, however, since this field is still under development [173]. Depositing carbon nanofillers on CF is an effective method to augment the fiber surface area thereby supporting the mechanical interlocking (the filler acts as "interlocking agent"). Likewise, gradient-like, graded interphase or local stiffening of the interphase allows a smooth stress transfer and helps to eschew stress concentrations which are the usual sources of premature failure. It should be highlighted that the nanoparticles' dimensions in the nanometric range are fully compatible with the highly packed structure of advanced composites containing high volume fractions of reinforcing fibers. Noticeably, the interphase is a key factor in composite performances both under transverse tensile and in-plane shear loads. In fact, the dominant failure modes in off-axis loaded fiber-reinforced polymers are

debonding between fiber and matrix and delamination within (intralaminar) or between (interlaminar) the plies [170], which is the core subject of this thesis.

Hence, major benefits of utilizing hierarchical fibers in polymer composites is to improve the matrix-controlled properties, notably the interfacial shear strength (IFSS), transverse tensile strength, the resistance to intra- and interlaminar failures as being addressed in this thesis. Another possible benefit is the improvement of the through-thickness properties of advanced composites without compromising the in-plane performance. It is noteworthy that the action traditionally implemented to improve the through-thickness properties (interleaving, z-pinning, stitching, braiding ...) are generally accompanied by a prominent reduction of the in-plane properties. Moreover, the use of multi-scale fibers in composite systems may result in additional functional properties, such as mechanical damping, sensing, self-healing, shape memory, morphing [170]. Nanofillers deposited on microscopic fibers can positively contribute in several ways, i.e. by roughening the fiber surface, reducing the stress transfer length (i.e. reduction of the critical aspect ratio of the fiber), and stress redistribution via stress field homogenization (i.e. diminishing stress concentration effects). In fact, stress field homogenization seems to be the main synergism observed in composites with micro- and nano-fillers [170]. Owing to the presence of nanofiller particles acting as local obstacles, a crack travelling at the interphase is forced to follow a zig-zag route which is schematically displayed in Figure 4.1 [170].

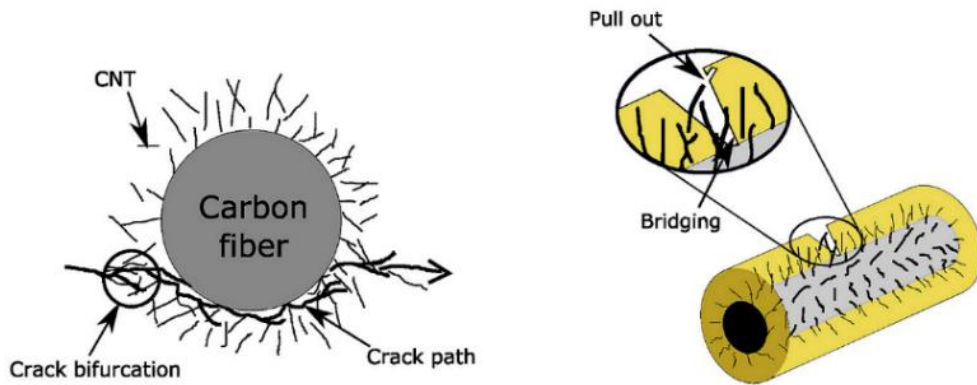


Figure 4.1: Schematic of crack bifurcation, deflection mechanisms owing to multi-scale CNT-coated fibers [170]

4.2 Processing and Fabrication Methods of NMHCs

There are currently multifarious techniques for directly placing CNTs onto the carbon fiber surface given in the literature as (1) direct growth of CNTs on fibers by means of chemical vapor deposition (CVD), (2) flame synthesis approach, (3) electrophoretic deposition of CNTs onto the fiber surface (4) chemical reactions between functionalized CNTs and fibers and (5) the deposition of CNTs by methods including dip coating of CFs with a CNT containing sizing [18] which are being addressed in this section concisely. Beyond all doubt, CVD is the most popular and

effective technique to produce CNTs and to grow CNTs on substrates. It is the only technique known to grow CNTs perpendicular to the carbon fiber surface [174]. But the CVD manufacturing process has the potential to cause a reduction in the strength of the carbon fibers and therefore compromise the tensile properties.

In chemical grafting approaches, nanofillers are grafted onto the traditional fibers employing techniques like CVD, electrophoresis, or using chemical groups. These nanomaterial-coated fibers or hierarchical fibers exhibit advanced interfacial properties. Apart from multi-functionality, nanomaterials grafted onto fibers provide improved out-of-plane properties in the final material [169].

All reinforcing fibers used for manufacturing polymer composites are surface treated and/or coated, usually during their production steps. This kind of coating is usually referred to as “sizing”. Sizing is commonly applied also on CFs. During their production, CFs may be subjected, however, to various surface treatments to remove the weak outer layer and introduce oxygen containing functional groups for a better adhesion. As 1D nanoparticles, carbon nanotubes (CNT) have been utilized in sizing formulation in various forms, such as single (SWCNT), double (DWCNT) and multi-walled (MWCNT) in oxidized or other functionalized forms [170].

The easiest and cheapest method to coat nanomaterials onto the fibers is dip coating, in which the fiber is dipped into an aqueous solution/ suspension of targeted nanomaterial and the coating is formed on both the outer and inner surfaces. There are many examples demonstrating that the properties of the materials were improved after coating the nanomaterials onto the fibers using dip-coating [169]. As suspension media for functionalized CNTs bearing hydroxyl and carboxyl groups, water, ethanol, and acetone are preferred because of their good dispersion ability and easy evaporation upon drying. For GO, usually water is selected as suspension medium since the functional groups typically present on the GO surface can help its convenient and fine dispersion. Nevertheless, acetone was also used for GO produced from oxidized expanded graphite. Sonication has been proved to be the right tool to avoid sedimentation and to promote the dispersion of the nanoparticles, sometimes, however, surfactants were additionally applied [170].

Another simple technique to coat nanomaterials onto the fibers is spray coating, which ameliorates the out-of-plane properties and introduces multi-functionality by restricting the localization of nanofillers. Zhang et al. coated a connected network of CNTs onto carbon fiber prepreg and found that even a very small amount of CNTs (0.047 wt%) improved the Mode-I fracture toughness by 50% [175]. Importantly, the CNTs provided in situ damage sensing capability for the composite.

As foregoing mentioned, CVD is the method to craft nanomaterials (especially CNTs) onto fiber; in this method, CNTs are directly grown on the fiber surface at high temperature in the presence of metal catalyst. Usually, hydrocarbon gases are used as a carbon source, and catalyst can be deposited onto the fiber surface by various methods like dipping, spraying, electrodeposition, sputtering, and thermal evaporation. Analogous to other grafting methods, this also increases the surface area

of the fiber and improves interfacial interlocking, which consequently leads to better stress transfer between the matrix and fibers [169]. Since glass fiber possesses a low thermal resistance, it is difficult to perform CVD on a glass fiber to grow CNTs. Nonetheless, some scientists have tried to grow CNTs on a glass fiber surface using CVD.

Akin to CVD method, electrophoretic deposition (EPD) is a practical, scalable, and cost-efficient method employed to graft nanomaterials onto fabrics. In EPD, two parallel electrodes (i.e., the working and counter electrodes) are connected to the power supply, and positively and negatively charged particles are deposited onto the cathode and anode, respectively. For instance, carbonyl iron microparticles (CIP) were deposited onto carbon fibers using EPD in which CIPs were dispersed in acetone-ethanol solution along with stabilizer. Similarly, negatively charged graphene oxide was also deposited onto glass fibers using EPD, and the thickness of the coating could be controlled by varying the voltage and time of EPD [169]. Likewise, acid-treated CNTs were deposited onto oxidized carbon fiber and showed a 60.2% enhancement in interlaminar shear strength [176]. It should be mentioned that the two electrodes must be in a parallel position to provide a uniform coating of nanomaterials. CNTs, graphene, and aramid nanofibers (ANF) could be also coated onto the carbon fibers utilizing EPD. In these deposition processes, charged particles are deposited on the CF having opposite electrical charges. Attractive forces between positively charged nanoparticles and negatively charged reinforcing materials (or vice versa), were exploited to acquire a homogeneous deposition of nanofillers. Figure 4.2 describes different coating techniques of fibers utilized in CCFM hybrid composites.

In selective placement method, a multi-scale structure at a nanoscale can also be achieved when the nanoparticles are selectively positioned by different methods. These methods can be grouped into wet, dry, and sacrificial methods. One will recognize that there is a clear analogy to the interleaving concept, however, using new materials. A simple way is to place the nanoparticles, dispersed in the matrix resins with or without additional solvent, or in a suitable dispersing medium (wet techniques), between the reinforcing layers by brushing, rolling, or other mechanical methods. Zhang et al. [177] provided an investigation moves along the same direction and could be considered as sacrificial placement as shown in Figure 4.3. The authors utilized an epoxy resin dissolvable thermoplastic (phenoxy) interleaf for the localization of CNTs. Thin phenoxy interleaves (30 μm in thickness) with 1 wt. % MWCNT contents were prepared by both solution casting and hot pressing and positioned in the mid plies of CF fabric/EP composites. Phenoxy, being enriched in the interphase, underwent phase inversion, and became the continuous phase locally in the epoxy matrix. The properties of the resulting CNT structure were exploited for damage sensing, measuring the volumetric electrical resistance, under mode-I loading.

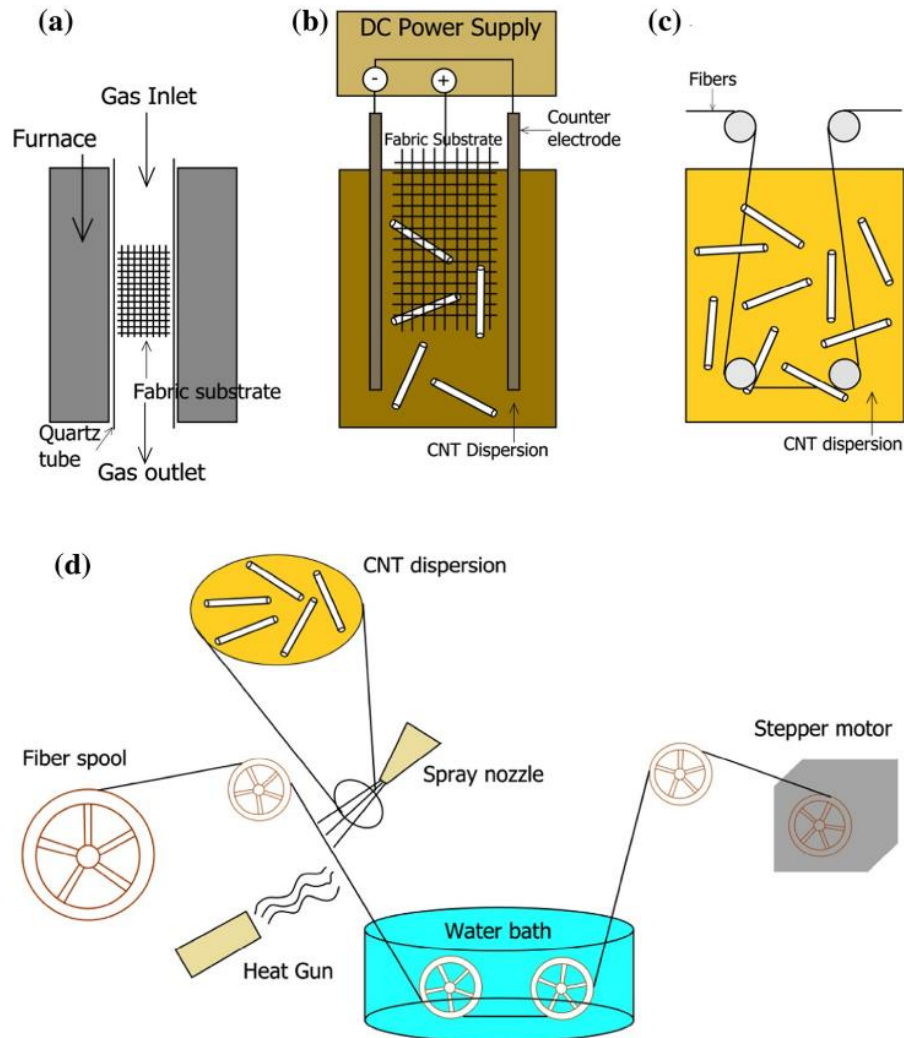


Figure 4.2: Schematics of typical surface coating techniques of fibers/fabrics: (a) CVD process (b) electrophoresis process (c) sizing process and (d) spray coating process [169]

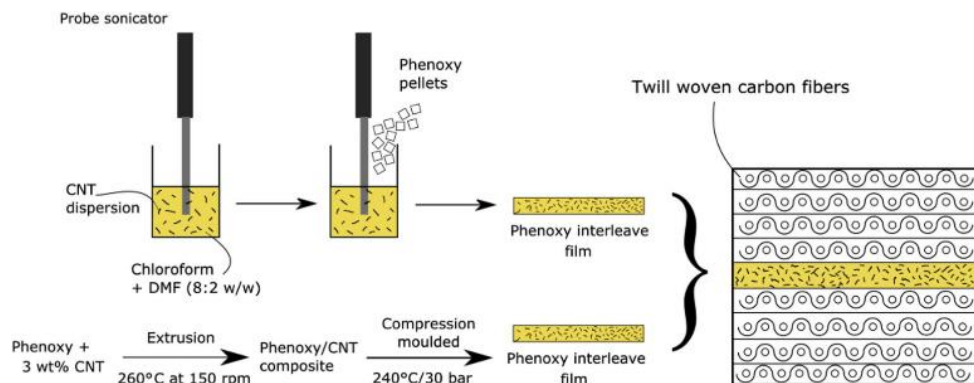


Figure 4.3: Scheme of 'sacrificial' interleaving with an epoxy resin soluble CNT-containing thermoplastic polymer [177]

A novel method was introduced by Li et al. [18] for preparing carbon fiber–carbon nanotube hybrid structures, by electrospraying solvent dispersed CNTs with a binder onto carbon fiber with an end aim to improve interfacial bonding in composites. The electrospray parameters controlling the modification of the CNT morphologies were assessed. High-speed camera observations found applied voltage played a critical role for determining spray mode development. Electric field simulations revealed a concentrated electric field region around each fiber. Both voltage and distance demonstrated a significant role in determining the CNT morphology by mediating anchoring strength and electric field force. The forming mechanism investigation of different surface morphologies suggested that binder with appropriate wetness imparts freedom to the CNTs, allowing them to orientate radially from the CF surface. The electrospraying of CNTs onto an array of single carbon fiber is depicted in Figure 4.4.

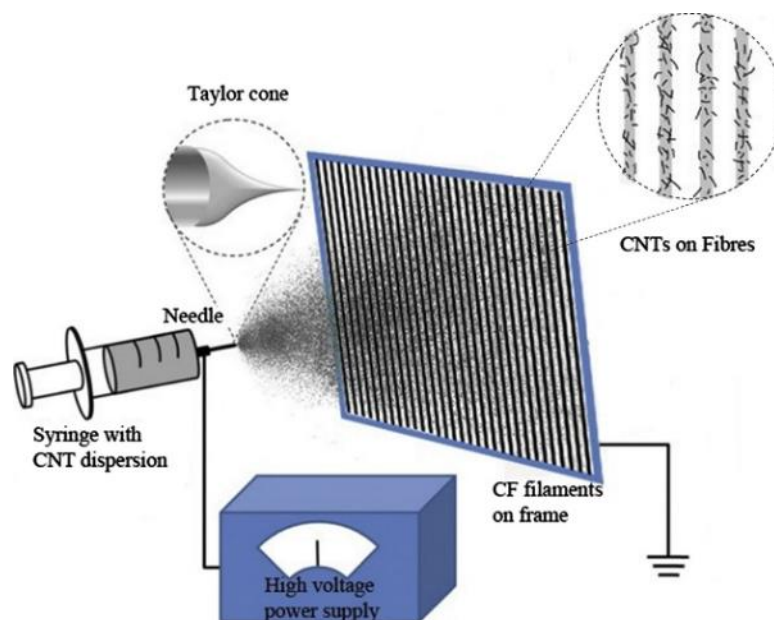


Figure 4.4: Schematic representation of the electrospraying of CNTs onto carbon fiber [18]

The equipment consists of a stainless-steel needle (0.8 mm inner diameter) and a steel platform (15 cm × 15 cm) as the ground electrode. The needle is connected to a precision high voltage power supply capable of delivering a maximum applied voltage of 50 kV to the needle with a resolution of 0.1 kV. The inlet of the needle is connected via silicone tubing to a hypodermic needle fitted to a 6 mL syringe. Single fiber filaments with a length of 15 cm were selected from a carbon fiber tow. Both ends of filaments were fixed onto an aluminum frame, and then placed onto a round metal platform which is connected to an earth wire. It is worth mentioning that in the electrospray method electrically charged CNTs sprayed from one side are able to wrap around the fiber for even coating which cannot be realized by traditional spray techniques. It has been demonstrated that electrospray atomization can be used as a

novel and flexible tool for the controlled deposition of CNTs onto the surfaces of carbon fibers. It should be emphasized that the applied voltage is a critical factor in determining the mode of electrospray.

4.3 Properties and Remarkable Engineering Advantages of NMHCs

4.3.1 Properties

Mechanical Properties: Multi-scale composites possess improved interfacial interactions and increased fiber surface area that helps the fibers to interact with a polymer matrix. The improved interlocking between polymer and fiber provides remarkable strength to the composite by advancing the stress transfer mechanism between fiber and matrix. Numerous reports demonstrate that the interlaminar shear strength (ILSS) is improved by incorporation of a nanophase in fiber-reinforced composites [178] [179]. MWCNT reinforced composites exhibited 44.2% and 29.4% increases in mode I and mode II toughness, respectively, in comparison to the neat composites [169]. A 40–67% increase in interfacial shear strength of aramid fiber was observed after grafting TiO₂ nanoparticles, which reduced the stress concentration between the fiber and the matrix by providing interfacial interlocking [169]. Du et al. reported 9.4% and 15.9% increases in flexural strength and flexural modulus, respectively, along with 10.2% and 25.4% increases in tensile strength and Young's modulus by coating graphene oxide on carbon fiber in carbon fiber-reinforced composites compared to untreated composites [180].

Thermal properties: A great number of studies showed that nanoparticle-reinforced fiber polymer composites possess very good thermal properties due to the thermal stability of the fibers and improved interactions between the filler and matrix by nanofillers that provide stability and restrict the mobility of polymer chains during thermal treatment [169] [179]. Multiscale composites with advanced thermal properties were synthesized from graphene foam filled with carbon fiber-reinforced PDMS polymer (CF/Graphene/PDMS) by Zhao et al. [181]. Moreover, the flame-retardant properties of the material were improved by reinforcing materials applied at different scales. Hapuarachchi et al. reported that the heat release capacity of polylactide was reduced by 58% after reinforcement of CNTs and sepiolite nanoclays, and it was reduced by 45% after reinforcement of hemp fiber into polylactide [182].

Electrical properties: Since multiscale composites possess improved interfacial strength, the fillers make very good continuous networks that lead toward advanced electrical properties. For instance, Cortes et al. [169] improved the transverse electrical conductivity of carbon fiber/ PEEK composites by at least 3 times by adding silver nanowires into the matrix. Furthermore, the electrical conductivity of

carbon fiber/ epoxy composites was improved by dispersing CNTs via a freeze-drying method. The electrical conductivity along the longitudinal, transverse, and through thickness was improved by 49%, 189%, and 160%, respectively, indicating the favorable dispersion state of CNTs in that particular direction [183]. Generally, conductive fiber-reinforced composites show low through-thickness electrical conductivity, which limits their applications. This obstacle can be removed by grafting conductive fillers onto the fibers that enhance both in-plane and through-thickness electrical conductivity by creating an interconnected electrically conductive network. Kwon et al. coated graphene and CNTs onto carbon fiber using electrophoretic deposition and showed an improvement in the through-thickness electrical conductivity of a carbon fiber-reinforced composite of $\sim 1400\%$ compared to the uncoated composites [184].

Self-healing: which is the process in which a material senses the damage and implements some actions or secretes a material to heal the damage. Self-healing can be divided into two types encompassing intrinsic and extrinsic. Regarding the intrinsic healing, the material reforms reversible covalent or non-covalent bonds to recover the damage, while in extrinsic healing, another phase or structure is added to the material. Micro-capsulation is a widely practiced method for extrinsic healing in which the capsuled healing agent polymerizes to heal the damage or crack. Numerous reports based on self-healing fiber-reinforced composites have been published in literature. However, after healing of a crack by polymerization of resin, the damaged area becomes resin rich and can lead to crack initiation due to the absence of reinforced fiber in that specific area. To preclude further crack initiation in that healed area, nanofillers are incorporated into the micro-capsules containing healing agent. Hence, the reinforced nanofillers increased the viscosity of the resin, resulting in appropriate self-healing properties [169]. The healing agent can be stored in many forms including nanotubes, microcapsules, and vessels. Since CNTs are extensively used in advanced composites, Lanzara et al. [185] performed a molecular dynamic study to investigate the role of CNTs as a reservoir to contain healing agents and found that, depending on crack size and temperature, CNTs can break and release the filled healing agent to repair damage as delineated in Figure 4.5. However, it is difficult to insert the healing agent into the tube and break the tube to release the healing fluid due to extremely small size and remarkable strength of CNTs.

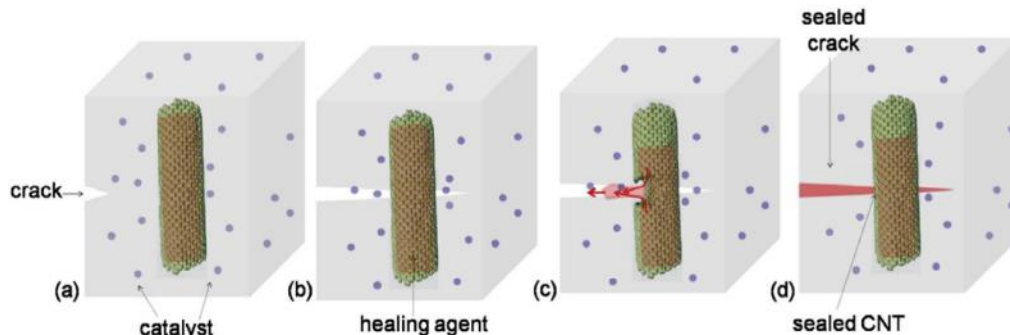


Figure 4.5: Concept of the self-healing process using carbon nanotubes [185]

Sensing Ability: Another remarkable property of multi-scale composites is sensing ability. Numerous reports are available on nanofibers decorated with different nanomaterials with great sensing ability. Fiber-reinforced composites are preferred to design sensors (especially mechanical sensors) due to their low-cost, flexibility, easy processing, and high sustainability. Embedding is another way to include the sensing material into fiber-reinforced composites that both sense damage or pressure and enhance sustainability [169].

4.3.2 Remarkable Engineering Advantages

Multiscale composites can be utilized in a large number of applications including automobile industry, aeronautics, and defense which need advanced lightweight materials, since the weight of the components is directly associated with fuel/ energy consumption and final cost of the product. In the automobile industry, advanced multiscale composites are replaced with heavy steel and injection molded automotive parts. Automotive components made of multiscale composites are lighter, safer, and more fuel-efficient. NMHCs provide excellent stiffness and strength along with good stability. It is worth noting that the strength of these composites can be tailored by incorporating various types of nanofillers with desirable weight percentage. However, these cars are still largely limited to racing cars. BMW's i3 and Volkswagen's XL1 are examples of commercialized carbon fiber-based multiscale composites. Regarding aerospace industry, e.g., Boeing and Airbus have designed aircraft utilizing multi-scale composite materials. These hybrid composites provide mechanical strength, damage tolerance, thermal stability, and corrosion resistivity. In addition, the advanced hybrid composites are being employed in space shuttles, fighter jets and gliders. The most common components made of multiscale composites are wing assemblies, helicopter rotor blades, fan blades, propellers, seats, and interiors [169]. Multi-scale composites are also exploited in marine applications where the corrosion phenomenon is a key factor that influences the life span of the material. The use of multiscale polymer composites both protects against corrosion and provides the convenience of manufacturing along with light weight. Multiscale composites are highly utilized in the sporting goods industry to satisfy the demand for light weight, high strength, and low-cost sports materials. The most common examples of advanced sports equipment made of multiscale composites are tennis rackets, bicycles, golf clubs, skis, football helmets, kayaks, and hockey sticks. Moreover, multiscale composites are highly desired in military applications due to their light weight, safety, durability, and multifunctionality for applications like drones, body armor, vehicle parts, ballistic panels, etc.

By designing the fiber-matrix interface using CNT and graphene oxide (GO), the properties of the carbon fiber-reinforced composite were changed significantly [186]. In this research, the interfacial shear strength between the fibers and the matrix was examined utilizing a microdroplet test. In addition, CNT-coated, GO-coated,

and pristine unidirectional carbon fiber fabrics were used to manufacture CF/epoxy composites via the vacuum-assisted resin transfer molding method, and their interlaminar shear strength were measured. The morphologies of different CF samples with CNT and GO are shown in Figure 4.6 [186].

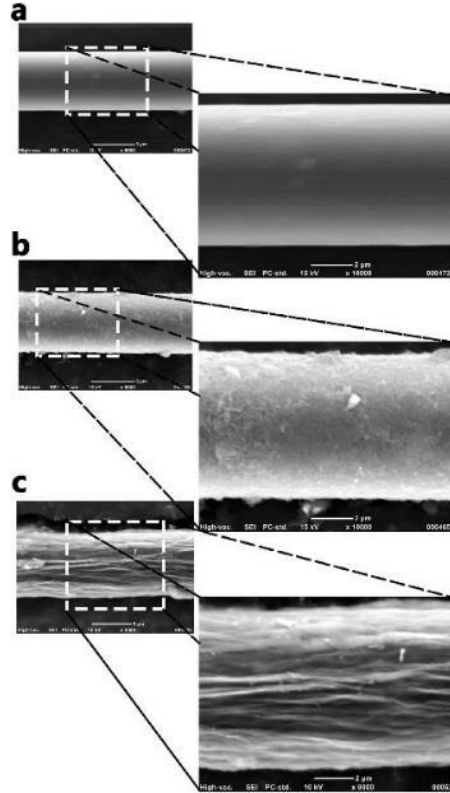


Figure 4.6: SEM images of the (a) desized CF, (b) CNTs/CF, and (c) GO/CF [186]

The interfacial bonding strength between the matrix and the above-mentioned fibers was evaluated by examining the IFSS, and the results are depicted in Figure 4.7 (a) [186]. The ILSS results are also presented in Figure 4.7. The ILSS of the desized CF composite and GO/CF/epoxy composite was 36.7 MPa and 56.9 MPa, respectively. The CNTs/CF/epoxy composite had the largest ILSS by 58.2 MPa. This result demonstrates that the interfacial and mechanical properties of the CF/epoxy composites can be enhanced remarkably by introducing CNTs and GO into the interphase of the composites.

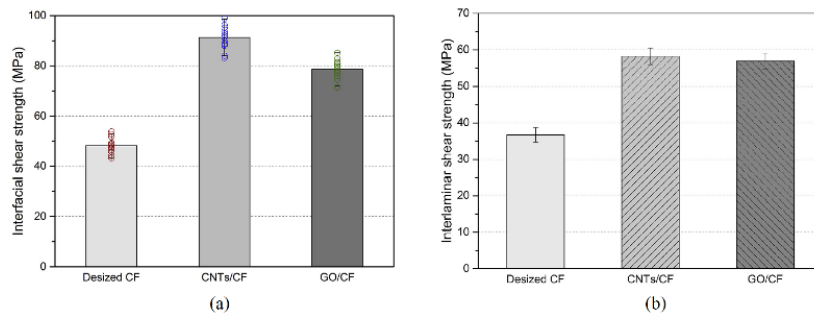


Figure 4.7: (a) Interfacial shear strength results of the composites (b) Interlaminar shear strength of the composites [186]

Chen et al. [173] introduced a gradient interphase reinforced by graphene sheets between carbon fibers and matrix to improve the interfacial properties of carbon fibers/epoxy composites. Due to the formation of this gradient interface layer, 28.3 % enhancement of unidirectional CF/epoxy composites in ILSS is observed with EG (graphene sheet) loading of 1 wt%. It is noteworthy to mention that after adding EG, the modulus drop from CF to matrix is found to be slowed significantly. This phenomenon plays a crucial role for improving stress transformation from CF to epoxy and then enhancing the interfacial performance. To verify the effect of gradient interphase on the interfacial properties of composites from a different angle, the gradient interphase is removed by sonicating the uncured composites with EG. Gradient interphase structures are disappeared, and interfacial performance of composites is found to be weakened. Figure 4.8 displays the procedure for preparation of graphene nanosheet-coated CF composites for both sonicated and hierarchical (with graded interphase) samples.

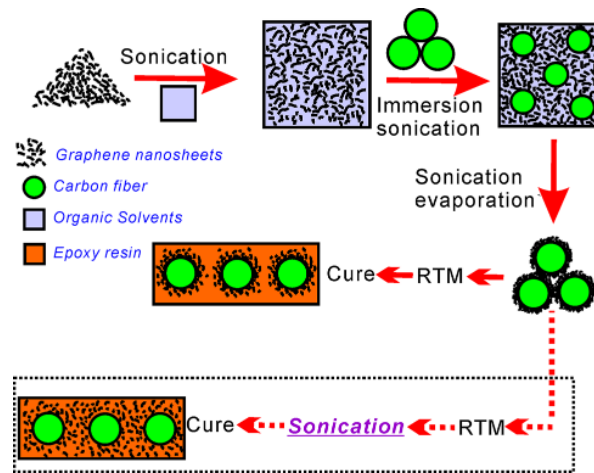


Figure 4.8: Schema illustration for the preparation of CF absorbed with EG [173]

The exact structure differences between the pristine, hierarchical, and sonicated composites are illustrated in Figure 4.9.

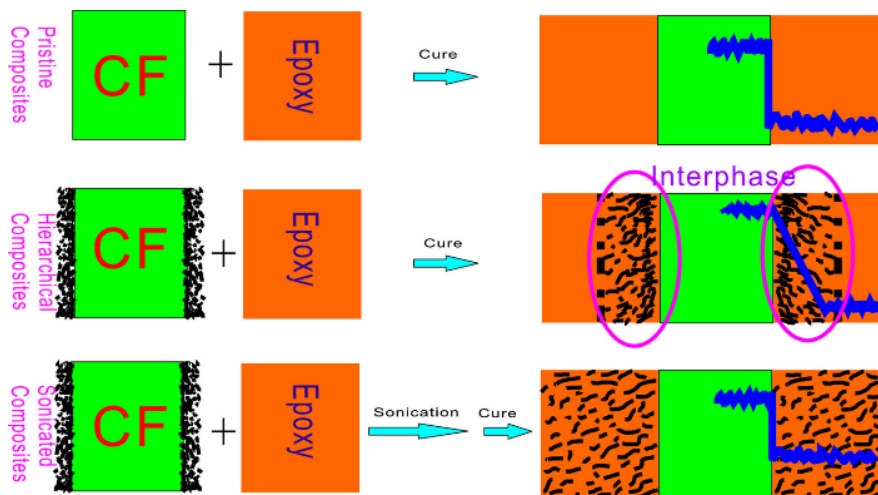


Figure 4.9: Schema for the differences between pristine, hierarchical, and sonicated composites [173]

As a significant outcome, Figure 4.10 demonstrates the ILSS of hierarchical composite with graded interphase and sonicated composites through experimental investigation. The results reveal the positive effect of graded interphase on the improvement of ILSS.

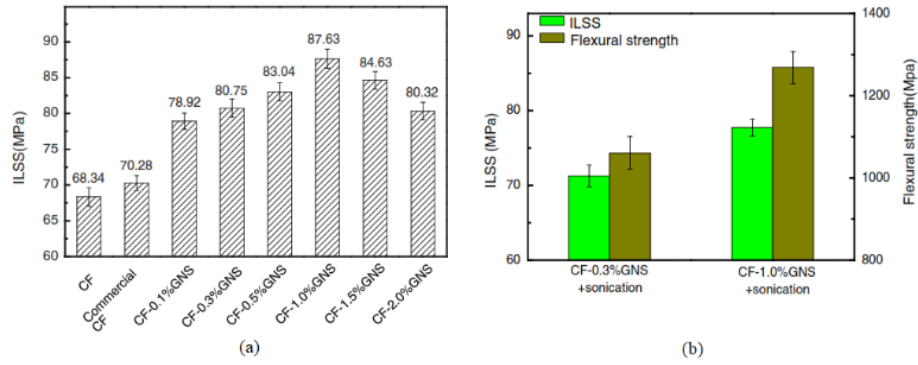


Figure 4.10: ILSS of (a) hierarchical composite with graded interphase, (b) sonicated composite [173]

An experimental work was carried out by Li et al. [187] to develop a deeper understanding of the interfacial reinforcing mechanism of carbon nanotube–carbon fiber hybrid composites. Figure 4.11 shows typical micrographs of the carbon fiber fracture morphology observed with and without the CNT coating.

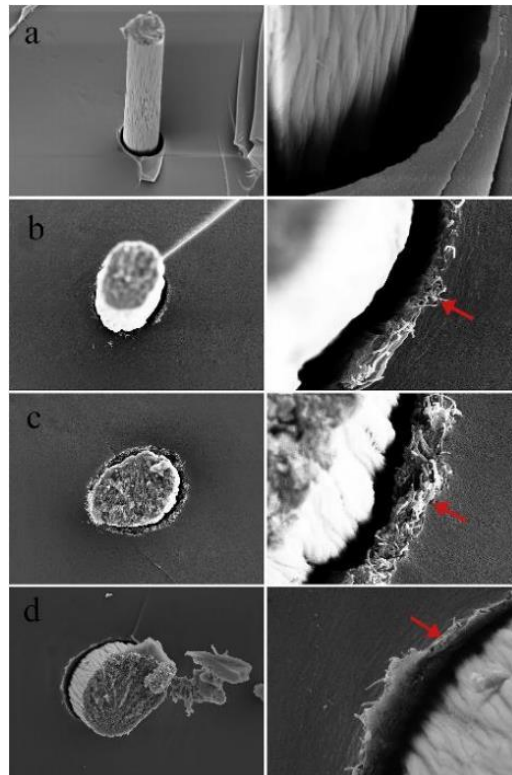


Figure 4.11: Fracture morphology of single fiber composite fragmentation tests: (a) CF, (b) 10 min CNT-coated CF by 20 kV/10 cm, 25 °C, (c) 10 min CNT-coated CF using 10 kV/5 cm, 100 °C, (d) 20 min CNT-coated CF by 20 kV/10 cm, 100 °C [187]

In accordance with the aforementioned test, at the interface of hybrid composite, the CNTs and epoxy together are bonding to the carbon fiber surface. The fracture surface of the composites prepared with CNT-coated fibers (Figure 4.11 b–d right) presented completely different morphologies with that of the CF without coating. Relatively small and shallow debonding areas appeared at the joint between the fiber and the CNT nanocomposite interphase which is significantly indicating that the CNTs have a higher adhesion force with the matrix and the fracture planes initiated at the interface between CNT nanocomposite and fiber.

The introduction of carbon nanotubes into fiber-reinforced polymer composites has been accomplished predominantly by Zhao et al. [188] via two routes: mixing CNTs entirely throughout the epoxy matrix (matrix modification- CF/EP-CNTs) or attaching CNTs onto reinforcing fibers (interface modification- CF-CNTs/EP). Employing single-fiber fragmentation test combined with energy dispersive X-ray spectroscopy, the interfacial shear strength with improvements of 45.2% and 10.14% were achieved for hierarchical composites based on CNT-modified fibers (CF-CNTs/EP) and composites based on CNT-reinforced matrix (CF/EP-CNTs), respectively. Figure 4.12 describes the ILSS of neat CF/EP composite, CF/EP-CNTs and CF-CNTs/EP.

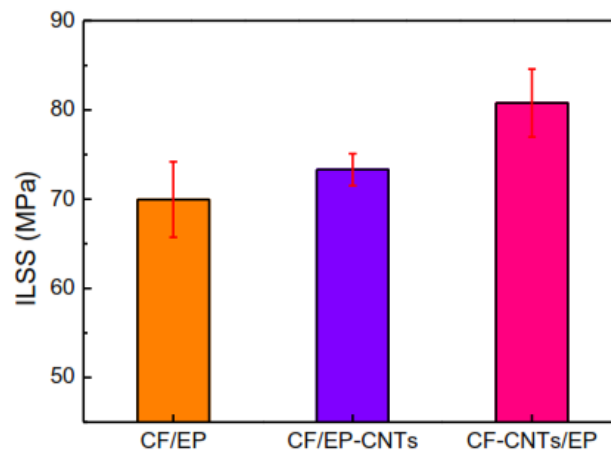


Figure 4.12: Interlaminar shear strengths of CF/EP, CF/EP-CNTs, and CF-CNTs/EP [188]

Ravindranath et al. [189] considered multi-walled carbon nanotube (MWNT) sheets wrapped around carbon fiber at room temperature to improve fiber-matrix interfacial properties which, in turn, influences compressive strength of the composite. The MWNT sheet was wrapped around a single carbon fiber or fiber tow with a scrolling (bias) angle α as schematically depicted in Figure 4.13 (a). The MWNT sheet overwrapped carbon fiber was subsequently embedded in a polymer matrix, which infiltrates the nanopores of the multilayer MWNT sheet to form mechanically interlocked MWNT/ polymer nanocomposite surrounding the fiber as observed using Atomic Force Microscopy (AFM) as shown in Figure 4.13 (c). The relatively high-volume fraction of the MWNT in the matrix provides the

reinforcement to the interface region of polymer and fiber due to mechanical interlocking. This approach directly influences the compressive strength of the composite without degrading fiber properties.

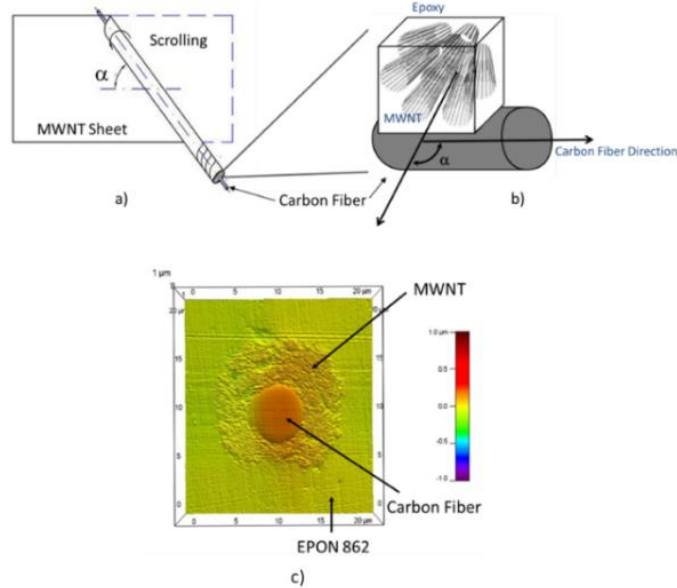


Figure 4.13: a) Macroscale view of MWNT sheet scrolled on carbon fiber, b) Schematic of nanoscale RVE of the interface region between epoxy-MWNT-carbon fiber, c) AFM Image of Epon 862, carbon fiber, MWNT interface [189]

A full schematic of the three-tier nano-micro-macro multiscale modeling approach is shown in Figure 4.14, depicting hierarchical coupling of nano, micro, and macro scale modeling.

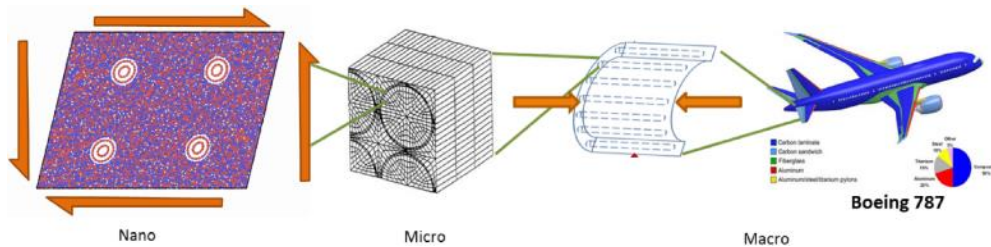


Figure 4.14: A schematic diagram showing a nano-micro-macro multiscale modeling approach to calculate the improvement in the Compressive Strength in MWNT scrolled Fiber/ Epoxy Composite (Boeing 787 Dreamliner) [189]

A method for the growth of carbon nanotubes on carbon fiber using a low temperature growth technique was reported by Pozegic et al. [190] which is infused using a standard industrial process, to create a fuzzy fiber composite with enhanced electrical characteristics. Conductivity tests revealed improvements of 510% in the out-of-plane and 330% in the in-plane direction for the nanocomposite compared to the reference composite. The electrical conductivity of CFRP and FCFRP ('fuzzy' carbon fiber reinforced polymer) in different directions is delineated in Figure 4.15.

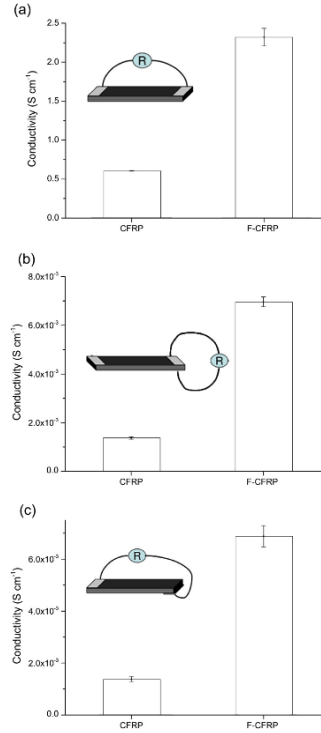


Figure 4.15: Electrical conductivity for CFRP and FCFRP in (a) in-plane, (b) the out-of- plane direction (thickness) and (c) the out-of-plane (volume) direction [190]

Joo et al. [191] performed damage sensing and self-healing of carbon fiber polypropylene (CFPP)/carbon nanotube (CNT) nanocomposite based on addressable conducting network (ACN). To increase damage sensing resolution of CFPP/CNT nanocomposite, through-thickness electrical conductivity was improved by adjusting press condition and spraying carbon nanotubes (CNT) between prepregs. From the results, electrical resistivity in thickness direction was reduced to 19.44 $\Omega \cdot \text{mm}$ under 1.0 MPa and 1.0 wt% of CNT condition. To further increase the electrical conductivity in thickness direction, CNT was additionally spread between prepregs. Figure 4.16 exhibits the electrical resistivity in thickness direction as a function of CNT amount. Notable change of electrical conductivity was observed about with increasing amount of CNT, it was greatly improved from 79.17 $\Omega \cdot \text{mm}$ (0 wt% case) to 19.44 $\Omega \cdot \text{mm}$ (1.5 wt% case). It is due to the addition of conductive path between carbon fibers by dispersing CNT between prepregs.

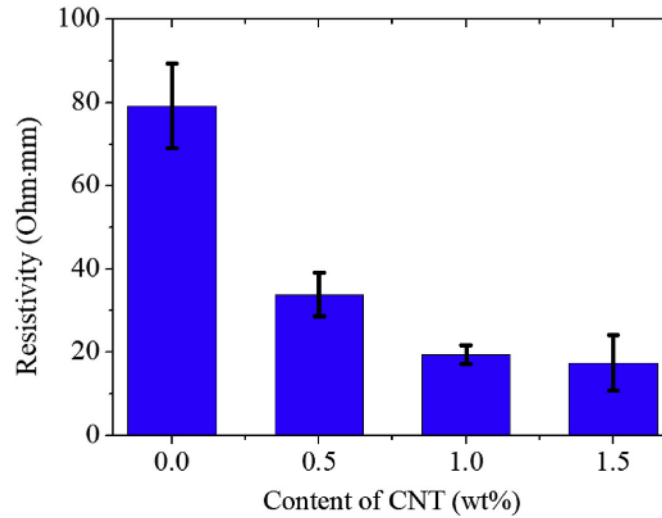


Figure 4.16: Resistivity measurement result with respect to wt% of CNT [191]

Based on resistive heating data, self-healing test was performed, and the data were compared with no healing case. The self-healing efficiency was calculated based on the maximum load measured by three-point bending test data. The results demonstrated that unhealed case showed low maximum load after fourth bending, only 27.53%. Meanwhile, 1.3 A (181 °C) heating case had relatively high self-healing efficiency (96.83%), in which damaged matrix was melted and healed under resistive heating process and delamination in composite was entirely eliminated. It is worthwhile to indicate that spreading CNT between prepregs not only enhance thermal conductivity at inter-ply area, but also improved overall thermal conductivity of composite. Therefore, matrix cracks were efficiently healed about CNT added case by spreading heat more smoothly [191].

Sebastian et al. [19] proposed a novel, multi-modal, nanomaterial-based sensor technology that can provide wide area detection of damage. The study could be used as a feasibility study into the incorporation of carbon nanomaterials into structural composites as sensors. The carbon nanotubes covered fiber (fuzzy fiber) sensors demonstrate similar sensitivity to conventional strain gages and are more easily integrated into composite structures as the sensor itself is a composite. The fuzzy fiber strain gages can be utilized to sense strain within composite structures and can be readily integrated into the structural laminate to provide sensing over large sections and in previously inaccessible locations. The unique properties of the fuzzy fiber lends itself to application in a wide range of sensing tasks within a structural composite including strain, temperature, degradation, etc. Figure 4.17 shows a typical cured panel with embedded sensor elements prior to cutting into individual specimen. Fine gauge insulated copper wire leads were bonded to the sensing element with conductive (silver filled) epoxy and extended beyond the isolation layer and out of the specimen where they could be attached to instrumentation.

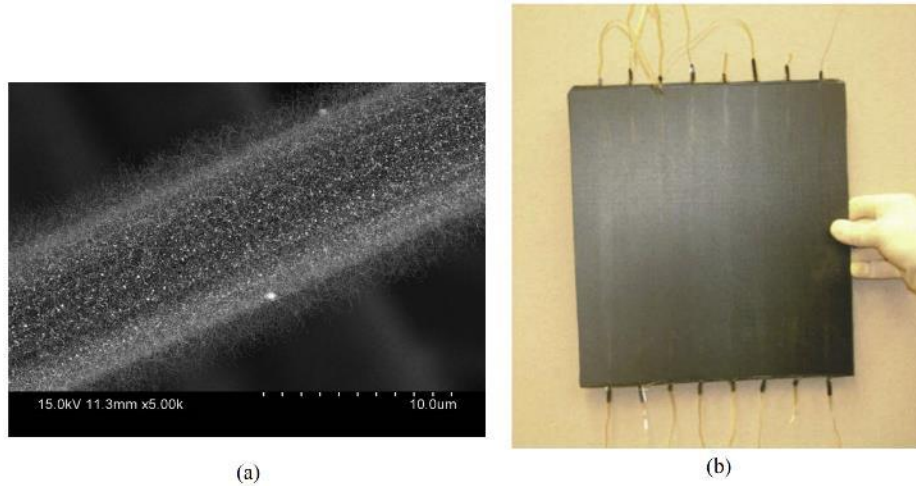


Figure 4.17: (a) SEM micrograph of CNT growth on glass fiber (sensor), (b) Composite panel with embedded strain sensors [19]

An interlaminar reinforcement using aligned carbon nanotubes was introduced by Garcia et al. [192] for prepreg unidirectional carbon tape composites. Aligned CNTs were grown at high temperature and then transfer printed to prepreg at room temperature, maintaining CNT alignment in the through-thickness direction. In initial testing, the CNT-modified interface was observed to increase fracture toughness 1.5–2.5X in Mode I, and 3X in Mode II. Both compliant interlayer and bridging are considered as mechanisms of toughening, with evidence of CNT bridging observed in fracture micrographs. Figure 4.18 describes the position of vertically aligned CNT (VACNT) between plies of a laminated composite and process of transfer-printing of VACNT.

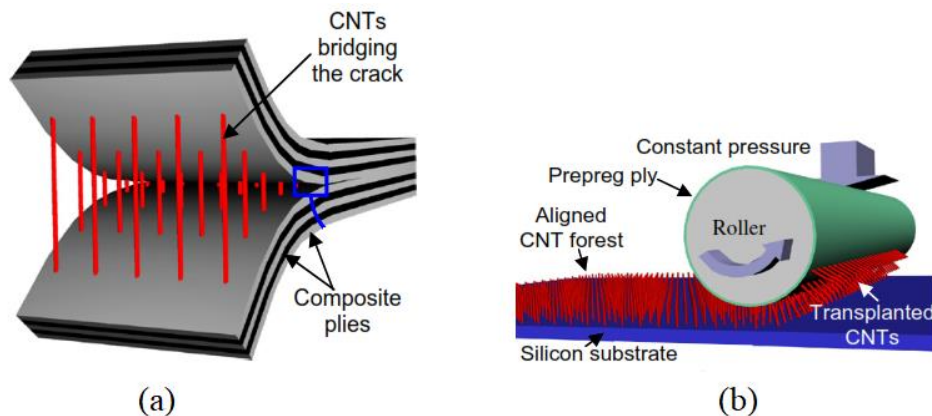


Figure 4.18: (a) VACNTs placed in between two plies of a laminated composite (b) Illustration of the 'transfer-printing' process [192]

The development of a hierarchically engineered micro-nano hybrid composite system was described by Zhang et al. [175] employing a spray coating technique as an effective way to deposit carbon nanotubes onto carbon fiber prepregs. The effectiveness of the technique was demonstrated by the extremely low CNT loading (0.047 wt.%) needed to significantly increase the Mode-I fracture toughness of the

carbon fiber laminates by about 50%, which was almost the largest reported improvement for such extremely low concentrations of non-functionalized CNTs. The spray coating process and electrical damage sensing test are depicted in Figure 4.19.

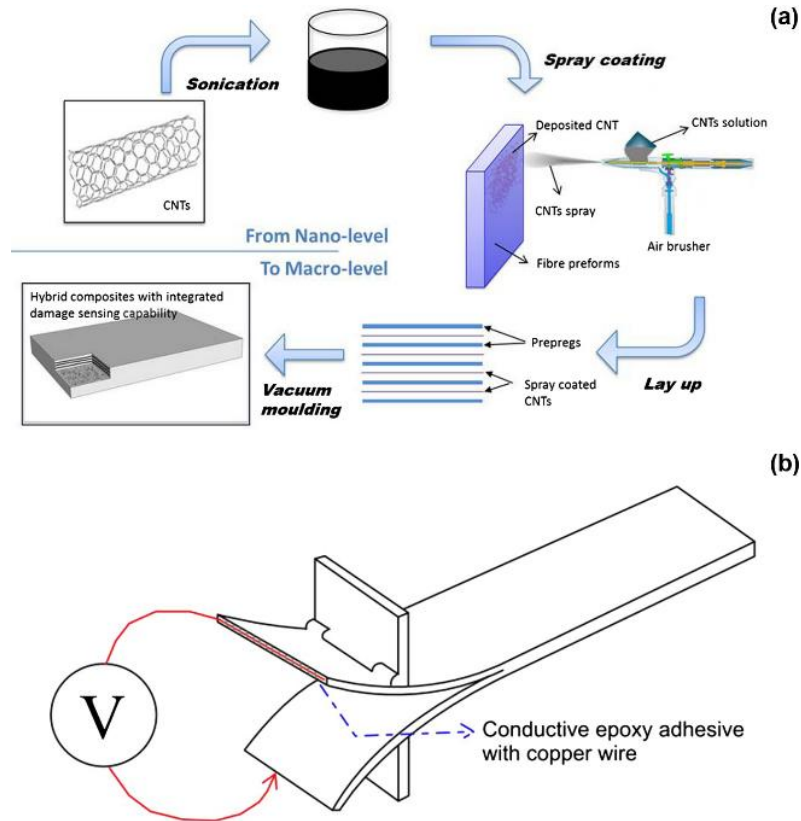


Figure 4.19: (a) spray coating process and (b) electrical in-situ damage sensing test set-up for DCB specimen [175]

The comparison of Mode-I interlaminar fracture toughness versus different CNT weight fraction is displayed in Figure 4.20.

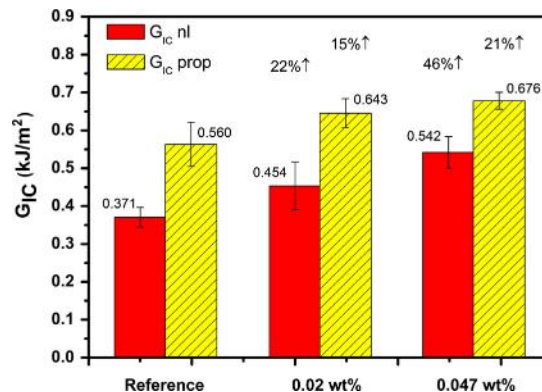


Figure 4.20: Comparison of Mode-I interlaminar fracture toughness for reference, 0.02 wt.% and 0.047 wt.% CNT concentration [175]

The graphene nanoplates (GnPs) and carbon nanotubes (CNTs) are simultaneously deposited on carbon fiber (CF) surface by fiber sizing method by Qin et al. [193].

The interlaminar shear strength of GnPs/CNTs hybrid coated CFRP composites was 90% higher than non-coated CF composites. The flexural and tensile strength of CFRP composites with GnPs/CNTs hybrid coating have an improvement of 52% and 70%, respectively, compared to non-coated CF.

4.4 Conclusion and future trends

The successful hybridization of the CF and CNT can be described as one of the great achievements in the evolution of nanoscience and nanotechnology [194]. Carbonaceous nanofillers can be conveniently deposited on the surface of CF and related fabrics by different techniques. The stability of multi-scale structures is based on physical, physico-chemical, and chemical interactions. For nanostructuring an interlaminar layer, various selective placement techniques may also be adopted [170].

Most of the scientific papers cited in this chapter highlight that multi-scale structuring of the interphase and interlaminar regions is an efficient approach to improve the out-of-plane properties of composites. Even though, at present, the main attention has been focused on the improvement of mechanical properties, also enhancement of electrical and thermal conductivities can be exploited. As such, the great architectural structure of the hybrid CF-CNT had rendered it as a huge potential to be used in the future structural and functional applications of polymer composites [194]. In the last two decades, there had been numerous investigations carried out by the research community to demonstrate and exploit this hybrid CF-CNT to be used in polymer composites. Although research has been dedicated to the development of hybrid CF-CNT reinforced polymer composites for various purposes, it is still in its infant stage of being realized on the real product. As such, the selection of the best fabrication method for producing the hybrid CF-CNT is found to be crucial prior to the implementation and introduction of the real invention. In this chapter various hybridization processes are included such as chemical vapour deposition, electrophoretic deposition, electrospray deposition, etc. Each of the mentioned fabrication methods were not only found to have its own advantages and limitations, but also were influenced by certain processing conditions that had affected the final properties of the hybrid CF-CNT. By keeping in mind on the superior properties revealed by this hybrid CF-CNT, this chapter has aimed to demonstrate the encouraging facts and findings obtained from the research community on the mechanical properties and various applications of hybrid CF-CNT reinforced composites.

Additional and not yet explored possibilities can be predicted for all- carbon multi-scale and hierarchical fibers, such as direct conversion of CF into a core-sheath type multi-scale fiber under suitable conditions [170]. Multiscale FE models seem to be the most suitable to clarify open issues related to the effects of hierarchical structuring of the interphase and interlaminar regions. Interestingly, the experimental

and modeling works on the damping performance of these novel composites are far behind the expectations, though multi-scale CFs are very promising intrinsic damping elements. Selective placement of free-standing nanostructured assemblies (interleaf concept) into the interlaminar region will be further explored. In this regard, the research will likely focus on dissolvable polymer carriers (as bulk or foam materials [170] [195]) of the nanoparticles which may work after curing for toughening, shape memory behavior [196], self-healing (for example by using nanoreinforced self-healable interleaving films [197]). Furthermore, sensing for structural health monitoring whereby exploiting the beneficial properties offered by all-carbon multi-scale fibers including CNTs will remain under spot of research interest. Finally, an interesting and prominent area in CNT-CF multi-scale hybrid composites has been recently introduced as vertically-aligned CNT (VACNT) forest at the interface between the plies of common prepreg material using a simple transfer-printing scheme by [192] [198]. This method can pronouncedly improve the interlaminar fracture toughness with respect to the baseline composite, by which, preliminary Mode I and II tests indicate enhanced toughness, mechanistically explained by either interleaving or bridging toughening. Clearly, more refined specimen manufacturing and additional characterization are needed to appropriately quantify toughening and the mechanisms at work [192]. Of great interest is fabricating shorter aligned CNT forests to reduce the interlayer thickness and thereby focus on bridging.

Characterization and modeling of the enhanced properties afforded by this architecture could be extended and broadened to properties such as thermal [199] and electrical conductivities. Significant modeling [200] and experimentation still remains to determine optimal characteristics of the VACNTs including length and volume fraction, effects of chemical functionalization, and dependence on polymer chemistry and fiber surface characteristics. The interlaminar reinforcement represented by the foregoing method likely has application in several sections consisting of bonded joints and repair of composites, as well as bonding of embedded or surface-mounted devices.

Chapter 5: Investigation of Interfacial Shear & Radial stresses of Carbon Nanotube Coated–Carbon Fiber Hybrid Composites

Abstract: This chapter provides novel approaches regarding multi-scale hybrid composites and is based on the author's paper during PhD program [178]. The mechanical properties of unidirectional carbon nanotube (CNT)–carbon fiber (CF) reinforced hybrid composites are scrutinized. Due to lack of comprehensive model, a 3D multi-scale model considering debonding damage is developed, covering from nano- to macro-scale. Considering three different configurations of grown CNTs on the fiber surface, the interfacial behavior is investigated. The results reveal that : (I) an extraordinary influence of CNTs on the fiber-matrix interfacial properties, particularly in the composites containing axially and randomly oriented CNTs, (II) considering two hybrid systems, composites with CNT coated–fibers demonstrate notable improvements in the interfacial behaviors than those with CNTs in matrix, (III) the pronounced effect of non-bonded interphase region on the interfacial properties, while no influence on the Young's moduli is observed, and (IV) the presence of CNTs augments the transverse Young's modulus, however, it exhibits negligible effect on the longitudinal direction. The outcomes are consistent with experimental data and can be utilized in designing of CNT–CF multi-scale composites.

5.1 Introduction

As a fundamental issue, fiber-matrix interfacial properties significantly influence on the mechanical behavior and load transferring phenomenon of composite structures [178]. Multifarious experimental, computational, and analytical investigations have been carried out to characterize and ameliorate the interfacial and interlaminar properties of composite structures. Thus, improvement of fiber-matrix interfacial properties plays a momentous role which augments the overall mechanical behaviors, however, with poor interfacial strength, debonding occurs, resulting in a weaker composite structure. On the other hand, breakthrough of carbon nanotubes (CNTs) and nanoparticles have flourished a novel research sphere among scientists because of their unique properties. Recalling from previous chapters, it has been demonstrated that dispersion of a few portion of carbon nanotubes in a matrix, increase remarkably the mechanical properties of composite materials. Having

implemented various experimental tests, noticeable growth in the mechanical properties of polymers have been reported in the literatures by incorporating 1–5% weight fractions of CNTs. Owing to the exceptional characteristics of carbon nanotubes, by incorporating CNTs, multi-scale hybrid composites are being developed due to their outstanding behaviors in obviating cardinal drawbacks of conventional composites regarding interfacial and interlaminar properties, by altering the fiber-matrix interface region. Depending on the dispersion of CNTs in the hybrid composites, it can be categorized into two types of systems encompassing ‘mixed CNT/matrix system’ and ‘hybrid fiber system’, while in the former the CNTs are mixed with resin, whereas in latter the forest of carbon nanotubes are grown on the surface of core fibers, so-called fuzzy-fiber reinforced composites (FFRC) [201]. Introducing small portion of carbon nanotubes on the surface of carbon fiber, significant enhancement of interfacial shear strength (IFSS) and interlaminar shear strength (ILSS) were attained by 89.4% and 58.6%, respectively, by Yao et. Al [186]. In addition to the significant influence of FFs on the interfacial properties between fiber and matrix, a basic drawback of unidirectional fiber reinforced composites ascribed to the low mechanical properties in the transverse direction to the fiber can be overcome by presence fuzzy fibers. From experimental investigation point of view, some studies have been accomplished in order to study the mechanical, thermal and electrical properties and health monitoring applications of fuzzy fiber reinforced hybrid composites [19] [20]. Growing the graphene oxide and carbon nanotubes on the carbon fiber surface, the interfacial properties have experimentally been investigated in the recent literatures. The outcomes divulged that all the foregoing nano-reinforcements, noticeably improve the interfacial and interlaminar properties of composites with only small portion of nanomaterials. Conducting a survey on the influence of the growth temperature and time of CNT on the fiber- matrix interfacial shear strength (IFSS), by Aziz et al. [202], the temperature of 700° with 30 minutes reaction time has exhibited the noticeable IFSS. Garcia and his co-worker [192] conducted a survey on the morphology control of aligned CNTs on the fibers and improving the interlaminar strength of prepreg unidirectional carbon tape composites by exploiting the bridging effect of aligned CNT’s. From multi-scale modeling point of view, some analytical investigations have been implemented considering some assumptions, however, due to novelty and complexity of such nano-engineered multi-scale materials, there still exist many aspects which should be clarified and characterized unambiguously. A general micromechanics method was developed by Chatzigeorgiou et al. [203], to attain the elastic moduli of hybrid composites consisting of carbon fiber coated with radially aligned CNTs. The results disclosed enhancement of elastic moduli by increasing the volume fraction of carbon fiber and CNT’s. Investigating the fatigue behavior of CF/ CNT hybrid composite, Dai and Mishnaevsky Jr. [204] carried out a finite element modeling in which superior fatigue performance was observed than those without CNTs reinforcements. Finite element analysis and experimental investigation were conducted by Kulkarni et. al [205] in order to acquire the elastic moduli of CNT/ CF hybrid composites. Considering

CNT/CF as a homogeneous solid model with larger diameter, it was determined that multiscale modeling can be effectively used to study nano-reinforced laminated composites. Kundalwal and collaborators [206] [207] studied the thermoelastic and mechanical properties of hybrid composites considering straight and waviness CNT's invoking micromechanics modeling. The results demonstrated remarkable enhancement in transverse young modulus and coefficients of thermal expansion of the CNT/ CF composite.

In accordance with the aforementioned studies, majority of them were dedicated to the elastic moduli of hybrid composites. Furthermore, a detailed 3D multi-phase model which is capable of capturing all length-scale parameters and considering CNT's orientations and debonding is lacking. Hence, to scrutinize the mechanical properties of CF–CNT hybrid composite, particularly interfacial properties, the present work proposes a 3D multiscale finite element (FE) model of carbon fiber-carbon nanotube reinforced hybrid composites, taking into account all the parameters covering from nano- to macro-scale and considering debonding damage between CNTs and surrounding matrix. Moreover, current research demonstrates the remarkable effect of grown CNTs on the interfacial shear and radial stresses considering three different orientations of CNTs, which is significant outcome from fiber-matrix interfacial adhesion point of view. Meanwhile, the influence of two different hybrid systems including ‘hybrid fiber system’ and ‘mixed CNT/matrix system’ on the interfacial properties are assessed. The nonlinear finite element analysis is also validated by user-defined FE code and published experimental data.

5.2 Framework of Multi-Scale Modeling

Recalling from the previous sections, different techniques for the deposition of CNTs on the surface of carbon fiber exist consisting of Chemical Vapor Deposition (CVD), electrophoresis, etc. which possess their advantageous and limitations. Although by systematically varying the catalyst concentration, catalyst pre-treatment time, and sample position within the tube furnace, the key factors governing CNT morphology could be likely achievable [208], CNTs are predominantly grown in radial and randomly orientations on the fiber surface. The presence of CNTs Forest on the surface of the fiber is depicted in Figure 5.1. To scrutinize the influence of CNT morphology on the mechanical properties of hybrid composite, therefore, CNT's with radially, axially, and randomly orientations are taking into account in the present work.

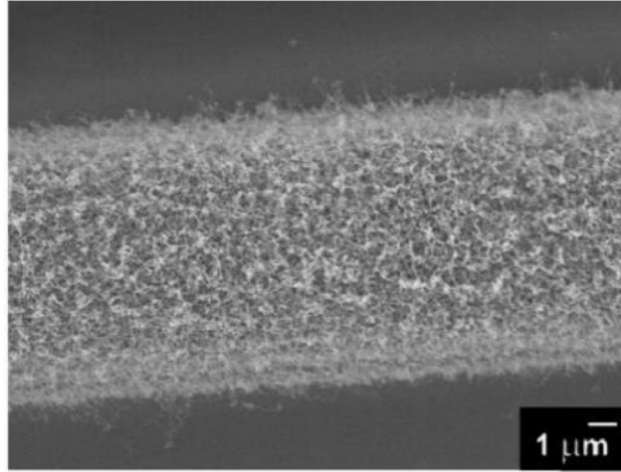


Figure 5.1: Randomly oriented CNTs on the surface of the carbon fiber [201]

Hence, irrefutably, the multiscale architecture of the fuzzy fiber reinforced composites (FFRC) can be quite complex. Therefore, a concurrent 3D multiscale finite element model has been proposed in the present work considering all length scale from nano to macro, in which the fine scale is directly embedded in the coarse scale simultaneously, excluding homogenized or effective/ equivalent material which the latter is usually employed by hierarchical approach. The proposed model is capable of capturing of the characteristics at each scale and taking into account the crucial features of the model comprising the CNT volume fraction, CNTs orientations, debonding between CNTs and matrix and fiber volume fraction in the hybrid composite. It is noteworthy to mention that the debonding damage between CNTs and surrounding matrix is simulated via cohesive zone model (CZM) considering mixed mode traction-separation law, while no fracture phenomenon or crack opening has been considered. Otherwise, in case of considering fracture in multi-scale modeling, the transfer of length scales and issues related to size effects will play a critical role.

Hence, to furnish an efficacious insight towards the design of FFRC with measurable and adjustable parameters, these features are profoundly investigated. The multiscale framework of CNT- coated carbon fiber hybrid composite is delineated in Figure 5.2. It is noteworthy to mention that a user-defined linear finite element formulation is also constructed to certify the elastic modulus obtained via concurrent multi-scale modeling.

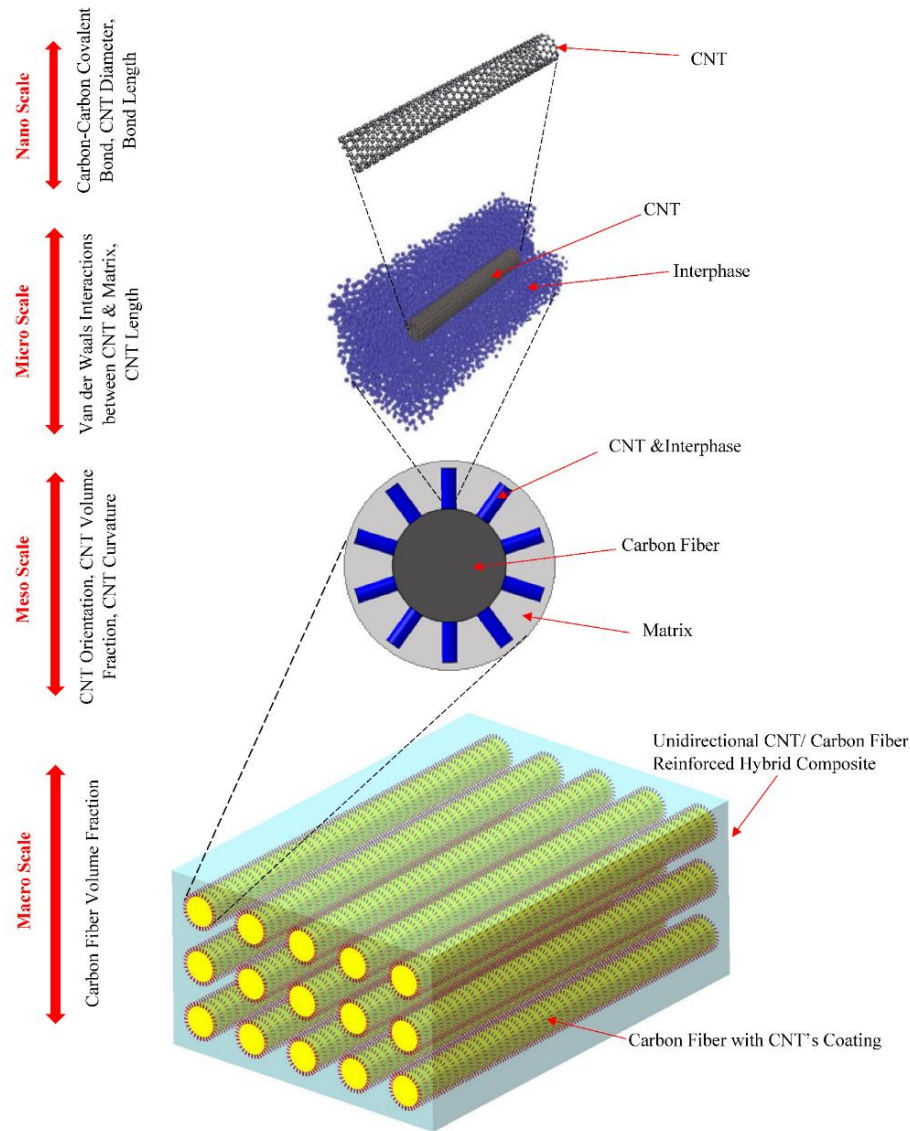


Figure 5.2: The multi-scale modeling framework of multi-scale hybrid composite and effective parameters at each scale [178]

5.3 Nano-Scale Modeling

At nanoscale, CNT's act as nano-reinforcement agent in the hybrid composite. The theoretical efforts in modeling CNT behavior can be classified in three categories as atomistic modeling, continuum modeling and nano-scale continuum modeling. Various approaches in the modeling of carbon nanotube were rigorously reviewed and analyzed by Rafiee and Malekimoghadam [77] concentrating on mechanical, buckling, vibrational and thermal properties. Developing a finite element model of the CNT lattice structure by Li and Chou [91], each Carbon–Carbon bond of the CNT nanostructure is replaced with equivalent beam element in which the geometrical and mechanical properties of the beam element are obtained correlating the interatomic potential energies of molecular space to the strain energies of structural mechanics. Different researchers applied continuum shell

models to study the CNT properties [78] [209] which the outcomes imply the similarities between MD simulation of CNTs and macroscopic shell model. Bagchi and Nomura [210] developed a model predicting the effective thermal conductivity of multi-walled nanotube polymer composite considering an equivalent shell model as CNT structure. Choi et al. [211] considered a transversely isotropic hollow cylinder solid model for finite element modeling of vibration behavior of multi-walled carbon nanotube.

Consequently, in the current research the multi-walled carbon nanotube is simulated as a straight transversely isotropic shell structure in which the thickness of each layer is considered as 0.34nm [67]. The required mechanical properties of carbon nanotube for finite element modeling are summarized in the Table.1 [94] [212] [213] [214]. Figure 5.3 exhibits the modeling procedure of CNT from atomistic scheme to equivalent continuum model.

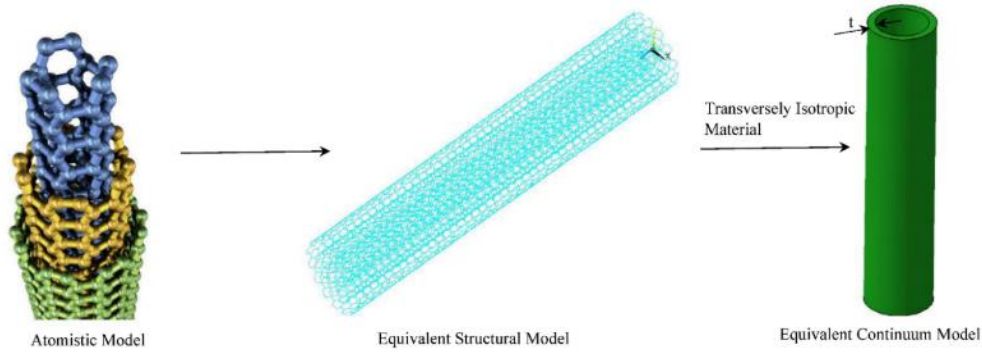


Figure 5.3: Equivalence molecular, finite element and continuum models [178]

Material	E_z [TPa]	E_x, E_y [GPa]	G_{xz}, G_{yz} [GPa]	G_{xy} [GPa]	ν_{xz}, ν_{yz}	ν_{xy}
CNT	1.3	40	440	13	0.19	0.469

Table 5.1: Mechanical properties of Carbon Nanotube [94] [212] [213] [214]

5.4 Interface region between Carbon Nanotube and Matrix (Cohesive zone formulation)

From atomistic point of view, the governing interactions between CNT and surrounding polymer are weakly non-bonded vdW interactions in absence of chemical functionalization, in which no covalent bonding is produced [215]. From structural point of view, two different approaches can be found in literatures for simulating interphase either as a continuum or as a discrete region exerting continuum hollow cylinder and truss/ nonlinear beam elements, respectively [121]. The vdW interactions are mostly modeled using Lennard–Jones (L–J) “6–12”

potential [116]. Utilizing nonlinear springs representing interphase region based on L-J potential, a multi-scale model of carbon nanotube reinforced composite was proposed by Rafiee and Malekimoghadam [97]. Due to inherently nonlinear behavior of vdW interactions, it could be simulated either by non-linear springs or cohesive zone model which the latter method has been adopted for this research. Based on the Lennard–Jones “6–12”, the vdW force in term of interatomic distance is presented by following equation [116].

$$V_{LJ}(r) = 4\varepsilon \left[\left(\frac{\sigma^{12}}{r} \right) - \left(\frac{\sigma^6}{r} \right) \right] \quad (5.1)$$

where ε and σ are the Lennard–Jones parameters as 0.4492 kJ/mol and 0.3825 nm, respectively. It should be noted the vdW interaction can be neglected when the inter-atomic distance is equal or greater than 0.85 nm [97]. Based on the L–J potential for the van der Waals interaction, the following cohesive law for CNT/polymer interfaces has been established as Eq (5.1) [216].

$$\sigma^{\text{int}} = 3.07 \sigma_{\text{max}} \left[\left(1 + 0.682 \frac{\sigma_{\text{max}}}{\varphi_{\text{total}}} [u] \right)^{-4} - \left(1 + 0.682 \frac{\sigma_{\text{max}}}{\varphi_{\text{total}}} [u] \right)^{-10} \right] \quad (5.2)$$

where σ^{int} and $[u]$ are the normal cohesive stress and opening displacement at the CNT/polymer interface, respectively. Furthermore, the cohesive strength (σ_{max}) and total cohesive energy (φ_{total}) are denoted by the below equations based on the parameters σ and ε in the L–J potential.

$$\sigma_{\text{max}} = \frac{6\pi}{5} \rho_p \rho_c \varepsilon \sigma^2 \quad (5.3)$$

$$\varphi_{\text{total}} = \frac{4\pi}{9} \sqrt{\frac{5}{2}} \rho_p \rho_c \varepsilon \sigma^3 \quad (5.4)$$

Where ρ_c and ρ_p are the CNT area density and the polymer volume density which equal $3.82 \times 10^{19} \text{ m}^{-2}$ and $3.1 \times 10^{28} \text{ m}^{-3}$, respectively [217]. It is worth mentioning that Eq (5.3) represents a rather high cohesive strength, however, Eq (5.4) exhibits a very low cohesive energy $\varphi_{\text{total}} = 0.107 \text{ Jm}^{-2}$, which is in correlation with the poor bonding between CNTs and encircling polymer. The normal cohesive stress versus the interface opening displacement is depicted in Figure 5.4 [217] in which the cohesive ascends rapidly at the maximum of 479 MPa at small opening displacement of 0.0542 nm.

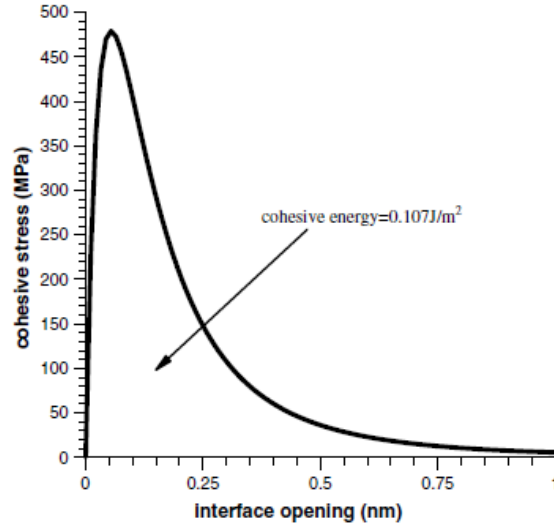


Figure 5.4: The cohesive law for a carbon nanotube and polymer matrix established from the van der Waals interactions at the CNT/matrix interface [217]

Some literatures have calculated the interfacial shear strength of the CNTs pull out from the matrix using MD simulation and experimental investigations. Different interfacial constitutive relations for various shapes of traction-separation curves, such as exponential, bilinear, and polynomial have been proposed by the researchers [218]. In the current research, the bilinear cohesive zone material (CZM) is introduced as non-bonded Van der Waals interactions at the interphase region between CNT and surrounding matrix, employing the zero thickness INTER204 3D element. This element is defined by 16 nodes having three degrees of freedom at each node in the x, y, z directions as shown in Figure 5.5 [118]. Likewise, it is capable of simulating an interface between two surfaces and the subsequent debonding damage process, where the separation is represented by an increasing displacement between initially coincident nodes, within the interface element itself. The CZM model consists of a constitutive relation between the traction “T” acting on the interface and the corresponding interfacial separation “ δ ” (displacement jump across the interface). Thus, the mixed mode bilinear cohesive law is exploited to simulate non-bonded interphase region between CNTs and matrix, in which the separation of material interfaces depends on both the normal and tangential components of displacement jumps which are displayed in Figure 5.5. Given that the difference in the normal and tangential jumps contributions to the separation of material interfaces, a non-dimensional effective displacement jump λ for mixed-mode fracture is defined.

The normal and tangential components of cohesive tractions and corresponding relations in mixed-mode type are expressed as:

$$T_n = K_n \delta_n (1 - D_m) \quad (5.5)$$

$$T_t = K_t \delta_t (1 - D_m) \quad (5.6)$$

$$\lambda = \sqrt{\left(\frac{\delta_n}{\delta_n^c}\right)^2 + \beta^2 \left(\frac{\delta_t}{\delta_n^c}\right)^2} \quad (5.7)$$

T_n , T_t , δ_n , δ_t , D_m describe normal traction, tangential traction, normal separation, tangential separation, and damage parameter, respectively.

The β is the non-dimensional parameters which assigns different weights to tangential and normal displacement jumps. The damage parameter associated with mixed-mode bilinear cohesive law is illustrated as:

$$D_m = \begin{cases} 0 & \lambda_{\max} = \lambda_\alpha \\ \text{Min}(1, d_m) & \lambda_{\max} > \lambda_\alpha \end{cases} \quad (5.8)$$

Where:

$$\lambda_{cr} = \frac{\delta_n^*}{\delta_n^c} = \beta \frac{\delta_t^*}{\delta_t^c} \quad (5.9)$$

$$d_m = \eta \left[\frac{\lambda_{\max} - \lambda_{cr}}{\lambda_{\max}} \right] \quad (5.10)$$

$$\eta = \frac{\delta_n^c}{\delta_n^c - \delta_n^*} = \frac{\delta_t^c}{\delta_t^c - \delta_t^*} \quad (5.11)$$

Where δ_n^c / δ_t^c and δ_n^* / δ_t^* , indicate normal/tangential displacement jump at the completion of debonding and normal/tangential displacement jump at maximum normal cohesive traction, respectively.

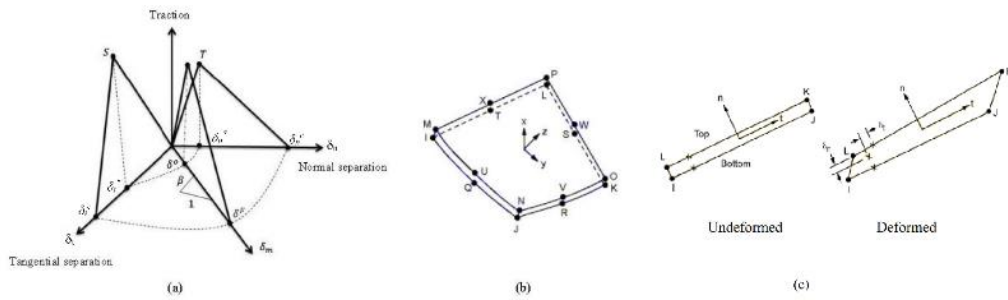


Figure 5.5: Cohesive zone material (a) Mixed-mode traction-separation behavior (b) INTER204 3D element geometry (c) Defining tangential and normal directions through the element [118]

Based on foregoing investigations, the maximum normal and shear interfacial strengths can be acquired for cohesive modeling [217]. There are six basic parameters to define the bilinear mixed-mode cohesive law in ANSYS which are depicted in Table 5.2 [178] [217] [219], provided by the Van der Waals interactions. Recalling the aforementioned parameters, the α and β can be attained accordingly:

$$\alpha = \frac{\delta_n^*}{\delta_n^c} = \beta \frac{\delta_t^*}{\delta_t^c} \quad (5.12)$$

$$\beta = \frac{\delta_n^* \times \delta_t^c}{\delta_n^c \times \delta_t^*} \quad (5.13)$$

T_{\max}^n [MPa]	δ_n^c [nm]	T_{\max}^t [MPa]	δ_t^c [nm]	α	β
479	1	75	1.2	0.0542	0.0766

Table 5.2: The input values of Cohesive Model for finite element modeling [178] [217] [219]

5.5 Numerical Modeling of CNT-coated Fiber Hybrid Composites

The dense of carbon nanotubes, practically, can be grown in different direction such as radially and randomly oriented [208], on the core fiber which will reflect different improvement in the properties of fuzzy fiber reinforced composites. Therefore, investigating the properties of FFRC with different CNTs orientation is a great of importance in such materials as well as accounting debonding damage between CNT and matrix. Hence three different cases of FFRC are considered in this research, in which the carbon nanotubes are radially aligned with respect to the fiber axis, axially aligned with respect to the fiber axis and randomly oriented, which are portrayed in Figure 5.6 [178].

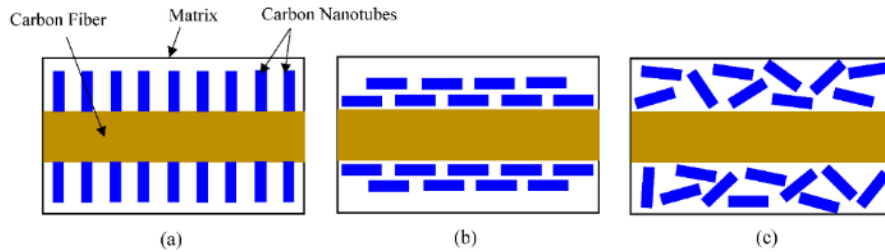


Figure 5.6: Schematic illustration of carbon nanotube configuration around core fiber (a) radially aligned CNTs (b) axially aligned CNTs (c) randomly distributed CNTs [178]

It should be mentioned that carbon fiber is simulated as transversely isotropic material and surrounding matrix is consider as a homogeneous isotropic material. The properties of carbon fiber (T300) are inserted in Table 5.3 [220] [221]. Considering the volume fraction of carbon fiber, the dimensions of surrounding matrix has been obtained and both core fiber and matrix have been simulated using solid element (SOLID 186) [118]. The element possesses three degrees of freedom per each node including translational in x, y and z directions which can tolerate irregular shapes without loss of accuracy due to usage of intermediate nodes on each edge of the element and therefor higher order shape function.

Material	E_z [GPa]	E_x, E_y [GPa]	G_{xz}, G_{yz} [GPa]	G_{xy} [GPa]	ν_{xz}	ν_{xy}
Carbon Fiber (T300)	230	28.7	25	7	0.3	0.42

Table 5.3: Elastic Properties of Carbon Fiber [220]

It worth mentioning that the CNTs orientation is controlled by defining local coordinate system in which the CNT longitudinal axis is parallel with the Z direction of local coordinate system whereas the longitudinal direction of carbon fiber is located in the Z direction of global coordinate system. Given that the CNTs are transversely isotropic materials with different orientations, therefore, the material properties of CNTs are defined on the local coordinate system. A schematic illustration of fuzzy fiber reinforced composite with corresponding global and local coordinate systems are delineated in Figure 5.7. Thus, hundreds of hollow cylinders should be constructed via the finite element model taking into account CNTs volume fraction and orientations. Recalling from previous section, carbon nanotubes are modeled as transversely isotropic material, consequently, a macro code has been written via ANSYS Parametric Design Language (APDL) in which a specific local nodal coordinate system and a specific local element coordinate system are defined for each CNT with respect to the CNT orientation. Having defined the local nodal and local element coordinate systems, the mechanical properties of each CNT are then introduced in the finite element model consecutively.

The dense of the CNTs which should be constructed in the finite element model leads to the massive computational analysis specially in the higher volume fraction. Hence, for ‘radially aligned’ and ‘axially aligned’ types of CNTs orientations, ‘Cyclic Symmetric Analysis’ technique has been adopted due to inherently axisymmetric circumstance of the foregoing CNT’s configurations.

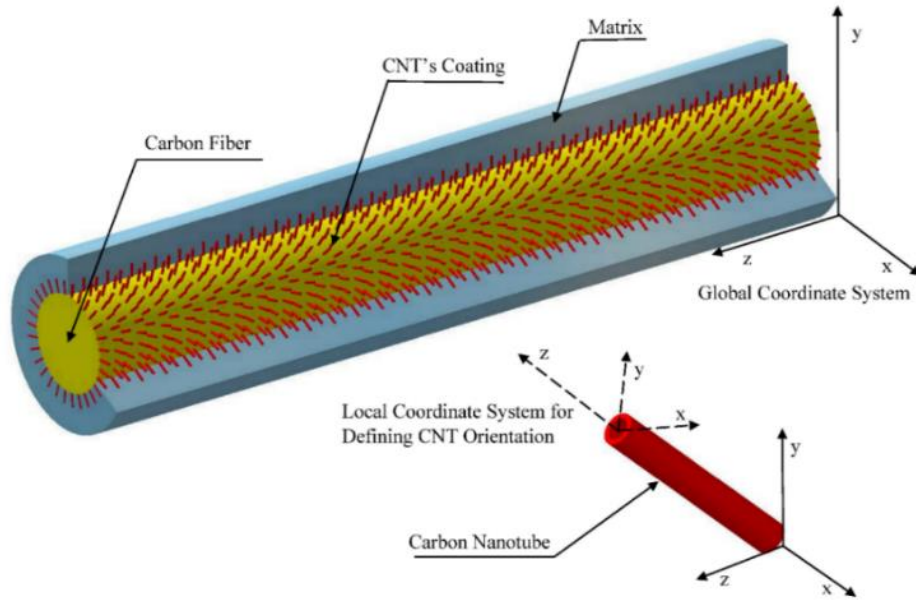


Figure 5.7: Schematic illustration of fuzzy fiber reinforced composite RVE with corresponding global and local coordinate systems [178]

Cyclic symmetry modeling is an analysis tool utilized to simulate structures having a repetitive geometric pattern in 360 degrees around an axis of symmetry. In order to execute the cyclic symmetry analysis, a single sector should be simulated, called the ‘basic sector’ which represents one part of a pattern. The angle α spanned by the basic sector should be such that $N\alpha = 360$, where N is an integer. It should be indicated the complete model will be produced by repeating N times of basic sector in cylindrical coordinate space. Since the hybrid composite with randomly oriented CNTs is not an axisymmetric model, therefore ‘Cyclic Symmetric Analysis’ is not capable of simulating of such RVE model. Ergo, for random normal distribution, a macro code has been developed in order to generate the positions and orientations of carbon nanotubes. It should be indicated that to model the random oriented CNTs reinforced hybrid composite, the condition of the minimum surface to surface distance between two adjacent CNTs which is the equilibrium van der Waals distance as 0.34 nm, should be met. Nonetheless, by altering the momentous parameters of growth process, various morphologies of CNT organization on the fiber surface will be observed comprising tangled growth, locally-group growth and Mohawk morphology [208]. The finite element models of CF–CNT hybrid composite with three configurations of CNTs around carbon fiber are shown in Figure 5.8.

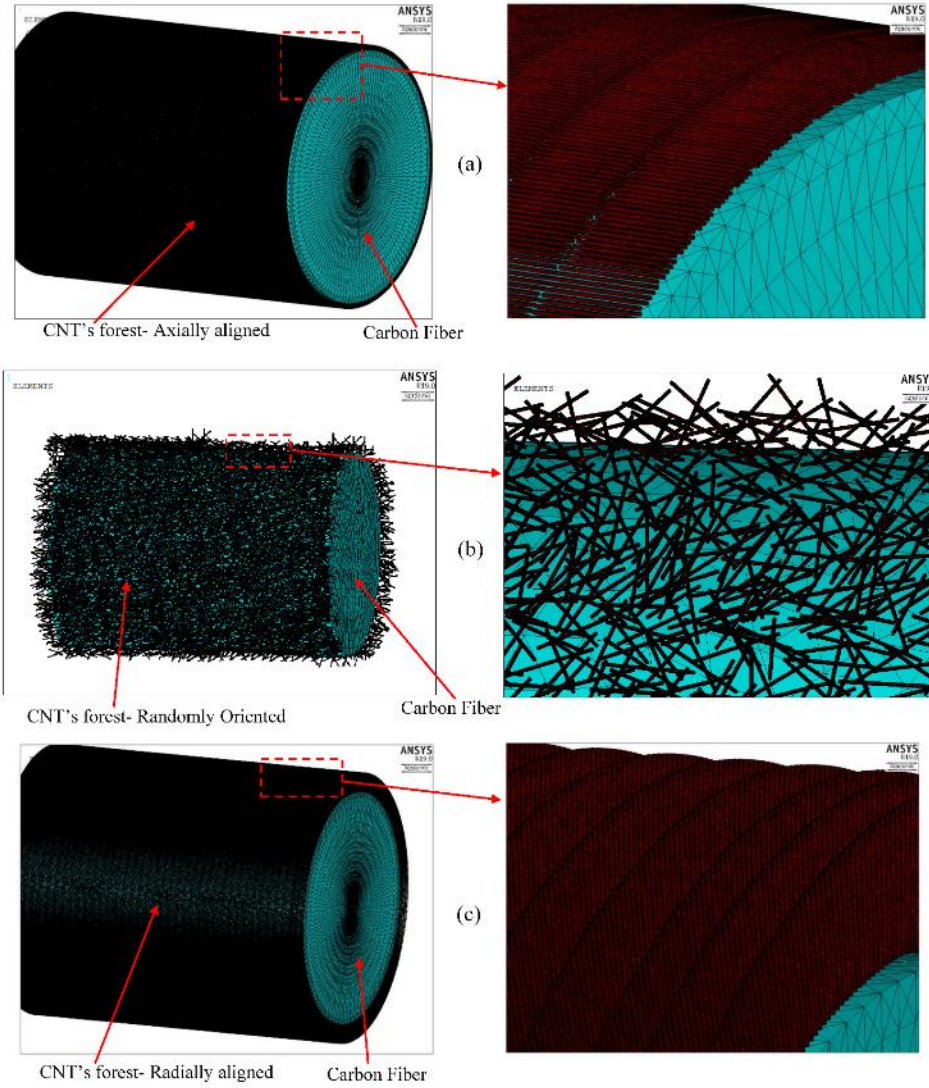


Figure 5.8: Finite element model of CF-CNT hybrid composite (a) with axially aligned CNTs, (b) with randomly oriented CNTs (c) with radially aligned CNTs [178]

User-Defined Finite Element Formulation/Analysis (UD-FEA):

RVE model construction: In order to obtain the elastic moduli of the hybrid composite and comparing with nonlinear concurrent multi-scale modeling, a user-defined finite element code is developed via MATLAB. Thus, a RVE is established through three concentric cylinders consisting of core fiber, micro-interphase region and surrounding matrix in which the micro-interphase contains matrix and randomly oriented CNT's. It should be mentioned that at this section, the carbon nanotube and interphase region are constructed as a nanofiber utilizing equivalent continuum modeling technique [97]. Consequently, Mori-Tanaka model [222] is employed in order to determine the effective elastic properties of micro-interphase region which is required as input to user-defined finite element formulation. It should be indicated that the details of Mori-Tanaka schemes for different types of inclusions and multi-phase systems have thoroughly been explicated in some literatures [223]. Exerting

the Mori-Tanaka method and taking into account the average over orientations of nanofibers, the effective stiffness tensor of micro-interphase region is defined accordingly [222]:

$$\mathbf{C} = \mathbf{C}_1 + \sum_{r=2}^N v_r \{(\mathbf{C}_r - \mathbf{C}_1) : \mathbf{T}_r\} : \left[\sum_{r=1}^N v_r \{\mathbf{T}_r\} \right]^{-1} \quad (5.14)$$

where \mathbf{C} is the stiffness tensor of the composite which here is considered as micro-interphase region, \mathbf{C}_1 and \mathbf{C}_r indicate the stiffness tensors of the matrix and the r th phase, respectively, and N denotes the number of the types of the reinforcements which in the present work is CNT. The volume fraction of the r th phase, is indicated by v_r . The Curly brackets $\{*\}$ represent an average over all possible orientations. The tensor \mathbf{T}_r is designated as:

$$\mathbf{T}_r = \left[\mathbf{I} + \mathbf{S}_r : \mathbf{C}_1^{-1} : (\mathbf{C}_r - \mathbf{C}_1) \right]^{-1} \quad (5.15)$$

where \mathbf{I} is the fourth-order symmetric unit tensor and \mathbf{S}_r is the Eshelby tensor. Accounting micro-interphase region as a two-phase composite including nanofibers and matrix, Eq (5.14) is then rewritten:

$$\mathbf{C} = \mathbf{C}_1 + v_2 \{(\mathbf{C}_2 - \mathbf{C}_1) : \mathbf{T}_r\} : \left[v_1 \mathbf{I} + v_2 \{\mathbf{T}_2\} \right]^{-1} \quad (5.16)$$

Where v_1 and v_2 indicate the volume fractions of matrix and CNT, respectively. The detailed expressions of \mathbf{S}_r for various shapes of inhomogeneities has entirely been illustrated by Mura [87]. Pursuant to the present work, the elements of Eshelby tensor [224] are represented in Appendix A, considering cylindrical inclusion. Considering the randomly orientated CNTs in the micro-interphase region, the acquired properties signify the isotropic behavior of this region. Thus, to establish the user-defined FE formulation, the carbon fiber is modeled as transversely isotropic materials while the matrix and micro-interphase region are simulated as two discrete homogeneous isotropic mediums.

Element formulation: Employing a mixed eight-nodes element with six degrees of freedom comprising three displacements and the three interlaminar stresses, the linear finite element analysis is conducted to obtain the elastic modulus of hybrid composites and making a comparison with nonlinear concurrent FEM which developed in the previous section. It is worthwhile to indicate that the statements of mixed formulation FE were comprehensively elaborated by Icardi and Atzori [225], therefore, hereafter the procedure will be summarized in this section. The Hellinger–

Reissner (HR) functional Π_{HR} [225] is introduced, by which the displacements and stresses are allowed to be varied separately that establishes the master fields.

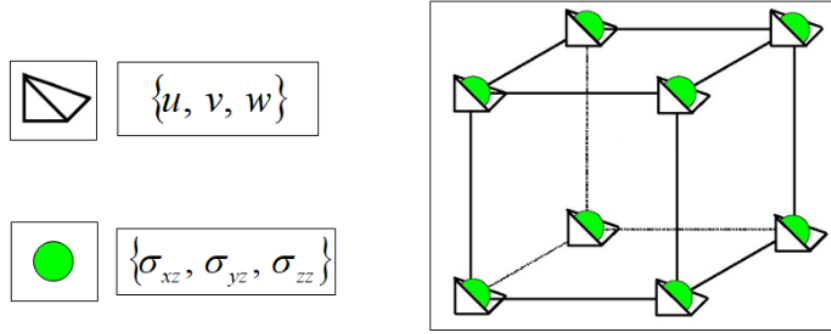


Figure 5.9: 8-nodes brick elements with relevant degrees of freedom [178]

The slave fields are the strains e^{σ}_{ij} and e^u_{ij} by the stress–strain and strain–displacement relations, respectively which are given as:

$$e^u_{ij} = \frac{1}{2}(u_{i,j} + u_{j,i}); \quad e^{\sigma}_{ij} = C_{ijkl} \sigma_{kl} \quad (5.17)$$

The functional Π_{HR} is expressed as:

$$\Pi_{HR}(u_i, \sigma_{ij}) = \int_V \left(\sigma_{ij} e^u_{ij} - \frac{1}{2} \sigma_{ij} C_{ijkl} \sigma_{kl} - b_i u_i \right) dV - \int_{S_i} \hat{t}_i u_i dS \quad (5.18)$$

where b_i and t_i represent the volume forces and the surface tractions, respectively.

From stability standpoint, the finite elements based on mixed formulations is governed by rather complex mathematical relations, as discussed by Babuska [226]. Notwithstanding relaxation of continuity requirements, certain choices of the individual shape functions could not lead to meaningful results in mixed formulations which is a consequence of the so-called Babuska–Brezzi [226] criterion for stability. In order to eschew occurring the mentioned outcome, the following condition should be satisfied, otherwise, non-convergent results with zero answer for $\{u\}$, or nonzero answer and locking will be produced.

$$n_u \geq n_{\sigma} \quad (5.19)$$

Where n_u and n_{σ} are the number of DOF in the vector $\{u\}$ of nodal displacements and the number of DOF in the vector $\{\sigma\}$ of nodal stresses, respectively. From solvability point of view, the adequate condition requires that the

number of zero eigenvalues of the element stiffness matrix is equal to the number of rigid body modes (which is six in the case of solid elements), as shown by Olson. Excluding stability considerations, present element has standard features [225], thus only the basic steps has been reported in this section. Three elastic displacement U_1 , U_2 , U_3 and three interlaminar stress components are defined as nodal degrees of freedom. Hence, following serendipity [225], linear polynomials are chosen as interpolation functions for every DOF.

$$\mu = \{N\} \{ \mu^e \} \quad (5.20)$$

Where μ and μ^e represent the displacements and stresses components inside the element and corresponding nodal values, respectively, while $\{N\} = \{N^1, N^2, N^3, N^4, N^5, N^6, N^7, N^8\}$ that is represented in Ref [225]. In order to uniform the computation of the integrals involved in the generation of the element stiffness matrix, commonly, a topological transformation from the physical volume $(x_1, x_2, x_3)^e$ to the natural volume $(\xi_1, \xi_2, \xi_3)^e$ is accomplished, at which the ξ_j is the local, non-dimensional nodal coordinates with origin at the center of the element. To this purpose, the physical coordinates x_i of any point inside the volume of the element are expressed in terms of nodal coordinates x_j^e and interpolation functions N .

$$x_i = \{N\} \{x_i^e\} \quad (i = 1, 3) \quad (5.21)$$

This transformation maps any element into a cube with corners at $(\xi_j = \pm 1)$. Then, the derivatives with respect to physical coordinates x_j appearing in the energy integrals are performed in terms of the transformed coordinates ξ_j .

Consequently, the stress vector is determined as:

$$\{\sigma\} = [S] \{q_e\} \quad (5.22)$$

Where $[S]$ is stiffness matrix and:

$$\{\sigma\}^T = \{\sigma_{11}, \sigma_{12}, \sigma_{22}, \sigma_{13}, \sigma_{23}, \sigma_{33}\} \quad (5.23)$$

5.6 Results and Discussion

Due to intrinsically nonlinear behavior of cohesive zone modeling, the nonlinear finite element analysis utilizing full Newton- Raphson iterative method is fulfilled in order to acquire longitudinal modulus (E_z), transverse modulus ($E_x = E_y$) and

interfacial shear and radial stresses of CNT–CF hybrid composite. The finite element result under axial loading is described in Figure 5.10 [178].

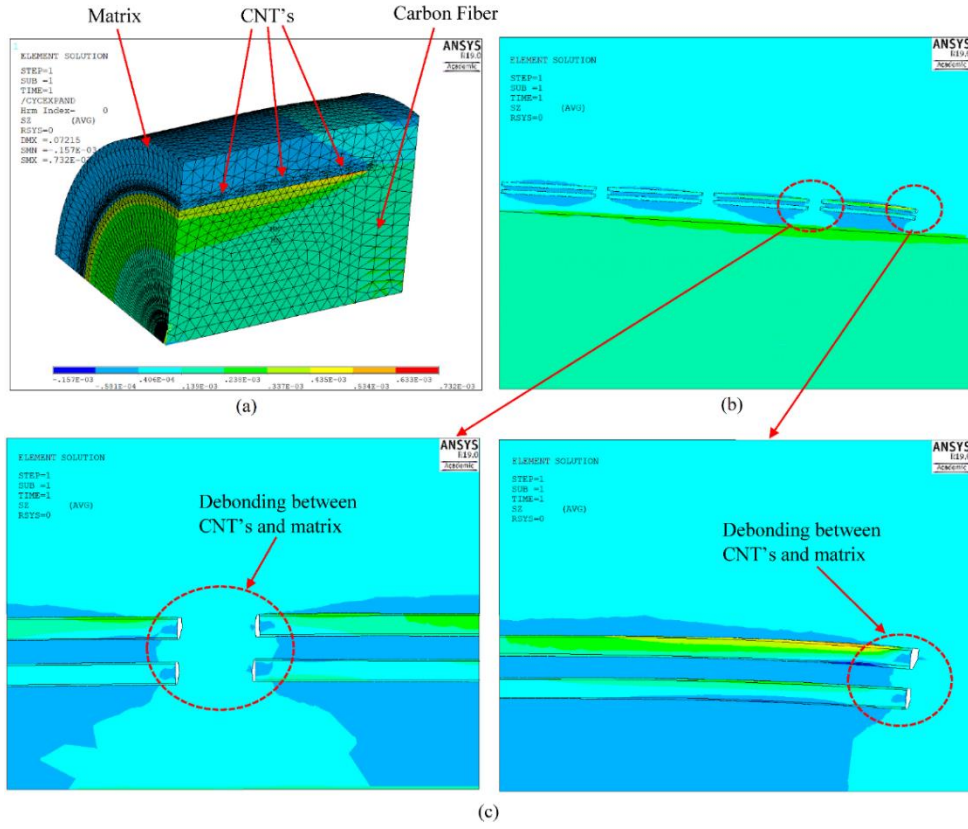


Figure 5.10: Stress contour of the hybrid composite (a) quarter of the RVE model (b) cut view at coating region (c) partial view, debonding damage between CNTs & matrix [178]

The uniform displacement is applied to the end of the model (up to $\varepsilon_{zz} = 3\%$) and the reaction forces are read from the constrained side of the model, which has been restrained from any movement except radial direction. The longitudinal modulus is expressed as below:

$$E_z = \frac{\sigma_{zz}}{\varepsilon_{zz}} = \frac{L}{\Delta L} \sigma_{ave} \quad ; \quad \sigma_{ave} = \frac{F_c}{A} \quad (5.24)$$

Where L , F_c and A are model length, reaction force at the restricted side and model cross section area, respectively. The mesh convergence study has been conducted in terms of maximum interfacial shear stress (at fiber-matrix interface) utilizing refined mesh which is depicted in the Figure 5.11, in which $D=1$ denotes 21000 elements.

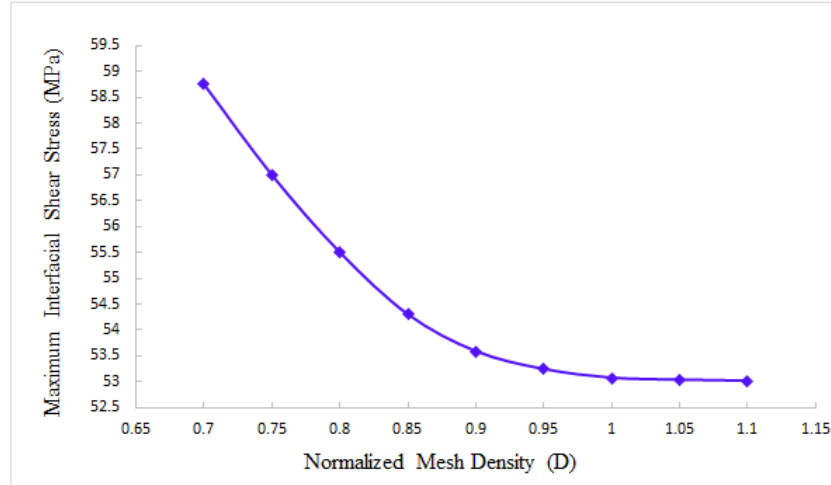


Figure 5.11: Normalized mesh density versus maximum interfacial shear stress [178]

The transverse and longitudinal moduli of hybrid composite model containing randomly oriented CNTs versus CNT volume fraction are described in Figure 5.12 [178]. From the graph supplied, it can be inferred that the carbon nanotubes enhance the transverse elastic modulus of CF–CNT hybrid composite pronouncedly which is about 10 % percent improvement with solely 1% volume fraction, however, the influence on the longitude elastic modulus is negligible. Therefore, employing the CNTs as reinforcement agent for augmenting the longitudinal elastic modulus in the hybrid composites is an unprofitable method. The results regarding the elastic modulus manifest excellent agreement with experimental investigations [227] and user-defined finite element formulation (UD-FEA). It should be notified that the effect of debonding between CNT and surrounding matrix on the transverse Young's modulus is about 0.5% at 1% volume fraction (which will rise by increasing the CNT volume fraction), whereas it doesn't show any alteration in the longitudinal young's modulus of the hybrid composite model. Moreover, the influence of debonding between CNT and surrounding matrix could be captured by comparing the outcomes of concurrent multi-scale modeling and UD-FEA.

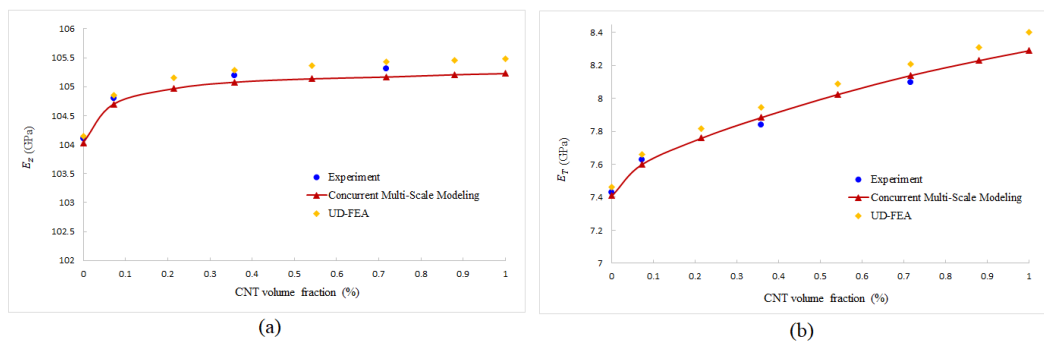


Figure 5.12: (a) The longitudinal and (b) transverse elastic moduli of CNT–CF reinforced hybrid composite versus CNT volume fraction [178]

Given that the CNT and matrix as ‘hollow micro-interphase’ region around carbon fiber, an outstanding contribution is made to the carbon fiber–matrix interfacial behavior in the hybrid composite. Therefore, interfacial properties as a fundamental issue in the fiber reinforced composites, is scrutinize in the current work. The distributions of interfacial shear and radial stresses along the carbon fiber length are illustrated in Figure 5.13 [178] at fiber-matrix interface. From the graphs provided, it can be inferred that growth of small portion of randomly oriented CNTs on the surface of core fiber (2 wt.%), will strikingly diminishes the interfacial shear and radial stresses by 19.2 % and 21.3%, respectively. As expected, the maximum value of interfacial shear stress occurs in contiguity of the fiber end. Furthermore, rather than the position of maximum stress, the amount of peak shear stress is of critical importance since the debonding between fiber and matrix will ensue if the maximum shear stress exceeds the interfacial shear strength. Employing analytical method, about 21% reduction of the maximum shear stress was gained by adding small amount of multi-walled carbon nanotubes [227]. Regarding the interfacial radial stress, it is almost zero over 60% of fiber length and rises sharply at the end that can be ascribed to the free-edge effect singularity. Accordingly, maximum magnitude of the radial stress at the ends of the fiber can result in a failure between fiber and matrix which has been mitigated considerably by solely 2 wt.% of CNT’s.

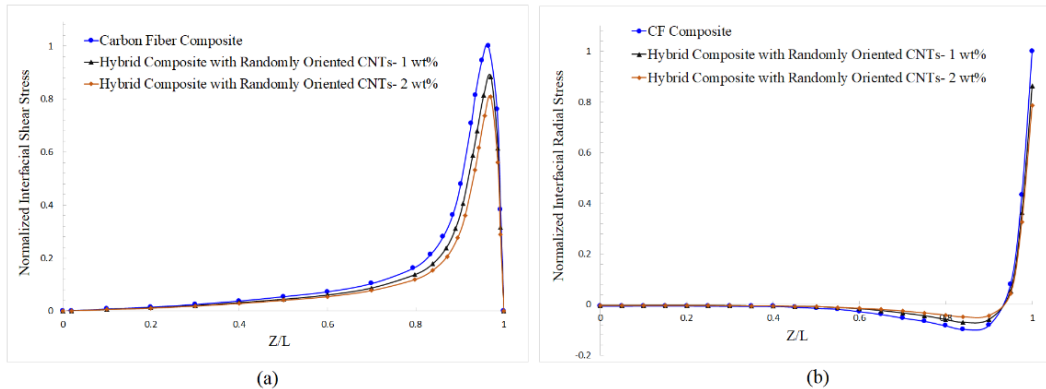


Figure 5.13: The normalized interfacial stress distribution, (a) Interfacial shear stress, (b) Interfacial radial stress [178]

It is noteworthy to mention that due to the surface area of core fiber and actual configuration and dispersion of CNTs at matrix, high volume fraction of CNTs doesn't reflect a feasible and practical issue which brings about agglomerated and tangled cluster of CNTs without significant effect on the mechanical properties of resulting multi-scale composite [208]. As it can be seen in Figure 5.13, increasing the CNT content in the interphase region, diminishes the maximum interfacial stresses, however, it doesn't alter the stress distribution and the positions of maximum stresses.

Considering various configurations of carbon nanotubes by 2 wt. %, the interfacial stresses of CF–CNT hybrid composite are delineated in the Figure 5.14.

The results reveal that the configuration of CNTs at micro-interphase region plays a prominent role in the load transferring mechanism and therefore leads to striking difference of interfacial properties. As it is displayed, axially aligned, and radially oriented CNT's exhibit the highest and lowest reinforcement impacts on the interfacial properties, respectively, while the hybrid composite with randomly oriented CNT's shows reinforcement magnitude between the two above-mentioned configurations. It is worth of notice that the models with radially oriented CNTs and axially aligned CNT's can be introduced as lower and upper bounds of reinforcement values, in which the latter makes a valuable contributes to reinforcing the interfacial properties under axial loading that can be used as a remarkable issue in designing advanced composite structure. Furthermore, as it can be seen in Figure 5.14 [178], the hybrid composite with randomly oriented CNTs represents much improved interfacial properties than those of with radially aligned CNT's. Similarly, and prominently, in accordance with the experimental investigations carried out by Sager et. Al [228], randomly oriented and radially aligned MWCNT coated fibers demonstrated a 71% and 11% increase in interfacial shear strength. Consequently, it can be concluded that by aligning the carbon nanotubes at micro-interphase region along the axial direction of core fiber, the maximum interfacial properties can be attained in unidirectional coated-fibers composites under axial loading.

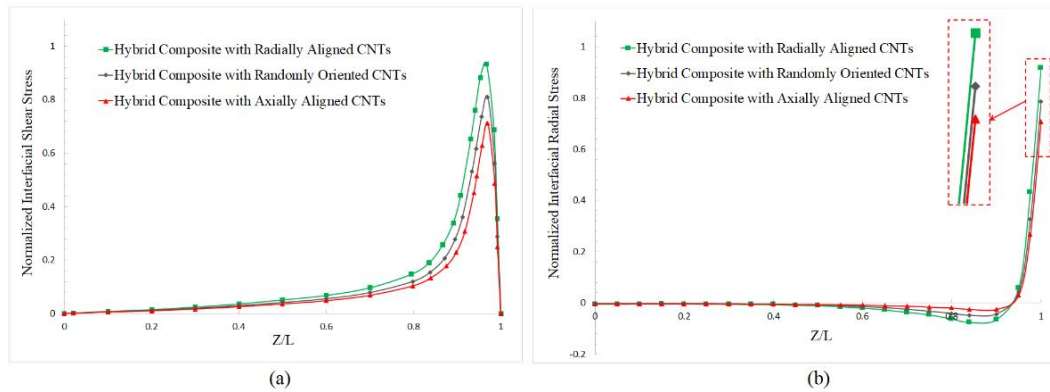


Figure 5.14: The normalized interfacial stress distribution for different CNT's configurations, (a) Interfacial shear stress, (b) Interfacial radial stress [178]

Multi-scale composites can be classified into two types of systems entitled as 'hybrid fiber system' and 'mixed CNT/matrix system' illustrated in Figure 5.15. As a crucial issue, both foregoing systems are deemed as hybrid multi-scale composites while they reflect dissonant interfacial properties which should be addressed during designing and analysis of such materials. Thus, in order to profound understanding of in situ morphology of nanomaterials influences on the multi-scale composites, this section of present work is allocated to the mentioned issue. Characterizing the in-situ properties of multi-scale composite materials, a new experimental technique was presented by Wood et. al [229] that enables local stiffness mapping of a CNT-reinforced matrix in the region surrounding fibers which provides a powerful tool to engineers who aim to appraise local reinforcement gradients.

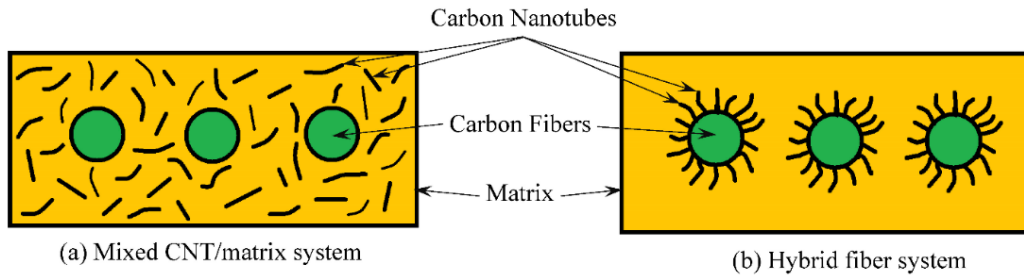


Figure 5.15: Schematic illustration of two systems of multi-scale hybrid composites; (a) Mixed CNT/ matrix system, (b) Hybrid fiber system [178]

Considering two aforementioned systems, the distribution of interfacial shear and radial stresses are represented in Figure 5.16 [178]. As it can be seen, employing ‘mixed CNT/ matrix system’ will weaken the influence of nano-reinforcement phase on the interfacial properties of such materials.

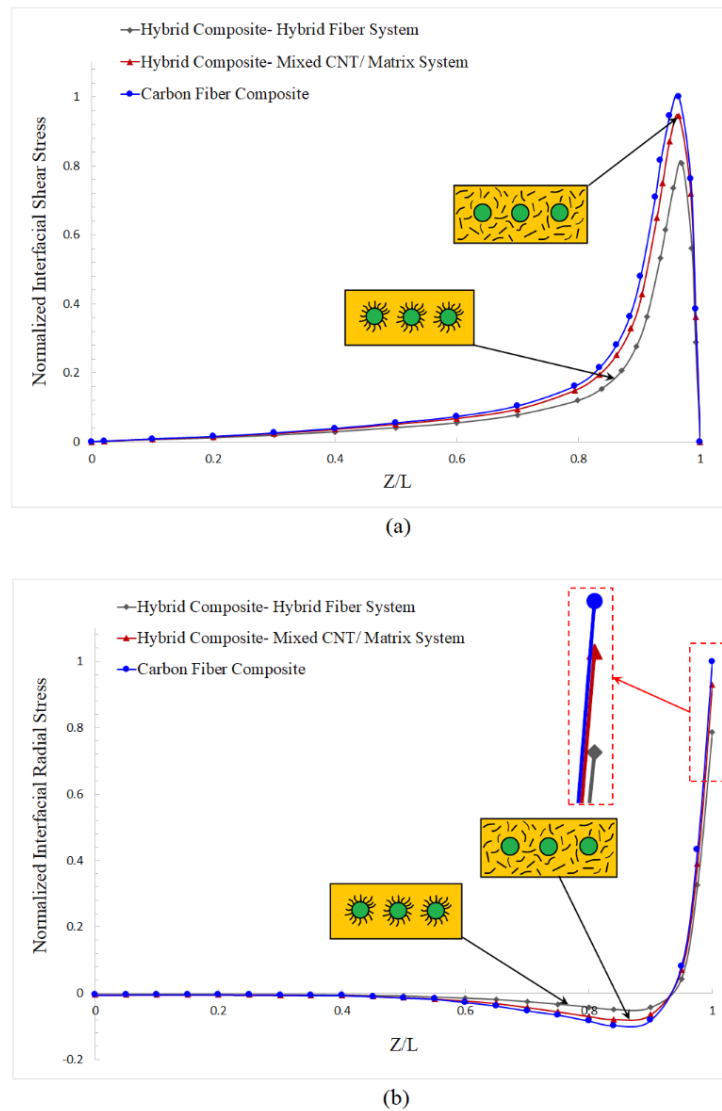


Figure 5.16: The interfacial stress distribution for different hybrid system (a) Interfacial shear stress (b) Interfacial radial stress [178]

Moreover, the maximum interfacial shear and radial stresses of ‘mixed CNT/matrix system’ decrease solely 5.3 % and 6.6 %, respectively, than CF–composite which is a vital outcome in designing multi-scale hybrid composites. Consequently, the presence of ‘mixed CNT/ Matrix system’ doesn’t make contribution to the interfacial behavior whereas the ‘hybrid fiber system’ demonstrates the outmost advantage into reduction of interfacial stresses. This outcome should be addressed in analysis and manufacturing of CNT–CF hybrid composites.

Figure 5.17 [178] describes a comparison of normalized maximum interfacial shear stress versus CNT content consisting of various CNTs orientations. From the graph supplied, it is evident that by increasing the CNTs quantity in the micro-interphase region, the maximum interfacial shear stress declines remarkably. Likewise, the differences between maximum stresses of various CNTs configurations are inconsequential at low weight percentage whereas it exhibits notable disparity at higher amount of CNTs. Adding only 2 wt.% of carbon nanotubes, engenders to diminish the maximum interfacial shear stress by 19.2 % and 28.9%, considering randomly and axially aligned CNTs, respectively.

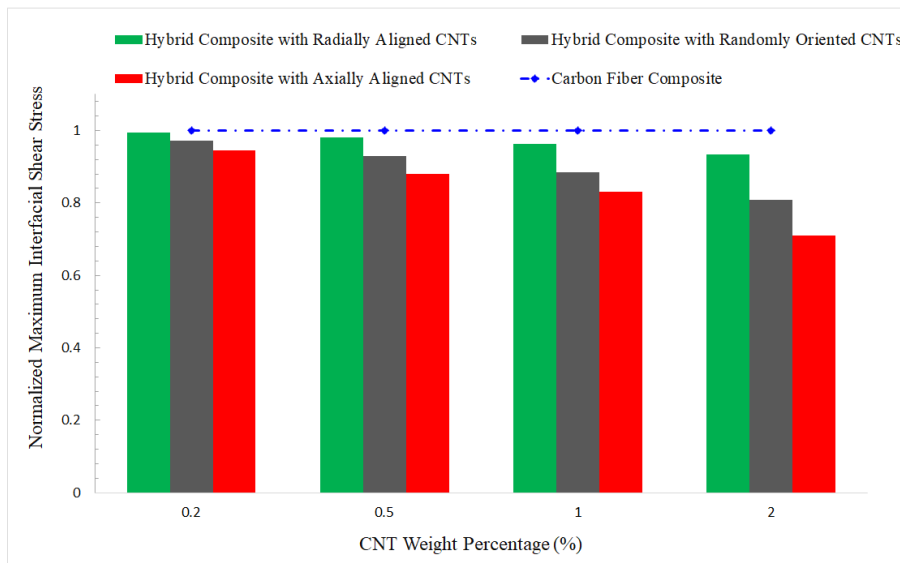


Figure 5.17: The normalized maximum interfacial shear stress versus CNT weight percentage [178]

As a momentous issue, load transferring phenomenon plays a crucial role in defining the mechanical properties of CNT–CF hybrid composites. It should be mentioned that imperfect bonding between the grown CNTs and encircling matrix at nanoscale, affects the micro-interphase mechanic behavior [121] and therefore impresses the load transfer phenomenon between fibers and matrix at macro-scale. Hence, to construct more accurate region around the core fiber, non-bonded interphase has been taken into account via vdW interactions between CNTs and matrix as stated previously.

The effect of non-bonded interphase on the maximum interfacial shear and radial stresses in terms of without CZM (perfect bonding) to with CZM ratio, can be seen in Figure 5.18 and Figure 5.19 [178], respectively, considering different orientations of carbon nanotubes in the micro-interphase region. A glance at the two figures provided discloses remarkable influence of non-bonded interphase region on the interfacial properties specially at higher volume fractions, indicating almost similar trends for both interfacial shear and radial stresses. Moreover, it can be understood that the influence of non-bonded interphase between CNT and matrix is more significant in axially and randomly orientations than radially grown configuration.

Hence, considering mere 2 wt% of CNTs, the imperfect bonding represents a pronounced discrepancy of interfacial shear stress with respect to perfect bonding, regarding axially aligned and randomly oriented configurations by 6.2 % and 5.11%, respectively. Analogously, considering non-bonded interphase and perfect bonding, notable reduction of interfacial radial stress is manifested regarding axially aligned and random oriented CNTs by 6.42 % and 5.25%, respectively. In contrast to elastic moduli, therefore, taking into account the non-bonded interphase region between CNTs and matrix precludes overestimating the outcomes and plays a momentous role on interfacial properties of nano-engineered multi-scale hybrid composites.

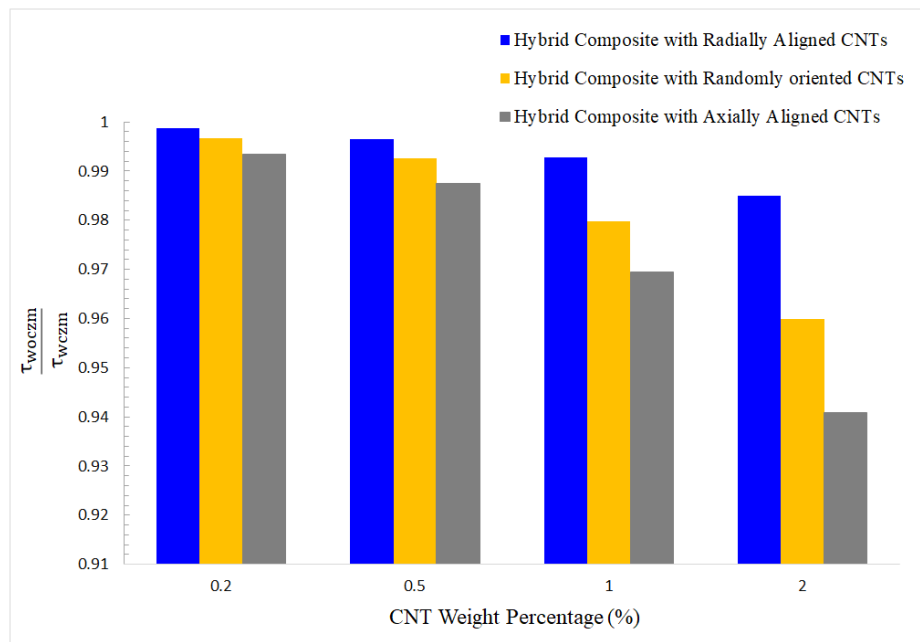


Figure 5.18: The maximum interfacial shear stress ratio considering perfect bond and debonding condition [178]

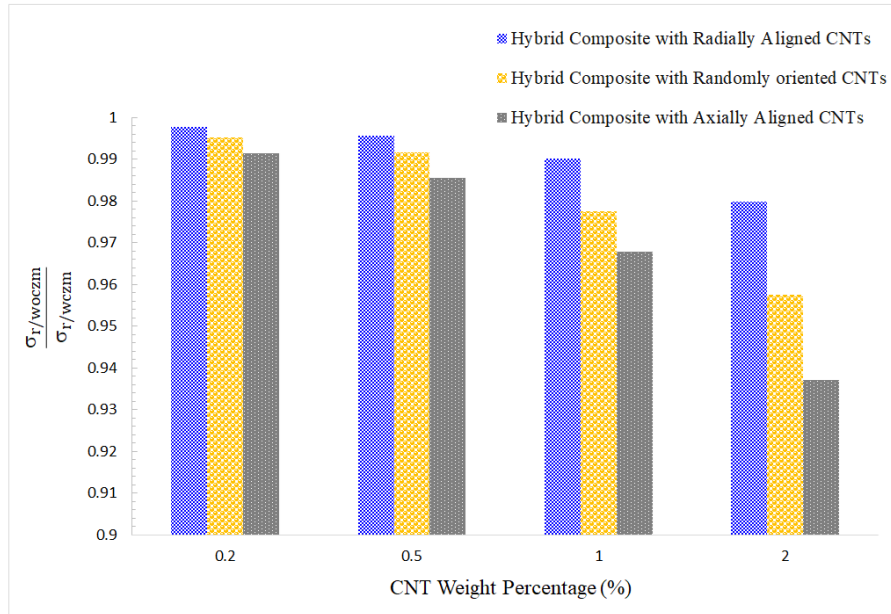


Figure 5.19: The maximum interfacial radial stress ratio considering perfect bond and debonding condition [178]

Similar to interfacial shear stress, in spite of small portion of CNTs in the micro-interphase region, the interfacial radial stress dwindles which yields higher interfacial strength and precluding debonding between fiber and matrix in the unidirectional composite materials. As it is shown in Figure 5.20 [178], a prominent reduction is gained by 21.3 % with only 2 wt.% of CNTs contents, considering randomly oriented carbon nanotubes.

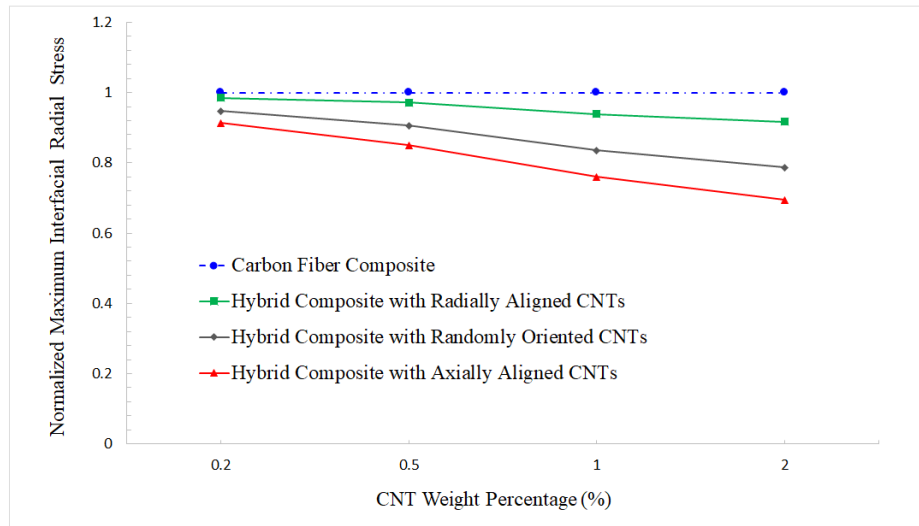


Figure 5.20: The normalized maximum interfacial radial stress versus CNT weight percentage [178]

5.7 Conclusion

By way of conclusion, this chapter is devoted to mechanical properties of unidirectional carbon nanotube–carbon fiber reinforced hybrid composites utilizing 3D finite element multi-scale modeling. The constructed multi-scale model consists of straight carbon nanotubes, carbon fiber, non-bonded interphase region and surrounding matrix, covering all incorporated scales of nano, micro and macro. The non-bonded interphase region between CNT's and matrix is established employing cohesive zone model (CZM). The interfacial behavior is assessed considering three different configurations of grown CNTs on the fiber surface, encompassing radially, axially, and randomly oriented CNTs. The outcomes divulge a considerable reduction of fiber-matrix interfacial shear stresses in the hybrid composite containing axially and randomly oriented CNTs by 28.9% and 19.2 %, respectively, with solely 2 wt.% of CNTs. Regarding the two proposed hybrid systems, it is remarkably disclosed that composites with CNTs–coated fibers represent less interfacial stresses than those with CNT reinforcements mixed in matrix. Considering non-bonded interphase region between CNTs and surrounding matrix, the results manifest pronounced effect on the interfacial properties, whereas no influence on the Young's moduli is observed, especially at lower volume fractions. Finally, the results demonstrate that the presence of CNTs improves the transverse Young's modulus, however, it shows negligible effect on the longitudinal Young's modulus.

Chapter 6: Effect of Carbon Nanotubes Coated–Carbon Fibers on Interfacial Residual Thermal Stresses

Abstract: This chapter provides a novel method regarding stress analysis of multi-scale hybrid composites and is based on the author's paper during PhD program [179]. The effect of carbon nanotube (CNT) coated-carbon fibers on thermal residual stresses of multi-scale hybrid composites is assessed employing analytical approach. The model comprises carbon fiber, coating region and surrounding matrix, in which the coating region around core fiber encompasses CNTs and matrix. Considering three configurations of grown CNTs on the fiber surface including axially, radially, and randomly oriented, the mechanical properties of various coating regions are acquired employing the Eshelby–Mori–Tanaka method in conjunction with an equivalent continuum approach. Utilizing the total energy minimization method, the closed-form solution of the thermal residual stresses of hybrid composite is obtained. The results disclose a noteworthy influence of CNT–coating on the reduction of interfacial stresses which precludes debonding at interface and attenuates the effect of thermal expansions mismatch between the carbon fiber and matrix. Furthermore, the results demonstrate that unlike radially oriented CNTs, the existence of axially and randomly oriented CNTs at the coating region has a remarkable diminishing effect on residual interfacial stresses. It is also shown that increasing the coating thickness leads to reduction of maximum interfacial stresses even at a constant CNT volume fraction. A close agreement exists between predicted outcomes by the proposed analytical approach and published data in the literature.

6.1 Introduction

Being cured or processed at elevated temperatures under pressure and/or in vacuum, the majority of composite materials attain their structural integrity. In manufacturing or cooling processes, therefore, the residual stress is generated due to discrepancy in coefficient of thermal expansion (CTE) between the fiber and matrix. Hence, as a fundamental issue, fiber-matrix interfacial stresses induced by thermal conditions, remarkably affect the mechanical behavior and load transferring phenomenon in composite materials. Thus, residual stress intrinsically emerges in almost all composite structures. Multifarious methods have been accomplished to

determine thermal residual stresses in the conventional fiber reinforced composites encompassing experimental investigations, elasticity solution and concentric cylinder theory in which thermal stresses are acquired for an infinitely long fiber surrounded by a matrix [179] [230] [231]. In the elasticity solution and concentric cylinder theory, the residual stresses are usually assumed to be independent of the fiber longitudinal direction [232]. In comparison with the aforementioned methods, the complementary energy method seems more advantageous because of (i) considering the stresses rather than the displacements as unknowns, (ii) introducing a better knowledge about residual stress distribution along the fiber direction and (iii) satisfying all boundary conditions especially at the fiber end [232].

Likewise, various finite element models (FEM) such as unit cell models of square and hexagonal arrays with different boundary conditions have been developed in order to obtain the thermoelastic behavior of composite structures [233]. Therefore, decreasing the fiber-matrix interfacial stress under thermal conditions plays a crucial role in augmenting the overall mechanical behavior through minimization of debonding. Consequently, CTE mismatch between the fiber and matrix is weakened by exploiting a suitable fiber coating [234] [235].

Invoking nanomaterials as an efficient solution for coating the fibers in the conventional composites has recently been introduced. The breakthrough of carbon nanotubes (CNTs) and nanoparticles have burgeoned a novel research sphere among scientists because of their unique properties [134] [138] [236]. Chief among the nanomaterials, carbon nanotubes have been widely utilized in the field of fiber-reinforced composites with the aim of improving interfacial properties or adding new functionalities in which the CNTs' deposition on the fiber surfaces is one of the most promising techniques [237]. It has even been demonstrated that dispersion of a few portions of CNTs in a matrix remarkably increases the thermal and mechanical properties of composite materials [238]. Owing to the superior characteristics of CNTs, multi-scale nano-engineered hybrid composites are being developed due to their outstanding behaviors in obviating cardinal drawbacks of conventional composites regarding interfacial and interlaminar properties by altering the fiber-matrix interface region [12]. Kundalwal and collaborators studied the thermomechanical properties and load transfer characteristics of the short fuzzy fiber reinforced composite utilizing shear lag model [239]. Chatzigeorgiou et al. [123] [240] investigated the mechanical properties and introduced a homogenization approach of fuzzy fiber composites using concentric cylinder theory. The analysis of thermal stresses in fibers of finite length embedded in a matrix is represented by Quek [241] employing a theoretical approach. The results revealed that the stress concentrations exist very close to the fiber ends which tend to enhance the likelihood of the fiber debonding due to mechanical loading and will influence the analysis of interfacial properties in fiber pull- and push-out tests. Mikata and Taya [242] investigated the stress field in a coated continuous fiber composite subjected to thermo-mechanical loadings, in which the results demonstrated that Ni-coating is

advantageous over SiC-coating from the crack resistance point of view. Thermal stresses in the composite structures comprising fiber, pyrolytic-carbon coating and matrix were calculated by Honjo [221] making use of actual properties of carbon coating which are elastically and thermally cylindrically anisotropic.

The majority of the foregoing literature was devoted to residual stress analysis of conventional composite materials. Owing to the lack of a straight and efficient method for interfacial stress analysis of multi-scale hybrid composites, a micromechanics modeling approach in conjunction with energy minimization method is developed in the present work, capable of obtaining a closed form solution for such materials and remarkably decreasing the computation time with respect to finite element analysis. To this end, a CNT-coating region with different configurations including axial, radial, and random oriented CNT is taken into account around the carbon fiber. Utilizing the proposed method, the influence of CNT-coating on the fiber–matrix thermal residual stresses is assessed parametrically. Notably, the axial, hoop and radial stresses are considered in the energy formulation, for sake of achieving more accurate outcomes of the residual stress distribution.

6.2 Constitutive Modeling of CNT– Coated Carbon Fiber Hybrid Composite

Recalling from previous chapter, different techniques are available for deposition of CNTs on the surface of carbon fiber such as Chemical Vapor Deposition (CVD), electrophoresis, electrospray technique, etc., each of which has its advantages and limitations [18] [187] [243]. By systematically varying the catalyst concentration, catalyst pre-treatment time, and sample position within the tube furnace in CVD method, the key factors governing CNT morphology are achievable [208], i.e., CNTs could be grown in radial, axial or random orientations on the fiber surface [201]. The presence of CNTs forest on the surface of the fiber is delineated in Figure 6.1 employing CVD and electrospray methods.

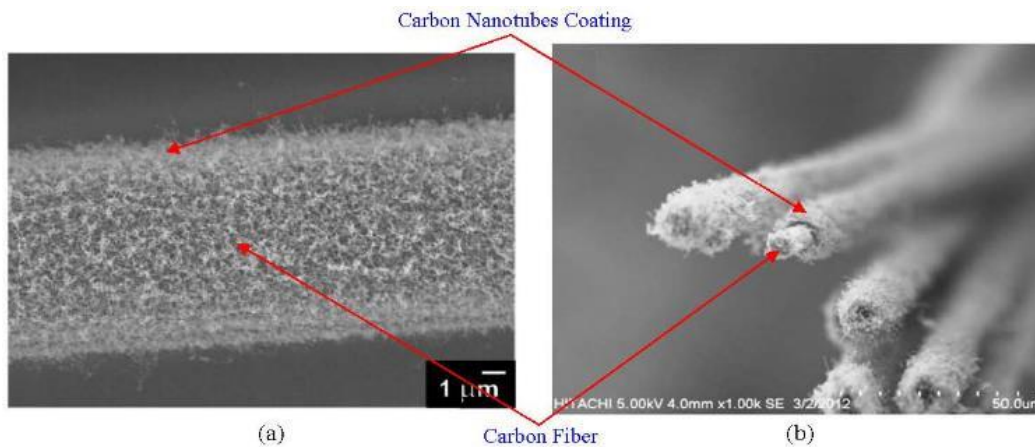


Figure 6.1: Carbon fiber coated with CNTs forest (a) randomly oriented CNTs on the surface of the carbon fiber [201] (b) Growth of CNTs with uniform distribution on the fiber surface [202]

In order to scrutinize the influence of CNT-coating on the core fiber and the effect of its morphology on the residual stress of hybrid composite, we take into account CNTs with radial, axial and random orientations at the coating region. A constitutive modelling approach is adopted to analyze hybrid composites with such layouts through constructing a cylindrical representative volume element (RVE) considering three disparate CNT orientations which are depicted in Figure 6.2. It should be noted that the subfigures of Figure 6.2 [179] are schematics, and carbon nanotubes possess high aspect ratios ($AR > 350$).

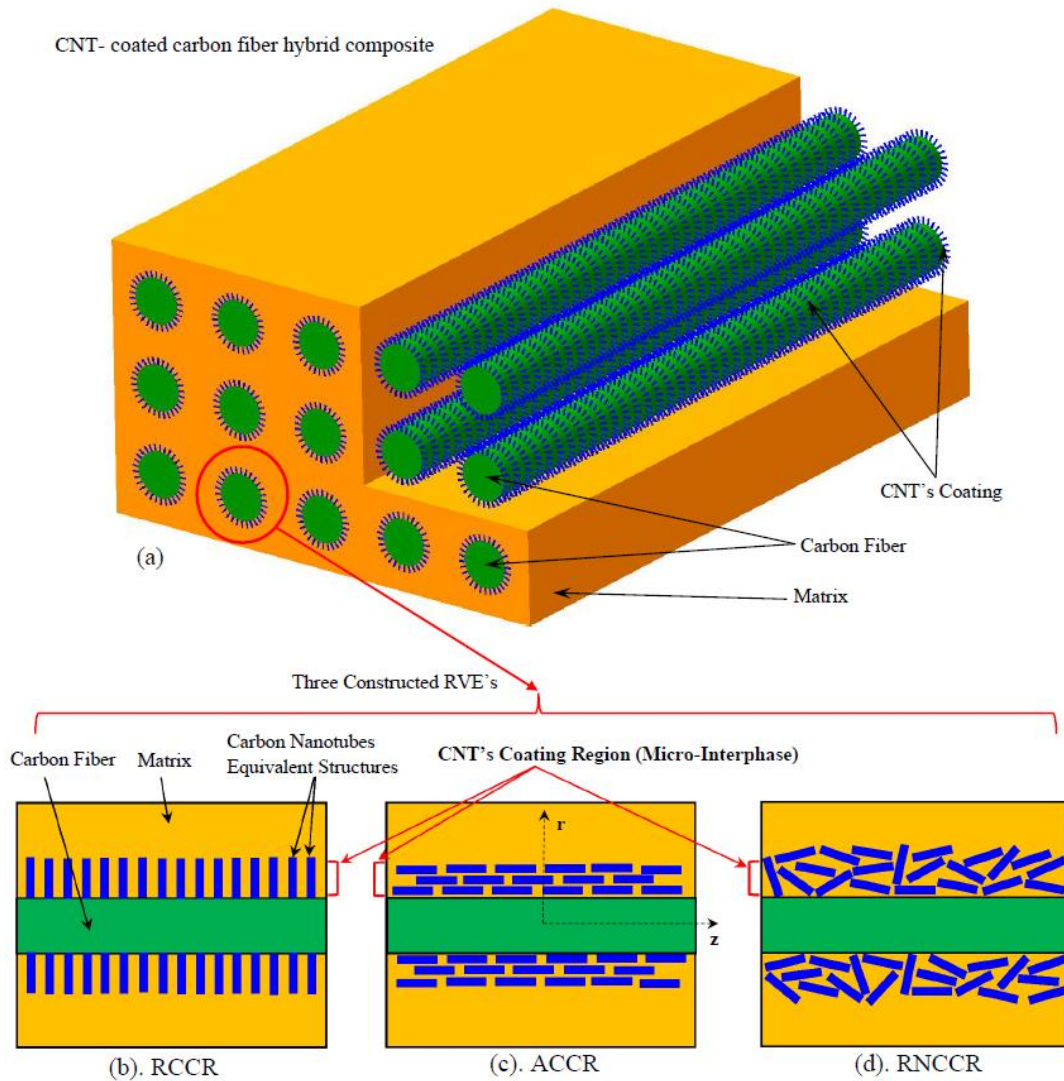


Figure 6.2: (a) CNT-coated CF Multi-scale hybrid composite (b) RVE with radially aligned CNTs (c) RVE with axially aligned CNTs (d) RVE with randomly oriented CNTs [179]

The RVEs are established through three concentric cylinders consisting of carbon fiber, CNT-coating region (henceforth referred to as CCR) and surrounding matrix. The CCR could be considered as a nanocomposite itself, in which the constituents are matrix and CNTs. For sake of clarification, the consecutive

modeling procedure in the present work is consolidated as a flowchart represented in Figure 6.3 [179].

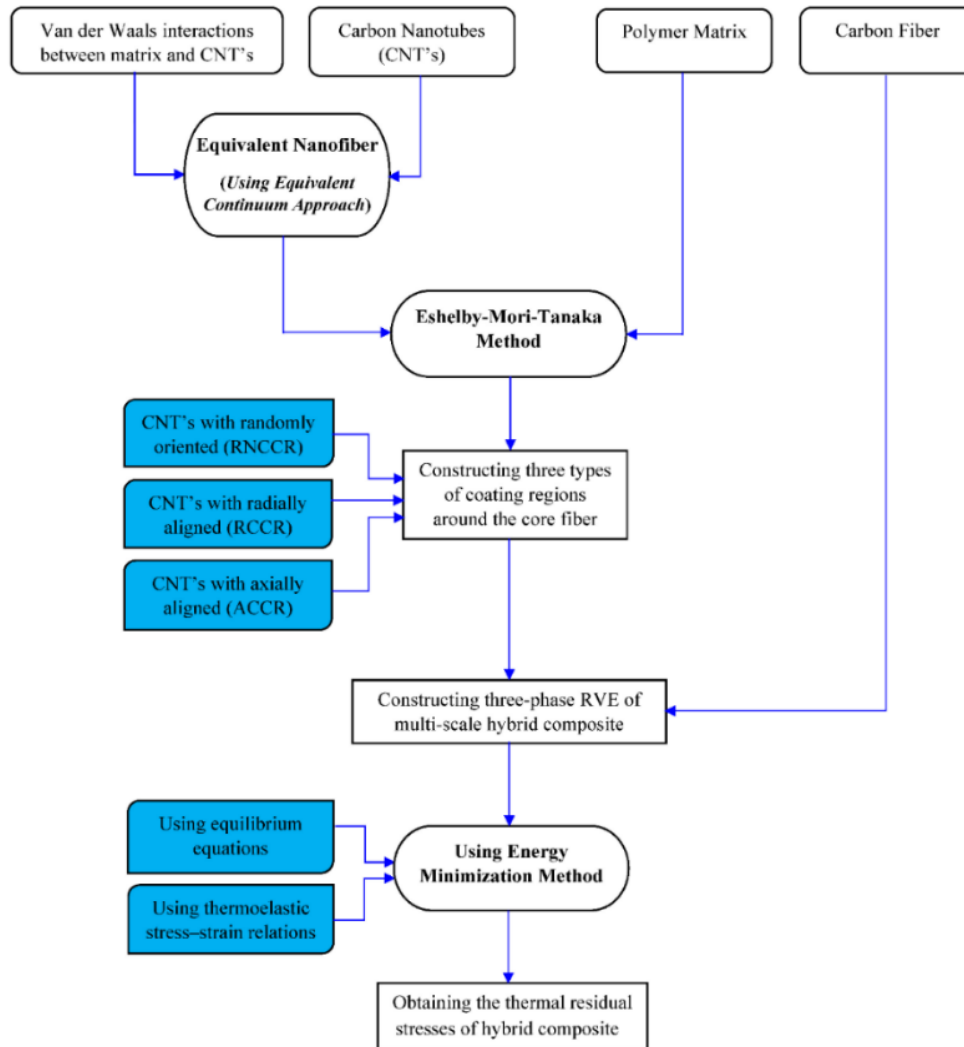


Figure 6.3: Flowchart of obtaining residual stress in CNT-coated CF hybrid composite [179]

6.2.1 Analytical Modelling of Carbon Nanotube Structure

At nanoscale, CNTs behave as nano-reinforcement agents in the hybrid composites. The theoretical investigations in modeling CNT behaviors are classified in three categories comprising atomistic modeling, continuum modeling and nano-scale continuum modeling. Concentrating on mechanical, buckling, vibrational and thermal properties, various approaches in the modeling of CNTs were rigorously reviewed and analyzed by Rafiee and Malekimoghadam [77]. Developing a finite element (FE) model of the CNT lattice structure by Li and Chou [91], each C–C bond of the CNT nanostructure is replaced with equivalent beam element in which the geometrical and mechanical properties of the beam element are obtained correlating the interatomic potential energies of molecular space to the strain

energies of structural mechanics. Utilizing equivalent continuum modeling [244], the CNT structure with surrounding non-bonded interphase is represented as equivalent nanofiber (ENF) which is described in Figure 6.4 and the ENF mechanical properties can be acquired using multi-scale finite element modeling proposed by Rafiee and Malekimoghadam [97]. It should be mentioned that the governing interactions between CNT and surrounding polymer are weakly non-bonded Van der Waals interactions. Conducting the multi-scale FE analysis, the non-bonded interphase region is simulated using nonlinear spring elements between CNT atoms and inner surface atoms of the polymer [97].

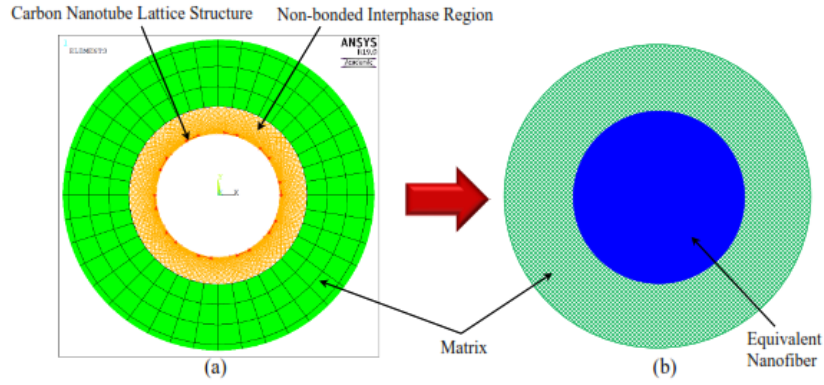


Figure 6.4: Description of CNT equivalent modeling (a) FE multi-scale model (b) Equivalent nanofiber [179]

Finally, the mechanical properties of the CNT equivalent structure (ENF) are computed [97] which are later employed as input data for theoretical stresses analysis of hybrid composites in the present work.

Thus, the ENF accurately accounts for the structural properties relationships at the nanoscale and furnishes a bridge to the continuum model. The Hill's elastic moduli [245] of the reinforcing phase, which is CNT in the present work, are attained by equality of two following matrices of ENF [246]:

$$\mathbf{C}_{ENF} = \begin{pmatrix} n_{ENF} & l_{ENF} & l_{ENF} & 0 & 0 & 0 \\ l_{ENF} & k_{ENF} + m_{ENF} & k_{ENF} - m_{ENF} & 0 & 0 & 0 \\ l_{ENF} & k_{ENF} - m_{ENF} & k_{ENF} + m_{ENF} & 0 & 0 & 0 \\ 0 & 0 & 0 & p_{ENF} & 0 & 0 \\ 0 & 0 & 0 & 0 & m_{ENF} & 0 \\ 0 & 0 & 0 & 0 & 0 & p_{ENF} \end{pmatrix} \quad (6.1)$$

$$\mathbf{C}_{ENF} = \begin{pmatrix} \frac{1}{E_L} & -\frac{\nu_{TL}}{E_T} & -\frac{\nu_{ZL}}{E_Z} & 0 & 0 & 0 \\ -\frac{\nu_{LT}}{E_L} & \frac{1}{E_T} & -\frac{\nu_{ZT}}{E_Z} & 0 & 0 & 0 \\ -\frac{\nu_{LZ}}{E_L} & -\frac{\nu_{TZ}}{E_T} & \frac{1}{E_Z} & 0 & 0 & 0 \\ 0 & 0 & 0 & \frac{1}{G_{TZ}} & 0 & 0 \\ 0 & 0 & 0 & 0 & \frac{1}{G_{ZL}} & 0 \\ 0 & 0 & 0 & 0 & 0 & \frac{1}{G_{LT}} \end{pmatrix}^{-1} \quad (6.2)$$

Where k_{ENF} , l_{ENF} , m_{ENF} , n_{ENF} , and p_{ENF} parameters are the Hill's elastic moduli of equivalent nanofiber. Since CNT is considered as transversely isotropic material, the compliance matrix of Eq (6.2) will contain five independent elastic parameters as E_L , E_T , G_{TZ} , ν_{TL} , ν_{TZ} which are derived from foregoing FEM and equivalent continuum modelling technique [97].

The material's properties of ENF for an armchair type of single walled CNT with chiral index of (10, 10) are given in Table 6.1 [205] [122].

Material	Longitudinal Young's modulus	Transverse Young's modulus	Transverse shear modulus	Poisson's ratio (ν_{LT})	Poisson's ratio (ν_{TZ})
Equivalent Nanofiber	649.12 [GPa]	11.27 [GPa]	5.13 [GPa]	0.284	0.14

Table 6.1: Mechanical Properties of Equivalent Nanofiber [122] [205]

6.2.2 Effective Elastic Properties of CNT– Coating Region (CCR)

The CCR which is also called micro-interphase region, encompasses grown CNTs, and polymer as a nanocomposite material surrounding carbon fiber. We take into account three configurations of CCR on the basis of the orientation of their constituent CNTs comprising radial, axial and random (henceforth referred to as RCCR, ACCR and RNCCR, respectively) as depicted in Figure 6.2 b-d. It should be also noted that the CNTs in the RCCR model span the entire interphase thickness, whereas in the ACCR configuration, they span the full length of the carbon fiber. In the RNCCR model, the CNTs span the full length in all orientations/ angles inside the coating region. To acquire the effective properties of fiber composites,

multifarious micromechanics models comprising dilute concentration model based on the Eshelby's equivalent inclusion, the self-consistent model, Mori–Tanaka models, the Halpin–Tsai equations and shear lag models were reviewed by Tucker and Liang [247]. For predicting the effective properties of composites, the Mori–Tanaka model has been reported to be the efficient analytical technique [247]. Therefore, the Mori-Tanaka model [222] is employed in order to determine the effective elastic properties of CCR which is required as input data for residual stress analysis. It is worthwhile to note that the details of Mori-Tanaka schemes for different types of inclusions and multi-phase systems have been thoroughly explicated in the literature [223]. Employing the Mori-Tanaka method and taking into account the average over orientations of nanofibers, the stiffness tensor of CCR as a composite medium can be defined [248]. For a two-phase composite material, the effective stiffness tensor of CCR is expressed as [249]:

$$\mathbf{C}_{CCR} = \mathbf{C}_m + V_{ENF} \{(\mathbf{C}_{ENF} - \mathbf{C}_m) \mathbf{A}_{ENF}\} \left[V_m \mathbf{I} + V_{ENF} \{\mathbf{A}_{ENF}\} \right]^{-1} \quad (6.3)$$

Where V_m and V_{ENF} indicate the volume fractions of matrix and CNT (effective nanofiber), respectively, \mathbf{I} is the fourth-order identity tensor, \mathbf{C}_{CCR} , \mathbf{C}_m and \mathbf{C}_{ENF} are the stiffness tensors of CCR, matrix and equivalent nano-fiber (ENF), and \mathbf{A}_{ENF} denotes the dilute mechanical strain concentration tensor of ENF which is described as below. The Curly brackets $\{\ast\}$ represent an average over all possible orientations.

$$\mathbf{A}_{ENF} = \left[\mathbf{I} + \mathbf{S} (\mathbf{C}_m)^{-1} (\mathbf{C}_{ENF} - \mathbf{C}_m) \right]^{-1} \quad (6.4)$$

Where \mathbf{S} is Eshelby's tensor [250] which is thoroughly elaborated by Mura [251] for various inclusions.

In view of the fact that the properties are different for each type of CNT coating, the stiffness matrices corresponding to RCCR, ACCR and RNCCR should be separately calculated. By obtaining the mechanical properties of three RVEs comprising different types of CNT coating (see Figure 6.2), the models are established for residual stress analysis.

It should be reaffirmed that the CNT structure treats as transversely isotropic material whereas the surrounding matrix behaves as an isotropic medium. Consequently, ACCR is transversely isotropic with an axis of symmetry along z direction (Figure 6.2-c). The stiffness matrix of ACCR in terms of Hill's moduli is expressed as following [61]:

$$\mathbf{C}_{ACCR} = \begin{pmatrix} k_{ACCR} + m_{ACCR} & l_{ACCR} & k_{ACCR} - m_{ACCR} & 0 & 0 & 0 \\ l_{ACCR} & n_{ACCR} & l_{ACCR} & 0 & 0 & 0 \\ k_{ACCR} - m_{ACCR} & l_{ACCR} & k_{ACCR} + m_{ACCR} & 0 & 0 & 0 \\ 0 & 0 & 0 & p_{ACCR} & 0 & 0 \\ 0 & 0 & 0 & 0 & m_{ACCR} & 0 \\ 0 & 0 & 0 & 0 & 0 & p_{ACCR} \end{pmatrix} \quad (6.5)$$

where k , l , m , n , and p are Hill's elastic moduli; k represents the plane-strain bulk modulus normal to the ENF direction, n denotes the uniaxial tension modulus along the ENF direction, l indicates the associated cross modulus, and m and p state the shear moduli in planes normal and parallel to the ENF direction, respectively. The non-vanishing components of the Eshelby tensor S are given as following for a straight ENF with circular cross section and sufficiently large aspect ratio along the z -direction [251]:

$$\begin{aligned} S_{1111} = S_{3333} &= \frac{5-4\nu_m}{8(1-\nu_m)}, & S_{1122} = S_{3322} &= \frac{\nu_m}{2(1-\nu_m)} \\ S_{1133} = S_{3311} &= \frac{4\nu_m-1}{8(1-\nu_m)}, & S_{1212} = S_{2323} &= \frac{1}{4}, & S_{1313} &= \frac{3-4\nu_m}{8(1-\nu_m)} \end{aligned} \quad (6.6)$$

Where ν_m is Poisson's ratio of the matrix. By substituting Eq (6.6) into Eq (6.4) the non-vanishing components of \mathbf{A} are obtained accordingly:

$$\begin{aligned} A_{1111} = A_{3333} &= -\frac{a_3}{a_1 a_2}, & A_{1133} = A_{3311} &= \frac{a_4}{a_1 a_2}, & A_{2323} &= \frac{E_m}{E_m + 2 p_{ENF} (1 + \nu_m)} \\ A_{1122} = A_{3322} &= \frac{l_{ENF} (1 - \nu_m - 2 \nu_m^2) - E_m \nu_m}{a_1}, & A_{1313} &= \frac{2 E_m (1 - \nu_m)}{a_2}, & A_{2222} &= 1 \end{aligned} \quad (6.7)$$

Where E_m and ν_m are elastic modulus and Poisson's ratio of matrix and a_1 , a_2 , a_3 , a_4 parameters are represented in Appendix B. The Hill's elastic moduli of CNTs are already obtained in previous section. By replacing the elements of tensor \mathbf{A} from Eq (6.7) into Eq (6.3), the stiffness tensor of ACCR is obtained. In particular, the Hill's elastic moduli of foregoing CNT configuration are expressed as following [252]:

$$k_{ACCR} = \frac{E_m \{E_m V_m + 2 k_{ENF} (1 + \nu_m) [1 + V_{ENF} (1 - 2 \nu_m)]\}}{2 (1 + \nu_m) [E_m (1 + V_{ENF} - 2 \nu_m) + 2 V_m k_{ENF} (1 - \nu_m - 2 \nu_m^2)]} \quad (6.8)$$

$$l_{ACCR} = \frac{E_m \{V_m \nu_m [E_m + 2k_{ENF} (1 + \nu_m)] + 2V_{ENF} l_{ENF} (1 - \nu_m^2)\}}{(1 + \nu_m) [2V_m k_{ENF} (1 - \nu_m - 2\nu_m^2) + E_m (1 + V_{ENF} - 2\nu_m)]} \quad (6.9)$$

$$n_{ACCR} = \frac{E_m^2 V_m (1 + V_{ENF} - V_m \nu_m) + 2V_m V_{ENF} (k_{ENF} n_{ENF} - l_{ENF}^2) (1 + \nu_m)^2 (1 - 2\nu_m)}{(1 + \nu_m) \{2V_m k_{ENF} (1 - \nu_m - 2\nu_m^2) + E_m (1 + V_{ENF} - 2\nu_m)\}} + \frac{E_m [2V_m^2 k_{ENF} (1 - \nu_m) + V_{ENF} n_{ENF} (1 - 2\nu_m + V_{ENF}) - 4V_m l_{ENF} \nu_m]}{2V_m k_{ENF} (1 - \nu_m - 2\nu_m^2) + E_m (1 + V_{ENF} - 2\nu_m)} \quad (6.10)$$

$$p_{ACCR} = \frac{E_m [E_m V_m + 2(1 + V_{ENF}) p_{ENF} (1 + \nu_m)]}{2(1 + \nu_m) [E_m (1 + V_{ENF}) + 2V_m p_{ENF} (1 + \nu_m)]} \quad (6.11)$$

$$m_{ACCR} = \frac{E_m [E_m V_m + 2m_{ENF} (1 + \nu_m) (3 + V_{ENF} - 4\nu_m)]}{2(1 + \nu_m) \{E_m [V_m + 4V_{ENF} (1 - \nu_m)] + 2V_m m_{ENF} (3 - \nu_m - 4\nu_m^2)\}} \quad (6.12)$$

Where k_{ACCR} , l_{ACCR} , m_{ACCR} , n_{ACCR} , and p_{ACCR} are Hill's elastic moduli of ACCR; k_{ACCR} is the plane-strain bulk modulus normal to the fiber direction, n_{ACCR} denotes the uniaxial tension modulus in the fiber direction (z- direction), l_{ACCR} indicates the associated cross modulus, and m_{ACCR} and p_{ACCR} state the shear moduli in planes normal and parallel to the fiber direction, respectively. Eventually, the longitudinal (E_z , parallel to CNT direction) and transverse elastic moduli ($E_{r,\theta}$) of ACCR are declared in terms of Hill's elastic moduli as [248]:

$$(E_z)_{ACCR} = n_{ACCR} - \frac{l_{ACCR}^2}{k_{ACCR}}, \quad (E_r)_{ACCR} = \frac{4m_{ACCR} (k_{ACCR} n_{ACCR} - l_{ACCR}^2)}{k_{ACCR} n_{ACCR} - l_{ACCR}^2 - m_{ACCR} n_{ACCR}} \quad (6.13)$$

On the other hand, the RCCR (Figure 6.2 b) is transversely isotropic with an axis of symmetry along r direction. Hence, after obtaining the mechanical properties of ACCR, the stiffness matrix of RCCR is also attained invoking below equation:

$$[C_{RCCR}] = [T][C_{ACCR}][T]^T \quad (6.14)$$

Where $[T]$ denotes the transformation matrix which is given as following [253]:

$$\mathbf{T} = \begin{pmatrix} \cos^2 \theta & \sin^2 \theta & 0 & 0 & 0 & -\sin 2\theta \\ \sin^2 \theta & \cos^2 \theta & 0 & 0 & 0 & -\sin 2\theta \\ 0 & 0 & 1 & 0 & 0 & 0 \\ 0 & 0 & 0 & \cos \theta & -\sin \theta & 0 \\ 0 & 0 & 0 & \sin \theta & \cos \theta & 0 \\ -\sin \theta \cos \theta & \sin \theta \cos \theta & 0 & 0 & 0 & \cos^2 \theta - \sin^2 \theta \end{pmatrix} \quad (6.15)$$

For the case of RNCCR (Figure 6.2 d), the orientation distribution of CNTs could be characterized by a probability density function $p(\alpha, \beta)$ satisfying the below normalization condition [254]:

$$\int_0^{2\pi} \int_0^{\pi/2} p(\alpha, \beta) \sin \alpha \, d\alpha d\beta = 1 \quad (6.16)$$

Where α and β are two Euler angles which characterize the orientation of a straight CNT. If CNTs are randomly oriented, the density function is $p(\alpha, \beta) = 1/2\pi$. Thus, akin to Eq (6.3), the effective modulus of the RNCCR can be stated as:

$$\mathbf{C}_{RNCCR} = (V_m \mathbf{C}_m + V_{ENF} \{ \mathbf{C}_{ENF} : \mathbf{A}_{ENF} \}) : [V_m \mathbf{I} + V_{ENF} \{ \mathbf{A}_{ENF} \}]^{-1} \quad (6.17)$$

It should be pointed out that if the CNTs are randomly distributed in the CCR, this region could be assumed as an isotropic material, and its bulk modulus K and shear modulus G are derived as [222]:

$$K_{RNCCR} = K_m + \frac{V_{ENF} (\delta_{ENF} - 3K_m \alpha_{ENF})}{3(V_m + V_{ENF} \alpha_{ENF})}, \quad G_{RNCCR} = G_m + \frac{V_{ENF} (\eta_{ENF} - 2G_m \beta_{ENF})}{2(V_m + V_{ENF} \beta_{ENF})} \quad (6.18)$$

Where V_{ENF} , V_m , K_m and G_m are the volume fraction of nanofiber, volume fraction of matrix, bulk and shear moduli of the matrix, respectively. The parameters α_{ENF} , β_{ENF} , δ_{ENF} and η_{ENF} are given in Appendix C. Finally, the effective Young's modulus (E) and Poisson's ratio (ν) of RNCCR are given as [248]:

$$E_{RNCCR} = \frac{9K_{RNCCR} G_{RNCCR}}{3K_{RNCCR} + G_{RNCCR}}, \quad \nu_{RNCCR} = \frac{3K_{RNCCR} - 2G_{RNCCR}}{6K_{RNCCR} + 2G_{RNCCR}} \quad (6.19)$$

It is indicated that MATLAB R2018 platform has been utilized to calculate the stiffness matrices of CCRs (see Figure 6.2 b-d) which are used as input data for subsequent section regarding interfacial residual stress analysis.

Since the CTE of CCR can be isotropic or anisotropic depending on the orientation of CNTs, a distinct CTE should be acquired for each CCR type. The effective CTEs of isotropic and anisotropic composite materials containing short and chopped fibers are derived by Marom and Weinberg [255] considering the fiber critical length. Making use of the shear-lag method, various investigations were carried out to develop expressions for the effect of the fiber aspect ratio (l/d) on the longitudinal (fiber-direction) CTE [256]. According to the foregoing investigation, the longitudinal CTE of CCR region can be express as:

$$(\alpha_{CCR})_L = \frac{K(E_{ENF})_L(\alpha_{ENF})_L V_{ENF} + E_m \alpha_m V_m}{K(E_{ENF})_L V_{ENF} + E_m V_m} \quad (6.20)$$

Where $(E_{ENF})_L$, $(\alpha_{ENF})_L$, V_{ENF} , E_m , α_m , and V_m are longitudinal Young's modulus of equivalent nanofiber (ENF), longitudinal CTE of ENF, volume fraction of ENF, Young's modulus of matrix, CTE of matrix and volume fraction of matrix, respectively. The fiber efficiency factor, K , is a function of the fiber length and orientation, given by [256]:

$$K = C \left(1 - \frac{\tanh(\gamma l / d)}{\gamma l / d} \right) \quad (6.21)$$

$$\gamma = (2 G_m / (E_{ENF})_L)^{1/2} (V_{ENF}^{-1/2} - 1)^{-1/2}$$

The factor $C=1$ is employed to allow ENF orientation in ACCR or RCCR, whereas $C=0.4$ is used for RNCCR [256]. With regard to the transverse CTE of short fiber composite, an expression was presented [255] which can be rewritten for ACCR and RCCR as following:

$$(\alpha_{ACCR/RCCR})_T = (1 + \nu_m) \alpha_m V_m + (1 + \nu_{ENF}) (\alpha_{ENF})_T V_{ENF} - (\alpha_{CCR})_L (\nu_{ENF} V_{ENF} + \nu_m V_m) \quad (6.22)$$

It is worthwhile to mention that the CTE of CNTs are extremely nonlinear with respect to the variation of temperature. The CTEs of various CNTs were predicted using molecular dynamics (MDs) by Alamusi et al. [257], in which it was found that the axial CTEs vary nonlinearly with the temperature, however, they decrease linearly as the CNT diameter increases. Likewise, a set of empirical formulations was proposed for evaluating the CTEs of armchair and zigzag SWCNTs considering both temperature and diameter of CNT [257]. For the armchair single walled CNT

with chiral index (10,10) which is employed in the current research, the below equations are given to acquire the axial and transverse CTEs of CNT [258] [259] [257]:

Low Temperature ($1-301K$)

$$\alpha_L = (2D-1) \times 10^{-10} T^4 - (2D-1) \times 10^{-7} T^3 + (2D-5) \times 10^{-5} T^2 - (30D-3) \times 10^{-2} T$$

High Temperature ($301-901K$)

(6.23)

$$\alpha_L = -0.9D - (2 \times 10^{-8} T^3 - 6 \times 10^{-5} T^2 + 3 \times 10^{-2} T)$$

$$\alpha_T = 3.7601 \times 10^{-10} \Delta T^2 - 3.2189 \times 10^{-7} \Delta T - 3.2429 \times 10^{-8}$$

Where α_L , α_T are axial and transverse CTEs of CNT, D is the diameter of CNT, and T denotes the temperature.

6.3 Problem Formulation and Analytical Implementation

By obtaining the mechanical properties of CCR considering three disparate CNT morphologies (three constructed RVEs) in the previous section, the interfacial residual stress analysis and parametric study of CNT-coated carbon fiber hybrid composite are carried out in this section. Hence, the selected RVE encompassing carbon fiber, CCR and surrounding matrix are introduced as three concentric cylinders and the cylindrical coordinate system (r, θ, z) is adopted in which the z -direction is coincident with the longitudinal axis of carbon fiber, forming an axisymmetric problem. It should be mentioned that carbon fiber is simulated as transversely isotropic material whereas the surrounding matrix is considered as a homogeneous isotropic material. It is worthwhile to emphasize that the CCR is considered as a transversely isotropic or isotropic material depending on the CNTs' configurations around carbon fiber.

Appropriate Airy stress functions [260] are used in order to define the stresses in the current research, satisfying the equilibrium equations. Figure 6.5 illustrates the RVE of multi-scale hybrid composite in which the R_m , R_{CCR} , R_f and L are matrix radius, CCR radius, carbon fiber radius and length of RVE, respectively.

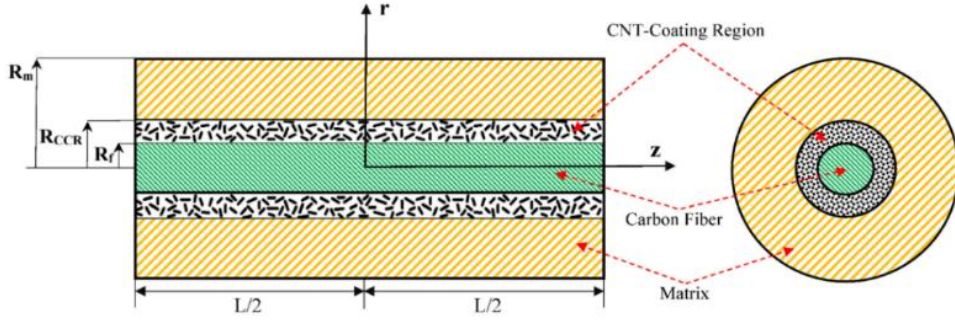


Figure 6.5: RVE model of CNT- Coated fiber hybrid composite and corresponding coordinate system [179]

6.3.1 Constructing the Stress Functions

In the cylindrical coordinate system, the equilibrium equation is expressed as [260]:

$$\frac{\partial \sigma_{zz}}{\partial z} + \frac{\partial \tau_{rz}}{\partial r} + \frac{\tau_{rz}}{r} = 0 \quad (6.24)$$

$$\frac{\partial \sigma_{rr}}{\partial r} + \frac{\partial \tau_{rz}}{\partial z} + \frac{\sigma_{rr} - \sigma_{\theta\theta}}{r} = 0 \quad (6.25)$$

The stress components in terms of Airy stress functions are stated as:

$$\sigma_{rr} = \frac{1}{r} \frac{\partial \varphi}{\partial r} + \frac{\partial^2 \varphi}{\partial z^2} \quad (6.26)$$

$$\sigma_{\theta\theta} = \frac{\partial^2 \varphi}{\partial z^2} \quad (6.27)$$

$$\sigma_{zz} = \frac{\partial^2 \varphi}{\partial r^2} + \frac{1}{r} \frac{\partial \varphi}{\partial r} \quad (6.28)$$

$$\tau_{rz} = -\frac{\partial^2 \varphi}{\partial r \partial z} \quad (6.29)$$

$$\tau_{z\theta} = \tau_{r\theta} = 0 \quad (6.30)$$

In order to determine the axisymmetric state of stresses in the 3D problem of CNT-coated fiber hybrid composite, the Airy stress functions are assumed as following [261]:

$$\varphi_j(r, z) = f_q(r) \cdot g_q(z) \quad q=1,2,3 \quad ; \quad j=f, m, CCR \quad (6.31)$$

Where the subscripts f, CCR and m refer to the fiber, CNT-coating region and matrix, respectively. $f_q(r)$ and $g_q(z)$ are functions of radial and axial coordinates, respectively. Incorporating Eq (6.31) in Equations (6.26)-(6.30), the stresses in the hybrid composite are attained accordingly:

$$\sigma_{rr}^j = \frac{1}{r} \frac{df_q(r)}{dr} g_q(z) + f_q(r) \frac{d^2 g_q(z)}{dz^2} \quad (6.32)$$

$$\sigma_{\theta\theta}^j = f_q(r) \frac{d^2 g_q(z)}{dz^2} \quad (6.33)$$

$$\sigma_{zz}^j = \left(\frac{d^2 f_q(r)}{dr^2} + \frac{1}{r} \frac{df_q(r)}{dr} \right) g_q(z) \quad (6.34)$$

$$\tau_{rz}^j = - \frac{df_q(r)}{dr} \frac{dg_q(z)}{dz} \quad (6.35)$$

It is worth mentioning that the number of unknown functions $f_1(r)$, $f_2(r)$ and $f_3(r)$ decreases by invoking boundary conditions of the stress-free state at the matrix surface as well as the stress continuity at the fiber–CCR interface and CCR–matrix interface along radial direction. Since the axial stress is assumed to be constant in radial direction (r) in each medium, the function $f_1(r)$, $f_2(r)$ and $f_3(r)$ can be described in terms of a constant B_q , while σ_{rr} and $\sigma_{\theta\theta}$ are still functions of r. Hence, by considering Eq (6.34), the axial stresses in the fiber, matrix and CCR are given by [261]:

$$\sigma_{zz}^f = B_1 \cdot g_1(z) \quad (6.36)$$

$$\sigma_{zz}^{CCR} = B_2 \cdot g_2(z) \quad (6.37)$$

$$\sigma_{zz}^m = B_3 g_3(z) \quad (6.38)$$

Considering the equilibrium condition in the axial direction leads to [232]:

$$\sigma_{zz}^f V_f + \sigma_{zz}^{CCR} V_{CCR} + \sigma_{zz}^m V_m = 0 \quad (6.39)$$

Where V_f , V_m and V_{CCR} denote the volume fractions of fiber, matrix and CCR, respectively. Replacing Eqs (6.36)- (6.38) into Eq (6.39) gives the below equation, whereby the three unknown functions $g_1(z)$, $g_2(z)$ and $g_3(z)$ are connected to each other that yields two unknown functions.

$$B_1 g_1(z) V_f + B_2 g_2(z) V_{CCR} + B_3 g_3(z) V_m = 0 \quad (6.40)$$

Utilizing the total complementary energy principle and Eq (6.40), the two foregoing unknown functions will be determined and consequently the third one could be achieved by Eq (6.40). Eventually, the axial, radial, shear and hoop stress components will be acquired in the constituents of the hybrid composite.

6.3.2 Stress components in the fiber

Taking into account Eq (6.36) and the first equilibrium equation, Eq (6.24), the fiber shear stress is expressed as:

$$\tau_{rz}^f = -\frac{B_1 r}{2} \frac{dg_1(z)}{dz} \quad (6.41)$$

Due to finite value condition of stress in the core region, the fiber Airy stress function is only a function of z coordinate, and Eq (6.26) and (6.27) can be stated as [14]:

$$\sigma_{rr}^f = \sigma_{\theta\theta}^f = \frac{\partial^2 \varphi}{\partial z^2} \quad (6.42)$$

Substituting Eq (6.41) and Eq (6.42) in the second equilibrium equation (Eq (6.25)), the radial and hoop stresses are given by:

$$\sigma_{rr}^f = \sigma_{\theta\theta}^f = \frac{B_1 r^2}{4} \frac{d^2 g_1(z)}{dz^2} + D_1(z) \quad (6.43)$$

6.3.3 Stress components in the CNT- coating region (CCR)

The stress components in CCR region are defined by substituting Eq (6.37) in the equilibrium equations (Eq (6.24) and Eq (6.25)):

$$\tau_{rz}^{CCR} = -\frac{1}{2r} \left\{ B_1 R_f^2 \frac{dg_1(z)}{dz} + B_2 (r^2 - R_f^2) \frac{dg_2(z)}{dz} \right\} \quad (6.44)$$

$$\sigma_{rr}^{CCR} = \sigma_{\theta\theta}^{CCR} = \frac{R_f^2}{2} \left\{ B_1 \frac{d^2 g_1(z)}{dz^2} - B_2 \frac{d^2 g_2(z)}{dz^2} \right\} \ln r + B_2 \frac{r^2}{4} \frac{d^2 g_2(z)}{dz^2} + D_2(z) \quad (6.45)$$

6.3.4 Stress components in the matrix

Inserting Eq (6.36) and Eq (6.37) into Eq (6.39) yields the axial stress in the surrounding matrix as following:

$$\sigma_{zz}^m = - \left\{ B_1 g_1(z) \frac{V_f}{V_m} + B_2 g_2(z) \frac{V_{CCR}}{V_m} \right\} \quad (6.46)$$

Replacing the matrix axial stress in the equilibrium equations leads to:

$$\tau_{rz}^m = -\frac{B_1}{2r} \left\{ R_f^2 - (r^2 - R_{CCR}^2) \frac{V_f}{V_m} \right\} \frac{dg_1(z)}{dz} - \frac{B_2}{2r} \left\{ (R_{CCR}^2 - R_f^2) - (r^2 - R_{CCR}^2) \frac{V_{CCR}}{V_m} \right\} \frac{dg_2(z)}{dz} \quad (6.47)$$

$$\begin{aligned} \sigma_{rr}^m = \sigma_{\theta\theta}^m = \frac{B_1}{4} \left\{ 2R_f^2 \ln r - (r^2 - 2R_{CCR}^2 \ln r) \frac{V_f}{V_m} \right\} \frac{d^2 g_1(z)}{dz^2} + \\ \frac{B_2}{4} \left\{ 2(R_{CCR}^2 - R_f^2) \ln r - (r^2 - 2R_{CCR}^2 \ln r) \frac{V_{CCR}}{V_m} \right\} \frac{d^2 g_2(z)}{dz^2} + D_3(z) \end{aligned} \quad (6.48)$$

6.3.5 Boundary Conditions

The half of RVE length (from $z=0$ to $z=L/2$) is utilized due to the symmetry of the model. Thus, the free surface conditions [241] engender zero axial and shear stresses at end of the fiber as following:

$$\begin{aligned}
&\rightarrow g_q(0) = 1, & q = 1, 2 \\
&\rightarrow g'_q(0) = \frac{dg_q(0)}{dz} = 0, \\
&\rightarrow g_q(L/2) = 0, \\
&\rightarrow g'_q(L/2) = \frac{dg_q(L/2)}{dz} = 0,
\end{aligned} \tag{6.49}$$

It is worth mentioning that the radial stress at the outermost surfaces of the polymer is zero and it also must be continuous across the fiber-CCR and CCR-matrix interfaces [261] [262]:

$$\sigma_{rr}^m = 0 \quad \text{at} \quad r = R_m, \quad -\frac{L}{2} < z < \frac{L}{2} \tag{6.50}$$

$$\begin{aligned}
\sigma_{rr}^f &= \sigma_{rr}^{CCR} \quad \text{at} \quad r = R_f, \quad -\frac{L}{2} < z < \frac{L}{2} \\
\sigma_{rr}^{CCR} &= \sigma_{rr}^m \quad \text{at} \quad r = R_{CCR}, \quad -\frac{L}{2} < z < \frac{L}{2}
\end{aligned} \quad \text{Continuity Conditions} \tag{6.51}$$

Satisfying the conditions of Eqs (6.50) and (6.51), the unknown functions $D_1(z)$, $D_2(z)$ and $D_3(z)$ in Eqs (6.43), (6.45) and (6.48) are obtained as follows:

$$\begin{aligned}
D_1 = & -\frac{B_1}{4} \frac{d^2 g_1(z)}{dz^2} \left[2R_f^2 \ln R_m - (R_m^2 - 2R_{CCR}^2 \ln R_m) \frac{V_f}{V_m} + (R_{CCR}^2 - 2R_{CCR}^2 \ln R_{CCR}) \frac{V_f}{V_m} \right. \\
& \left. - R_f^2 \ln R_f \right] - \frac{B_2}{4} \frac{d^2 g_2(z)}{dz^2} \left[2(R_{CCR}^2 - R_f^2) \ln R_m - (R_m^2 - 2R_{CCR}^2 \ln R_m) \frac{V_{CCR}}{V_m} \right. \\
& \left. - 2(R_{CCR}^2 - R_f^2) \ln R_{CCR} + (R_{CCR}^2 - 2R_{CCR}^2 \ln R_{CCR}) \frac{V_{CCR}}{V_m} - 2R_f^2 \ln R_{CCR} + R_{CCR}^2 \right. \\
& \left. + 2R_f^2 \ln R_f - R_f^2 \right]
\end{aligned} \tag{6.52}$$

$$\begin{aligned}
D_2 = & -\frac{B_1}{4} \frac{d^2 g_1(z)}{dz^2} \left[2 R_f^2 \ln R_m - (R_m^2 - 2 R_{CCR}^2 \ln R_m) \frac{V_f}{V_m} + (R_{CCR}^2 - 2 R_{CCR}^2 \ln R_{CCR}) \frac{V_f}{V_m} \right] \\
& - \frac{B_2}{4} \frac{d^2 g_2(z)}{dz^2} \left[2 (R_{CCR}^2 - R_f^2) \ln R_m - (R_m^2 - 2 R_{CCR}^2 \ln R_m) \frac{V_{CCR}}{V_m} - 2 (R_{CCR}^2 - R_f^2) \ln R_{CCR} \right. \\
& \quad \left. + (R_{CCR}^2 - 2 R_{CCR}^2 \ln R_{CCR}) \frac{V_{CCR}}{V_m} - 2 R_f^2 \ln R_{CCR} + R_{CCR}^2 \right] \quad (6.53)
\end{aligned}$$

$$\begin{aligned}
D_3 = & -\frac{B_1}{4} \frac{d^2 g_1(z)}{dz^2} \left[2 R_f^2 \ln R_m - (R_m^2 - 2 R_{CCR}^2 \ln R_m) \frac{V_f}{V_m} \right] - \frac{B_2}{4} \frac{d^2 g_2(z)}{dz^2} \\
& \left[2 (R_{CCR}^2 - R_f^2) \ln R_m - (R_m^2 - 2 R_{CCR}^2 \ln R_m) \frac{V_{CCR}}{V_m} \right] \quad (6.54)
\end{aligned}$$

6.3.6 Thermo- elastic equations

The thermoelastic stress–strain relations of the hybrid composite are expressed as:

$$\varepsilon_{zz}^j = \frac{1}{(E^j)_z} [\sigma_{zz}^j - \nu_L^j (\sigma_{rr}^j + \sigma_{\theta\theta}^j)] + \alpha_L^j \Delta T \quad (6.55)$$

$$\varepsilon_{rr}^j = \frac{1}{(E^j)_r} [\sigma_{rr}^j - \nu_T^j (\sigma_{zz}^j + \sigma_{\theta\theta}^j)] + \alpha_T^j \Delta T \quad (6.56)$$

$$\varepsilon_{\theta\theta}^j = \frac{1}{(E^j)_\theta} [\sigma_{\theta\theta}^j - \nu_T^j (\sigma_{zz}^j + \sigma_{rr}^j)] + \alpha_T^j \Delta T \quad (6.57)$$

$$\gamma_{rz}^j = \frac{\tau_{rz}^j}{G_{rz}^j} \quad (6.58)$$

Where superscript j indicates the hybrid composite constituents, i.e., fiber, CCR and matrix. E_z , E_r , G , ν_L , ν_T , α_L and α_T represent the longitudinal elastic modulus, transverse elastic modulus, shear modulus, longitudinal Poisson's ratio, transverse Poisson's ratio, longitudinal CTE and transverse CTE, respectively.

6.3.7 Energy minimization

The two unknown constants B_1 , B_2 and two unknown functions $g_1(z)$ and $g_2(z)$ will be acquired by minimizing the total complementary energy of the multi-scale hybrid composite (HC). The total complementary energy is described as:

$$\Pi_{HC} = U_{HC} + V_{HC} \quad (6.59)$$

where U_{HC} and V_{HC} are the complementary strain energy and the complementary potential energy of hybrid composite, respectively. Since the hybrid composite is free of any tractions and external loads, $V_{HC}=0$. Consequently, the total complementary energy can be stated as:

$$\begin{aligned} \Pi_{HC} &= \iiint_{V_i} \frac{1}{2} \boldsymbol{\tau}_{ij} \boldsymbol{\varepsilon}_{ij} dv \quad (t = f, m, CCR) \\ &= \iiint_{V_i} \left(\frac{1}{2} \sigma_{zz}^t \varepsilon_{zz}^t + \frac{1}{2} \sigma_{rr}^t \varepsilon_{rr}^t + \frac{1}{2} \sigma_{\theta\theta}^t \varepsilon_{\theta\theta}^t + \tau_{rz}^t \varepsilon_{rz}^t \right) r dr d\theta dz \end{aligned} \quad (6.60)$$

It should be mentioned that for axial symmetry, $\tau_{r\theta} = \tau_{\theta z} = 0$. The total energy of hybrid composite expressed in Eq (6.60) has 12 terms consisting of axial, radial, hoop and shear stresses for all three domains as fiber, CCR and matrix. The integrations of axial, radial and shear terms of the CCR in Eq (6.60) are calculated in the Appendix D. For sake of conciseness, the integration of matrix and fiber phases are excluded since they possess the same procedures to CCR.

Having obtained the function $D_1(z)$, $D_2(z)$ and $D_3(z)$ by satisfying boundary and continuity conditions, they are then embedded into Eqs (6.43), (6.45) and (6.48) in order to acquire the radial and tangential stresses.

Eventually, by incorporating Eqs (6.36), (6.37), (6.41), (6.43) and (6.44)- (6.48) and the thermo-elastic Eqs (6.55)- (6.58) into Eq (6.60), the total complementary energy is established.

Implementing the integration of total complementary energy with respect to r and θ engenders an integral function in terms of two unknown functions $g_1(z)$ and $g_2(z)$ and their derivatives, and two unknown constants B_1 and B_2 [232]:

$$\Pi_{HC} = 2\pi \int_{-L/2}^{L/2} F [B_1, B_2, g_1(z), g_1'(z), g_1''(z), g_2(z), g_2'(z), g_2''(z)] dz \quad (6.61)$$

Invoking the calculus of variation, the Euler–Lagrange equation is expressed as:

$$\begin{aligned}
-\frac{d^2}{dz^2}\left(\frac{\partial F}{\partial g_1''(z)}\right) + \frac{d}{dz}\left(\frac{\partial F}{\partial g_1'(z)}\right) - \frac{\partial F}{\partial g_1(z)} &= 0 \\
-\frac{d^2}{dz^2}\left(\frac{\partial F}{\partial g_2''(z)}\right) + \frac{d}{dz}\left(\frac{\partial F}{\partial g_2'(z)}\right) - \frac{\partial F}{\partial g_2(z)} &= 0
\end{aligned} \tag{6.62}$$

After inserting F from Eq (6.61) into Eq (6.62), we have obtained the two coupled fourth-order ordinary differential equations of multi-scale hybrid composites with respect to $g_1(z)$ and $g_2(z)$ which are:

$$\begin{cases}
B_1^2 A_1 \left(\frac{d^4 g_1(z)}{dz^4} \right) + B_1^2 A_2 \left(\frac{d^2 g_1(z)}{dz^2} \right) + B_1^2 A_3 g_1(z) + \left[B_2 B_1 A_4 \left(\frac{d^4 g_2(z)}{dz^4} \right) + B_2 B_1 A_5 \left(\frac{d^2 g_2(z)}{dz^2} \right) + B_2 B_1 A_6 g_2(z) + B_1 A_7 \right] = 0 \\
B_2^2 A_8 \left(\frac{d^4 g_2(z)}{dz^4} \right) + B_2^2 A_9 \left(\frac{d^2 g_2(z)}{dz^2} \right) + B_2^2 A_{10} g_2(z) + \left[B_2 B_1 A_{11} \left(\frac{d^4 g_1(z)}{dz^4} \right) + B_2 B_1 A_{12} \left(\frac{d^2 g_1(z)}{dz^2} \right) + B_2 B_1 A_{13} g_1(z) + B_2 A_{13} \right] = 0
\end{cases} \tag{6.63}$$

Due to the complexity, the mathematical software Maple 2019 [263] is utilized to solve the equations. The coefficients A_1 - A_{13} signify the functions of materials and geometry properties of CNT-coated CF hybrid composite obtained by Maple 2019. These coefficients are excluded from the thesis since they are too lengthy expressions. By solving the aforementioned equations, eight unknown constants emerge in $g_1(z)$ and $g_2(z)$, which are obtained by applying the boundary condition expressed in the section 6.3.5 (eight boundary conditions). However, two unknown constants B_1 and B_2 still appear in Eq (6.63). By replacing the solutions achieved for $g_1(z)$ and $g_2(z)$ and their derivatives into Eq (6.61) and integrating with respect to z , the total complementary energy is attained in terms of B_1 and B_2 . Through minimizing this equation, a set of linear equations is established and the unknown constants B_1 and B_2 are finally defined.

$$\begin{aligned}
\frac{d\Pi_{HC}}{dB_1} &= 0 \\
\frac{d\Pi_{HC}}{dB_2} &= 0
\end{aligned} \tag{6.64}$$

By substituting the $g_1(z)$, $g_2(z)$, B_1 and B_2 into equations (6.41) – (6.48), the distributions of the interfacial thermal residual stresses are obtained in the constituents of the hybrid composite including fiber, CCR and matrix. The present

work is validated with close agreement by multi-scale finite element modeling (see Figure 6.6) proposed by Malekimoghadam and Icardi [178] for randomly oriented CNTs as displayed in Figure 6.7.

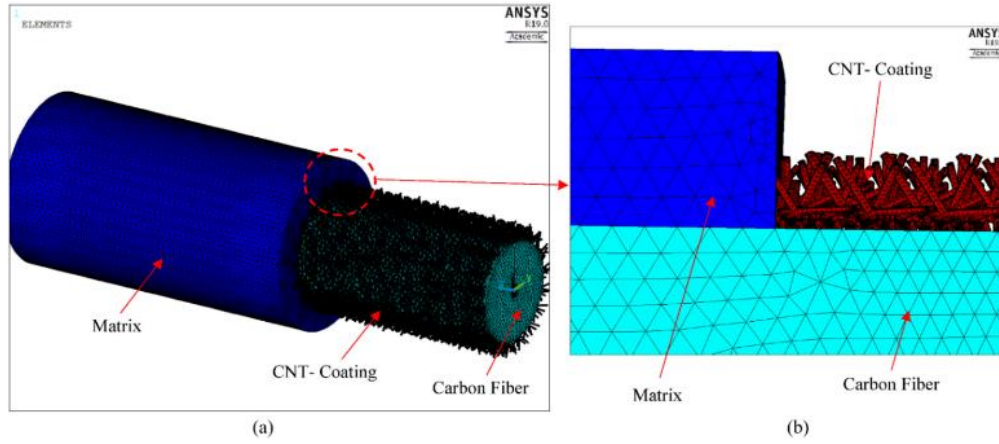


Figure 6.6: Multi-scale Finite element model (a) CNT–Carbon Fiber hybrid composite (b) Cut-view [179]

6.4 Result and Discussion

In this section the influence of CNTs coating on the carbon fiber surface is assessed on the distributions of thermal residual interfacial stresses. Subsequently, a parametric study is conducted based on the different effective parameters at each scale such as CNTs' orientations, CNT volume fraction and coating thickness. Having acquired the stresses distributions, the results are then compared with the residual stress in the conventional composites implemented by Quek [241] and verified with multi-scale finite element modeling [178]. The properties of carbon fiber [220] [221] and polymer matrix [264] are presented in Table 6.2. It should be mentioned the radius of the carbon fiber is considered as $3.5 \mu\text{m}$ [242].

Material	E_z [GPa]	E_x, E_y [GPa]	G_{xz}, G_{yz} [GPa]	G_{xy} [GPa]	ν_{xz}	ν_{xy}	CTE_z [$10^{-6}/^\circ\text{C}$]	CTE_r [$10^{-6}/^\circ\text{C}$]
Carbon Fiber	230	28.7	25	7	0.3	0.42	1.1	6.8
Epoxy	4.20	-	-	-	0.31	-	60	-

Table 6.2: Elastic Properties of Carbon Fiber and Polymer Matrix [220] [221] [264]

Given that the maximum interfacial stresses play the most crucial roles in debonding between fiber and matrix and failure of composite structures, applying the CNTs coating on the core fiber will reduce the interfacial stresses. Introducing the CNTs at the coating region represents relatively small and shallow debonding areas at the connection between the fiber and the CCR than the debonding area at fiber-matrix interface in the composite without fiber coating [187]. Furthermore, the

above-mentioned issue indicates that the CNTs have a higher adhesion force with the matrix and debonding will take place between fiber and coating region which reveals that fracture mode of carbon fiber–matrix composites is affected by CNT deposition [187]. The distributions of thermal residual stresses of multi-scale hybrid composite for RNCCR are represented in Figure 6.7. It should be mentioned that in all figures the radial and axial interfacial residual stresses are obtained at the fiber-CCR interface. Furthermore, the stresses are normalized by the interfacial stresses of fiber-matrix composite (without coating) developed by Quek [241]. The normalized length in all figures is acquired by (z/l) , in which z is the longitudinal position along the fiber axis and l denotes the length of fiber. It can be inferred from Figure 6.7 that growth of solely 1wt.% of randomly oriented CNTs on the surface of carbon fiber markedly reduces the residual interfacial shear and radial stresses by 27% and 21%, respectively, assuming the temperature variation (ΔT) of 50 K and coating thickness of 900 nm. It is also worth mentioning that by increasing the CNTs content in the CCR by 2 wt.%, the coating stiffness increases which leads to reduction of interfacial stresses. According to experimental investigation [227], about 21% reduction of the maximum interfacial stress was acquired by adding a small portion of multi-walled CNTs. It should be noted that the maximum interfacial shear and radial stresses in the finite element modeling are 5.8% and 4.9% higher than the analytical approach proposed in the present work, respectively. The foregoing issue is ascribed to the direct presence of debonding damage between CNTs and matrix in the FEM work, whereas in the present work the effect of interphase is taken into account indirectly, using the equivalent continuum approach introduced in section 6.2.1. More details of the influence of debonding damages on the interfacial stresses can be found in Ref [178]. Likewise, the result of the residual interfacial shear and radial stresses of conventional fiber reinforced composites considering perfect bond between fiber and matrix, performed by Quek [241], is inserted in Figure 6.7 as the upper bound criteria. As expected, the maximum value of interfacial shear and radial stresses occur in contiguity of the fiber end and exactly at the fiber end, respectively.

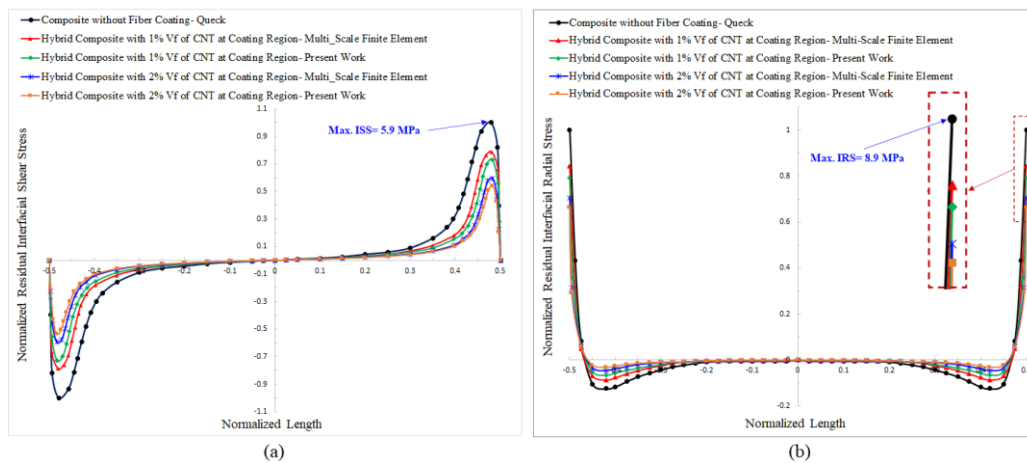


Figure 6.7: Distribution of thermal residual interfacial stresses of hybrid composite, with coating thickness of 900 nm and $\Delta T = 50$ K (a) Shear stress (b) Radial stress [179]

In addition to the position of maximum stress, the amount of peak shear stress is of great importance since the debonding between fiber and matrix will ensue if the maximum interfacial stress transgresses the interfacial strength. Consequently, due to coating the core fiber with nanomaterials, the advanced multi-scale hybrid composites will represent strikingly lower interfacial residual thermal stresses which improve the performance of composite structures under different temperature gradient conditions.

Including various configurations of CNTs at the coating region, namely, RCCR, RNCCR and ACCR, the thermal residual interfacial stresses of CNT–CF multi-scale hybrid composite are depicted in Figure 6.8 considering a coating thickness of 900 nm and $\Delta T = 50$ K. The results disclose that the configuration of CNTs at the coating region not only affects the mechanical properties of the coating medium, but also leads to significant difference of interfacial stresses which consequently varies the load transferring between fiber and matrix.

As it is described, ACCR and RCCR demonstrate the highest and lowest contribution towards reduction of thermal residual interfacial stresses, respectively, while the multi-scale hybrid composite with RNCCR represents reinforcement magnitude between the two aforementioned configurations. It is noteworthy to indicate that the models containing ACCR can make a valuable contribution to the reduction of residual interfacial shear and radial stresses under thermal loading. Furthermore, by introducing RCCR and RNCCR on the fiber surface, the residual interfacial shear stresses decrease by 7% and 27%, respectively, in comparison with a composite without fiber coating. Thus, the multi-scale hybrid composite comprising RNCCR exhibits much improved interfacial properties than that with RCCR which reveals the slight influence of radially grown CNTs at coating region on the interfacial properties. Consequently, it can be postulated that by aligning the CNTs at coating region along the axial direction of core fiber, the minimum interfacial stresses can be achieved which weaken the effect of mismatch between the CTEs of fiber and matrix under thermal loading. Interestingly, by employing the single-fiber fragmentation test, Sager et. al [228] demonstrated that randomly oriented and radially oriented MWCNT coated fibers augment the interfacial shear strength by 71% and 11%, respectively, which reaffirm the pronounced effect of randomly oriented CNTs on the fiber coating.

It should be asserted that two methods could be considered regarding the production of multi-scale hybrid composites, namely mixing CNTs entirely throughout the matrix and depositing CNTs on core fibers (fiber coating). Taking into account the similar CNT volume fraction, the former makes negligible influence on reduction of the interfacial stresses between fiber and matrix, while the latter provides graded interphase (coating region) around core fiber with diminishing effect

on the interfacial stresses [173] [178] [188]. It should be mentioned, if the graded interphase is considered for improving the interfacial properties, gradual gradation will occur instead of steep gradation which is the key issue in attenuating CTE mismatch between fiber and matrix.

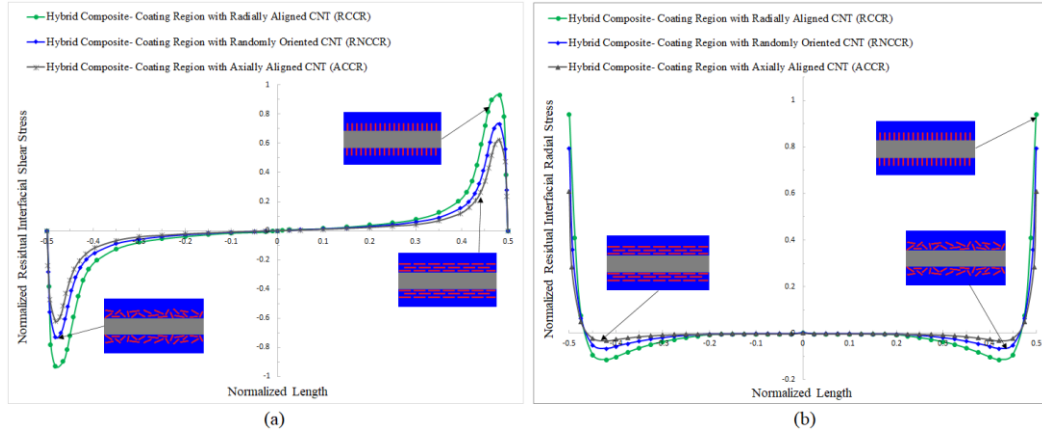


Figure 6.8: Distribution of thermal residual interfacial stresses of hybrid composite considering different CNT's orientations at coating region and $\Delta T = 50$ K (a) Shear stress (b) Radial stress [179]

As one of the crucial parameters in the fiber coating, the effect of coating thickness on the residual interfacial stresses and fiber axial stress is displayed in Figure 6.9 for $\Delta T = 100$ K. Different coating thicknesses around core fiber in the range of 300-1000 nm are usually obtained [201]. However, the thickness of CNT-coating around carbon fiber is demonstrated to be a function of CNT growth time and temperature in CVD technique, and it is difficult to determine the exact value since it varies in different specimens due to the parameters during growing of CNTs [202]. Moderately thick coating regions up to 2- 3 μm at specific reaction time and temperature are also reported [265] [266]. Moreover, some studies [178] demonstrated that the quality and quantity of depositing nanomaterials on the carbon fiber were increased and improved by introducing the ultrasonic during the electrophoresis deposition (EPD) process.

Our models which their results are represented in Figure 6.9 encompass CCR thicknesses of 500 nm, 700 nm, 900 nm and 1.1 μm with the same CNT volume fraction to scrutinize the effect of mere coating thickness on the residual stresses.

Our results indicate that increasing the coating thickness around carbon fiber leads towards the reduction of residual interfacial shear (Figure 6.9 a) and radial (Figure 6.9 b) stresses as well as the fiber axial stress (Figure 6.9 c). Even the lowest coating thickness (green curves) decrease the residual stresses remarkably in comparison with the case without coating (gray curves). However, it is observed that the rate of such diminishing effect on residual stresses reduces slightly as the coating thickness enlarges. Moreover, it is manifested from Figure 6.9 c that the maximum axial stress of fiber occurs at the mid-span, remains almost constant over 80% of the fiber length (slight differences for various coating thicknesses), and plummets near

the end of the carbon fiber. Notwithstanding the small portion of CNT at the coating region with a thickness of $1.1\mu\text{m}$, the residual interfacial shear and radial stresses and fiber axial stress drop by 39.6 %, 32.8 % and 19.6 %, respectively.

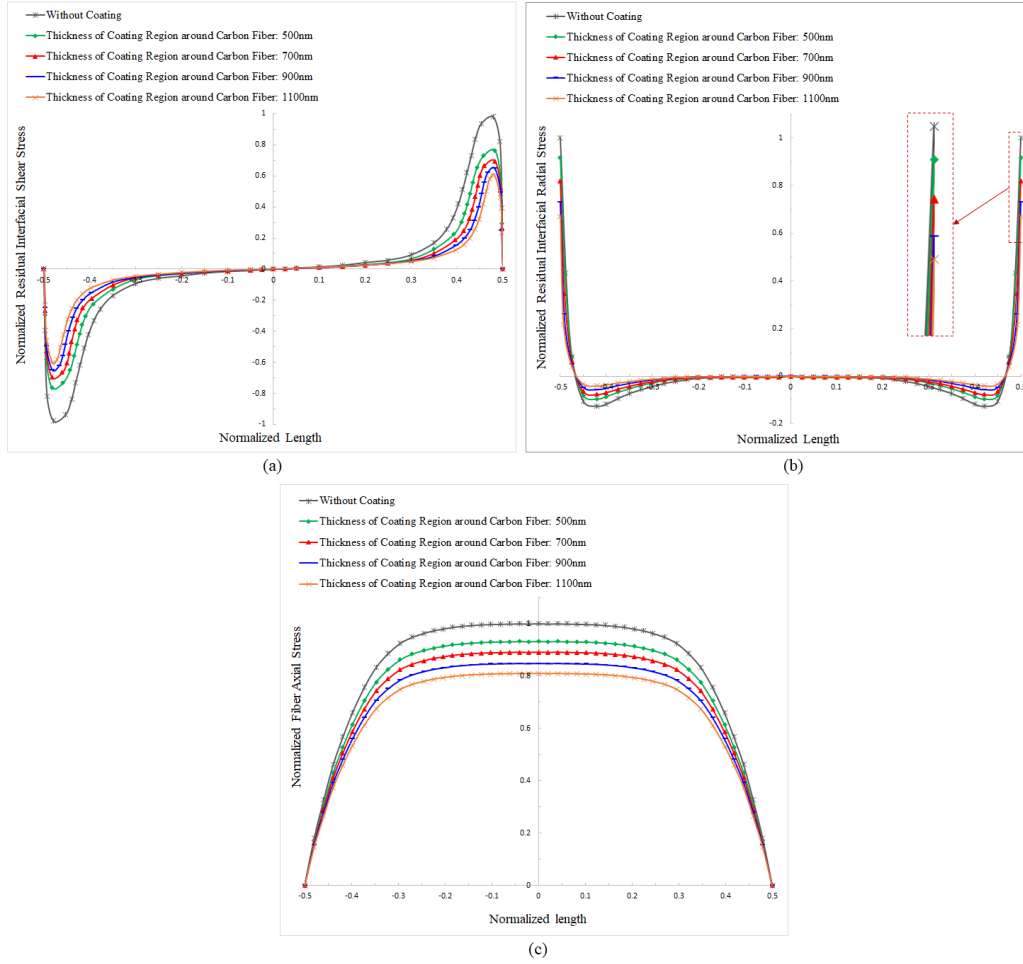


Figure 6.9: Distribution of thermal residual interfacial stresses of hybrid composite at different coating thickness and $\Delta T = 100\text{ K}$ (a) Shear stress (b) Radial stress (c) Fiber axial stress [179]

Figure 6.10 describes the influence of temperature variations magnitude (ΔT) on the residual interfacial stresses and axial fiber stress for a hybrid composite with $1\mu\text{m}$ thickness of RNCCR. The results indicate that the distributions of stresses for different ΔT s are analogous, and their magnitude increases with elevating ΔT . The minimizing effect of coating on the thermal residual stresses, however, is more effective for higher magnitudes of ΔT . According to Figure 6.10 a, RNCCR reduces the maximum residual shear stress by 29.1 % and 37.6 % for $\Delta T = 50\text{ K}$ and $\Delta T = 100\text{ K}$, respectively. Likewise, utilizing fiber coating leads to decrease of fiber axial stress by 14.2 % and 18.1 % for $\Delta T = 50\text{ K}$ and $\Delta T = 100\text{ K}$, respectively (see Figure 6.10 c), which indicates that the coating medium around core fiber makes a notable contribution towards decreasing the interfacial stresses and therefore load transferring phenomenon between fiber and matrix.

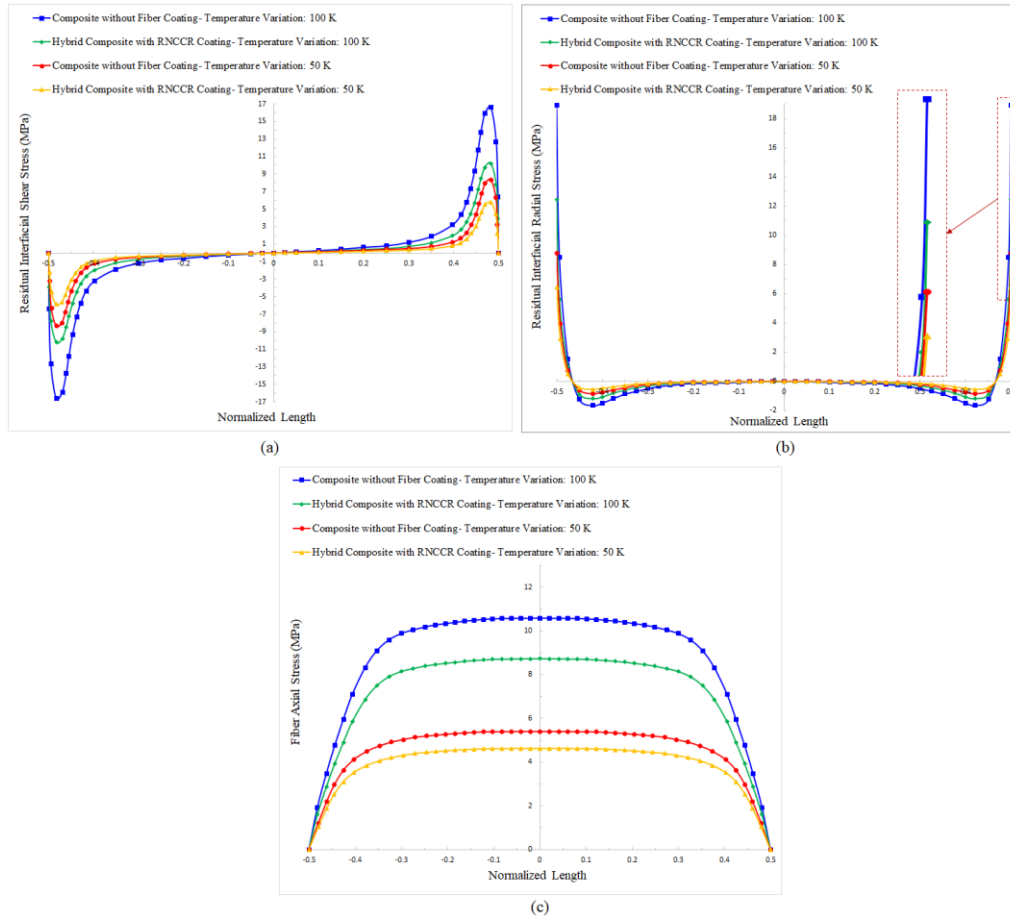


Figure 6.10: Distribution of thermal residual interfacial stresses of hybrid composite at different temperature variations (a) Shear stress (b) Radial stress (c) Fiber axial stress with coating thickness of 1 μm [179]

Figure 6.11 illustrates simultaneously the influence of various coating types (RCCR, RNCCR and ACCR) with different thicknesses on maximum interfacial shear and radial stresses and fiber axial stress, for 1% volume fraction (V_f) of CNTs at each coating region and $\Delta T = 100\text{ K}$. The maximum stresses are normalized by the maximum stresses of composite without fiber coating. A glance at the figures provided shows the extraordinary influence of coating with ACCR and RNCCR in which by increasing the coating thickness, the maximum interfacial stresses fall gradually. In contrast, RCCR exhibits low contribution to the reduction of maximum interfacial stresses and fiber axial stress, even for high coating thicknesses. According to Figure 6.11, a considerable reduction of 23.8%, 30%, 35.1% and 39.5% is gained in maximum residual interfacial shear stress of hybrid composites with RNCCR thicknesses of 0.5 μm , 0.7 μm , 0.9 μm and 1.1 μm , respectively. Similarly, their interfacial radial stress falls remarkably in comparison with composites without coatings, although the reducing rate is slightly lower than residual interfacial shear stress. The fiber axial stress, however, is the lowest influenced stress in the case of RNCCR, with decrease percentages of 6.8%, 11%, 15.3% and 20.1% for the aforementioned coating thicknesses.

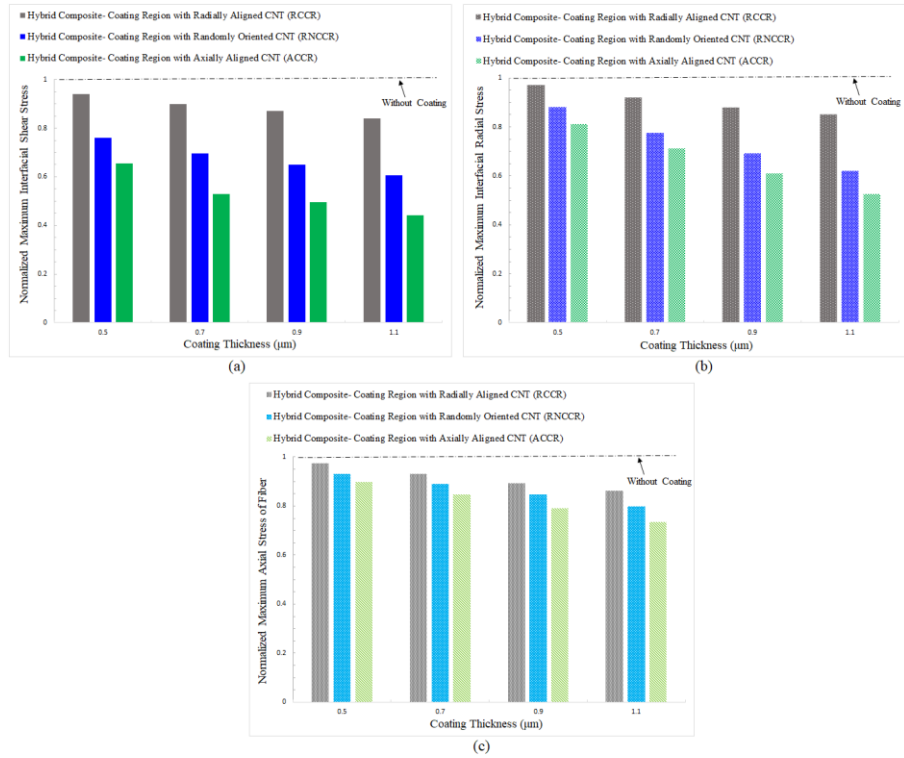


Figure 6.11: Normalized maximum stresses versus different coating thicknesses & CNTs orientations (a) Interfacial shear stress (b) Interfacial radial stress (c) Fiber axial stress [179]

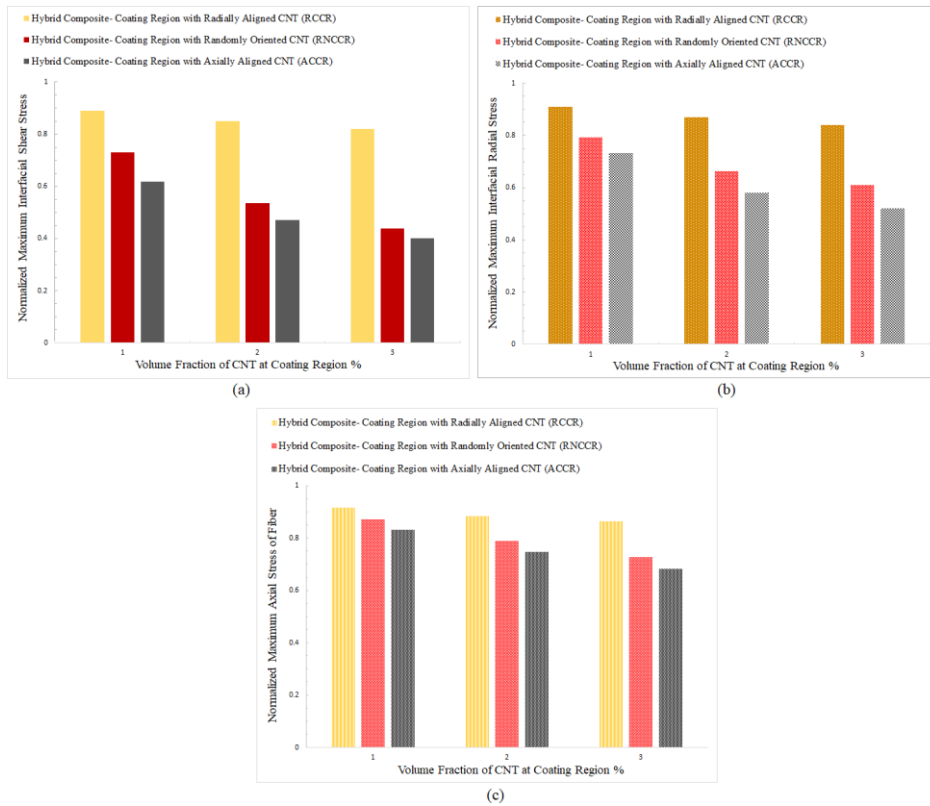


Figure 6.12: Normalized maximum stresses versus different CNT volume fractions & CNTs orientations (a) Interfacial Shear stress (b) Interfacial radial stress (c) Fiber axial stress [179]

Figure 6.12 portrays simultaneously the effect of the coating types and CNT volume fractions on the maximum interfacial shear and radial stresses and maximum fiber axial stress, for a coating thickness of 900 nm and $\Delta T = 50$ K. The hybrid composite models containing RNCCR, and ACCR demonstrate noteworthy improvement on the interfacial properties (Figure 6.12a-b) and fiber axial stress (Figure 6.12c) while RCCR makes a trivial contribution especially at lower CNT volume fractions. Among the attained stresses, the utmost improvement is acquired in hybrid composite with RNCCR in which the residual interfacial shear stress reduces by 27.2%, 47.3% and 55.4% for CNT volume fractions of 1%, 2% and 3%, respectively. Moreover, taking into account 1%, 2% and 3% of CNT volume fractions yields considerable decrease of fiber axial stress as 13%, 21% and 27.2%, respectively.

6.5 Conclusion

By way of conclusion, this chapter is allocated to scrutinize the influence of carbon nanotube-coated carbon fibers on the thermal residual stresses of multi-scale hybrid composites. The established model includes unidirectional carbon fiber, coating region and surrounding matrix, in which the coating region around core fiber encompasses CNT and the polymer matrix. Three types of coating regions are considered around carbon fiber based on the three different configurations of grown CNTs on the fiber surface comprising axially, radially, and randomly oriented CNTs. Employing the Eshelby–Mori–Tanaka method in conjunction with an equivalent continuum approach, the mechanical properties of three different coating regions are acquired. Consequently, the closed-form solution of the thermal residual stresses of multi-scale hybrid composite is attained utilizing the total complementary energy minimization method. The results reveal an extraordinary decrease in the residual interfacial shear and radial stresses by 27% and 21%, respectively, in the hybrid composite with a coating region consisting of solely 1wt. % of randomly oriented CNTs. Significantly, the mentioned reduction of the interfacial residual stresses not only precludes the debonding between the fiber and matrix, but also attenuates the effect of coefficient of thermal expansions mismatch between the carbon fiber and surrounding matrix. Furthermore, the results manifest a noticeable reduction of interfacial shear stress in the models with coating region comprising axially (ACCR) and randomly oriented CNTs (RNCCR) by 36.5% and 27%, respectively, whereas coating region with radially oriented CNTs make a slight contribution. Likewise, it is disclosed that increasing the coating thickness reduces the maximum interfacial shear stress, radial stress, and fiber axial stress by 39.6 %, 32.8 % and 19.6 %, respectively, considering coating thickness of 1.1 μm and small portion of CNTs at coating region.

Chapter 7: Bending Analysis of CNT Coated–Fiber Multi-Scale Composite (CFMC) Beams Using the Refined Zigzag Theory (RZT)

Abstract: This chapter provides a novel method regarding stress analysis of multi-scale hybrid composites and is based on the author's paper during PhD program [267]. This chapter aims to investigate the bending analysis of sandwich and laminated carbon nanotube coated–fiber multi-scale composite (CFMC) beams employing the Refined Zigzag theory (RZT). The model encompasses core fiber, surrounding carbon nanotube (CNT) coating region and polymer matrix covering all scales from nano to macro-scale. The CNT coating region (CCR) consists of CNT, matrix, and non-bonded interphase that its mechanical properties with core fiber are computed utilizing the Eshelby–Mori–Tanaka method and composite cylinder assemblage (CCA) in conjunction with an equivalent continuum approach. Considering different configurations of grown CNTs around the core fiber, two CCRs are constructed comprising axially aligned and randomly oriented CCRs. Utilizing the RZT, four kinematic variables are obtained for CFMC beams and the effect of CNT volume fraction, coating thickness and coating types are thoroughly investigated for various laminated and sandwich beams. The results reveal a remarkable reduction in the transverse displacements of CFMC beams with respect to conventional composite beams. Moreover, by employing a combination of ACCR and RNCCR for the layers in the sandwich CFMC beams, a pronounced decrease is demonstrated in the transverse shear stress of the core medium which can postpone the core shear failure in the sandwich structures.

7.1 Introduction

Recently, the area of multi-scale hybrid composites has received remarkable interest by the engineering community because of its superior and unique structural and mechanical properties than conventional composites. After breakthrough of carbon nanotubes (CNTs) and nano-particles, as a coating phase in the multi-scale hybrid composites, a novel research sphere has burgeoned among scientists because of their unique properties [77] [134] [149] [140] [115]. It has been demonstrated that dispersion of a few portion of carbon nanotubes in a matrix, increase remarkably the mechanical properties of composite materials [244]. Having implemented various experimental tests, noticeable growth in the mechanical properties of neat polymers

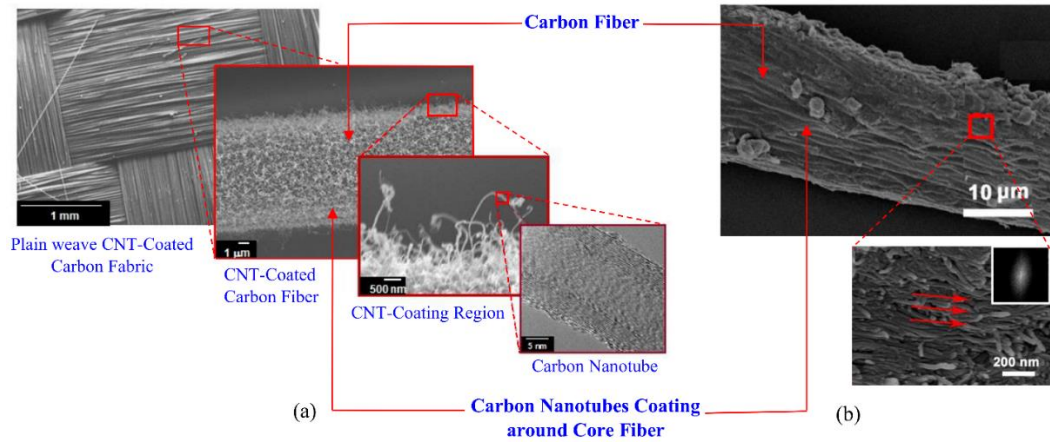
have been reported in the literatures by incorporating 1–5% weight fractions of CNTs [268] [269]. In addition, by grafting CNTs on core fibers, the CNT-coated multi-scale hybrid composites are being developed due to their outstanding behaviors in obviating cardinal drawbacks of conventional composites regarding interfacial and interlaminar properties, by altering the fiber-matrix interface [12] [270]. Due to the type of nanomaterials and fabricating process, the improvement levels vary significantly [172], for example, for the fiber/matrix interfacial strength (IFS) the increase is in the range of 28%–175% [271]. Malekimoghadam and Icardi carried out a thorough investigation on the interfacial strength and thermal residual stresses of CNT coated- carbon fiber multi-scale composites through finite element analysis and energy minimization method, respectively [178] [179]. Yao et al. [186] reported a significant enhancement of interfacial shear strength (IFSS) and interlaminar shear strength (ILSS) by 89.4% and 58.6%, respectively. As another drawback of unidirectional fiber reinforced composites, premature failure occurs ascribed to the low mechanical properties in the transverse direction to the fiber that can be overcome by presence CNT coated-fibers [272] [203]. Regarding the experimental methods, some studies have been accomplished to investigate the mechanical, thermal, and electrical properties and health monitoring applications of fuzzy fiber reinforced hybrid composites [273] [19]. Garcia and his co-worker conducted a survey on the morphology control of vertical aligned CNTs between the layers and improving the interlaminar strength of prepreg unidirectional carbon tape composites by exploiting the bridging effect of aligned CNTs [192] [274]. From multi-scale modeling point of view, some analytical investigations have been conducted to attain the mechanical properties, however, due to novelty and complexity of such nano-engineered multi-scale materials, there still exist many aspects which should be clarified and characterized unambiguously [275] [276] [277] [278]. Kulkarni et al. [205] performed finite element analysis accompanied with experimental tests to acquire the mechanical properties of CNT-CF hybrid composites. Considering CNT-CF as a homogeneous solid cylinder model with larger diameter, it was determined that multiscale modeling can be effectively used to study nano-reinforced laminated composites. Various analytical approaches have been utilized to scrutinize the mechanical properties of fuzzy fiber hybrid composites with their advantages and limitations, however, there is still lack of an accurate and efficient procedure for stress analysis. Proposing a micromechanical approach aimed at identifying the response of unidirectional fuzzy fiber composites, Chatzigeorgiou and co-workers [240] [279] [280] obtained the elastic moduli using the asymptotic expansion homogenization (AEH) method and Transformation Field Analysis (TFA) technique. Utilizing shear lag method, Kundalwal and collaborators [239] [281] studied the thermomechanical properties and load transfer characteristics of the short fuzzy fiber reinforced composite. A new refined ‘zigzag’ theory (RZT) for conventional laminated-composite and sandwich beams and plates exhibiting a high degree of transverse shear flexibility has been presented by Tessler and collaborators [282] [283] [284]. Comparisons with the results obtained from exact two-

dimensional elasticity analyses, high-fidelity finite element analyses, and other beam theories demonstrated that the RZT provides highly accurate predictions of displacements, stresses, and force resultants. Adopting the mixed Refined Zigzag Theory (RZT (m)), Gherlone [285] [286] developed and assessed a class of plate finite elements for the analysis of multilayered composite and sandwich structures. Ascione and Gherlone [287] proposed a new model based on the Refined Zigzag Theory (RZT) formulation that includes geometric nonlinearities for buckling, post-buckling, and nonlinear static response analyses of geometrically imperfect composite beams with piezoelectric actuators. To the best of the authors' knowledge, there is still marked lack of a comprehensive, efficient, and straightforward method to model and stress analysis of CNT coated- fiber multi-scale composites. To this end, the present work furnishes a thorough analytical technique encompassing multi-scale modeling and bending stress analysis in which the former comprises the effective parameters spanning over different length scales from nano- to macro-scale whereas the latter is conducted through the Refined Zigzag Theory (RZT). The hierarchical multi-scale modeling is performed utilizing the Eshelby–Mori–Tanaka method and composite cylinder assemblage (CCA) in conjunction with an equivalent continuum approach. Developing a Maple code for both modeling and stress analysis, therefore, four RZT kinematic variables are acquired for CNT coated- fiber multiscale composite beam which is capable of applying parametric study in terms of CNT volume fraction, coating thickness, CNT orientation in the coating region and material and volume fraction of core fiber. A great agreement is exhibited between predicted results by the proposed analytical method and the results obtained from the finite element analysis.

7.2 Framework of Modeling Procedure of CNT Coated–Fiber Multi-Scale Composites

The stress transfer from matrix to fibers is of crucial importance in composite structures. Nanomaterials deposited on microscopic fibers can positively contribute by several ways such as roughening the fiber surface, reducing the stress transfer length (i.e., reduction of the critical aspect ratio of the fiber), and stress redistribution via graded micro-interphase by diminishing stress concentration effects. In fact, stress field homogenization/reducing stress concentration seems to be the main mechanism observed in composites with micro- and nano-fillers [170] [288]. There are different techniques for grafting CNTs on the surface of carbon fiber such as dip coating (as the easiest and cheapest approach), chemical vapor deposition (CVD), electrophoresis and electrospray method which have their own pros and cons [243] [187]. The morphology of CNTs on the core fibers is controlled by tuning coating catalyst, growth process conditions, etc. [208], by which the fuzzy fiber with different CNT-coating orientations will achieved including random or radial orientation. Furthermore, alternating current (AC) electric field during

nanocomposites curing process is usually utilized to induce the formation of aligned nanotube networks [289].



7.1: (a) Top-down description of plain weave CNT coated-carbon fabric with randomly oriented CNTs on the fiber [290] (b) Carbon fiber with axially aligned CNT coating; the red arrows indicate the axial direction of the carbon fiber [291]

To conduct the stress analysis of CNT coated-fiber multi-scale composite (CFMC) beam with different types/ morphology of CNT coating regions around the core fiber, axially aligned and randomly oriented CNT coating regions (according to 7.1) are taken into account in this research. Prior to employing RZT, a hierarchical constitutive modelling approach is adopted to acquire the mechanical properties of multi-scale hybrid composite beam. Having obtained the mechanical properties of the layers, the sandwich and laminated CFMC beams are then constructed, and the properties are fed into RZT method for the CFMC beam. A schematic representation of hierarchical multi-scale modeling of the CNT coated-fiber multi-scale composite is depicted in Figure 7.2, accompanied with the effective parameters at each scale.

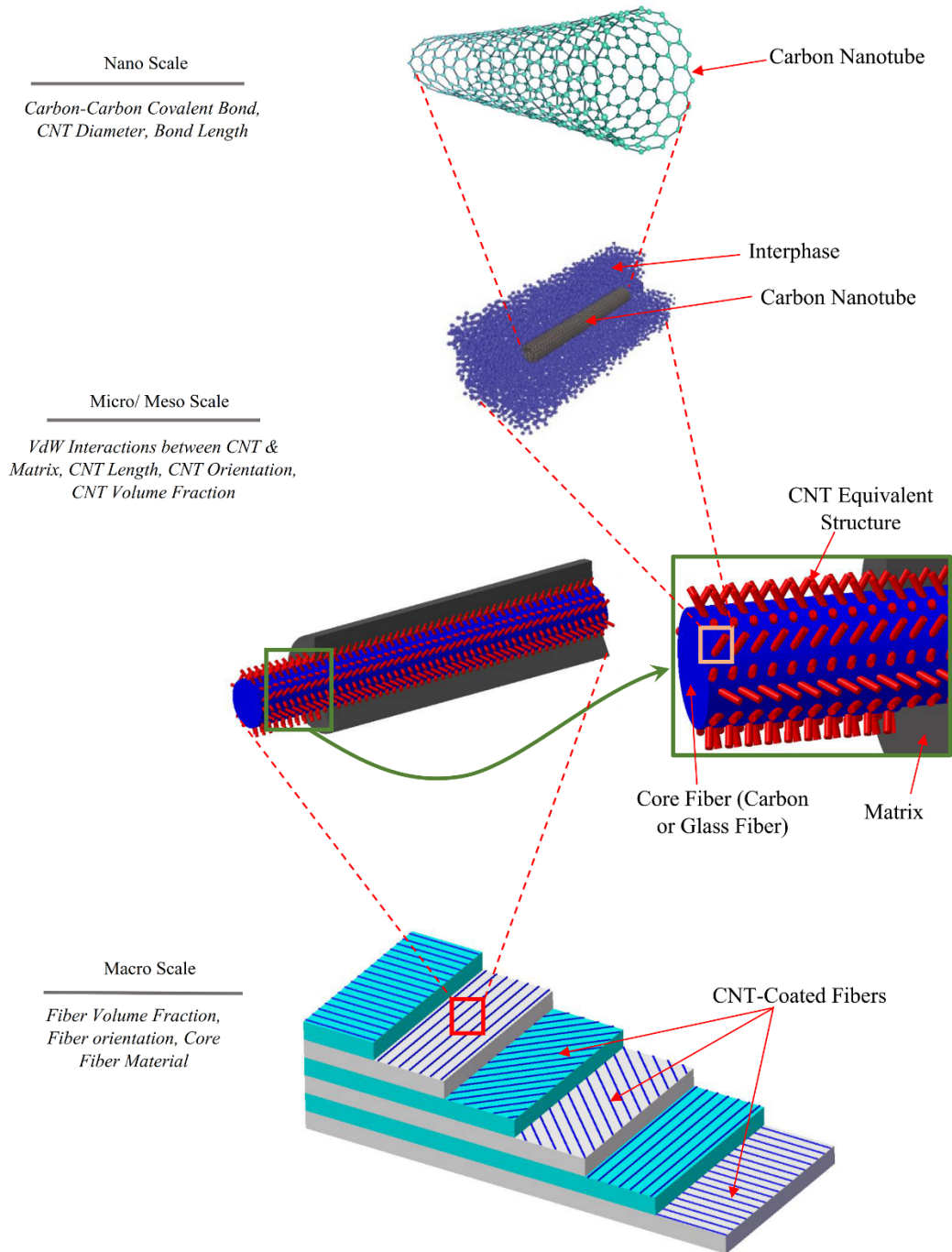


Figure 7.2: The procedure of hierarchical multi-scale modeling of CNT coated– fiber hybrid composites [267]

As it can be seen in the above figure, the ‘CNT coating region’ (henceforth referred to as CCR) encompasses carbon nanotubes and polymer matrix which wrap around core fiber. An appropriate representative volume element (RVE) has been defined at each scale to calculate its effective mechanical properties that are later used as input data for the upper scale. A process flowchart is shown in Figure 7.3, to demonstrate the various analytical approaches utilized at each scale regarding the bending analysis of CFMC beam through RZT method.

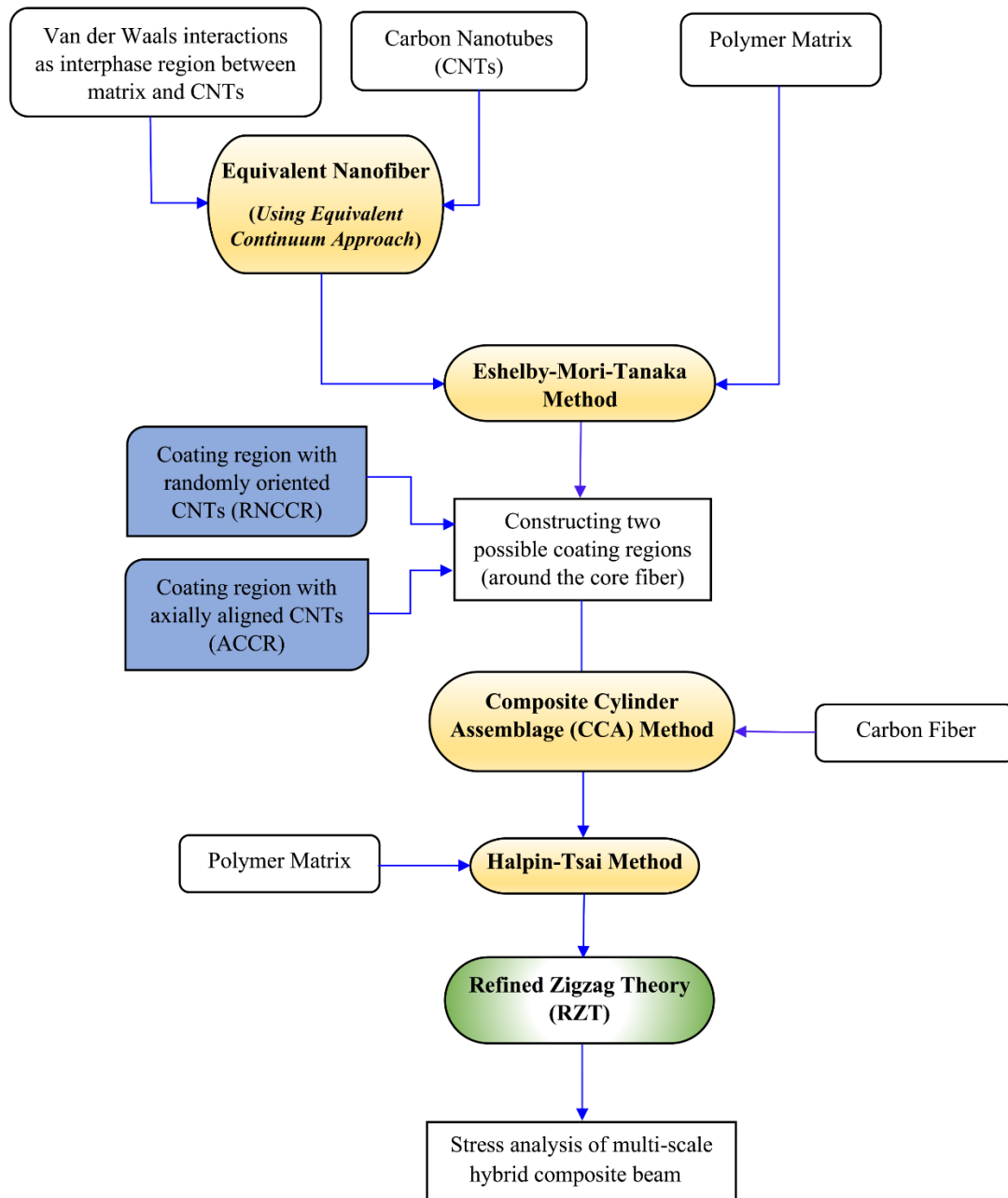


Figure 7.3: Flowchart of stress analysis of CNT coated-fiber composite beam through RZT method [267]

7.2.1 Simulating of Carbon Nanotube (CNTs) with Surrounding Interphase

At the lowest scale, nanoscale, CNTs act as nano-reinforcement agents in the CFMC beams. The modeling procedures of CNT structure are classified in three categories consisting of atomistic modeling, continuum modeling and nano-scale

continuum modeling [94]. Focusing on mechanical, buckling, vibrational and thermal properties, various techniques in the modeling of CNTs were meticulously reviewed and analyzed by Rafiee and Malekimoghadam [77]. Developing a finite element (FE) model of the CNT lattice structure by Li and Chou [91], each C–C bond of the CNT nanostructure is substituted with equivalent beam element in which the geometrical and mechanical properties of the beam element are obtained correlating the interatomic potential energies of molecular space to the strain energies of structural mechanics. Employing equivalent continuum technique [292], the CNT structure with surrounding non-bonded interphase is represented as an equivalent nanofiber (ENF) which is illustrated in Figure 7.4. In this method, a straight CNT embedded in a polymer matrix with non-bonded interphase region is replaced with the developed equivalent nanofiber, in order to predict the mechanical behavior of the CNT/polymer nanocomposite which this nanocomposite medium constructs the coating region around the core fiber in the present work. Then, the mechanical properties of ENF are achievable using multi-scale finite element modeling carried out by Rafiee and Malekimoghadam [97]. It should be mentioned that the governing interactions between CNT and surrounding polymer are weakly non-bonded Van der Waals (vdW) interactions. Therefore, to perform the multi-scale finite element analysis (FEA), the non-bonded interphase region (vdW interaction) is simulated using nonlinear spring elements between CNT atoms and inner surface atoms of the polymer matrix [97]. Figure 7.4-a and b show a representative volume element (RVE) of nanocomposite material constructed at the lower scales (Nano and Micro) consisting of CNT lattice structure, surrounding matrix and vdW interactions between CNT and matrix.

Finally, the mechanical properties of the ENF are obtained by using the results of foregoing technique [97] utilized as input data for the upper scale calculations. It is worth mentioning that the nanocomposite material comprising ENFs and matrix are considered as CCR in the next upper scale and its relevant mechanical properties will be determined by Eshelby–Mori–Tanaka method.

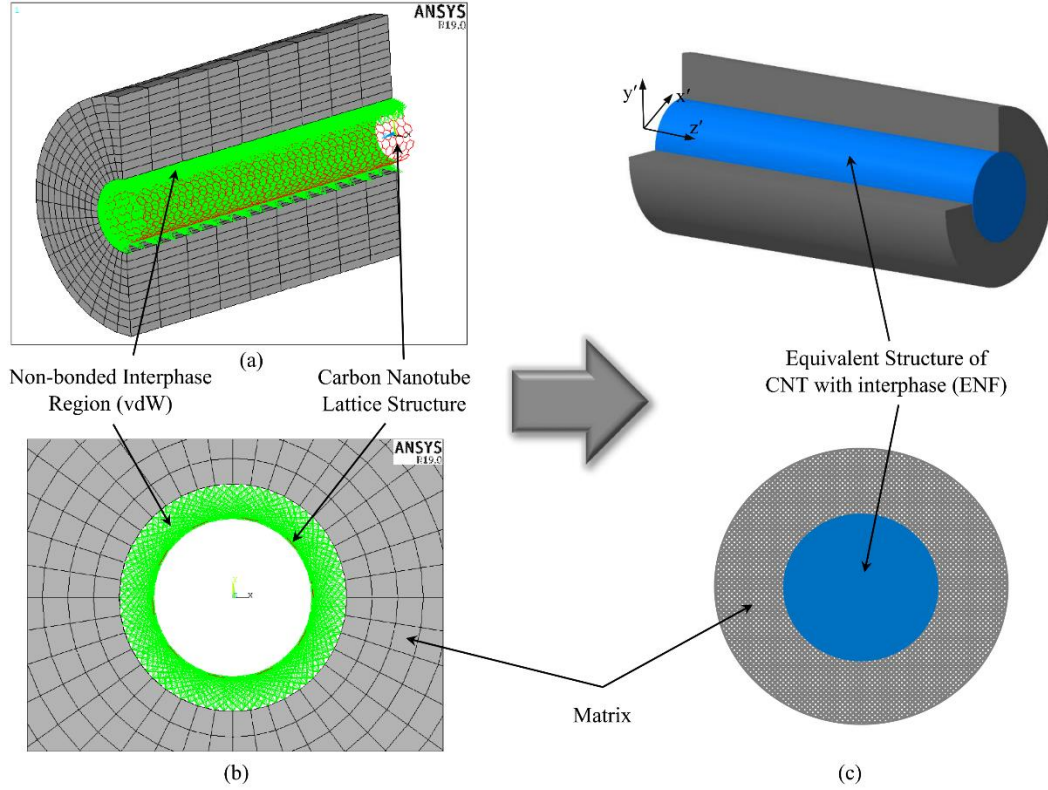


Figure 7.4: Description of equivalent nanofiber (a) Finite element model–Cut view of the RVE, (b) Finite element model–Cross section of the RVE, (c) Schematic of equivalent nanofiber [267]

Hence, the ENF accurately accounts for the structural properties relationships at the nanoscale and provides a bridge to the continuum model. The Hill's elastic moduli [51] [246] of the reinforcing phase, which is CNT in the present work, are defined by equality of the two following matrices of ENF:

$$\mathbf{C}_{ENF} = \begin{pmatrix} n_{ENF} & l_{ENF} & l_{ENF} & 0 & 0 & 0 \\ l_{ENF} & k_{ENF} + m_{ENF} & k_{ENF} - m_{ENF} & 0 & 0 & 0 \\ l_{ENF} & k_{ENF} - m_{ENF} & k_{ENF} + m_{ENF} & 0 & 0 & 0 \\ 0 & 0 & 0 & p_{ENF} & 0 & 0 \\ 0 & 0 & 0 & 0 & m_{ENF} & 0 \\ 0 & 0 & 0 & 0 & 0 & p_{ENF} \end{pmatrix} \quad (7.1)$$

Where k_{ENF} , l_{ENF} , m_{ENF} , n_{ENF} , and p_{ENF} parameters are the Hill's elastic moduli of equivalent nanofiber.

$$\mathbf{C}_{ENF} = \begin{pmatrix} \frac{1}{E_{x'}} & -\frac{\nu_{x'y'}}{E_{x'}} & -\frac{\nu_{x'z'}}{E_{x'}} & 0 & 0 & 0 \\ -\frac{\nu_{y'x'}}{E_{y'}} & \frac{1}{E_{y'}} & -\frac{\nu_{y'z'}}{E_{y'}} & 0 & 0 & 0 \\ -\frac{\nu_{z'x'}}{E_{z'}} & -\frac{\nu_{z'y'}}{E_{z'}} & \frac{1}{E_{z'}} & 0 & 0 & 0 \\ 0 & 0 & 0 & \frac{1}{G_{x'z'}} & 0 & 0 \\ 0 & 0 & 0 & 0 & \frac{1}{G_{y'z'}} & 0 \\ 0 & 0 & 0 & 0 & 0 & \frac{2(1+\nu_{x'y'})}{E_{x'}} \end{pmatrix}^{-1} \quad (7.2)$$

Where $\frac{\nu_{z'x'}}{E_{z'}} = \frac{\nu_{x'z'}}{E_{x'}} = \frac{\nu_{z'y'}}{E_{z'}} = \frac{\nu_{y'z'}}{E_{y'}}$ and $E_{x'} = E_{y'}$, $\nu_{x'z'} = \nu_{y'z'}$, $G_{x'z'} = G_{y'z'}$

Since CNT is considered as transversely isotropic material (with axis of symmetry along z'), the stiffness matrix of Eq.(7.2) contains five independent elastic parameters including $E_{z'}$, $E_{x'}$, $G_{x'z'}$, $\nu_{x'y'}$, $\nu_{z'x'}$ which have been already acquired from equivalent continuum modelling technique [97]. It should be mentioned that x' , y' and z' represent local coordinate system at nano and micro scales where z' is placed along longitudinal direction of CNT and x' / y' denote transverse direction of the CNT structures (according to Figure 7.4-c).

Based on the aforementioned approach, the material properties of ENF for an armchair-type single walled CNT with chiral index of (10, 10) are provided in Table 7.1 [122] [205].

Material	Longitudinal Young's modulus	Transverse Young's modulus	Transverse shear modulus	Poisson's ratio (ν_{LT})	Poisson's ratio (ν_{TZ})
Equivalent Nanofiber	649.12 [GPa]	11.27 [GPa]	5.13 [GPa]	0.284	0.14

Table 7.1: Mechanical Properties of Equivalent Nanofiber [122] [205]

7.2.2 Effective Elastic Properties of the CNT Coating Region (CCR)

The CCR contains grown CNTs, and polymer as a nanocomposite material surrounding the core fiber. Two configurations of CCRs are considered in this research based on the CNT orientation in the coating region encompassing ‘axially

aligned' and 'randomly oriented' CCRs (hereafter referred to as ACCR and RNCCR, respectively) as the relevant RVEs (representative volume element) are depicted in Figure 7.5 with the global coordinate system. It should be also pointed out that the CNTs in the ACCR configuration span the full length of the core fiber along its longitudinal direction, whereas in the RNCCR type, the CNTs span the full length in all orientations/ angles inside the coating region.

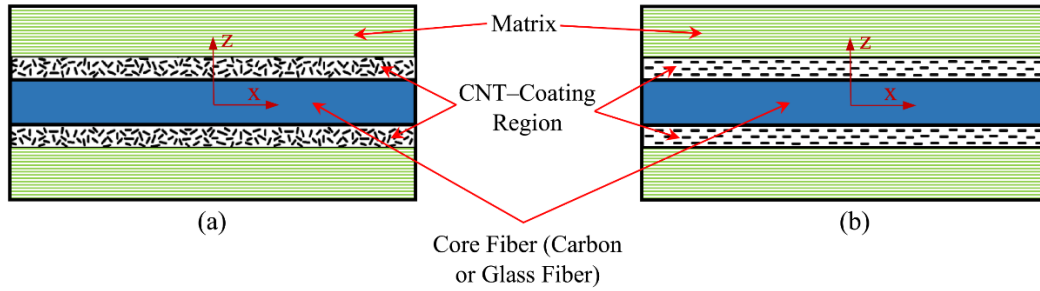


Figure 7.5: RVE representation consisting of two CNT coating regions (a) RNCCR, (b) ACCR [267]

To acquire the effective properties of fiber composites, various micromechanics models including dilute concentration model based on the Eshelby's equivalent inclusion, the self-consistent model, Mori–Tanaka models, the Halpin–Tsai equations and shear lag models were reviewed by Tucker and Liang [247]. For predicting the effective properties of composites, the Mori–Tanaka model has been reported to be the efficient analytical technique [247]. Therefore, the Mori–Tanaka model [222] is employed in the present work to determine the effective elastic properties of CCR which is required as input data for next upper scale. It is worthwhile to note that the details of Mori–Tanaka schemes for different types of inclusions and multi-phase systems have been thoroughly presented in the literature [249] [223]. Employing the Mori–Tanaka method and taking into account the average over orientations of nanofibers, the stiffness tensor of CCR as a nanocomposite medium can be defined [248]. For a two-phase nanocomposite material consisting of CNT and matrix, the effective stiffness tensor of CCR is expressed as [249] [252]:

$$\mathbf{C}_{CCR} = \mathbf{C}_m + V_{ENF} \{ (\mathbf{C}_{ENF} - \mathbf{C}_m) \mathbf{A}_{ENF} \} [V_m \mathbf{I} + V_{ENF} \{ \mathbf{A}_{ENF} \}]^{-1} \quad (7.3)$$

Where V_m and V_{ENF} indicate the volume fractions of matrix and CNT (effective nanofiber) in the coating region, respectively, \mathbf{I} is the fourth-order identity tensor, \mathbf{C}_{CCR} , \mathbf{C}_m and \mathbf{C}_{ENF} are the stiffness tensors of CCR, matrix and equivalent nanofiber (ENF), and \mathbf{A}_{ENF} denotes the dilute mechanical strain concentration tensor of ENF which is described as below. The Curly brackets $\{*\}$ represent an average over all possible orientations.

$$\mathbf{A}_{ENF} = \left[\mathbf{I} + \mathbf{S} (\mathbf{C}_m)^{-1} (\mathbf{C}_{ENF} - \mathbf{C}_m) \right]^{-1} \quad (7.4)$$

Where \mathbf{S} is Eshelby's tensor [250] which is thoroughly elaborated by Mura [251] for various inclusions.

In view of the fact that the properties are different for each type of CNT coating, the stiffness matrices corresponding to ACCR and RNCCR should be individually obtained. By obtaining the mechanical properties of two RVEs comprising different types of CNT coating (see Figure 7.5), the models are established at this scale. It should be reaffirmed that the CNT structure treats as transversely isotropic material whereas the surrounding matrix behaves as an isotropic medium. Consequently, ACCR is transversely isotropic with an axis of symmetry along longitudinal direction of the core fiber (Figure 7.5-b). The stiffness matrix of ACCR in terms of Hill's moduli is given as following:

$$\mathbf{C}_{ACCR} = \begin{pmatrix} k_{ACCR} + m_{ACCR} & l_{ACCR} & k_{ACCR} - m_{ACCR} & 0 & 0 & 0 \\ l_{ACCR} & n_{ACCR} & l_{ACCR} & 0 & 0 & 0 \\ k_{ACCR} - m_{ACCR} & l_{ACCR} & k_{ACCR} + m_{ACCR} & 0 & 0 & 0 \\ 0 & 0 & 0 & p_{ACCR} & 0 & 0 \\ 0 & 0 & 0 & 0 & m_{ACCR} & 0 \\ 0 & 0 & 0 & 0 & 0 & p_{ACCR} \end{pmatrix} \quad (7.5)$$

where k_{ACCR} , l_{ACCR} , m_{ACCR} , n_{ACCR} , and p_{ACCR} are Hill's elastic moduli of ACCR; k_{ACCR} represents the plane-strain bulk modulus normal to the ENF direction, n_{ACCR} denotes the uniaxial tension modulus along the ENF direction, l_{ACCR} indicates the associated cross modulus, and m_{ACCR} and p_{ACCR} state the shear moduli in planes normal and parallel to the ENF direction, respectively. The non-vanishing components of the Eshelby tensor \mathbf{S} and tensor \mathbf{A} are given in Eq. (6.6) and Eq. (6.7), respectively, for a straight ENF with circular cross section and sufficiently large aspect ratio [251].

The Hill's elastic moduli of CNTs have been already acquired in previous section. By replacing the elements of tensor \mathbf{A} into Eq.(7.3), the stiffness tensor of ACCR is obtained. In particular, the Hill's elastic moduli of ACCR are expressed as following [252]:

$$k_{ACCR} = \frac{E_m \{ E_m V_m + 2 k_{ENF} (1 + \nu_m) [1 + V_{ENF} (1 - 2 \nu_m)] \}}{2 (1 + \nu_m) [E_m (1 + V_{ENF} - 2 \nu_m) + 2 V_m k_{ENF} (1 - \nu_m - 2 \nu_m^2)]} \quad (7.6)$$

$$l_{ACCR} = \frac{E_m \{ V_m \nu_m [E_m + 2 k_{ENF} (1 + \nu_m)] + 2 V_{ENF} l_{ENF} (1 - \nu_m^2) \}}{(1 + \nu_m) [2 V_m k_{ENF} (1 - \nu_m - 2 \nu_m^2) + E_m (1 + V_{ENF} - 2 \nu_m)]} \quad (7.7)$$

$$n_{ACCR} = \frac{E_m^2 V_m (1 + V_{ENF} - V_m \nu_m) + 2 V_m V_{ENF} (k_{ENF} n_{ENF} - l_{ENF}^2) (1 + \nu_m)^2 (1 - 2 \nu_m)}{(1 + \nu_m) \{ 2 V_m k_{ENF} (1 - \nu_m - 2 \nu_m^2) + E_m (1 + V_{ENF} - 2 \nu_m) \}} + \frac{E_m [2 V_m^2 k_{ENF} (1 - \nu_m) + V_{ENF} n_{ENF} (1 - 2 \nu_m + V_{ENF}) - 4 V_m l_{ENF} \nu_m]}{2 V_m k_{ENF} (1 - \nu_m - 2 \nu_m^2) + E_m (1 + V_{ENF} - 2 \nu_m)} \quad (7.8)$$

$$p_{ACCR} = \frac{E_m [E_m V_m + 2(1 + V_{ENF}) p_{ENF} (1 + \nu_m)]}{2(1 + \nu_m) [E_m (1 + V_{ENF}) + 2 V_m p_{ENF} (1 + \nu_m)]} \quad (7.9)$$

$$m_{ACCR} = \frac{E_m [E_m V_m + 2 m_{ENF} (1 + \nu_m) (3 + V_{ENF} - 4 \nu_m)]}{2(1 + \nu_m) \{ E_m [V_m + 4 V_{ENF} (1 - \nu_m)] + 2 V_m m_{ENF} (3 - \nu_m - 4 \nu_m^2) \}} \quad (7.10)$$

Making use of Hill's parameters of ACCR, the elastic moduli of ACCR are attained as below, considering the global coordinate system presented in Figure 7.5-b [248] [293]:

$$(E_x)_{ACCR} = n_{ACCR} - \frac{l_{ACCR}^2}{k_{ACCR}} \quad (7.11)$$

$$(E_z)_{ACCR} = \frac{4 m_{ACCR} (k_{ACCR} n_{ACCR} - l_{ACCR}^2)}{k_{ACCR} n_{ACCR} - l_{ACCR}^2 + m_{ACCR} n_{ACCR}} \quad (7.12)$$

$$(\nu_{xz})_{ACCR} = (\nu_{xy})_{ACCR} = \frac{l_{ACCR}}{2 k_{ACCR}} \quad (7.13)$$

$$(\nu_{zy})_{ACCR} = \frac{n_{ACCR} (k_{ACCR} - m_{ACCR}) - (l_{ACCR})^2}{n_{ACCR} (k_{ACCR} + m_{ACCR}) - (l_{ACCR})^2} \quad (7.14)$$

$$(G_{xz})_{ACCR} = (G_{xy})_{ACCR} = p_{ACCR} \quad (7.15)$$

$$(G_{zy})_{ACCR} = m_{ACCR} = \frac{(E_z)_{ACCR}}{2(1 + (\nu_{zy})_{ACCR})} \quad (7.16)$$

$$K_{ACCR} = \frac{(E_z)_{ACCR}}{3(1 - 2(\nu_{zy})_{ACCR})} \quad (7.17)$$

Where $(E_x)_{ACCR}$, $(E_z)_{ACCR}$, $(\nu_{xz})_{ACCR}$, $(\nu_{zy})_{ACCR}$, $(G_{xz})_{ACCR}$, $(G_{zy})_{ACCR}$ and K_{ACCR} indicate longitudinal Young's modulus of ACCR (along axial direction of core fiber shown in Figure 7.5), transverse Young's modulus of ACCR, longitudinal Poisson's ratio of ACCR, transverse Poisson's ratio of ACCR, longitudinal shear modulus of ACCR, transverse shear modulus of ACCR and bulk modulus of ACCR,

respectively. In contrast to ACCR, the CNTs are randomly oriented in different directions in RNCCR type around core fiber (Figure 7.5-a). Thus, RNCCR treats as an isotropic material and its bulk modulus K_{RNCCR} and shear modulus G_{RNCCR} are given as [248]:

$$K_{RNCCR} = K_m + \frac{V_{ENF} (\delta_{ENF} - 3K_m \alpha_{ENF})}{3(V_m + V_{ENF} \alpha_{ENF})} \quad (7.18)$$

$$G_{RNCCR} = G_m + \frac{V_{ENF} (\eta_{ENF} - 2G_m \beta_{ENF})}{2(V_m + V_{ENF} \beta_{ENF})} \quad (7.19)$$

Where V_{ENF} , V_m , K_m and G_m are the volume fraction of nanofiber in the coating region, volume fraction of matrix in the coating region and bulk and shear moduli of matrix, respectively. The parameters α_{ENF} , β_{ENF} , δ_{ENF} and η_{ENF} are given in Appendix C. Finally, the Young's modulus (E_{RNCCR}), Poisson's ratio (ν_{RNCCR}) and bulk modulus of RNCCR are computed as:

$$E_{RNCCR} = \frac{9K_{RNCCR} G_{RNCCR}}{3K_{RNCCR} + G_{RNCCR}} \quad (7.20)$$

$$\nu_{RNCCR} = \frac{3K_{RNCCR} - 2G_{RNCCR}}{6K_{RNCCR} + 2G_{RNCCR}} \quad (7.21)$$

It should be noted that MAPLE 2021 [263] platform has been utilized to calculate the mechanical properties of ACCR and RNCCR which are used as input data for the next upper scale and subsequently for the RZT method.

7.2.3 Modelling of the Core Fiber with Surrounding CCR

At this scale, the core fiber and surrounding CNT coating region (CCR) are considered as two concentric cylinders. Therefore, the mechanical properties of the core fiber with its surrounding CCR are computed by using Composite Cylinder Assemblage (CCA) method developed by Z. Hashin [294] [295]. The mechanical properties of different types of CCR (ACCR and RNCCR) have been already obtained in previous section. Thus, mechanical properties of the core fiber and surrounding CCR are then inserted into CCA formulation to calculate the mechanical properties of the core fiber and CCR as a fuzzy fiber. The obtained properties at this scale are used to acquire the mechanical properties of CFMC composite beam in the next upper scale (macro scale). The mechanical properties of the core fibers (glass or carbon fiber) and polymer matrix are presented in Table 7.2.

Material	E_x [GPa]	E_z, E_y [GPa]	G_{xz}, G_{xy} [GPa]	G_{zy} [GPa]	ν_{xz}	ν_{zy}	Diameter (μm)
Carbon Fiber (IM7)	294	18.5	25	7.1	0.27	0.3	5
S-Glass Fiber	90	-	-	-	0.17	0.17	9
Epoxy (EPIKOTE 862)	3	-	-	-	0.3	0.3	-

Table 7.2: Elastic Properties of IM7 Carbon Fiber, Glass Fiber and Polymer Matrix [14] [296] [297]

Depending on the selected coating region (ACCR or RNCCR), the mechanical properties of the core fiber and surrounding CCR are quantified by the following equations. It should be mentioned that the subscript COF and FC are referred to ‘core fiber’ and ‘fiber with surrounding coating’, respectively. It is worthwhile to indicate that the x, y, and z directions signify the global coordinate system of CCFM composite at macro scale in which “x” is put along longitudinal direction of the core fiber and “z” denotes through-thickness direction (see Figure 7.5). Hence, mechanical properties of FC (fiber with surrounding coating) containing ACCR are computed as below. It is worthwhile to be highlighted that the ACCR region behaves as a transversely isotropic material around core fiber. Recalling from previous section, therefore, five independent elastic constants of ACCR are available to be inserted in the below equations.

$$(E_x)_{FC} \big|_{ACCR} = (E_x)_{ACCR} V_{CCR} + (E_x)_{COF} V_{COF} + \frac{4((\nu_{xz})_{COF} - (\nu_{xz})_{ACCR})^2 V_{CCR} V_{COF}}{\frac{V_{CCR}}{K_{COF}} + \frac{V_{COF}}{K_{ACCR}} + \frac{1}{(G_{zy})_{ACCR}}} \quad (7.22)$$

$$(\nu_{xz})_{FC} \big|_{ACCR} = (\nu_{xz})_{ACCR} V_{CCR} + (\nu_{xz})_{COF} V_{COF} + \frac{((\nu_{xz})_{COF} - (\nu_{xz})_{ACCR}) \left(\frac{1}{K_{ACCR}} - \frac{1}{K_{COF}} \right) V_{CCR} V_{COF}}{\frac{V_{CCR}}{K_{COF}} + \frac{V_{COF}}{K_{ACCR}} + \frac{1}{(G_{zy})_{ACCR}}} \quad (7.23)$$

$$K_{FC} \big|_{ACCR} = K_{ACCR} + \frac{V_{COF}}{\frac{1}{K_{COF} - K_{ACCR}} + \frac{V_{CCR}}{K_{ACCR} + (G_{zy})_{ACCR}}} \quad (7.24)$$

$$(\nu_{zy})_{FC}|_{ACCR} = \frac{K_{FC}|_{ACCR} - m_{FC}|_{ACCR} (G_{zy})_{FC}|_{ACCR}}{K_{FC}|_{ACCR} + m_{FC}|_{ACCR} (G_{zy})_{FC}|_{ACCR}} \quad (7.25)$$

Thus, by obtaining $m_{FC}|_{ACCR}$ and $(G_{zy})_{FC}|_{ACCR}$ by using the following equations, Eq. (7.25) will be solved.

$$m_{FC}|_{ACCR} = 1 + \frac{4(K_{FC}|_{ACCR}) ((\nu_{xz})_{FC}|_{ACCR})^2}{(E_x)_{FC}|_{ACCR}} \quad (7.26)$$

$$(G_{zy})_{FC}|_{ACCR} = (G_{zy})_{ACCR} + \frac{\frac{V_{COF}}{1} + \frac{V_{CCR} (K_{ACCR} + 2(G_{zy})_{ACCR})}{2(G_{zy})_{ACCR} (K_{ACCR} + (G_{zy})_{ACCR})}}{(G_{zy})_{COF} - (G_{zy})_{ACCR}} \quad (7.27)$$

Finally, the transverse Young's modulus and longitudinal shear modulus of FC including ACCR are given by:

$$(E_z)_{FC}|_{ACCR} = 2[1 + (\nu_{zy})_{FC}|_{ACCR}](G_{zy})_{FC}|_{ACCR} \quad (7.28)$$

$$(G_{xz})_{FC}|_{ACCR} = (G_{xz})_{ACCR} + \frac{\frac{V_{COF}}{1} + \frac{V_{CCR}}{2(G_{xz})_{ACCR}}}{(G_{xz})_{COF} + (G_{xz})_{ACCR}} \quad (7.29)$$

Where $(E_x)_{FC}|_{ACCR}$, $(E_z)_{FC}|_{ACCR}$, $(G_{xz})_{FC}|_{ACCR}$, $(G_{zy})_{FC}|_{ACCR}$, $(\nu_{xz})_{FC}|_{ACCR}$, $(\nu_{zy})_{FC}|_{ACCR}$ and $K_{FC}|_{ACCR}$ denote longitudinal Young's modulus of FC (fiber with surrounding coating), transverse Young's modulus of FC, longitudinal shear modulus of FC, transverse shear modulus of FC, longitudinal Poisson's ratio of FC, transverse Poisson's ratio of FC and bulk modulus of FC, respectively. It is worth noting that the above FC model comprises ACCR and V_{CCR} and V_{COF} indicate CCR volume fraction and core fiber volume fraction inside the FC, respectively.

Analogous to aforementioned procedure, mechanical properties of FC including RNCCR are computed as follows. It should be reaffirmed that the RNCCR exhibits an isotropic behavior around core fiber. Therefore, in the below equations, only two independent elastic constants are required for RNCCR which have been already calculated in the preceding section.

$$(E_x)_{FC}|_{RNCCR} = (E_x)_{RNCCR} V_{CCR} + (E_x)_{COF} V_{COF} + \frac{4((\nu_{xz})_{COF} - \nu_{RNCCR})^2 V_{CCR} V_{COF}}{\frac{V_{CCR}}{K_{COF}} + \frac{V_{COF}}{K_{RNCCR}} + \frac{1}{G_{RNCCR}}} \quad (7.30)$$

$$\begin{aligned}
(\nu_{xz})_{FC} \Big|_{RNCCR} = & \nu_{RNCCR} V_{CCR} + (\nu_{xz})_{COF} V_{COF} + \\
& \frac{((\nu_{xz})_{COF} - \nu_{RNCCR}) \left(\frac{1}{K_{RNCCR}} - \frac{1}{K_{COF}} \right) V_{CCR} V_{COF}}{\frac{V_{CCR}}{K_{COF}} + \frac{V_{COF}}{K_{RNCCR}} + \frac{1}{G_{RNCCR}}}
\end{aligned} \quad (7.31)$$

$$K_{FC} \Big|_{RNCCR} = K_{RNCCR} + \frac{V_{COF}}{\frac{1}{K_{COF} - K_{RNCCR}} + \frac{V_{CCR}}{K_{RNCCR} + G_{RNCCR}}} \quad (7.32)$$

$$(\nu_{zy})_{FC} \Big|_{RNCCR} = \frac{K_{FC} \Big|_{RNCCR} - m_{FC} \Big|_{RNCCR} (G_{zy})_{FC} \Big|_{RNCCR}}{K_{FC} \Big|_{RNCCR} + m_{FC} \Big|_{RNCCR} (G_{zy})_{FC} \Big|_{RNCCR}} \quad (7.33)$$

Therefore, by calculating $m_{FC} \Big|_{RNCCR}$ and $(G_{zy})_{FC} \Big|_{RNCCR}$, the transverse Poisson's ratio of FC containing RNCCR can be obtained.

$$m_{FC} \Big|_{RNCCR} = 1 + \frac{4(K_{FC} \Big|_{RNCCR}) ((\nu_{xz})_{FC} \Big|_{RNCCR})^2}{(E_x)_{FC} \Big|_{RNCCR}} \quad (7.34)$$

$$(G_{zy})_{FC} \Big|_{RNCCR} = G_{RNCCR} + \frac{V_{COF}}{\frac{1}{(G_{zy})_{COF} - G_{RNCCR}} + \frac{V_{CCR} (K_{RNCCR} + 2 G_{RNCCR})}{2 G_{RNCCR} (K_{RNCCR} + G_{RNCCR})}} \quad (7.35)$$

Hence, the transverse Young's modulus and longitudinal shear modulus of FC consisting of RNCCR are obtained as:

$$(E_z)_{FC} \Big|_{RNCCR} = 2[1 + (\nu_{zy})_{FC} \Big|_{RNCCR}] (G_{zy})_{FC} \Big|_{RNCCR} \quad (7.36)$$

$$(G_{xz})_{FC} \Big|_{RNCCR} = G_{RNCCR} + \frac{V_{COF}}{\frac{1}{(G_{xz})_{COF} + G_{RNCCR}} + \frac{V_{CCR}}{2 G_{RNCCR}}} \quad (7.37)$$

Where $(E_x)_{FC} \Big|_{RNCCR}$, $(E_z)_{FC} \Big|_{RNCCR}$, $(G_{xz})_{FC} \Big|_{RNCCR}$, $(G_{zy})_{FC} \Big|_{RNCCR}$, $(\nu_{xz})_{FC} \Big|_{RNCCR}$, $(\nu_{zy})_{FC} \Big|_{RNCCR}$ and $K_{FC} \Big|_{RNCCR}$ represent longitudinal Young's modulus of FC (fiber with surrounding coating), transverse Young's modulus of FC, longitudinal shear modulus of FC, transverse shear modulus of FC, longitudinal Poisson's ratio of FC, transverse Poisson's ratio of FC and bulk modulus of FC, respectively.

7.2.4 Macro-Scale Modeling of CNT Coated–Fiber Multi-Scale Composites

Having attained the mechanical properties of constituents at the lower scale, the elastic moduli of CNT coated–fiber multiscale composite beam are then computed utilizing Halpin–Tsai formulation [298] [299] at macro-scale. As well as volume fraction and orientation of the core fiber, two materials are considered as core fiber, carbon fiber and glass fiber, to make a comprehensive assessment of the parameters at this scale. Consequently, two materials are constructed for the layers of the composite structures as C and G indicating Carbon fiber–Epoxy and Glass fiber–Epoxy, respectively. It should be mentioned that the volume fraction of glass and carbon fibers are 40% in both composite beams and CFMC beams. Furthermore, two materials including Rohacell foam and PVC are considered as core materials for the sandwich structures. The mechanical properties of C, G, and the core materials are summarized in Table 7.3.

Materials	E_x [GPa]	E_y [GPa]	G_{xz} [GPa]	G_{yz} [GPa]	ν_{xz}
C (Carbon Fiber-Epoxy)	119.23	6.05	2.48	1.94	0.29
G (Glass Fiber -Epoxy)	37.77	8.12	2.55	2.24	0.25
R (Rohacell ® foam)	40.3×10^{-3}	40.3×10^{-3}	12.4×10^{-3}	12.4×10^{-3}	0.3
P(PVC)	103.9×10^{-3}	103.9×10^{-3}	40×10^{-3}	40×10^{-3}	0.3

Table 7.3 : Mechanical properties of composite beam [267] [285]

At this scale the CFMC consists of FCs (with different orientations) and surrounding matrix. Thus, longitudinal (x direction) and transverse Young's moduli of CFMC are expressed as:

$$(E_x)_{CFMC} \Big|_{ACCR \text{ or } RNCCR} = E_m \left(\frac{(1 + \zeta_x \eta_x V_{FC})}{1 - \eta_x V_{FC}} \right), \quad \eta_x = \frac{\frac{(E_x)_{FC} \Big|_{ACCR \text{ or } RNCCR} - 1}{E_m}}{\frac{(E_x)_{FC} \Big|_{ACCR \text{ or } RNCCR}}{E_m} + \zeta_x} \quad (7.38)$$

$$\zeta_x = \frac{2L}{D_{FC}}, \quad D_{FC} = D_{COF} + TH_{CCR}$$

$$(E_z)_{CFMC} \Big|_{ACCR \text{ or } RNCCR} = E_m \left(\frac{(1 + 2\eta_z V_{FC})}{1 - \eta_z V_{FC}} \right) , \quad \eta_z = \frac{\frac{(E_z)_{FC} \Big|_{ACCR \text{ or } RNCCR}}{E_m} - 1}{\frac{(E_z)_{FC} \Big|_{ACCR \text{ or } RNCCR}}{E_m} + 2} , \quad \zeta_z = 2 \quad (7.39)$$

Where E_m , D_{COF} , TH_{CCR} and V_{FC} imply on Young's modulus of matrix, core fiber diameter, thickness of CNT coating around core fiber and volume fraction of FC, respectively. It should be mentioned that $(E_x)_{FC}$ and $(E_z)_{FC}$ are longitudinal and transverse Young's moduli of FC obtained in the preceding section; as by selecting the type of CCR at the lower scale (ACCR or RNCCR), the mechanical properties of their corresponding laminates are calculated at the current/upper scale (macro scale). It is noteworthy to indicate that the volume fraction of FC is computed by volume fraction of the core fiber plus volume fraction of CCR utilizing COF diameter and CCR thickness in the constructed RVE at this scale. For longitudinal and transverse shear moduli below equations are given, using Halpin–Tsai method:

$$(G_{xz})_{CFMC} \Big|_{ACCR \text{ or } RNCCR} = G_m \left(\frac{(1 + \zeta_{sx} \eta_{sx} V_{FC})}{1 - \eta_{sx} V_{FC}} \right) , \quad \eta_{sx} = \frac{\frac{(G_{xz})_{FC} \Big|_{ACCR \text{ or } RNCCR}}{G_m} - 1}{\frac{(G_{xz})_{FC} \Big|_{ACCR \text{ or } RNCCR}}{G_m} + \zeta_{sx}} , \quad (7.40)$$

$$\zeta_{sx} = 1$$

$$(G_{zy})_{CFMC} \Big|_{ACCR \text{ or } RNCCR} = G_m \left(\frac{(1 + \zeta_{sz} \eta_{sz} V_{FC})}{1 - \eta_{sz} V_{FC}} \right) , \quad \eta_{sz} = \frac{\frac{(G_{zy})_{FC} \Big|_{ACCR \text{ or } RNCCR}}{G_m} - 1}{\frac{(G_{zy})_{FC} \Big|_{ACCR \text{ or } RNCCR}}{G_m} + \zeta_{sz}} \quad (7.41)$$

$$\zeta_{sz} = \frac{\frac{K_m}{G_m}}{\frac{K_m}{G_m} + 2}$$

Where K_m and G_m represent bulk modulus and shear modulus of matrix. $(G_{xz})_{FC}$ and $(G_{zy})_{FC}$ denote longitudinal and transverse shear moduli of FC that have been computed at the lower scale. Hence, employing hierarchical multi-scale modeling from nano to macro, the mechanical properties of final CNT coated–fiber composite can be acquired based on the various parameters such as CNT type, CNT diameter, CNT-matrix non-bonded interactions, CNT orientation, core fiber material and core fiber orientation and volume fraction.

Different coating thicknesses around core fiber are available in literature estimated through experimental investigation or molecular dynamic (MD) method which are usually in the range of 500-1500 nm [300] [201]. However, the thickness

of CNT coating around carbon fiber is demonstrated to be a function of CNT growth time and temperature in CVD technique, and it is difficult to determine the exact value since it varies in different specimens due to the parameters during growing of CNTs [202]. Moderately thick coating regions up to 2- 4 μ m with intensively grown CNTs have been also reported at specific reaction time and temperatures of 700 °C and 800 °C [265] [301]. It is noteworthy to mention that the high density of CNT is desirable and beneficial with the aim of producing high performance fiber reinforced composites [302]. Likewise, it was deduced that the higher temperature led to a higher degree of catalyst agglomeration which affected the homogeneous growth of CNT whereas a lower synthesis temperature is suitable to minimize heating energy and to protect the carbon fiber from being damaged by unnecessary high heat level [301]. Moreover, Deng et al. [176] demonstrated that the quality and quantity of depositing nanomaterials on the carbon fiber were increased and improved by introducing the ultrasonic during the electrophoresis deposition (EPD) process. Therefore, in the current work, CCRs with thicknesses of 800 nm, 1000 nm, 1200 nm, and 1400 nm with the same CNT volume fractions are considered in order to scrutinize the influence of mere coating thickness on the bending analysis. Accordingly, two composite structures are established including CNT coated-carbon fiber multi-scale composite (CCFMC) and CNT coated-glass fiber multi-scale composite (CGFMC) which the former with Epoxy matrix is recognized by C* while the latter with Epoxy matrix is identified by G*. Table 7.4 provides generated mechanical properties of C* and G* versus various coating thicknesses considering ACCR and RNCCR as coating types around the core fiber at CNT volume fraction of 0.08. It is evident from data supplied in Table. 4 that the ACCR type makes a remarkable contribution on the axial Young's modulus since the CNTs are aligned along the core fiber in the coating region, however, the RNCCR type improves the transverse Young's modulus significantly.

Material	E_x [GPa]		E_y [GPa]		G_{xz} [GPa]		G_{yz} [GPa]		ν_{xz}	
C* (CCFMC-Epoxy) with V_{CNT} : 0.08										
Thickness of CNT coating [μm]	RNCCFF	ACCFF	RNCCFF	ACCFF	RNCCFF	ACCFF	RNCCFF	ACCFF	RNCCFF	ACCFF
0.80	122.07	134.14	9.23	6.36	4.14	2.60	2.99	2.05	0.277	0.287
1	122.89	138.51	10.45	6.49	4.93	2.63	3.48	2.08	0.274	0.287
1.20	123.76	143.14	11.99	6.64	6.06	2.66	4.18	2.11	0.270	0.287
1.40	124.68	148.02	13.95	6.82	7.79	2.69	5.23	2.14	0.269	0.286
G* (CGFMC-Epoxy) with V_{CNT} : 0.08										
0.80	39.22	45.51	9.99	8.72	3.33	2.62	2.86	2.34	0.239	0.246

1	39.62	47.65	10.63	8.72	3.59	2.64	3.08	2.37	0.237	0.245
1.20	40.03	49.86	11.34	8.72	3.90	2.65	3.34	2.39	0.234	0.245
1.40	40.46	52.15	12.14	8.75	4.26	2.67	3.65	2.42	0.232	0.244

Table 7.4: Obtained Mechanical properties of CCFMC & CGFMC beams versus CNT coating thicknesses [267]

Moreover, it is apparent that the influence of CNT coating on the axial Young's modulus is more prominent in glass fibers than carbon fibers arising from the lower longitudinal Young's modulus of the glass fiber. For instance, by considering $V_{CNT}=0.08$ and coating thickness of $1.4\mu\text{m}$, the improvements in the longitudinal Young's moduli of C^* for RNCCR and ACCR are 4.67 % and 24.14 %, respectively; whereas for G^* including RNCCR and ACCR achieve 7.1% and 38%, respectively. On the other hand, the improvements in the transverse Young's moduli of C^* and G^* for RNCCR reach 52.52% and 23.05 %, respectively. Subramanian et al. [270] demonstrated that the comparison of the obtained transverse modulus of fuzzy fiber (core fiber plus surrounding CCR) composite yields a 31.7% improvement with respect to traditional fiber reinforced composites. Depending on the volume fraction of the CNTs grown on a core fiber, greater improvement in the transverse Young's modulus could be achieved up to 54.5% and 100% according to the reported data in the literature [272] [203].

The computed mechanical properties of C^* and G^* are summarized in Table 7.5 with respect to the CNT contents considering constant coating thickness ($1.4\mu\text{m}$) for both ACCR and RNCCR types. The amount of CNT volume fraction and coating thickness can be increased up to a desirable value by keeping in mind about the limitations of producing process which can confine the maximum values of them such as reaction time, temperature, catalyst, CNT agglomeration, etc. Hence, four amounts of CNT volume fractions are selected in the current work with the aim of investigating their influence on the bending stress analysis of the CFMC beams.

Material	E_x [GPa]		E_y [GPa]		G_{xz} [GPa]		G_{yz} [GPa]		ν_{xz}	
C* (CCFMC-Epoxy) with coating thickness of 1.4μm										
V_{CNT} at coating region	RNCCFF	ACCFF	RNCCFF	ACCFF	RNCCFF	ACCFF	RNCCFF	ACCFF	RNCCFF	ACCFF
2%	120.68	125.82	8.00	6.31	4.05	2.53	2.99	2.03	0.276	0.287
4%	121.98	133.22	10.27	6.56	5.44	2.58	3.85	2.07	0.272	0.286
6%	123.32	140.62	12.23	6.70	6.67	2.64	4.58	2.10	0.269	0.286
8%	124.68	148.02	13.95	6.82	7.79	2.69	5.23	2.14	0.267	0.286
G* (CGFMC-Epoxy) with coating thickness of 1.4μm										

2%	38.45	41.02	8.57	8.31	3.29	2.58	2.86	2.34	0.236	0.244
4%	39.10	44.73	10.12	8.54	3.74	2.61	3.23	2.37	0.234	0.244
6%	39.77	48.44	11.26	8.66	4.04	2.64	3.47	2.39	0.233	0.244
8%	40.46	52.15	12.15	8.75	4.26	2.67	3.65	2.42	0.232	0.244

Table 7.5: Obtained Mechanical properties of CCFMC & CGFMC beams with respect to CNT contents [267]

Upon obtaining the mechanical properties of the models constructed at macro scale and defining the stacking sequences of the composite structures, the outcomes are ready to be utilized in RZT formulation regarding CNT coated–fiber multiscale composite beams.

7.3 Formulation of the Refined Zigzag Theory (RZT)

Consider a narrow multilayered beam with of length L , thickness $2h$, the cross-sectional area A made of N orthotropic material layers that are perfectly bonded to each other which its longitudinal axis is located along x axis as delineated in Figure 7.6. The thickness of the beam and layers are constant. The material properties of each layer made of CFMC are adopted from the previous section. The CFMC beam is established on an orthogonal cartesian coordinate system $X = \{x, y, z\}$ where z direction denotes through-thickness direction of the beam, and the origin of the reference frame is positioned at the left edge of the beam. Thus, the range of x is specified in $[x_a, x_b]$, y in $[-t/2, t/2]$ and z $[-h, h]$. It should be mentioned that only planar deformations are taken into consideration under the static loading consisting of a distributed transverse pressure $q(x)$ (force/length) and the prescribed axial (T_{xa} , T_{xb}) and shear (T_{za} , T_{zb}) tractions at the two reference cross-sections $x = x_a$ and x_b as described in Figure 7.6.

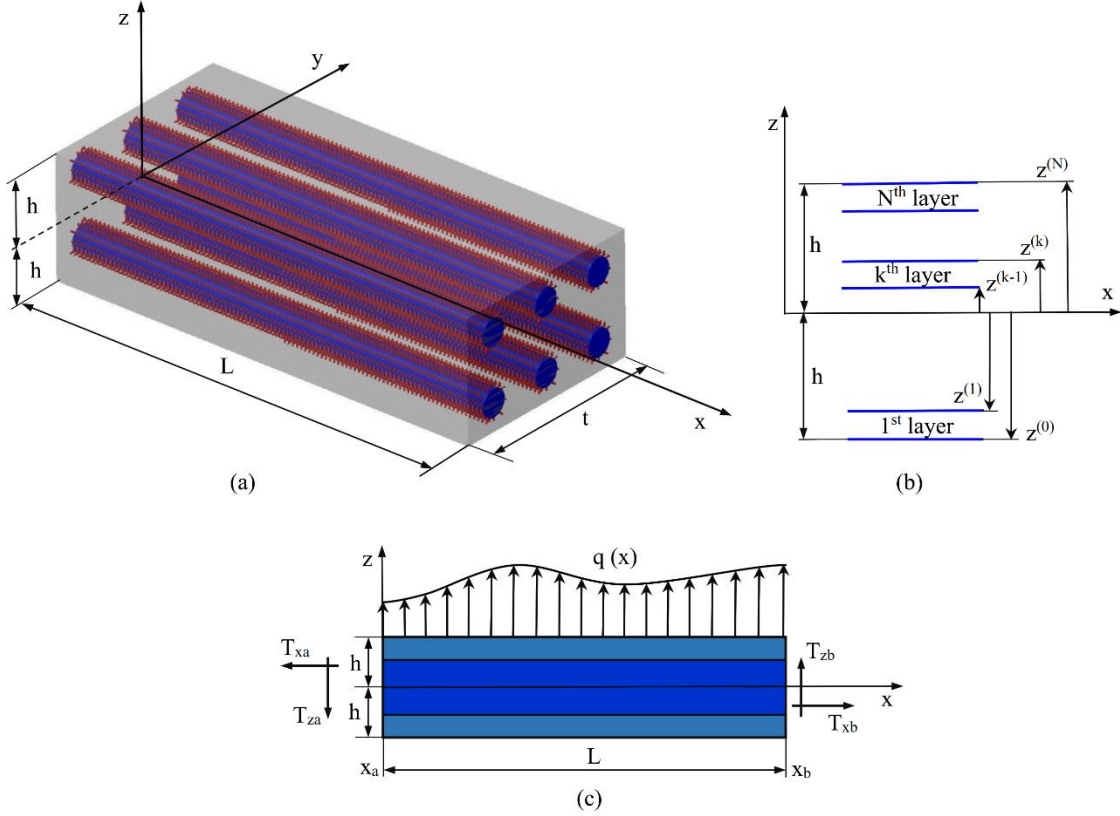


Figure 7.6: Schematic description: (a) CFMC beam geometry and Coordinate System, (b) layers numbering, (c) applied loads [267]

The components of the displacement field of RZT for CFMC beam within the k^{th} layer are expressed as:

$$u_x^{(k)}(x, z) = u(x) + z\theta(x) + \phi^{(k)}(z)\psi(z)$$

$$u_z^{(k)}(x, z) = w(x) \quad (7.42)$$

Where four kinematic variables $u(x)$, $\theta(x)$, $w(x)$ and $\psi(x)$ denote uniform axial displacement, bending rotation, transverse deflection, and zigzag rotation (amplitude of the zigzag), respectively. The displacement field of RZT mentioned in Eq. (7.42), is attained by adding to the axial displacement of the Timoshenko beam theory a piecewise linear (zigzag), through-the-thickness C^0 -continuous contribution, namely $\phi^{(k)}(z)\psi(x)$ [282]. The magnitude of this contribution is quantified by the zigzag rotation $\psi(x)$. The through-the-thickness shape of the contribution is described by the zigzag function, $\phi^{(k)}(z)$, that can be defined in terms of its layer-interface values, $\phi_{(i)}$ ($i=0$ to $N-1$). It should be mentioned that $\phi^{(k)}(z)$ is linear along thickness direction, z , within the k^{th} layer between the values $\phi_{(k-1)}$ and $\phi_{(k)}$ [303]. Furthermore, the zigzag component, $\phi^{(k)}(z)\psi(x)$, permits the distortion of the cross-section within the interior of the laminate. It is worth mentioning that the superscript (k) represents the quantities corresponding to a k^{th} layer ($k = 1$ to N), whereas the subscript (k) determines quantities corresponding to the k^{th}

interface ($k = 1$ to $N-1$) between the k th and $(k+1)$ th layer. As previously mentioned, the layers are perfectly bonded in CFMC beam, however, if delamination along the layer interfaces are taken into account, the zigzag function may be represented having jump conditions along such interfaces [304]. The linear strains associated with the displacement field in Eq. (7.42) are stated as:

$$\begin{aligned}\varepsilon_x^{(k)}(x, z) &= u_{x,x}^{(k)} = u_{,x} + z\theta_{,x} + \phi^{(k)}\psi_{,x} \\ \gamma_{xz}^{(k)}(x, z) &= u_{x,z}^{(k)} + u_{z,x}^{(k)} = \gamma + \beta^{(k)}\psi\end{aligned}\quad (7.43)$$

$$\begin{cases} \beta^{(k)} = \phi_{,z}^{(k)} \\ \gamma = w_{,x} + \theta \end{cases}$$

Where γ indicates an average shear strain (or shearing angle) within the assumptions of Timoshenko theory. It is worth noting that since $\phi^{(k)}(z)$ is piecewise linear along cross-section of the beam, $\beta^{(k)}$ exhibits piecewise constant function based on Eq. (7.43). In other word, $\beta^{(k)}$ is constant across each material layer. The CFMC beam is assumed to display a plane-stress behavior in the (x, z) plane with the orthotropy axes of each layer corresponding to the x - and z -axis. Furthermore, the transverse normal stress, $\sigma_z^{(k)}$, is negligible with respect to the axial stress and transverse shear stress. Hence, based on the Hooke's stress-strain relations, the constitutive relations of the k th layer of CFMC beam are given by:

$$\begin{bmatrix} (\sigma_x)_{CFMC}^{(k)} \\ (\tau_{xz})_{CFMC}^{(k)} \end{bmatrix} = \begin{bmatrix} (E_x)_{CFMC}^{(k)} & 0 \\ 0 & (G_{xz})_{CFMC}^{(k)} \end{bmatrix} \begin{bmatrix} \varepsilon_x^{(k)} \\ \gamma_{xz}^{(k)} \end{bmatrix} \quad (7.44)$$

Where $(E_x)_{CFMC}^{(K)}$ and $(G_{xz})_{CFMC}^{(K)}$ indicate axial and shear moduli of CFMC beam which can be calculated through proposed technique in preceding section. The zigzag functions are independent of the state of deformation while depend on the thickness of each layer and interior interface displacements. In the RZT, the zigzag functions are set to vanish on the top and bottom laminate faces which are described in Figure 7.7.

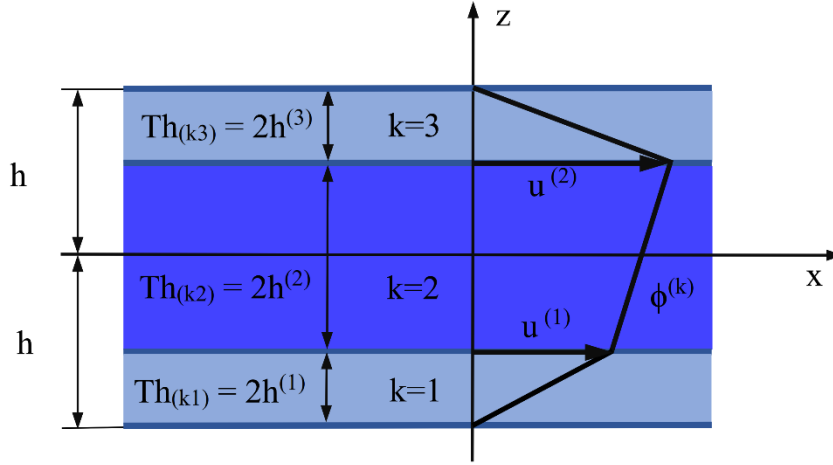


Figure 7.7: Zigzag functions and layer notation of the Refined Zigzag Theory for a three-layered laminate [283]

The $\phi^{(k)}(z)$ zigzag function is determined in terms of layer thickness coordinate $\xi^{(k)}$ ($k= 1$ to N) and the normalized displacement $u^{(k)}$ defined along the layers interfaces as below:

$$\begin{aligned} \phi_{CFMC}^{(k)} &= \frac{1}{2}(1 - \xi^{(k)})u_{CFMC}^{(k-1)} + \frac{1}{2}(1 + \xi^{(k)})u_{CFMC}^{(k)} \\ \left\{ \begin{aligned} \phi^{(1)}(z = z^{(0)} = -h) &= 0 \\ \phi^{(N)}(z = z^{(N)} = +h) &= 0 \end{aligned} \right. \end{aligned} \quad (7.45)$$

Since $\beta^{(k)} = \phi_{,z}^{(k)}$, so it can be stated as:

$$\beta_{CFMC}^{(k)} = \frac{u_{CFMC}^{(k)} - u_{CFMC}^{(k-1)}}{2h^{(k)}} \quad (7.46)$$

On the other hand, the local thickness coordinates, $\xi^{(k)}$, are specified in terms of the laminate thickness coordinate z as:

$$\begin{aligned} \xi^{(k)} &= \frac{z - (z^{(k-1)} + h^{(k)})}{h^{(k)}} \\ \left\{ \begin{aligned} z^{(0)} &= -h \\ z^{(k)} &= z^{(k-1)} + 2h^{(k)} \end{aligned} \right. \end{aligned} \quad (7.47)$$

To obtain the unknown interface displacements $u_{(k)}$ ($k= 1$ to $N-1$) and therefore defining $\phi^{(k)}$ and $\beta^{(k)}$, the shear stress equilibrium is not enforced along the interior layer interfaces, however, the shear coefficient, $(G_{xz})_{CFMC}^{(k)} (1 + \beta_{CFMC}^{(k)})$, is considered as a constant value [282] for each layer in the CFMC laminated beam as following:

$$G_{CFMC} = (G_{xz})_{CFMC}^{(k)} (1 + \beta_{CFMC}^{(k)}) \quad \text{Constant}$$

or

$$(G_{xz})_{CFMC}^{(k)} (1 + \beta_{CFMC}^{(k)}) = (G_{xz})_{CFMC}^{(k+1)} (1 + \beta_{CFMC}^{(k+1)}) \quad (k = 1 \text{ to } N-1) \quad (7.48)$$

Hence, utilizing Eq. (7.46) and Eq. (7.48) the interior interface displacement and $\beta(k)$ are computed respectively, as follows:

$$u_{CFMC}^{(k)} = u_{CFMC}^{(k-1)} + 2h^{(k)} \beta_{CFMC}^{(k)} \quad (k = 1 \text{ to } N-1)$$

$$\beta_{CFMC}^{(k)} = \frac{G_{CFMC}}{(G_{xz})_{CFMC}^{(k)}} - 1 \quad (7.49)$$

where G_{CFMC} denotes a zigzag weighted-average shear modulus of the CFMC beam cross section as:

$$G_{CFMC} = \left(\frac{1}{A} \int_A \frac{dA}{(G_{xz})_{CFMC}^{(k)}} \right)^{-1} = h \left(\sum_{k=1}^N \frac{h^{(k)}}{(G_{xz})_{CFMC}^{(k)}} \right)^{-1} \quad (7.50)$$

Where $(G_{xz})_{CFMC}^{(k)}$ is the longitudinal shear modulus of the k th layer in the CFMC beam. Thus, by acquiring G_{CFMC} , $\beta^{(k)}$ and $u^{(k)}$ are available for calculating the zigzag functions for each layer. Applying Virtual Work Principle (VWP) and considering transverse pressure and prescribed axial and transverse tractions (see Figure 7.6) the equilibrium equation of the beam can be obtained according to the RZT method [283]:

$$\begin{aligned} (N_{x,x})_{CFMC} &= 0 \\ (M_{x,x})_{CFMC} - (V_x)_{CFMC} &= 0 \\ (V_{x,x})_{CFMC} + q(x) &= 0 \\ (M_{\phi,x})_{CFMC} - (V_\phi)_{CFMC} &= 0 \end{aligned} \quad (7.51)$$

Where $(N_x)_{CFMC}$, $(M_x)_{CFMC}$, and $(V_x)_{CFMC}$ designate the conventional axial force, bending moment, and shear force, respectively; $(M_\phi)_{CFMC}$ and $(V_\phi)_{CFMC}$ represent the bending moment and shear force due to the zigzag distortion of the beam's cross-section. The below integrals define the stress resultants:

$$\begin{bmatrix} (N_x)_{CFMC} \\ (M_\phi)_{CFMC} \\ (M_x)_{CFMC} \\ (V_x)_{CFMC} \\ (V_\phi)_{CFMC} \end{bmatrix} = \begin{bmatrix} \int_A (\sigma_x)^{(k)}_{CFMC} dA \\ \int_A z (\sigma_x)^{(k)}_{CFMC} dA \\ \int_A \phi(k) (\sigma_x)^{(k)}_{CFMC} dA \\ \int_A (\tau_{xz})^{(k)}_{CFMC} dA \\ \int_A \beta^{(k)}_{CFMC} (\tau_{xz})^{(k)}_{CFMC} dA \end{bmatrix} \quad (7.52)$$

The VWP provides the consistent boundary conditions as below:

$$\left. \begin{array}{ll} u(x_\alpha) = \bar{u}_\alpha & or \quad N_x(x_\alpha) = \bar{N}_{x\alpha} \\ w(x_\alpha) = \bar{w}_\alpha & or \quad V_x(x_\alpha) = \bar{V}_{x\alpha} \\ \theta(x_\alpha) = \bar{\theta}_\alpha & or \quad M_x(x_\alpha) = \bar{M}_{x\alpha} \\ \psi(x_\alpha) = \bar{\psi}_\alpha & or \quad M_\phi(x_\alpha) = (\bar{M}_{\phi\alpha})_{CFMC} \end{array} \right\} \quad (\alpha = a, b) \quad (7.53)$$

Where:

$$\begin{bmatrix} \bar{N}_{x\alpha} \\ \bar{M}_{x\alpha} \\ (\bar{M}_{\phi\alpha})_{CFMC} \\ \bar{V}_{x\alpha} \end{bmatrix} = \begin{bmatrix} \int_A T_{x\alpha} dA \\ \int_A z T_{x\alpha} dA \\ \int_A \phi^{(k)}_{CFMC} T_{x\alpha} dA \\ \int_A T_{z\alpha} dA \end{bmatrix} \quad (7.54)$$

The integrals exhibited in Eq. (7.54) indicate the prescribed-stress resultants at the beam ends. Integrating Eq. (7.52) yields the constitutive equations of the beam theory, expressing the relation between stress resultants and derivatives of the kinematic unknowns as follows:

$$\begin{bmatrix} (N_x)_{CFMC} \\ (M_x)_{CFMC} \\ (M_\phi)_{CFMC} \\ (V_x)_{CFMC} \\ (V_\phi)_{CFMC} \end{bmatrix} = \begin{bmatrix} A_{CFMC} & B_{CFMC} & A^\phi_{CFMC} & 0 & 0 \\ B_{CFMC} & D_{CFMC} & B^\phi_{CFMC} & 0 & 0 \\ A^\phi_{CFMC} & B^\phi_{CFMC} & D^\phi_{CFMC} & 0 & 0 \\ 0 & 0 & 0 & Q_{CFMC} + \mu_{CFMC} & -\mu_{CFMC} \\ 0 & 0 & 0 & -\mu_{CFMC} & \mu_{CFMC} \end{bmatrix} \begin{bmatrix} (u_{,x})_{CFMC} \\ (\theta_{,x})_{CFMC} \\ (\psi_{,x})_{CFMC} \\ (\theta + w_{,x})_{CFMC} \\ \psi \end{bmatrix} \quad (7.55)$$

Where the stiffness coefficients are determined as below:

$$\begin{bmatrix} A_{CFMC} \\ B_{CFMC} \\ D_{CFMC} \end{bmatrix} = \begin{bmatrix} \int_A (E_x)_{CFMC}^{(k)} dA \\ \int_A (E_x)_{CFMC}^{(k)} z dA \\ \int_A (E_x)_{CFMC}^{(k)} z^2 dA \end{bmatrix} \quad \begin{bmatrix} A_{CFMC}^\phi \\ B_{CFMC}^\phi \\ D_{CFMC}^\phi \end{bmatrix} = \begin{bmatrix} \int_A (E_x)_{CFMC}^{(k)} \phi_{CFMC}^{(k)} dA \\ \int_A (E_x)_{CFMC}^{(k)} \phi_{CFMC}^{(k)} z dA \\ \int_A (E_x)_{CFMC}^{(k)} (\phi_{CFMC}^{(k)})^2 dA \end{bmatrix} \quad (7.56)$$

Where:

$$\begin{aligned} Q_{CFMC} &= \int_A (G_{xz})_{CFMC}^{(k)} (1 + \beta_{CFMC}^{(k)})^2 dA = G_{CFMC} A \\ \mu_{CFMC} &= \mu_0 \left(\int_A (G_{xz})_{CFMC}^{(k)} dA - G_{CFMC} A \right) \end{aligned} \quad (7.57)$$

Substituting Eq. (7.55) into Eq. (7.51) leads to the equilibrium equations of the CFMC beam in terms of the kinematic variables of the theory which are expressed as:

$$\begin{cases} A_{CFMC} (u_{,xx})_{CFMC} + B_{CFMC} (\theta_{,xx})_{CFMC} + A_{CFMC}^\phi (\psi_{,xx})_{CFMC} = 0 \\ (Q_{CFMC} + \mu_{CFMC}) ((w_{,xx})_{CFMC} + (\theta_{,x})_{CFMC}) + (-\mu_{CFMC}) (\psi_{,x})_{CFMC} = -q(x) \\ B_{CFMC} (u_{,xx})_{CFMC} + D_{CFMC} (\theta_{,xx})_{CFMC} + B_{CFMC}^\phi (\psi_{,xx})_{CFMC} - (Q_{CFMC} + \mu_{CFMC}) ((w_{,x})_{CFMC} + \theta_{CFMC}) \\ - (-\mu_{CFMC}) \psi_{CFMC} = 0 \\ A_{CFMC}^\phi (u_{,xx})_{CFMC} + B_{CFMC}^\phi (\theta_{,xx})_{CFMC} + D_{CFMC}^\phi (\psi_{,xx})_{CFMC} - (-\mu_{CFMC}) ((w_{,x})_{CFMC} + \theta_{CFMC}) \\ - (\mu_{CFMC}) \psi_{CFMC} = 0 \end{cases} \quad (7.58)$$

Utilizing the developed Maple code, the solution to the above boundary value problem, Eq. (7.58), is acquired encompassing integration of the four equilibrium equations subjected to the boundary conditions in Eq. (7.53), whereas obeying the constitutive relations of (7.55) and Eq. (7.56).

7.4 Results and Discussion

The results presented in this section refer to the linear boundary value problem of bending of simply supported composite beam and CFMC beam considering Eq.(7.58); to solve the problem in the framework of RZT. In the present work a simply supported CFMC beam of length L is considered that is subjected to the sinusoidal transverse load $q(x) = q_0 \sin(\pi x/L)$. The boundary conditions at the ends of the beam $x=0$ and $x=L$ are:

$$\begin{cases} x = 0 \\ x = L \end{cases} : \quad w_{CFMC} = N_x = M_x = M_\phi = 0 \quad (7.59)$$

The following trigonometric expressions are given for the four kinematic variables which exactly satisfy the aforementioned boundary conditions:

$$\begin{aligned} w(x)_{CFMC} &= W_{CFMC} \sin\left(\frac{\pi x}{L}\right) \\ \begin{Bmatrix} u(x)_{CFMC} \\ \theta(x)_{CFMC} \\ \psi(x)_{CFMC} \end{Bmatrix} &= \begin{Bmatrix} U_{CFMC} \\ \Theta_{CFMC} \\ \Psi_{CFMC} \end{Bmatrix} \cos\left(\frac{\pi x}{L}\right) \end{aligned} \quad (7.60)$$

The amplitudes W_{CFMC} , U_{CFMC} , Θ_{CFMC} , and Ψ_{CFMC} are defined by substituting Eq. (7.60) into the equilibrium equations, Eq. (7.58), then the resulting equations are solved by making use of Maple [263]. The solutions of four kinematic variables of the CFMC beam are extracted from Maple and are provided in Appendix E. The stacking sequences of sandwich and laminated composites are presented in Table 7.6. As it is shown, laminates and cores with different materials are considered including C^* , G^* , P and R .

Laminate Number	Normalized laminate thickness, $2h^{(k)}/2h$	Laminates materials (Composite beam CFMC beam)	Laminate Orientation ($^\circ$)	Beam Thickness
L1 L1*	(0.05/0.05/ 0.8 /0.05/0.05)	(G/G/R/G/G) ($G^*_{ACCR} / G^*_{RNCCR} / R / G^*_{RNCCR} / G^*_{ACCR}$)	[0/90/Core/90/0]	Thick
L2 L2*	(0.1/ 0.7 /0.2)	(G/P/G) ($G^*_{ACCR} / P / G^*_{RNCCR}$)	[0/Core/90]	Thick
L3 L3*	(0.1/ 0.7 /0.2)	(C/P/C) ($C^*_{ACCR} / P / C^*_{RNCCR}$)	[0/Core/90]	Thick
L4 L4*	(0.075/0.075/ 0.7 /0.075/0.075)	(C/C/R/C/C) ($C^*_{RNCCR} / C^*_{RNCCR} / R / C^*_{RNCCR} / C^*_{RNCCR}$)	[0/90/Core/90/0]	Thick
L5 L5*	(0.3/0.4/0.3)	(C/C/C) ($C^*_{RNCCR} / C^*_{RNCCR} / C^*_{RNCCR}$)	[90/0/90]	Moderately Thick
L6 L6*	(0.3/0.4/0.3)	(G/G/G) ($G^*_{RNCCR} / G^*_{RNCCR} / G^*_{RNCCR}$)	[90/0/90]	Moderately Thick
L7 L7*	(0.2/0.2/0.2/0.2/0.2)	(C/C/C/C/C) ($C^*_{ACCR} / C^*_{RNCCR} / C^*_{ACCR} / C^*_{RNCCR} / C^*_{ACCR}$)	[0/90/0/90/0]	Moderately Thick

Table 7.6: Laminate stacking sequences used for sandwich/ laminated composite beams and sandwich/laminated CFMC beams (from bottom to top direction) [267]

1. The materials/ laminates indicated with superscript (*) are associated with CFMC beams
2. The subscripts RNCCR and ACCR refer to the types of the CNT coating regions in the CFMC beams

The laminates stacking sequences are identical to make a comparison between conventional composite beam and CFMC beam, while the former is made of pristine

fibers, whereas the latter is reinforced with CNT coated–fibers. The models are constructed based on two types of moderately thick ($L/2h=10$) and thick ($L/2h=5$) [305] composite beams with rectangular cross-sections which $2h$ and L indicate total thickness and length of composite beam, respectively. The parameters marked with (*) are referred to CFMC models. Based on the laminate number, the bending analysis is carried out for different types of materials with various stacking sequences for sandwich and laminated CFMC beams. For all problems, the length of the beam, L , is considered as 10 cm. It is worth noting that for the two models comprising laminated and sandwich CFCM beams (L^*5 and L^*4), a validation process is performed with finite element analysis (FEA) for all stresses and displacements. A comparison of the through-thickness distributions of the transverse shear stress, axial stress, axial displacement, and maximum transverse displacement are delineated in Figure 7.8 for the laminated composite beam (L5) and laminated CCFMC beam (L^*5). Regarding CCFMC beam in this figure, the coating type and thickness around carbon fiber are considered as RNCCR and $1.4\mu\text{m}$, respectively, with CNT volume fraction (V_{CNT}) of 0.04.

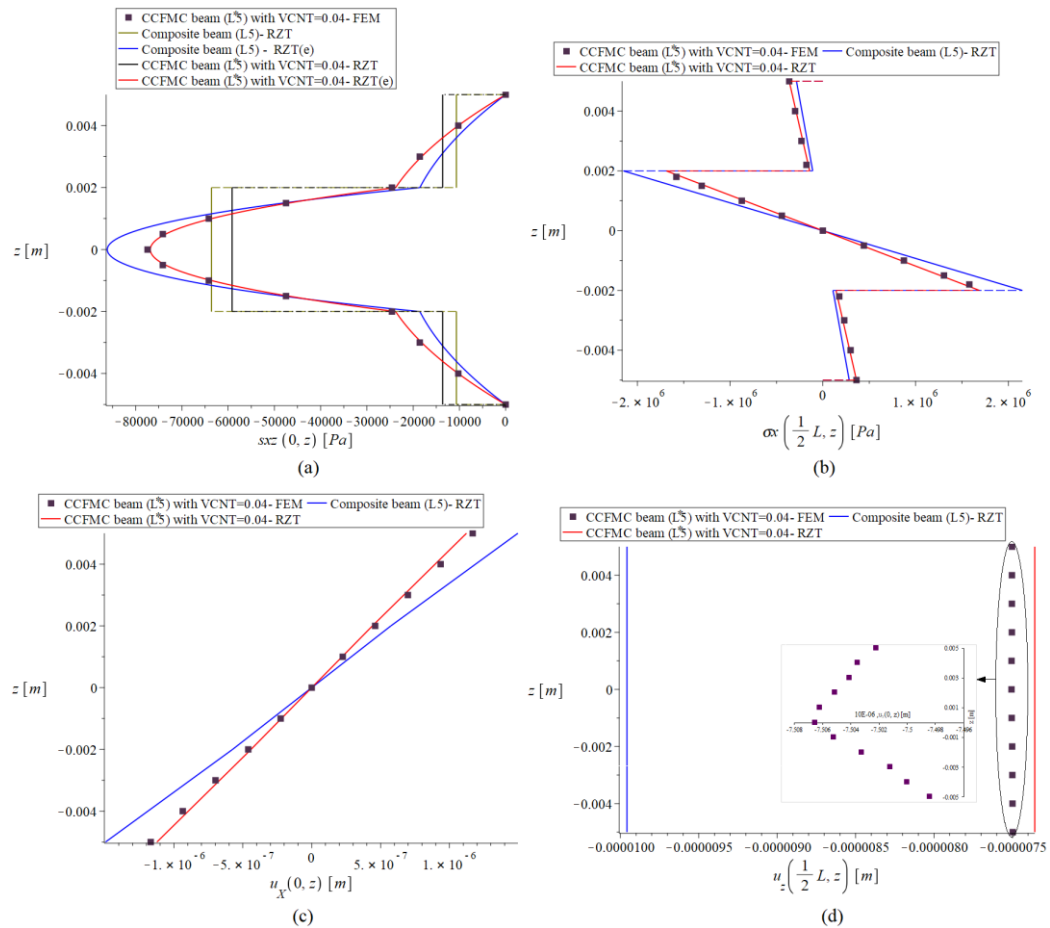


Figure 7.8: Through-thickness distributions for the laminated beams L5 and L*5; L*5 comprises RNCCR with coating thickness of $1.4\mu\text{m}$ (a) transverse shear stress, (b) axial stress, (c) axial displacement and (d) maximum transverse displacement [267]

A glance at the graphs provided (Figure 7.8) shows a striking improvement in the stiffness of the laminated CFMC beam by which the maximum transverse deflection has been reduced by 26.13 % with respect to conventional composite beam. It should be emphasized that the improvements are achieved in presence of small portion of CNTs at coating region and consequently the weight alteration from conventional composite beam to CFMC beam is negligible. Furthermore, the axial stress and transverse shear stress in the 0° layers have been remarkably decreased in the laminated CFMC beam due highly increased stiffness in the 90° layers. This issue has arisen from the significant fact that the RNCCR coating augments the mechanical properties of the layers in the radial direction of the core fiber more than longitudinal direction which have been previously obtained in previous section by Eshelby–Mori–Tanaka method. In laminated CFMC beams, 90° layers are therefore reinforced more pronounced than 0° layers. The results provided in Figure 7.8 are validated by finite element analysis (FEA) carried out with ANSYS APDL R19.0 [306] which demonstrates excellent agreement between the FEA and the proposed technique in this research with the Refined Zigzag theory (RZT) for laminated CFMC beams. Finite element analysis is conducted for stress analysis of both L^*_5 (laminated) and L^*_4 (sandwich) beams employing plane element (PLANE 183). PLANE183 is a higher order 2-D, 8-node element with two degrees of freedom at each node as translations in the nodal x and y directions. This possesses quadratic displacement behavior and is well suited for modeling irregular meshes and it can be utilized as a plane element (plane stress, plane strain and generalized plane strain) or as an axisymmetric element (with or without torsion) [118]. Regarding discretization for L^*_5 , the mesh convergence study is carried out in terms of maximum axial stress using refined mesh depicted in Figure 7.9, in which $R=1$ denotes 4000 elements and the final model of L^*_5 has 24,882 degrees of freedom. The layers of the CFMC beam are connected through glue command in ANSYS which provides perfect bonding between the layers whereas different material properties are introduced into the layers. Simply supported boundary conditions are considered in FEA in accordance with those of the RZT method. A sinusoidal transverse load is determined similar to the loading condition imposed in the RZT method through function definition applying on the upper edge of the beam. Figure 7.9 exhibits the constructed finite element model of L^*_5 consisting of applied sinusoidal transverse load and mesh convergence study.

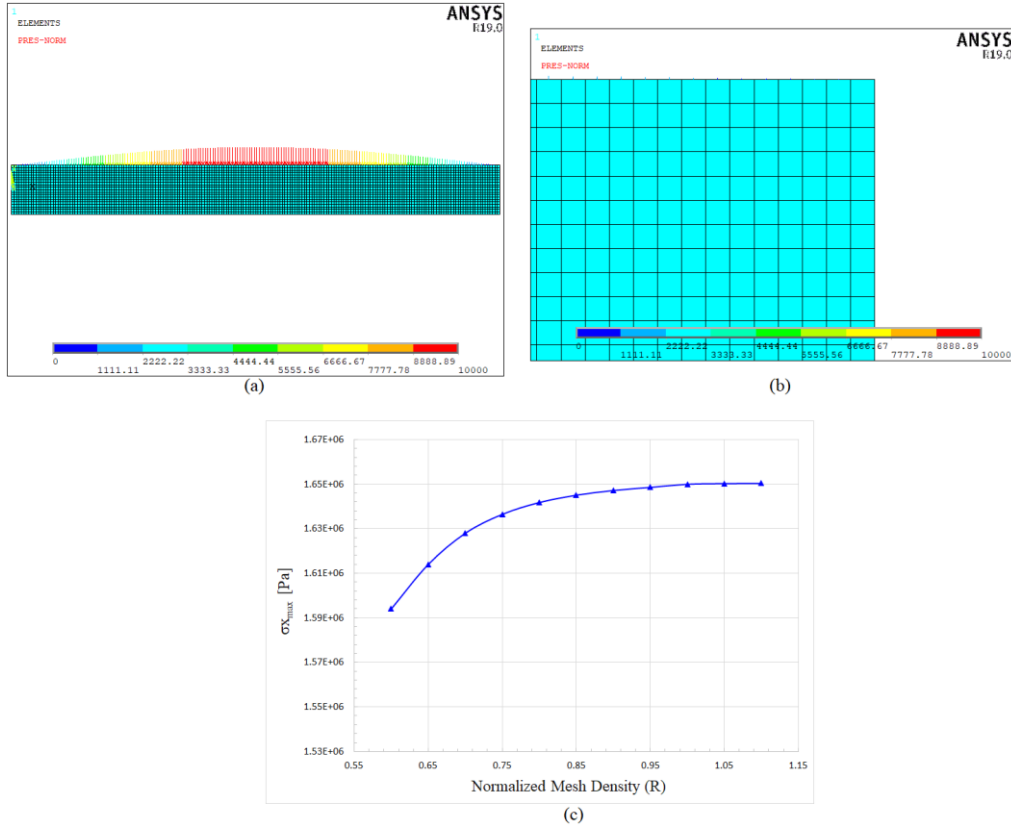


Figure 7.9: Finite element model of the laminated CFMC beam (L_5^*) (a) geometry and sinusoidal loading (b) partial view exhibiting mesh density (c) normalized mesh density versus maximum axial stress [267]

The FEA outcomes which have been already utilized for validation in Figure 7.8, are depicted in Figure 7.10 including transverse displacement and axial stress of L_5^* . It should be restated that the laminated CFMC beam, L_5^* , possesses RNCCR with coating thickness of $1.4 \mu\text{m}$ and $V_{\text{CNT}} = 0.04$.

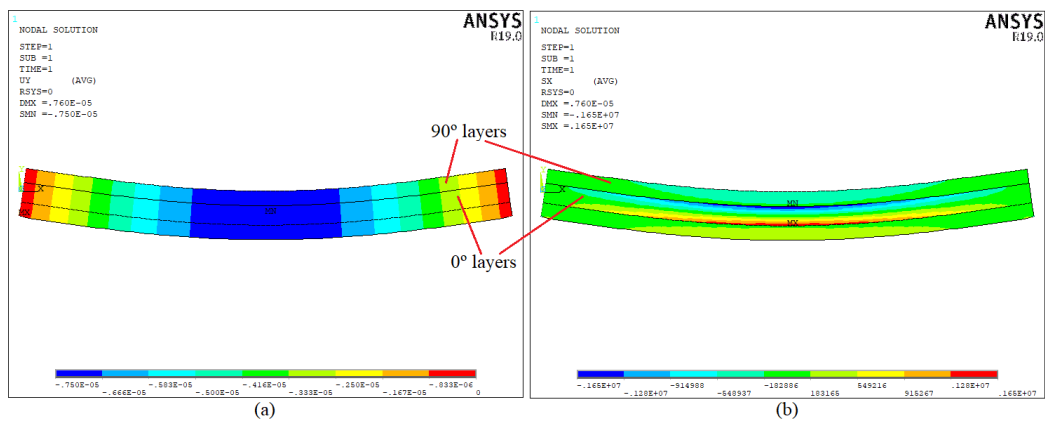


Figure 7.10: FEA contours of the laminated CCFMC beam (L_5^*) (a) transverse displacement (b) axial stress [267]

Regarding sandwich beams, Figure 7.11 describes the through-thickness distributions of the transverse shear stress, axial stress, axial displacement, and

maximum transverse displacement for the sandwich beams L4 and L^{*}4, in which L^{*}4 contains RNCCR with coating thickness of 1.4μm and CNT volume fraction (V_{CNT}) of 0.08 in the coating region.

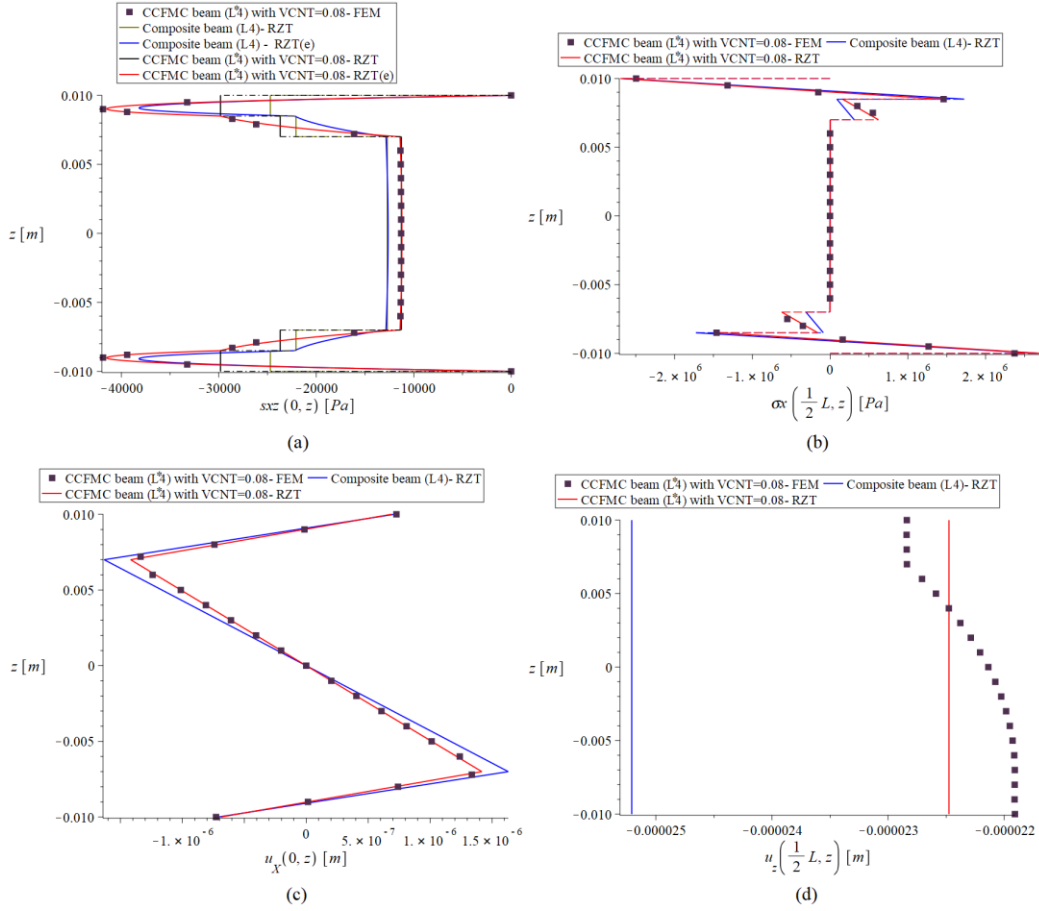


Figure 7.11: Through-thickness distributions for the sandwich beams L4 and L^{*}4; L^{*}4 comprises RNCCR with coating thickness of 1.4μm (a) transverse shear stress, (b) axial stress, (c) axial displacement and (d) maximum transverse displacement [267]

Regarding the sandwich beams, only the mechanical properties of the face sheets are augmented by CNT coating while the core materials remain the same in both sandwich composite beam and sandwich CFMC beam. It is evident from Figure 7.11 that by adding small amount of CNTs in the coating region, the transverse displacement of the sandwich CFMC beam has noticeably decreased by 10.71% with respect to sandwich beam. In comparison with laminated beams, the amount of reduction in transverse displacement is lower in sandwich beams originating from the fact that the thickness of the layers reinforced with CNT coating are much lower than laminated beams due to present of core materials. As well as decrease in deflection, a significant reduction is achieved in the transverse shear stress of the core medium of the sandwich CFMC beam by 11.23 % with respect to sandwich composite beam incorporating very low CNT contents. Since core shear is one of the well-known failure modes in the sandwich structures,

therefore, reinforcing the face-sheets by CNT coating in the CFMC beams can remarkably postpone this failure mode. This important consequence has stemmed from enhancement of mechanical properties of the face-sheets by CNT coating which gives rise to higher load carrying capacity of them and decrease the transverse shear stress in the core materials. Analogous to the laminated beam, the mesh convergence study is performed for the sandwich CFMC beam (L^*) in terms of maximum axial stress. Figure 7.12 delineates the finite element model of L^* with applied sinusoidal loading and mesh convergence study. $R=1$ denotes 8000 elements, and the final model has 48,962 degrees of freedom.

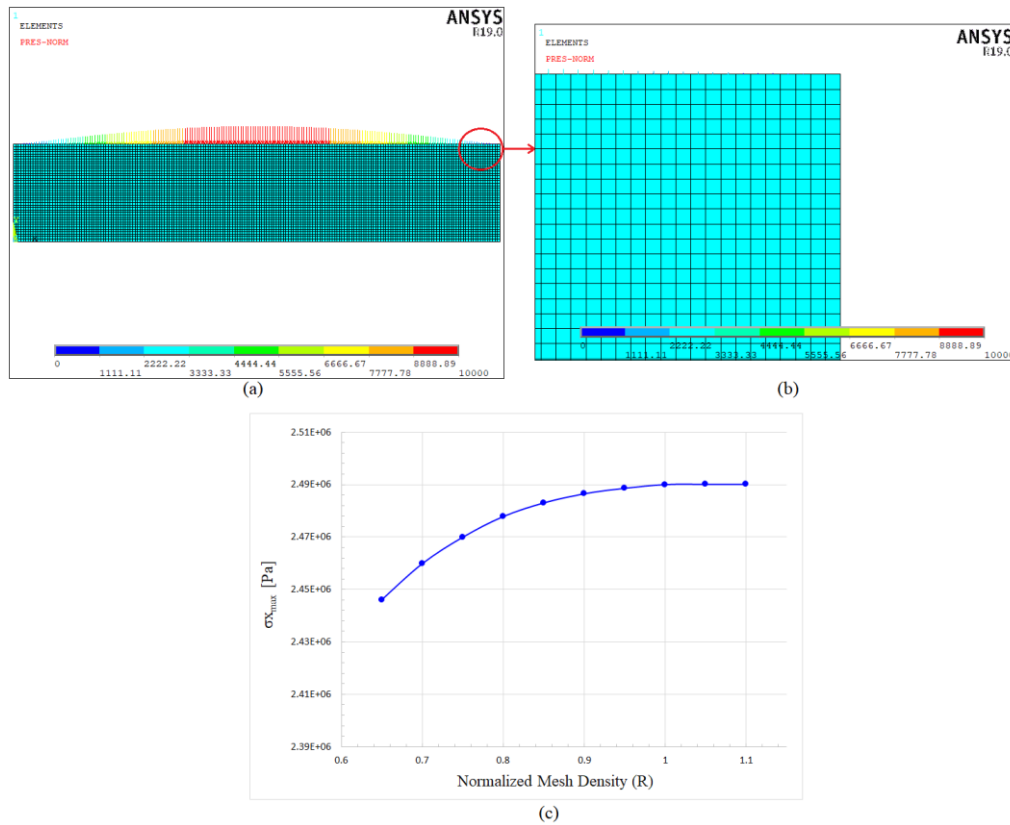


Figure 7.12: Finite element model of the sandwich CFMC beam (L^*) (a) geometry and sinusoidal loading (b) partial view exhibiting mesh density (c) normalized mesh density versus maximum axial stress [267]

Figure 7.13 portrays the FEA results of the transverse displacement and axial stress for L^* containing RNCCR with coating thickness of $1.4\mu\text{m}$ and $V_{\text{CNT}}=0.04$. These results have been already used in Figure 7.11 to validate the analytical method proposed in the current work.

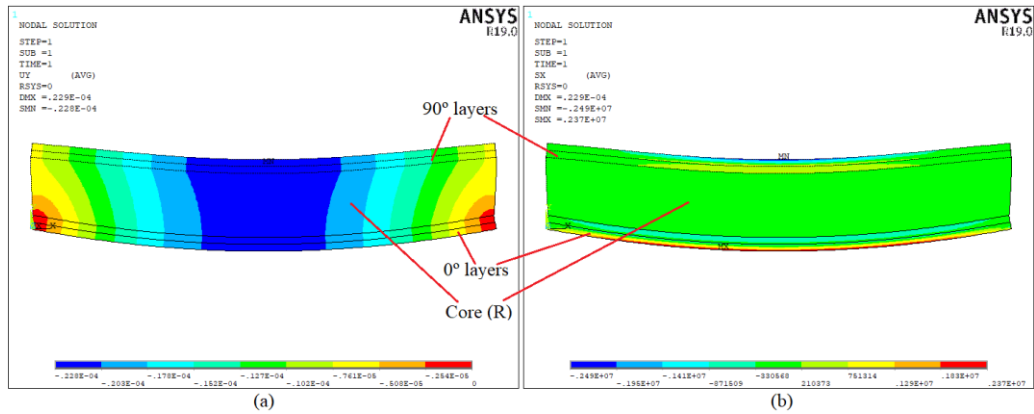


Figure 7.13: FEA contours of the sandwich CCFMC beam (L*4) (a) transverse displacement (b) axial stress [267]

Figure 7.14 demonstrates the influence of CNT coating thickness around the carbon fiber on the through-thickness distributions of the transverse shear stress, axial stress, and axial and transverse displacements in the sandwich beams L3 and L*3. It is noteworthy to indicate that the volume fraction is 0.08 for all thicknesses and was kept constant to investigate the mere effect of the coating thickness increment. Furthermore, the combination of RNCCR and ACCR coatings is utilized for 90° and 0° layers, respectively, in the sandwich beam L*3. The reason has arisen from the matter which was already mentioned as RNCCR type augments the mechanical properties in radial/ transverse direction while ACCR reinforce the composite structure in longitudinal direction. A glance at the Figure 7.14-d reveals a pronounced reduction of maximum transverse displacement with respect to the conventional composite beam for CNT coating thickness of 1μm and 1.4μm by 7.81 % and 11.489 %, respectively. Akin to the laminated beam, the increase of the structure's weight is negligible in this model due to the low volume fraction of the CNT in the coating region. Moreover, by reinforcing the laminates located upper and lower of the core materials by CNT coating, the transverse shear stress at the core medium (PVC) has diminished for coating thicknesses of 1μm and 1.4μm by 4.491 % and 6.667 %, respectively. Analogous to the outcomes of L*4, this reduction of the transverse shear stress in the core material postpones the likelihood of the failure mode, core shear, in the sandwich CFMC beam (L*3) with respect to the conventional sandwich beam (L3). It should be noted that the load carrying capacity has been considerably increased in the 90° layers since the CNT coating substantially enhances the Young's modulus in transverse/ radial direction with only CNT volume fraction of 0.08.

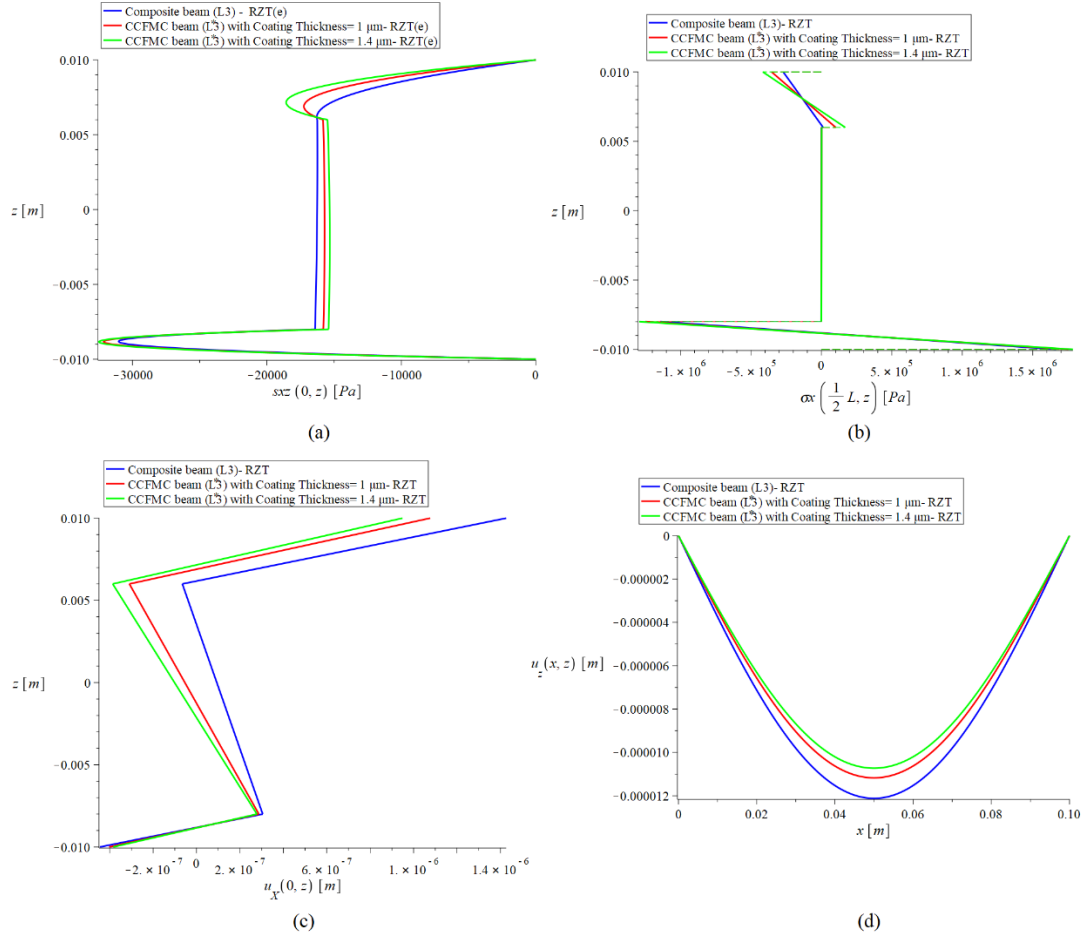


Figure 7.14: Through-thickness distributions for the sandwich beams L3 and L3*; L3* contains CNT volume fraction of 0.08 (a) transverse shear stress, (b) axial stress, (c) axial displacement and (d) transverse displacement along x-direction [267]

The effect of CNT volume fraction (inside the coating region) on the through-thickness distributions of the stresses and displacements are displayed in Figure 7.15 for laminates L7 and L7*. The CNT coating thickness of 1.4 μm is kept constant for all CNT volume fractions in L7* to assess the mere effect of CNT contents in the coating region. Given the graphs provided in Figure 7.15, an outstanding decrease in deflection of the laminated CFMC beam is demonstrated with respect to composite beam by 17.075 % and 26.473 % associated with CNT volume fractions of 0.04 and 0.08, respectively.

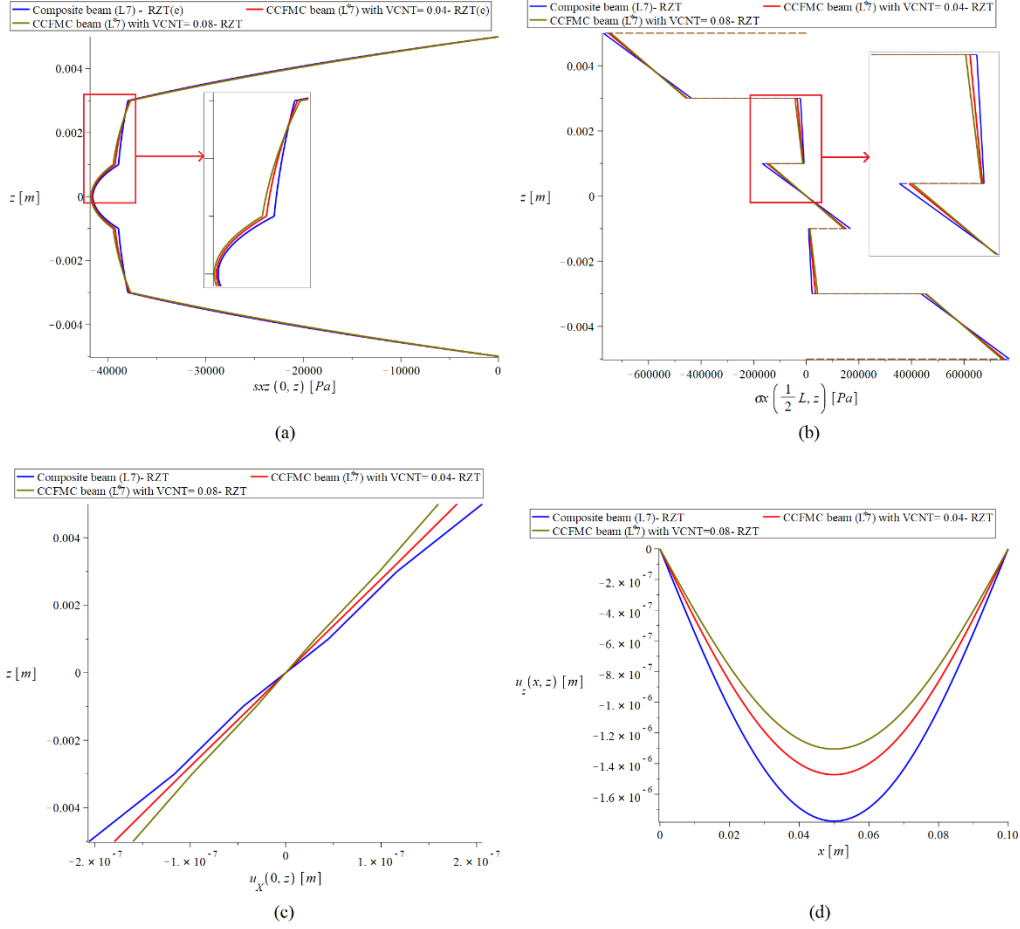


Figure 7.15: Through-thickness distributions versus CNT volume fraction for the laminated beams L7 and L7*; L7* consists of CNT coating thickness of 1.4 μm (a) transverse shear stress, (b) axial stress, (c) axial displacement and (d) transverse displacement along x-direction [267]

To provide a comparison regarding CNT volume fraction influence between laminated beam (represented in Figure 7.15) and sandwich beam, the stress analysis is also conducted for the sandwich beams considering various CNT contents. Figure 7.16 portrays the influence of CNT volume fraction on the through-thickness distributions of stresses and displacement for the sandwich beams L4 and L4*. The results reveal a notable decrease in transverse displacement of CFMC beam by 7.638 % and 13.635 % considering $V_{\text{CNT}} = 0.04$ and $V_{\text{CNT}} = 0.08$, respectively. Despite the low CNT loading in the coating region, the transverse shear stress of the core medium (which is Rohacell \textregistered foam in this model) has strikingly diminished in CFMC beam with respect to the conventional composite beam by 7.857 % (for $V_{\text{CNT}} = 0.04$) and 13.977 % (for $V_{\text{CNT}} = 0.08$).

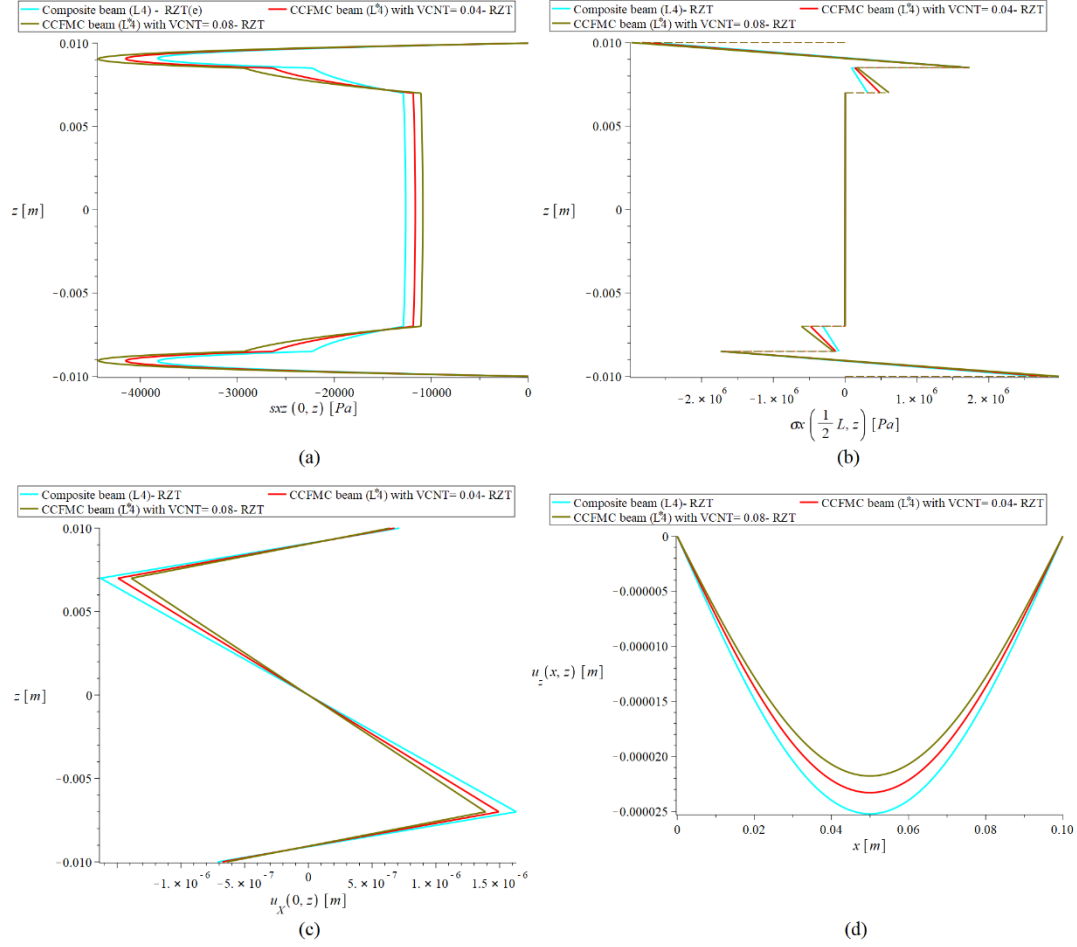


Figure 7.16: Through-the-thickness distributions versus CNT volume fraction for the sandwich beams L4 and L4*; L4* includes CNT coating thickness of 1.4 μm (a) transverse shear stress, (b) axial stress, (c) axial displacement and (d) transverse displacement along x-direction [267]

7.5 Conclusion

The current work is devoted to conduct the bending analysis of sandwich and laminated carbon nanotube coated–fiber multi-scale composite (CFMC) beams employing the Refined Zigzag theory (RZT). The model comprises core fiber, surrounding carbon nanotube (CNT) coating region and polymer matrix covering all scales from nano to macro-scale. The CNT coating region (CCR) includes CNT, matrix, and non-bonded interphase that its mechanical properties are acquired making use of the Eshelby–Mori–Tanaka method in conjunction with an equivalent continuum approach. Considering different configurations of grown CNTs around the core fiber, two CCRs are constructed consisting of axially aligned CCR (ACCR) and randomly oriented CCR (RNCCR). Appropriate techniques are employed at each scale and the outcomes are fed into the upper scale as input data. Having obtained the models' characteristics at macro scale, the RZT is utilized for stress analysis under transverse sinusoidal loading considering simply supported boundary conditions for both CFMC beam and conventional composite beam. The four RZT kinematic variables are obtained for CFMC beams and the effect of CNT volume fraction, coating thickness and coating types are thoroughly investigated for various laminated and sandwich beams. The results reveal a striking improvement in the stiffness of the laminated CFMC beam by which the maximum transverse deflection has been reduced by 26.13 % with respect to conventional composite beam. Regarding sandwich CFMC beam, the results manifest a remarkable decrease in transverse displacement by 10.71% with respect to sandwich beam, by adding small amount of CNTs in the coating region. Furthermore, a pronounced reduction is achieved in the transverse shear stress of the core medium of the sandwich CFMC beam by 11.23 % with respect to sandwich composite beam incorporating very low CNT contents which can postpone the core shear failure in the sandwich structures. In addition, the results disclose a significant decrease in maximum transverse displacement with respect to the conventional composite beam for CNT coating thickness of $1\mu\text{m}$ and $1.4\mu\text{m}$ by 7.81 % and 11.489 %, respectively. An outstanding decrease is demonstrated in deflection of the laminated CFMC beam with respect to composite beam by 17.075 % and 26.473 % associated with CNT volume fractions of 0.04 and 0.08, respectively. The results are in excellent agreement with the outcomes obtained by the finite element analysis; and the proposed technique can be employed as an accurate and efficient tool in designing of CNT coated–fibers multi-scale hybrid composites.

Conclusion/ Major Contributions/ Perspectives

The thesis aims to investigate the mechanical properties and stress analysis of carbon nanotube (CNT) coated–fiber multi-scale hybrid composites, which is called CCFM hybrid composite, through proposing analytical and numerical methods. Firstly, the mechanical properties of the CNT coating region have been calculated at the lower scales, nano, and micro scales. The outcomes are then utilized as input data for modeling at macro scale. The models consist of a core fiber, CNT coating region (CCR) and surrounding matrix, in which the coating region around the core fiber encompasses CNTs and matrix.

Regarding 3D finite element multi-scale modeling, a multi-scale model is constructed including carbon nanotubes, carbon fiber, non-bonded interphase region and surrounding matrix, spanning over different length scales from nano to macro scale. The non-bonded interphase region between CNTs and matrix is established employing cohesive zone model (CZM). The interfacial strength is assessed considering three different configurations of grown CNTs on the fiber surface, comprising radially, axially, and randomly oriented CNTs. The outcomes show a considerable reduction of fiber-matrix interfacial shear stresses in the hybrid composite containing axially and randomly oriented CNTs by 28.9% and 19.2 %, respectively, with solely 2 wt.% of CNTs. Regarding the two proposed hybrid systems, it is disclosed that composites with CNTs–coated fibers represent less interfacial stresses than those with CNT reinforcements mixed in matrix. Taking into account non-bonded interphase region between CNTs and surrounding matrix, the results manifest pronounced effect on the interfacial stresses, whereas no influence on the Young's moduli is observed, especially at lower volume fractions.

In the next step, the influence of carbon nanotube-coated carbon fibers on the thermal residual stresses of multi-scale hybrid composites is scrutinized. The established model encompasses unidirectional carbon fiber, coating region and surrounding matrix, in which the coating region around core fiber contains CNT and the polymer matrix. Three types of coating regions are considered around carbon fiber based on the three different configurations of grown CNTs on the fiber surface comprising axially, radially, and randomly oriented CNTs. Employing the Eshelby–Mori–Tanaka method in conjunction with an equivalent continuum approach, the mechanical properties of three different coating regions are calculated. A closed-form solution of the thermal residual stresses of multi- scale hybrid composite is attained utilizing the total energy minimization method. The results reveal a considerable decrease in the residual interfacial shear and radial stresses by 27% and 21%, respectively, in the hybrid composite with a coating region consisting of 1wt. % of randomly oriented CNTs. Significantly, the mentioned reduction of the interfacial residual stresses not only precludes the debonding between the fiber and

matrix, but also attenuates the effect of coefficient of thermal expansions mismatch between the carbon fiber and surrounding matrix. Furthermore, the results manifest a noticeable reduction of interfacial shear stress in the models with coating region comprising axially (ACCR) and randomly oriented CNTs (RNCCR) by 36.5% and 27%, respectively, whereas the coating region with radially oriented CNTs makes a slight contribution. In addition, it is disclosed that increasing the coating thickness reduces the maximum interfacial shear stress, radial stress, and fiber axial stress by 39.6 %, 32.8 % and 19.6 %, respectively, considering coating thickness of 1.1 μ m and small portion of CNTs at coating region.

Employing RZT and MT methods, the bending analysis of sandwich and laminated carbon nanotube coated–fiber multi-scale composite (CFMC) beams is carried out. The CNT coating region (CCR) includes CNT, matrix, and non-bonded interphase. Considering different configurations of grown CNTs around the core fiber, two CCRs are constructed consisting of axially aligned CCR (ACCR) and randomly oriented CCR (RNCCR). Appropriate techniques are employed at each scale and the outcomes are fed into the upper scale as input data. The RZT kinematic variables are obtained for CFMC beams and the effect of CNT volume fraction, coating thickness and coating types are thoroughly investigated for various laminated and sandwich beams. The results reveal a striking improvement in the stiffness of the laminated CFCM beam by which the maximum transverse deflection has been reduced by 26.13 % with respect to conventional composite beam. Regarding sandwich CFMC beam, the results manifest a remarkable decrease in transverse displacement by 10.71% with respect to sandwich beam, by adding small amount of CNTs in the coating region. Furthermore, a pronounced reduction is achieved in the transverse shear stress of the core medium of the sandwich CFMC beam by 11.23 % with respect to sandwich composite beam incorporating very low CNT contents which can postpone the core shear failure in the sandwich structures. In addition, the results disclose a significant decrease in maximum transverse displacement with respect to the conventional composite beam for CNT coating thickness of 1 μ m and 1.4 μ m by 7.81 % and 11.489 %, respectively. Regarding laminated CFMC beam, a considerable decrease is demonstrated in deflection with respect to composite beam by 17.075 % and 26.473 % associated with CNT volume fractions of 0.04 and 0.08, respectively. The results are in excellent agreement with the outcomes obtained by the finite element analysis and the proposed technique can be employed as an accurate and efficient tool in designing of CNT coated–fibers multi-scale hybrid composites. The major contributions/ achievements are highlighted as follows:

(i) Proposing a comprehensive multi-scale modeling (both concurrent and hierarchical approaches) to calculate the mechanical properties and interfacial stresses of CCFM Hybrid Composites. Covering all scales (and effective parameters at each scale) from nano to macro and taking into account deboning damage/ non-bonded interphase in the multi-scale modeling. A pronounced reduction of

interfacial stresses is obtained by introducing a gradient interphase around core fiber including CNT and matrix with negligible increase in the structure's weight.

(ii) Proposing an analytical approach to calculate the residual thermal stresses in CCFM hybrid composites utilizing MT method and total energy minimization method. The obtained reduction in the residual stresses not only prevents the debonding between the core fiber and matrix, but also attenuates the effect of coefficient of thermal expansions mismatch between the core fiber and surrounding matrix.

(iii) Proposing an analytical approach to carry out the bending analysis of laminated and sandwich CFMC beams employing RZT and MT methods. By incorporating very low portion of CNT in the coating region, significant reductions in maximum transverse deflection and transverse shear stress are obtained.

Some important points are mentioned by the author for future developments and a continuation of the research:

- (i) Considering CNT waviness and agglomeration at the nano and meso scales. The foregoing items could affect the mechanical properties of the CNTs and the mechanical properties of the CNT-coating regions by degree of agglomeration and CNT sinusoidal shape (including number of CNT's waves, amplitude of CNT wave and the starting angle).
- (ii) Performing a stress analysis through RZT, MT and multi-scale modeling for: a composite plate without considering through the thickness stretch/ deformation.
- (iii) Performing a stress analysis through RZT, MT and multi-scale modeling for: a composite plate considering through the thickness stretch/ deformation and delamination between the layers)
- (iv) Introducing other types of nanomaterials in the coating region such as nano-clay, graphene nano-platelet (GNPs), graphene oxide (GOs), etc.
- (v) Introducing the CNTs between the layers (interleaf concept) in the laminated composite structures to improve the interlaminar shear strength (ILSS) which is called nano-stitched structures.

References

- [1] B. Miller, P. Muri and L. Rebenfeld, "A microbond method for determination of the shear strength of a fiber/resin interface," *Compos Sci Technol*, vol. 28, no. 17–32, 1987.
- [2] U. Icardi, M. D. Sciuva and L. Librescu, "Dynamic response of adaptive cross-ply cantilevers featuring interlaminar bonding imperfections," *AIAA J*, vol. 38, p. 499–506, 2000.
- [3] U. Icardi and F. Sola, "Recovering critical stresses in sandwiches using through thickness reinforcement," *Compos Part B Eng*, vol. 54, p. 269–77, 2013.
- [4] U. Icardi and F. Sola, "Analysis of bonded joints with laminated adherends by a variable kinematics layerwise model," *Int J Adhes Adhes*, vol. 50, p. 244–54, 2014.
- [5] J.-K. Kim and Y.-W. Mai, *Engineered interfaces in fiber reinforced composites*, Elsevier, 1998.
- [6] C. Wang, X. He, L. Tong, Q. Peng, R. Wang, Y. Li and Y. Li, "Theoretical prediction and experimental verification of pulling carbon nanotubes from carbon fiber prepared by chemical grafting method," *Compos. A Appl. Sci. Manuf*, vol. 50, pp. 1-10, 2013.
- [7] S. I. Mohammad, D. Yan, T. Liyong, N. F. Shaikh, K. R. Anup, I. M. Andrew and G. G. Vincent, "Grafting carbon nanotubes directly onto carbon fibers for superior mechanical stability: Towards next generation aerospace composites and energy storage applications," *Carbon*, vol. 96, pp. 701-710, 2016.
- [8] L. Drzal, M. Rich and P. Lloyd, "Adhesion of graphite fibers to epoxy matrices: I. The role of fiber surface treatment," *J Adhes*, vol. 16, no. 1–30, 1983.
- [9] B. Agarwal and R. Bansal, "Effect of an interfacial layer on the properties of fibrous composites: a theoretical analysis," *Fibre Sci Technol*, vol. 12, no. 149–58, 1979.
- [10] M. Ho, H. Wang, K. Lau and J. Lee, "Interfacial bonding and degumming effects on silk fibre/polymer biocomposites," *Compos Part B Eng*, vol. 43, p. 2801–12, 2012.
- [11] H. Ghasemi, P. Kerfriden, S. Bordas, J. Muthu, G. Zi and T. Rabczuk, "Interfacial shear stress optimization in sandwich beams with polymeric core using non-uniform distribution of reinforcing ingredients," *Compos Struct*, vol. 120, p. 221–30, 2015.
- [12] A. Rodriguez, M. Guzman, C.-S. Lim and B. Minaie, "Mechanical properties of carbon nanofiber/fiber-reinforced hierarchical polymer composites manufactured with multiscale-reinforcement fabrics," *Carbon N Y*, vol. 49, p. 937–48, 2011.
- [13] Q. Song, K.-z. Li, H.-l. Li, H.-j. Li and C. Ren, "Grafting straight carbon nanotubes radially onto carbon fibers and their effect on the mechanical properties of carbon/carbon composites," *Carbon*, vol. 50, pp. 3949-3952, 2012.
- [14] M. Hassanzadeh-Aghdam, R. Ansari and A. Darvizeh, "Micromechanical analysis of carbon nanotube-coated fiber-reinforced hybrid composites," *International Journal of Engineering Science*, vol. 130, pp. 215-229, 2018.

- [15] V. Popov, "Carbon nanotubes: properties and application," *Materials Science and Engineering: R: Reports*, vol. 43, pp. 61-102, 2004.
- [16] P.-C. Ma, N. Siddiqui, G. Marom and J.-K. Kim, "Dispersion and functionalization of carbon nanotubes for polymer-based nanocomposites: A review," *Composites Part A: Applied Science and Manufacturing*, vol. 41, pp. 1345-1367, 2010.
- [17] D. Anthony, H. Qian, A. Clancy, E. Greenhalgh, A. Bismarck and M. Shaffer, "Applying a potential difference to minimise damage to carbon fibres during carbon nanotube grafting by chemical vapour deposition," *Nanotechnology*, vol. 28, p. 305602, 2017.
- [18] Q. Li, J.-S. Church, M. Naebe and B.-L. Fox, "A systematic investigation into a novel method for preparing carbon fibre–carbon nanotube hybrid structures," *Composites Part A: Applied Science and Manufacturing*, vol. 90, pp. 174-185, 2016.
- [19] J. Sebastian, N. Schehl, M. Bouchard, M. Boehle, L. Li, A. Lagounov and K. Lafdi, "Health monitoring of structural composites with embedded carbon nanotube coated glass fiber sensors," *Carbon N Y*, vol. 66, p. 191–200, 2014.
- [20] R. Li, N. Lachman, P. Florin, H. Wagner and B. Wardle, "Hierarchical carbon nanotube carbon fiber unidirectional composites with preserved tensile and interfacial properties," *Composites Science and Technology*, vol. 117, pp. 139-145, 2015.
- [21] B. Chen, X. Li, X. Li, Y. Jia, J. Yang, G. Yang and C. Li, "Friction and Wear Properties of Polyimide-Based Composites with a Multiscale Carbon Fiber-Carbon Nanotube Hybrid," *Tribol Lett*, vol. 65, p. 111, 2017.
- [22] R. Grow, "Electromechanical properties and applications of carbon nanotubes," in *Carbon Nanotubes: Properties and Applications*, Boca Raton, FL, CRC Press, 2006.
- [23] R. Ghasempour and H. Narei, "CNT Basics and Characteristics," in *Carbon Nanotube-Reinforced Polymers*, Elsevier, 2018, pp. 1-24.
- [24] S. Iijima, "Helical microtubules of graphitic carbon," *Nature*, vol. 354, p. 56–58, 1991.
- [25] S. Iijima and T. Ichihashi, "Single-shell carbon nanotubes of 1-nm diameter," *Nature*, vol. 363, p. 603–605, 1993.
- [26] D. Bethune, C. Klang, M. d. Vries, G. Gorman, R. Savoy, J. Vazquez and e. al, "Cobalt-catalysed growth of carbon nanotubes with single-atomic-layer walls," *Nature*, vol. 363, p. 605–607, 1993.
- [27] Q. Zhang, *Carbon Nanotubes and Their Applications*, Jenny Stanford Publishing, 2012.
- [28] C. Rao, R. Voggu and A. Govindaraj, "Selective generation of single-walled carbon nanotubes with metallic, semiconducting and other unique electronic properties," *Nanoscale* 1, p. 96–105, 2009.
- [29] R. Ghasempour, S. Mortazavi, A. I. zad and F. Rahimi, "Hydrogen sensing properties of multiwalled carbon nanotube films sputtered by Pd," *Int. J. Hydrogen Energy*, vol. 35 (2), no. 2010, p. 4445–4449.

- [30] L. Wen, F. Li and H. Cheng, "Carbon Nanotubes and Graphene for Flexible Electrochemical Energy Storage: from Materials to Devices," *Advance. Material*, vol. 28, p. 4306–4337, 2016.
- [31] R. Ghasempour, A. Irajizad and M. H. Nezhad, "Design and fabrication of sensitive carbon nanotubes/PMMA film for Acetone vapour detection," *Int. J. Nanomanuf*, vol. 5 , p. 268–277, 2010.
- [32] M. Meyyappan, Carbon Nanotubes: Science and Applications, Boca Raton, FL: CRC Press, 2005.
- [33] M. Dresselhaus, G. Dresselhaus and A. Jorio, "Unusual properties and structure of carbon nanotubes," *Annu. Rev. Mater. Res.*, vol. 34, p. 247–278, 2004.
- [34] N. Hamada, S. Sawada and A. Oshiyama, "New one-dimensional conductors: graphitic microtubules," *Phys. Rev. Lett.*, vol. 68, p. 1579–1581, 1992.
- [35] T. Odom, J. Huang, P. Kim and C. Lieber, "Atomic structure and electronic properties of singlewalled carbon," *Nature*, vol. 391, p. 62–64, 1998.
- [36] R. Saito, M. Fujita, G. Dresselhaus and M. Dresselhaus, "Electronic structure of chiral graphene tubules," *Appl. Phys. Lett.*, vol. 60, p. 2204, 1992.
- [37] J. Bernholc, D. Brenner, M. Nardelli, V. Meunier and C. Roland, "Mechanical and electrical properties of nanotubes," *Annu. Rev. Mater. Res.*, vol. 32, p. 347–375, 2002.
- [38] S. Tans, M. Devoret, H. Dai, A. Thess, R. Smalley, L. Geerligs and e. al, "Individual single-wall carbon nanotubes as quantum wires," *Nature* , vol. 386, p. 474–477, 1997.
- [39] M. Bockrath, D. Cobden, P. McEuen, B. Chspira, N. Ettl, A. Thess and e. al, "Single-electron transport in ropes of carbon nanotubes," *Science*, vol. 80 (275), p. 1922–1925, 1997.
- [40] S. Frank, P. Poncharal, Z. Wang and W. d. Heer, "Carbon nanotube quantum resistors," *Science* , vol. 80 (280), p. 1744–1746, 1998.
- [41] J. Lu, "Elastic properties of carbon nanotubes and nanoropes," *Phys. Rev. Lett.*, vol. 79, p. 1297–1300, 1997.
- [42] E. Wong, P. Sheehan and C. Lieber, "Nanobeam mechanics: elasticity, strength, and toughness of nanorods and nanotubes," *Science* , vol. 80 (277), p. 1971–1975, 1997.
- [43] R. Malekimoghadam, S. Hosseini and M. Salehi, "The influence of Stone–Thrower–Wales defect on vibrational characteristics of single-walled carbon nanotubes incorporating Timoshenko beam element," *Physica E: Low-dimensional Systems and Nanostructures*, vol. 62, pp. 80-89, 2014.
- [44] J. Lu and J. Han, "Carbon nanotubes and nanotube-based nano devices," *Int. J. High Speed Electron. Syst.*, vol. 9, p. 101–123, 1998.
- [45] R. Rafiee and M. Heidarhaei, "Investigation of chirality and diameter effects on the Young's modulus of carbon nanotubes using non-linear potentials," *Compos. Struct.*, vol. 94 , p. 2460–2464, 2012.
- [46] S. Iijima, C. Brabec, A. Maiti, J. Bernholc and S. Iijima, "Structural flexibility of carbon nanotubes," *J. Chem. Phys.*, vol. 104, p. 2089–2092, 1996.
- [47] J. Hone, M. Whitney, C. Piskoti and A. Zettl, "Thermal conductivity of single-walled carbon nanotubes," *Phys. Rev. B* , vol. 59, p. 2514–2516, 1999.

- [48] J. Saxby, S. Chatfield, A. Palmisano, A. Vassallo, M. Wilson and L. Pang, "Thermogravimetric analysis of buckminsterfullerene and related materials in air," *J. Phys. Chem.*, vol. 96, p. 17–18, 1992.
- [49] S. Jafari, "Engineering Applications of Carbon Nanotubes," in *Carbon Nanotube-Reinforced Polymers*, Elsevier, 2018, pp. 25-40.
- [50] B. Edwards and E. Westling, *The Space Elevator*, San Francisco: Spaseo Inc., 2003.
- [51] G. Overney, W. Zhong and D. Tomanek, "Structural rigidity and low frequency vibrational modes of long carbon tubules," *Z. Phys. D.*, vol. 27 (93), p. 406, 1993.
- [52] M. Treacy, T. Ebbesen and J. Gibson, "Exceptionally high Young's modulus observed for individual carbon nanotubes," *Nature*, vol. 381, p. 678–680, 1996.
- [53] R. Jatli, K. Arora, N. Anuragi, R. Kaushal and V. Jain, "Carbon nanotubes: advancement in science and technology," *World J. Pharm. Pharm. Sci.*, vol. 4 (07), p. 1533–1550, 2015.
- [54] L. Jin, C. Bower and O. Zhou, "Alignment of carbon nanotubes in a polymer matrix by mechanical stretching," *Appl. Phys. Lett.*, vol. 73, p. 1197–1199, 1998.
- [55] J. Coleman, U. Khan, W. Blau and Y. Gun'ko, "Small but strong: a review of the mechanical properties of carbon nanotube–polymer composites," *Carbon*, vol. 44, p. 1624, 2006.
- [56] T. Chou, L. Gao, E. Thostenson and J. B. Z. Zhang, "An assessment of the science and technology of carbon nanotube-based fibers and composites," *Compos. Sci. Technol.*, vol. 70 (1), p. 1–19, 2010.
- [57] E. A. Thomson, MIT News Office, 5 March 2009. [Online]. Available: <http://news.mit.edu/2009/nanostitching-could-lead-much-stronger-airplane-skins-more>.
- [58] K. Ng, W. Lam and S. Pichiah, "A review on potential applications of carbon nanotubes in marine current turbines," *Renew. Sust. Energ. Rev.*, vol. 28, p. 331–339, 2013.
- [59] Z. Wu, "Transparent, conductive carbon nanotube films," *Science*, vol. 305, p. 1273, 2004.
- [60] I. Akyildiz and J. Jornet, "Electromagnetic wireless nanosensor networks," *J. Nano Commun. Netw.*, vol. 1 (1), p. 3–19, 2010.
- [61] S. Park, P. Theilmann, P. Asbeck and P. Bandaru, "Enhanced electromagnetic interference shielding through the use of functionalized carbon nanotube-reactive polymer composites," *IEEE, TNANO-00013*, p. 1–6, 2009.
- [62] M. Orcutt, "IBM reports breakthrough on carbon nanotube transistors," *MIT Technol. Rev.*, 1 October 2015. [Online]. Available: <https://www.technologyreview.com/s/541921/ibm-reports-breakthrough-oncarbon-nanotube-transistors/>.
- [63] R. Malekimoghadam and R. Rafiee, "Carbon Nanotubes Processing," in *Carbon Nanotube-Reinforced Polymers*, Elsevier, 2018, pp. 41-59.
- [64] G. Pal and S. Kumar, "Mechanical Properties of Isolated Carbon Nanotube," in *Carbon Nanotube-Reinforced Polymers*, Elsevier, 2018, pp. 173-199.

- [65] J. Muster, M. Burghard, S. Roth, G.-S. Duesberg, E. Hernandez and A. Rubio, "Scanning force microscopy characterization of individual carbon nanotubes on electrode arrays," *J. Vac. Sci. Technol.*, vol. 16, no. 5, p. 2796–2801, 1998.
- [66] A. Krishnan, E. Dujardin, T.-W. Ebbesen, P.-N. Yianilos and M.-M.-J. Treacy, "Young's modulus of single-walled nanotubes," *Phys. Rev. B*, vol. 58, p. 14013–14019, 1998.
- [67] J.-P. Salvetat, G.-A. Briggs, J.-M. Bonard, R.-R. Bacsa, A.-j. Kulik, T. Stöckli and e. al, "Elastic and shear moduli of single-walled carbon nanotube ropes," *Phys Rev Lett*, vol. 82, p. 944, 1999.
- [68] M.-F. Yu, B.-S. Files, S. Arepalli and R.-S. Ruoff, "Tensile loading of ropes of single wall carbon nanotubes and their mechanical properties," *Phys. Rev. Lett.*, vol. 84, p. 5552–5555, 2000.
- [69] T.-W. Tombler, C. Zhou, L. Alexseyev, J. Kong, H. Dai, L. Liu, C.-S. Jayanthi, M. Tang and S.-Y. Wu, "Reversible electromechanical characteristics of carbon nanotubes under local-probe manipulation," *Nature*, vol. 405, p. 769–772, 2000.
- [70] B.-G. Demczyk, Y.-M. Wang, J. Cumings, M. Hetman, W. Han, A. Zettl and R.-O. Ritchie, "Direct mechanical measurement of the tensile strength and elastic modulus of multiwalled carbon nanotubes," *Mater. Sci. Eng. A*, vol. 334, no. 12, p. 173–178, 2002.
- [71] G. Guhados, W.-K. Wan, X.-L. Sun and J.-L. Hutter, "Simultaneous measurement of Young's and shear moduli of multiwalled carbon nanotubes using atomic force microscopy," *J. Appl. Phys.*, vol. 101, p. 033514, 2007.
- [72] W. Ding, L. Calabri, K.-M. Kohlhaas, X. Chen, D.-A. Dikin and R.-S. Ruoff, "fracture strength, and brittle vs. plastic response of the outer shell of arc-grown multiwalled carbon nanotubes," *Exp. Mech.*, vol. 47, no. 1, p. 25–36, 2007.
- [73] Y. Wu, M. Huang, F. Wang, X.-M.-H. Huang, S. Rosenblatt, L. H. Yan, S.-P. O'Brien, J. Hone and T.-F. Heinz, "Determination of the Young's modulus of structurally defined carbon nanotubes," *Nano Lett.*, vol. 8, no. 12, p. 4158–4161, 2008.
- [74] W.-H. Chen, H.-C. Cheng and Y.-L. Liu, "Radial mechanical properties of single-walled carbon nanotubes using modified molecular structure mechanics," *Comput. Mater. Sci.*, vol. 47 (4), p. 985–993, 2010.
- [75] M. Ganji, A. Fereidoon, M. Jahanshahi and M. Ahangari, "Investigation of the mechanical properties of multiwalled carbon nanotubes using density functional theory calculations," *J. Comput. Theor. Nanosci.*, vol. 9 (7), p. 980–985, 2012.
- [76] K.-M. Liew, X.-Q. He and C.-H. Wong, "On the study of elastic and plastic properties of multi-walled carbon nanotubes under axial tension using molecular dynamics simulation," *Ada Mater.*, vol. 52 (9), p. 2521–2527, 2004.
- [77] R. Rafiee and R. Malekimoghadam, "On the modeling of carbon nanotubes: A critical review," *Composites Part B: Engineering*, vol. 56, pp. 435–449, 2014.
- [78] B.-I. Yakobson, C.-J. Brabec and J. Bernholc, "Structural mechanics of carbon nanotubes: from continuum elasticity to atomistic fracture," *J Comput Aided Mater Des*, vol. 3, p. 173–82, 1996.
- [79] N. Silvestre, C.-MWang, Y.-Y. Z. YY and Y. Xiang, "Sanders shell model for buckling of single-walled carbon nanotubes with small aspect ratio," *Compos Struct*, vol. 93, p. 1683–91, 2011.

- [80] L.-H. Donnell, "Stability of thin-walled tubes under torsion," 1933NACA Report, No. 479.
- [81] J.-L. Sanders, "Non-linear theories for thin shells," *Quart J Appl Math*, vol. 21, p. 21–36, 1963.
- [82] K.-I. Tserpes, P. Papanikos, G. Labeas and S.-G. Pantelakis, "Multi-scale modeling of tensile behavior of carbon nanotube-reinforced composites," *Theoretical and Applied Fracture Mechanics*, vol. 49, pp. 51-60, 2008.
- [83] L.-H. Donnell, "Stability of thin-walled tubes under torsion," 1933NACA Report, No. 479.
- [84] L. Li, Y. Hu and L. Ling, "Flexural wave propagation in small-scaled functionally graded beams via a nonlocal strain gradient theory," *Composite Structures*, vol. 133, pp. 1079-1092, 2015.
- [85] A. Eringen, "On differential equations of nonlocal elasticity and solutions of screw dislocation and surface waves," *Journal of Applied Physics*, vol. 54 , no. 9, pp. 4703-4710, 1983.
- [86] L. Li and Y. Hu, "Wave propagation in fluid-conveying viscoelastic carbon nanotubes based on nonlocal strain gradient theory," *Computational Materials Science*, vol. 112, pp. 282-288, 2016.
- [87] C.-W. Lim, G. Zhang and J.-N. Reddy, "A higher-order nonlocal elasticity and strain gradient theory and its applications in wave propagation," *Journal of the Mechanics and Physics of Solids*, vol. 78, pp. 298-313, 2015.
- [88] N. Challamel and C.-M. Wang, "The small length scale effect for a non-local cantilever beam: a paradox solved," *Nanotechnology*, vol. 19, no. 34, p. 345703, 2008.
- [89] E.-C. Aifantis, "On the role of gradients in the localization of deformation and fracture," *International Journal of Engineering Science*, vol. 30, no. 10, pp. 1279-1299, 1992.
- [90] M. Fakhraadi, "Application of Modified Couple Stress Theory and Homotopy Perturbation Method in Investigation of Electromechanical Behaviors of Carbon Nanotubes," *Advances in Applied Mathematics and Mechanics*, vol. 9, no. 1, pp. 23-42, 2017.
- [91] C. Li and T.-W. Chou, "A structural mechanics approach for the analysis of carbon nanotubes," *International Journal of Solids and Structures*, vol. 40, no. 10, pp. 2487-2499, 2003.
- [92] G. Domínguez-Rodríguez, A. Tapia and F. Avilés, "An assessment of finite element analysis to predict the elastic modulus and Poisson's ratio of singlewall carbon nanotubes," *Computational Materials Science*, vol. 82, pp. 257-263, 2014.
- [93] K.-I. Tserpes and P. Papanikos, "Finite element modeling of single-walled carbon nanotubes," *Composites: Part B*, vol. 36, p. 468–77, 2005.
- [94] A.-L. Kalamkarov, A.-V. Georgiades, S.-K. Rokkam, V.-P. Veedu and M.-N. Ghasemi-Nejhad, "Analytical and numerical techniques to predict carbon nanotubes properties," *International Journal of Solids and Structures*, vol. 43, no. 22–23, pp. 6832-6854, 2006.
- [95] G.-I. Giannopoulos, P.-A. Kakavas and N.-K. Anifantis, "Evaluation of the effective mechanical properties of single walled carbon nanotubes using a spring based finite element approach," *Comput Mater Sci*, vol. 41, p. 561–9, 2008.

- [96] M.-. M. Shokrieh and R. Rafiee, "On the tensile behavior of an embedded carbon nanotube in polymer matrix with non-bonded interphase region," *Composite Structures*, vol. 92, no. 3, pp. 647-652, 2010.
- [97] R. Rafiee and R. Malekimoghadam, "Simulation of impact and post-impact behavior of carbon nanotube reinforced polymer using multi-scale finite element modeling," *Computational Materials Science*, vol. 63, pp. 261-268, 2012.
- [98] A. Sakhaee-Pour, M.-T. Ahmadian and A. Vafai, "Vibrational analysis of single-walled carbon nanotubes using beam element," *Thin-Walled Structures*, vol. 47, no. 6-7, pp. 646-652, 2009.
- [99] M. Meo and M. Rossi, "Prediction of Young's modulus of single wall carbon nanotubes by molecular-mechanics based finite element modelling," *Composites Science and Technology*, vol. 66, no. 11-12, pp. 1597-1605, 2006.
- [100] T.-K. Gupta and S. Kumar, "Fabrication of Carbon Nanotube/Polymer Nanocomposites," in *Carbon Nanotube-Reinforced Polymers*, Elsevier, 2018, pp. 61-81.
- [101] T.-K. Gupta, B.-P. Singh, S. Teotia, V. Katyal, S.-R. Dhakate and R.-B. Mathur, "Designing of multiwalled carbon nanotubes reinforced polyurethane composites as electromagnetic interference shielding materials," *J. Polym. Res.* , vol. 20 (6) , p. 1-7, 2013.
- [102] C.-A. Cooper, D. Ravich, D. Lips, J. Mayer and H.-D. Wagner, "Distribution and alignment of carbon nanotubes and nanofibrils in a polymer matrix," *Compos. Sci. Technol.* , vol. 62 (7), p. 1105-1112, 2002.
- [103] S. Srivastava and N.-A. Kotov, "Composite layer-by-layer (LBL) assembly with inorganic nanoparticles and nanowires," *Acc. Chem. Res.*, vol. 41 (12), no. 12, p. 1831-1841, 2008.
- [104] S. Teotia, B.-P. Singh, I. Elizabeth, V.-N. Singh, R. Ravikumar, A.-P. Singh and e. al., "Multifunctional, robust, light-weight, free-standing MWCNT/phenolic composite paper as anodes for lithium ion batteries and EMI shielding material," *RSC Adv.* 4, vol. 63, p. 33168-33174, 2014.
- [105] A. Pantano, "Mechanical Properties of CNT/Polymer," in *Carbon Nanotube-Reinforced Polymers*, Elsevier, 2018, pp. 201-232.
- [106] M. E. Achaby and A. Qaiss, "Processing and properties of polyethylene reinforced by graphene nanosheets and carbon nanotubes," *Mater. Des.* , vol. 44, p. 81, 2013.
- [107] B.-X. Yang, K.-P. Pramoda, G.-Q. Xu and S.-H. Goh, "Mechanical Reinforcement of Polyethylene Using Polyethylene-Grafted Multiwalled Carbon Nanotubes," *Adv. Funct. Mater.* , vol. 17, p. 2062, 2007.
- [108] R.-E. Gorga and R.-E. Cohen, "Toughness enhancements in poly(methyl methacrylate) by addition of oriented multiwall carbon nanotubes," *J. Polym. Sci. B* , vol. 42, p. 2690, 2004.
- [109] K.-H. Kim and W.-H. Jo, "Improvement of tensile properties of poly(methyl methacrylate) by dispersing multi-walled carbon nanotubes functionalized with poly(3-hexylthiophene)-graft-poly(methyl methacrylate)," *Compos. Sci. Technol.* , vol. 68, p. 2120, 2008.

- [110] Y.-S. Song and J.-R. Youn, "Influence of dispersion states of carbon nanotubes on physical properties of epoxy nanocomposites," *Carbon*, vol. 43, p. 1378, 2005.
- [111] H. Rajoria and N. Jalili, "Passive vibration damping enhancement using carbon nanotube-epoxy reinforced composites," *Compos. Sci. Technol.*, vol. 65, p. 2079, 2005.
- [112] J. Cha, G.-H. Jun, J.-K. Park, J.-C. Kim, H.-J. Ryu and S.-H. Hong, "Improvement of modulus, strength and fracture toughness of CNT/Epoxy nanocomposites through the functionalization of carbon nanotubes," *Composites Part B: Engineering*, vol. 129, pp. 169-179, 2017.
- [113] A.-V. Desai and M.-A. Haque, "Mechanics of the interface for carbon nanotube polymer composites," *Thin Wall. Struct.*, vol. 43, p. 1854–1860, 2011.
- [114] N. Vu-Bac, T. Rabczuk and X. Zhuang, "Continuum/Finite Element Modeling of Carbon Nanotube–Reinforced Polymers," in *Carbon Nanotube-Reinforced Polymers*, Elsevier, 2018, pp. 385-409.
- [115] N. Vu-Bac, T. Lahmer, Y. Zhang, X. Zhuang and T. Rabczuk, "Stochastic predictions of interfacial characteristic of polymeric nanocomposites (PNCs)," *Compos. B*, vol. 59, p. 80–95, 2014.
- [116] L. Battezzati, C. Pisani and F. Ricca, "Equilibrium conformation and surface motion of hydrocarbon molecules physisorbed on graphit," *J Chem Soc Faraday Trans 2 Mol Chem Phys*, vol. 71, p. 1629–39, 1975.
- [117] J.-M. Wernik and S.-A. Meguid, "Multiscale modeling of the nonlinear response of nano-reinforced polymers," *Acta Mech.*, vol. 1, p. 1–16, 2011.
- [118] ANSYS, "Mechanical APDL Theory Reference," ANSYS Inc., 2019.
- [119] S.-B. Sinnott, "Chemical Functionalization of Carbon Nanotubes," *J. Nanosci. Nanotechnol.*, vol. 2, p. 113–123, 2002.
- [120] H. Wan, F. Delale and L. Shen, "Effect of CNT length and CNT-matrix interphase in carbon nanotube (CNT) reinforced composites," *Mechanics Research Communications*, vol. 32, no. 5, pp. 481-489, 2005.
- [121] C. Li and T.-W. Chou, "Multiscale modeling of compressive behavior of carbon nanotube/polymer composites," *Composites Science and Technology*, vol. 66, no. 14, pp. 2409-2414, 2006.
- [122] M.-M. Shokrieh and R. Rafiee, "Prediction of mechanical properties of an embedded carbon nanotube in polymer matrix based on developing an equivalent long fiber," *Mechanics Research Communications*, vol. 37, no. 2, pp. 235-240, 2010.
- [123] S.-K. Georgantzinos, G.-I. Giannopoulos and N.-K. Anifantis, "Investigation of stress–strain behavior of single walled carbon nanotube/rubber composites by a multi-scale finite element method," *Theoretical and Applied Fracture Mechanics*, vol. 52, no. 3, pp. 158-164, 2009.
- [124] R. Hill, "Elastic properties of reinforced solids: some theoretical principles," *J. Mech. Phys. Solids*, vol. 11, p. 357–372, 1963.
- [125] M. Silani, H. Talebi, S. Ziaei-Rad, P. Kerfriden, S. Bordas and T. Rabczuk, "Stochastic modeling of clay/ epoxy nanocomposites," *Compos. Struct.*, vol. 118, p. 241–249, 2014.

- [126] R. Rafiee and V. Firouzbakht, "Stochastic Multiscale Modeling of CNT/Polymer," in *Carbon Nanotube-Reinforced Polymers*, Elsevier, 2018, pp. 503-520.
- [127] M.-M. Shokrieh and R. Rafiee, "Stochastic multi-scale modeling of CNT/polymer composites," *Computational Materials Science*, vol. 50, no. 2, pp. 437-446, 2010.
- [128] R.-M. Jones, *Mechanics of Composite Materials*, Taylor & Francis, Inc., 1999.
- [129] T. Belytschko and J.-H. Song, "Coarse-graining of multiscale crack propagation," *Int. J. Numer. Meth. Eng.*, vol. 81 (5), p. 537–563, 2010.
- [130] M. Silani, T. Rabczuk and X. Zhuang, "Computational Multiscale Modeling of Carbon Nanotube–Reinforced Polymers," in *Carbon Nanotube-Reinforced Polymers*, Elsevier, 2018, pp. 465-477.
- [131] H.-B. Dhia, "The Arlequin method: a partition of models for concurrent multiscale analyses," in *Proceedings of the Challenges in Computational Mechanics Workshop*, 2006 (10,p.12).
- [132] A. Montazeri and B. Mehrafrooz, "Theoretical Modeling of CNT–Polymer Interactions," in *Carbon Nanotube-Reinforced Polymers*, Elsevier, 2018, pp. 347-383.
- [133] F. Avilés and A.-I. O.-A. J. Kú-Herrera, "Deposition of Carbon Nanotubes on Fibers," in *Carbon Nanotube-Reinforced Polymers*, Elsevier, 2018, pp. 117-144.
- [134] M. Zahedi, R. Malekimoghadam, R. Rafiee and U. Icardi, "A study on fracture behavior of semi-elliptical 3D crack in clay-polymer nanocomposites considering interfacial debonding," *Engineering Fracture Mechanics*, vol. 209, pp. 245-259, 2019.
- [135] J.-H. Park and S.-C. Jana, "The relationship between nano- and micro-structures and mechanical properties in PMMA–epoxy–nanoclay composite," *Polymer*, vol. 44, no. 7, p. 2091–100, 2003.
- [136] Y. Zhou, F. Pervin, M.-A. Biswas, V.-K. Rangari and S. Jeelani, "Fabrication and characterization of montmorillonite clay-filled SC-15 epoxy," *Mater Lett*, vol. 60, no. 7, p. 869–73, 2006.
- [137] S. Saber-Samandari, A. Afaghi-Khatibi and D. Basic, "An experimental study on clay-epoxy nanocomposites produced in a centrifuge," *Composites Part B*, vol. 38, no. 1, pp. 102-107, 2007.
- [138] S.-A. Hosseini, S. Saber-Samandari and R. Malekimoghadam, "Multiscale modeling of interface debonding effect on mechanical properties of nanocomposites," *Polym Compos*, vol. 38, p. 789–96, 2017.
- [139] M. Zappalorto, M. Salviato and M. Quaresimin, "A multiscale model to describe nanocomposite fracture toughness enhancement by the plastic yielding of nanovoids," *Compos Sci Technol*, vol. 72, pp. 1683-1691, 2012.
- [140] N. Vu-Bac, M. Silani, T. Lahmer, X. Zhuang and T. Rabczuk, "A unified framework for stochastic predictions of mechanical properties of polymeric nanocomposites," *Comput Mater Sci*, vol. 96, pp. 520-535, 2015.
- [141] M. Silani, H. Talebi, S. Ziaei-Rad, P. Kerfriden, S. Bordas and T. Rabczuk, "Stochastic Modelling of Clay/Epoxy Nanocomposites," *Compos Struct*, vol. 118, pp. 241-249, 2014.

- [142] M. Heydari-Meybodi, S. Saber-Samandari and M. Sadighi, "A new approach for prediction of elastic modulus of polymer/nanoclay composites by considering interfacial debonding: Experimental and numerical investigations," *Compos Sci Technol* , vol. 117, pp. 379-385, 2015.
- [143] B. Wang, N. Qi, W. Gong, X.-W. Li and Y.-P. Zhen, "Study of microstructure and mechanical properties for epoxy resin/montmorillonite nanocomposites by positron," *Radiat Phys Chem* , vol. 76, p. 146–9, 2007.
- [144] H.-Z. Shi, T. Lan and T.-J. Pinnavaia, "Interfacial effects on the reinforcement properties of polymer–organoclay nanocomposites," *Chem Mater* , vol. 8, p. 1584–7, 1996.
- [145] R. Rafiee and R. Shahzadi, "Mechanical Properties of Nanoclay and Nanoclay Reinforced Polymers:A Review," *Polym. Compos.*, vol. 40, pp. 431-445, 2019.
- [146] W.-j. Boo, L. Sun, J. Liu, E. Moghbelli, A. Clearfield, H.-J. Sue, H. Pham and N. Verghese, "Effect of nanoplatelet dispersion on mechanical behaviour of polymer nanocomposites," *J. Polym. Sci., Part B: Polym. Phys.*, vol. 45, p. 1459–69, 2007.
- [147] S.-C. Tjong and S.-P. Bao, "Fracture toughness of high density polyethylene/SEBS-g-MA/montmorillonite nanocomposites," *Compos Sci Technol* , vol. 67, no. 2, pp. 314-323, 2007.
- [148] Y. Rostamiyan, A.-B. Fereidoon, A. H. Mashhadzadeh and M.-A. Khalili, "Augmenting epoxy toughness by combination of both thermoplastic and nanolayered materials and using artificial intelligence techniques for modeling and optimization," *J Polym Res* , vol. 20, p. 135, 2013.
- [149] R. Malekimoghadam, S. Saber-Samandari and S.-A. Hosseini, "On the tensile behavior of clay–epoxy nanocomposite considering interphase debonding damage via mixed-mode cohesive zone material," *Composites Part B: Engineering*, vol. 89, pp. 303-315, 2016.
- [150] G.-S. Venkatesh, A. Deb and A. Karmarkar, "Characterization and finite element modeling of montmorillonite/polypropylene nanocomposites," *Mater. Des.*, vol. 35, p. 425–433, 2012.
- [151] L. Figiel, "Effect of the interphase on large deformation behaviour of polymer–clay nanocomposites near the glass transition: 2D RVE computational modeling," *Comput Mater Sci* , vol. 84, p. 44–254, 2014; .
- [152] M. Silani, S. Ziaei-Rad, M. Esfahanian and V.-B.-C. Tan, "On the experimental and numerical investigation of clay/epoxy nanocomposites," *Compos Struct* , vol. 94, p. 3142–3148, 2012.
- [153] G. Dai and L. M. Jr, "Damage evolution in nanoclay-reinforced polymers: A three-dimensional computational study," *Compos Sci Technol* , vol. 74, p. 67–77, 2013.
- [154] M. Silani, S. Ziaei-Rad, H. Talebi and T. Rabczuk, "A Semi-Concurrent Multiscale Approach for Modeling Damage in Nanocomposites," *Theor Appl Fract Mec* , vol. 74, pp. 30-38, 2014.
- [155] M.-A. Msekh, N.-H. Cuong, G. Zi, P. Areias, X. Zhuang and T. Rabczuk, "Fracture properties prediction of clay/epoxy nanocomposites with interphase zones using a phase field model," *Eng Fract Mech*, vol. 188, pp. 287-299, 2018.

- [156] P.-R. Budarapu, R. Gracie, S.-W. Yang, X. Zhuang and T. Rabczuk, "Efficient coarse graining in multiscale modeling of fracture," *Theor Appl Fract Mec* , vol. 69, pp. 126-143, 2014.
- [157] H. Talebi, M. Silani and T. Rabczuk, "Concurrent multiscale modeling of three dimensional crack and dislocation propagation," *Adv Eng Softw* , vol. 80, pp. 82-92, 2015.
- [158] K. Anoukou, F. Zaïri, M. Naït-Abdelaziz, A. Zaoui, T. Messenger and J.-M. Gloaguen, "On the overall elastic moduli of polymer–clay nanocomposite materials using a self-consistent approach. Part I: Theory," *Composites Science and Technology*, vol. 71, no. 2, pp. 197-205.
- [159] A. Usuki, Y. Kojima, M. Kawasumi and e. al., "Synthesis of nylon 6-clay hybrid," *Journal of Materials Research*, vol. 8, p. 1179–1184, 1993.
- [160] G. Zhang, Z. Wei and R.-E. Ferrell, "Elastic modulus and hardness of muscovite and rectorite determined by nanoindentation," *Applied Clay Science*, vol. 43, no. 2, pp. 271-281, 2009.
- [161] J.-J. Luo and I.-M. Daniel, "Characterization and modeling of mechanical behavior of polymer/clay nanocomposites," *Composites Science and Technology*, vol. 63, no. 11, pp. 1607-1616, 2003.
- [162] X. Li, H. Gao, W.-A. Scrivens, D. Fei, V. Thakur, M.-A. Sutton, A.-P. Reynolds and M.-L. Myrick, "Structural and mechanical characterization of nanoclay-reinforced agarose nanocomposites," *Nanotechnology* , vol. 16, p. 2020–9, 2005.
- [163] G.-S. Venkatesh, A. Deb and A. Karmarkar, "Characterization and finite element modeling of montmorillonite/polypropylene nanocomposites," *Mater Des.*, vol. 35, pp. 425-33, 2012.
- [164] Y. Chen, J.-Y.-H. Chia, Z.-C. Su, T.-E. Tay and V.-B.-C. Tan, "Mechanical characterization of interfaces in epoxy-clay nanocomposites by molecular simulations," *Polymer*, vol. 54, no. 2, pp. 766-773, 2013.
- [165] S. Saber-Samandari and A. Afaghi-Khatibi, "The effect of interphase on the elastic modulus of polymer based nanocomposites," *Key Eng Mater*, vol. 312, pp. 199-204, 2006.
- [166] S. Saber-Samandari and A. Afaghi-Khatibi, "Evaluation of elastic modulus of polymer matrix nanocomposites," *Polym Comp* , vol. 28, no. 3, pp. 405-11, 2007.
- [167] A. Saxena, *Nonlinear Fracture Mechanics*, CRC, 1998.
- [168] A.-R. Shahani and S.-E. Habibi, "Stress intensity factors in a hollow cylinder containing a circumferential semi-elliptical crack subjected to combined loading," *International Journal of Fatigue*, vol. 29, no. 1, pp. 128-140, 2007.
- [169] G. Mittal, K.-Y. Rhee, V. Mišković-Stanković and D. Hui, "Reinforcements in multi-scale polymer composites: Processing, properties, and applications," *Composites Part B: Engineering*, vol. 138, pp. 122-139, 2018.
- [170] J. Karger-Kocsis, H. Mahmood and A. Pegoretti, "All-carbon multi-scale and hierarchical fibers and related structural composites: A review," *Composites Science and Technology*, vol. 186, p. 107932, 2020.
- [171] J.-K. Kim and Y.-W. Mai, *Engineered Interfaces in Fiber Reinforced Composites*, Amsterdam, The Netherlands: Elsevier, 1998.

- [172] H. Qian, E.-S. Greenhalgh, M.-S.-P. Shaffer and A. Bismarck, "Carbon nanotube-based hierarchical composites: a review," *J. Mater. Chem.*, vol. 20, no. 23, p. 4751, 2010.
- [173] L. Chen, H. Jin, Z. Xu, J. Li, Q. Guo, M. Shan, C. Yang, Z. Wang, W. Mai and B. Cheng, "Role of a gradient interface layer in interfacial enhancement of carbon fiber/ epoxy hierarchical composites," *J. Mater. Sci.*, vol. 50, no. 1, p. 112–121, 2015.
- [174] M. Kumar and Y. Ando, "Chemical vapor deposition of carbon nanotubes: a review on growth mechanism and mass production," *J Nanosci Nanotechnol*, vol. 10, no. 6, p. 3739–58, 2010.
- [175] H. Zhang, Y. Liu, M. Kuwata, E. Bilotti and T. Peijs, "Improved fracture toughness and integrated damage sensing capability by spray coated CNTs on carbon fibre prepreg," *Compos Part A Appl Sci Manuf*, vol. 70, p. 102–110, 2015.
- [176] C. Deng, J. Jiang, F. Liu, L. Fang, J. Wang, D. L. D and e. al, "Influence of carbon nanotubes coatings onto carbon fiber by oxidative treatments combined with electrophoretic deposition on interfacial properties of carbon fiber composite," *Appl Surf Sci*, vol. 357, p. 1274–80, 2015.
- [177] H. Zhang, Y. Liu, M. Huang, E. Bilotti and T. Peijs, "Dissolvable thermoplastic interleaves for carbon nanotube localization in carbon/epoxy laminates with integrated damage sensing capabilities," *Struct. Health Monit.*, vol. 17, no. 1, p. 59–66, 2018.
- [178] R. Malekimoghadam and U. Icardi, "Prediction of mechanical properties of carbon nanotube–carbon fiber reinforced hybrid composites using multi-scale finite element modelling," *Composites Part B: Engineering*, vol. 177, p. 107405, 2019.
- [179] R. Malekimoghadam, U. Icardi and S.-A. Hosseini, "The influence of carbon nanotube coated-carbon fibers on thermal residual stresses of Multi-Scale hybrid composites: Analytical approach," *International Journal of Solids and Structures*, vol. 233, p. 111212, 2021.
- [180] S.-S. Du, F. Li, H.-M. Xiao, Y.-Q. Li, N. Hu and S.-Y. Fu, "Tensile and flexural properties of graphene oxide coated-short glass fiber reinforced polyethersulfone composites," *Compos Part B Eng*, vol. 99, p. 407–15, 2016.
- [181] Y.-H. Zhao, Y.-F. Zhang, S.-L. Bai and X.-W. Yuan, "Carbon fibre/graphene foam/polymer composites with enhanced mechanical and thermal properties," *Compos Part B Eng*, vol. 94, p. 102–8, 2016.
- [182] T.-D. Hapuarachchi and T. Peijs, "Multiwalled carbon nanotubes and sepiolite nanoclays as flame retardants for polylactide and its natural fibre reinforced composites," *Compos Part A Appl Sci Manuf*, vol. 41, p. 954–63, 2010.
- [183] L. Dong, Y. Li, L. Wang, F. Hou and J. Liu, "Spatial dispersion state of carbon nanotubes in a freeze-drying method prepared carbon fiber based preform and its effect on electrical conductivity of carbon fiber/epoxy composite," *Mater. Lett.*, vol. 130, p. 292–5, 2014.
- [184] Y.-J. Kwon, Y. Kim, H. Jeon, S. Cho, W. Lee and J.-U. Lee, "Graphene/carbon nanotube hybrid as a multi-functional interfacial reinforcement for carbon fiber-reinforced composites," *Compos Part B Eng*, vol. 122, p. 23–30, 2017.

- [185] G. Lanzara, Y. Yoon, H. Liu, S. Peng and W.-I. Lee, "Carbon nanotube reservoirs for selfhealing materials," *Nanotechnology* , vol. 20, p. 335704, 2009.
- [186] X. Yao, X. Gao, J. Jiang, C. Xu, C. Deng and J. Wang, "Comparison of carbon nanotubes and graphene oxide coated carbon fiber for improving the interfacial properties of carbon fiber/epoxy composites," *Composites Part B: Engineering*, vol. 132, pp. 170-177, 2018.
- [187] Q. Li, J.-S. Church, M. Naebe and B.-L. Fox, "Interfacial characterization and reinforcing mechanism of novel carbon nanotube – Carbon fibre hybrid composites," *Carbon*, vol. 109, pp. 74-86, 2016.
- [188] Z. Zhao, K. Teng, N. Li, X. Li, Z. Xu, L. Chen, J. Niu, H. Fu, L. Zhao and Y. Liu, "Mechanical, thermal and interfacial performances of carbon fiber reinforced composites flavored by carbon nanotube in matrix/interface," *Composite Structures*, vol. 159, pp. 761-772, 2017.
- [189] P.-K. Ravindranath, S. Roy, V. Unnikrishnan, X. Wang, T. Xu, R. Baughman and H. Lu, "A multiscale model to study the enhancement in the compressive strength of multi-walled CNT sheet overwrapped carbon fiber composites," *Composite Structures*, vol. 219, pp. 170-178, 2019.
- [190] T.-R. Pozegic, I. Hamerton, J.-V. Anguita, W. Tang, P. Balocchi, P. Jenkins and S.-R.-P. Silva, "Low temperature growth of carbon nanotubes on carbon fibre to create a highly networked fuzzy fibre reinforced composite with superior electrical conductivity," *Carbon*, vol. 74, pp. 319-328, 2014.
- [191] S.-J. Joo, M.-H. Yu, W.-S. Kim and H.-S. Kim, "Damage detection and self-healing of carbon fiber polypropylene (CFPP)/carbon nanotube (CNT) nano-composite via addressable conducting network," *Composites Science and Technology*, vol. 167, pp. 62-70, 2018.
- [192] E.-J. Garcia, B.-L. Wardle and A.-J. Hart, "Joining prepreg composite interfaces with aligned carbon nanotubes," *Composites Part A: Applied Science and Manufacturing*, vol. 39, no. 6, pp. 1065-1070, 2008.
- [193] W. Qin, C. Chen, J. Zhou and J. Meng, "Synergistic Effects of Graphene/Carbon Nanotubes Hybrid Coating on the Interfacial and Mechanical Properties of Fiber Composites," *Materials*, vol. 13, p. 1457, 2020.
- [194] M.-R. Zakaria, H. M. Akil, M.-H. A. Kudus, F. Ullah, F. Javed and N. Nosbi, "Hybrid carbon fiber-carbon nanotubes reinforced polymer composites: A review," *Composites Part B: Engineering*, vol. 176, p. 107313, 2019.
- [195] O. Maxian, D. Pedrazzoli and I. Manas-Zloczower, "Conductive polymer foams with carbon nanofillers – modeling percolation behavior," *Express Polym. Lett.*, vol. 11, p. 406–418, 2017.
- [196] J. Karger-Kocsis and S. Keki, "Review of progress in shape memory epoxies and their composites," *Polymers*, vol. 10 , no. 1, p. 34, 2018.
- [197] V. Kostopoulos, A. Kotrotsos, A. Baltopoulos, S. Tsantzalis, P. Tsokanas, T. Loutas and e. al., "Mode II fracture toughening and healing of composites using supramolecular polymer interlayers," *Express Polym. Lett.* , vol. 10 , p. 914–926, 2016.
- [198] X. Ni, C. Furtado, E. Kalfon-Cohen, Y. Zhou, G.-A. Valdes, P.-P. C. T.-J. Hank and B.-L. Wardle, "Static and fatigue interlaminar shear reinforcement in aligned

- carbon nanotube-reinforced hierarchical advanced composites," *Composites Part A: Applied Science and Manufacturing*, vol. 120, pp. 106-115, 2019.
- [199] Y.-A. Kim, L. Kamio, T. Tajiri, T. Hayashi, S.-M. Song, M. Endo and e. al., "Enhanced thermal conductivity of carbon fiber/phenolic resin composites by the introduction of carbon nanotubes," *Appl Phys Lett*, vol. 90, p. 093125–7, 2007.
- [200] L. Tong, P. Tan and X. Sun, "Effect of long multi-walled CNTs on delamination toughness of laminated composites," *J Comp Mat*, vol. 42, p. 5–23, 2008.
- [201] E.-T. Thostenson, W.-Z. Li, D.-Z. Wang, Z.-F. Ren and T.-W. Chou, "Carbon nanotube/carbon fiber hybrid multiscale composites," *J Appl Phys*, vol. 91, p. 6034–7, 2002.
- [202] S. Aziz, S.-A. Rashid, S. Rahmanian and M.-A. Salleh, "Experimental evaluation of the interfacial properties of carbon nanotube coated carbon fiber reinforced hybrid composites," *Polym Compos*, vol. 36, p. 1941–50, 2015.
- [203] G. Chatzigeorgiou, G.-D. Seidel and D.-C. Lagoudas, "Effective mechanical properties of “fuzzy fiber” composites," *Compos Part B Eng*, vol. 43, p. 2577–93, 2012.
- [204] G. Dai and L. M. Jr, "Carbon nanotube reinforced hybrid composites: Computational modeling of environmental fatigue and usability for wind blades," *Compos Part B Eng*, vol. 78, p. 349–60, 2015.
- [205] M. Kulkarni, D. Carnahan, K. Kulkarni, D. Qian and J.-L. Abot, "Elastic response of a carbon nanotube fiber reinforced polymeric composite: a numerical and experimental study," *Compos Part B Eng*, vol. 41, p. 414–21, 2010.
- [206] S.-I. Kundalwal and S.-A. Meguid, "Multiscale modeling of regularly staggered carbon fibers embedded in nano-reinforced composites," *Eur J Mech*, vol. 64, p. 69–84, 2017.
- [207] S.-I. Kundalwal and M.-C. Ray, "Effective properties of a novel continuous fuzzy-fiber reinforced composite using the method of cells and the finite element method," *Eur J Mech- A/Solids*, vol. 36, p. 191–203, 2012.
- [208] N. Yamamoto, A.-J. Hart, E.-J. Garcia, S.-S. Wicks, H.-M. Duong, A.-H. Slocum and e. al, "High-yield growth and morphology control of aligned carbon nanotubes on ceramic fibers for multifunctional enhancement of structural composites," *Carbon N Y*, vol. 47, p. 551–60, 2009.
- [209] N. Silvestre, "On the accuracy of shell models for torsional buckling of carbon nanotubes," *Eur J Mech A/Solids*, vol. 32, pp. 103-108, 2012.
- [210] A. Bagchi and S. Nomura, "On the effective thermal conductivity of carbon nanotube reinforced polymer composites," *Compos Sci Technol*, vol. 66, p. 1703–12, 2006.
- [211] M. Choi, K. Eom, K. Gwak, M.-D. Dai, A. Olshevskiy and C.-W. Kim, "Dynamical response of multi-walled carbon nanotube resonators based on continuum mechanics modeling for mass sensing applications," *J Mech Sci Technol*, vol. 31, p. 2385–91, 2017.
- [212] I. Palaci, S. Fedrigo, H. Brune, C. Klinke, M. Chen and E. Riedo, "Radial elasticity of multiwalled carbon nanotubes," *Phys Rev Lett*, vol. 94, p. 175502, 2005;.

- [213] R.-C. Batra and A. Sears, "Continuum models of multi-walled carbon nanotubes," *International Journal of Solids and Structures* , vol. 44 , p. 7577–7596, 2007.
- [214] X.-B. Dai, H. Merlitz and C.-X. Wu, "Transverse elasticity of multi-walled carbon nanotubes," *Eur. Phys. J. B* , vol. 54, p. 109–112 , 2006.
- [215] S.-B. Sinnott, "Chemical functionalization of carbon nanotubes," *J Nanosci Nanotechnol*, vol. 2, p. 113–23, 2002.
- [216] L.-Y. Jiang, Y. Huang, H. Jiang, G. Ravichandran, H. Gao, K.-C. Hwang and e. al, "A cohesive law for carbon nanotube/polymer interfaces based on the van der Waals force," *J Mech Phys Solids* , vol. 54, p. 2436–52, 2006.
- [217] H. Tan, L.-Y. Jiang, Y. Huang, B. Liu and K.-C. Hwang, "The effect of van der Waals-based interface cohesive law on carbon nanotube-reinforced composite materials," *Compos Sci Technol* , vol. 67, p. 2941–6, 2007.
- [218] K.-Y. Volokh, "Comparison between cohesive zone models," *Commun Numer Methods Eng* , vol. 20, p. 845–56, 2004.
- [219] J. Gou, B. Minaie, B. Wang, Z. Liang and C. Zhang, "Computational and experimental study of interfacial bonding of single-walled nanotube reinforced composites," *Comput Mater Sci*, vol. 31, p. 225–36, 2004.
- [220] H. Miyagawa, T. Mase, C. Sato, E. Drown, L.-T. Drzal and K. Ikegami, "Comparison of experimental and theoretical transverse elastic modulus of carbon fibers," *Carbon N Y* , vol. 44, p. 2002–8, 2006.
- [221] K. Honjo, "Thermal stresses and effective properties calculated for fiber composites using actual cylindrically-anisotropic properties of interfacial carbon coating," *Carbon N Y* , vol. 45, p. 865–72, 2007.
- [222] T. Mori and K. Tanaka, "Average stress in matrix and average elastic energy of materials with misfitting inclusions," *Acta Metallurgica*, vol. 21, no. 5, pp. 571-574, 1973.
- [223] P. Lu, Y.-W. Leong, P.-k. Pallathadka and C.-B. He, "Effective moduli of nanoparticle reinforced composites considering interphase effect by extended double-inclusion model–Theory and explicit expressions," *Int J Eng Sci* , vol. 73, p. 33–55, 2013.
- [224] Y.-P. Qiu and G.-J. Weng, "On the application of Mori-Tanaka's theory involving transversely isotropic spheroidal inclusions," *Int J Eng Sci* , vol. 28, p. 1121–37, 1990.
- [225] U. Icardi and A. Atzori, "Simple, efficient mixed solid element for accurate analysis of local effects in laminated and sandwich composites," *Adv Eng Softw*, vol. 35, p. 843–59, 2004.
- [226] I. Babuška, "The finite element method with Lagrangian multipliers," *Numer Math*, vol. 20, p. 179–92, 1973.
- [227] M.-M. Shokrieh, A. Daneshvar and S. Akbari, "Reduction of thermal residual stresses of laminated polymer composites by addition of carbon nanotubes," *Mater Des*, vol. 53, p. 209–16, 2014.
- [228] R.-J. Sager, P.-J. Klein, D.-C. Lagoudas, Q. Zhang, J. Liu, L. D. L and e. al, "Effect of carbon nanotubes on the interfacial shear strength of T650 carbon fiber in an epoxy matrix," *Compos Sci Technol* , vol. 69, p. 898–904, 2009.

- [229] C.-D. Wood, M.-J. Palmeri, K.-W. Putz, G. Ho, R. Barto and L.-C. Brinson.
- [230] S. C.-H and P.-F. Becher, "Thermal expansion coefficient of unidirectional fiber reinforced ceramics," *J Am Ceram Soc* , vol. 71, p. 438–441, 1988.
- [231] K. Jayaraman and K.-L. Reifsnider, "The interphase in unidirectional fiber-reinforced epoxies: Effect on residual thermal stresses," *Compos Sci Technol* , vol. 47, p. 119–29, 1993.
- [232] M.-M. Shokrieh and M. Safarabadi, "Three-dimensional analysis of micro-residual stresses in fibrous composites based on the energy method: a study including interphase effects," *J Compos Mater* , vol. 46, p. 727–35, 2012.
- [233] M.-M. Aghdam and A. Khojeh, "More on the effects of thermal residual and hydrostatic stresses on yielding behavior of unidirectional composites," *Compos Struct*, vol. 62, p. 285–90, 2003.
- [234] R. Naik, "Simplified Micromechanical Equations for Thermal Residual Stress Analysis of Coated Fiber Composites," *J Compos Technol Res* , vol. 14, p. 182–6, 1992.
- [235] S.-M. Arnold, V.-K. Arya and M.-E. Melis, "Elastic/plastic analyses of advanced composites investigating the use of the compliant layer concept in reducing residual stresses resulting from processing," NASA Technical Reports, 1990.
- [236] R.-M. Moghadam, S. Saber-Samandari and S.-A. Hosseini, "On the tensile behavior of clay–epoxy nanocomposite considering interphase debonding damage via mixed-mode cohesive zone material," *Compos Part B Eng* , vol. 89, p. 303–15, 2016.
- [237] V. Romanov, S.-V. Lomov, I. Verpoest and L. Gorbatikh, "Inter-fiber stresses in composites with carbon nanotube grafted and coated fibers," *Compos Sci Technol* , vol. 114, p. 79–86, 2015.
- [238] Z. Shen, S. Bateman, D.-Y. Wu, P. McMahon, M. Dell’Olio and J. Gotama, "The effects of carbon nanotubes on mechanical and thermal properties of woven glass fibre reinforced polyamide-6 nanocomposites," *Compos Sci Technol* , vol. 69, p. 239–44, 2009.
- [239] M.-C. Ray and S.-I. Kundalwal, "A thermomechanical shear lag analysis of short fuzzy fiber reinforced composite containing wavy carbon nanotubes," *Eur J Mech - A/Solids* , vol. 44, p. 41–60, 2014.
- [240] G. Chatzigeorgiou, F. Meraghni, N. Charalambakis and A. Benaarbia, "Multiscale modeling accounting for inelastic mechanisms of fuzzy fiber composites with straight or wavy carbon nanotubes," *International Journal of Solids and Structures*, vol. 202, p. 39–57, 2020.
- [241] M.-Y. Quek, "Analysis of residual stresses in a single fibre–matrix composite," *Int J Adhes Adhes* , vol. 24, p. 379–88, 2004.
- [242] Y. Mikata and M. Taya, "Stress Field in a Coated Continuous Fiber Composite Subjected to Thermo-Mechanical Loadings," *J Compos Mater* , vol. 19, p. 554–78, 1985.
- [243] E. Bekyarova, E.-T. Thostenson, H. K. A. Yu, J. Gao, J. Tang and e. al., "Multiscale Carbon Nanotube–Carbon Fiber Reinforcement for Advanced Epoxy Composites," *Langmuir* , vol. 23, p. 3970–4, 2007.

- [244] G.-M. Odegard, T.-S. Gates, K.-E. Wise, C. Park and E.-j. Siochi, "Constitutive modeling of nanotube-reinforced polymer composites," *Compos Sci Technol*, vol. 63, pp. 1671-1687, 2003.
- [245] R. Hill, "A self-consistent mechanics of composite materials," *J Mech Phys Solids*, vol. 13, p. 213-22, 1965.
- [246] M.-H. Yas and M. Heshmati, "Dynamic analysis of functionally graded nanocomposite beams reinforced by randomly oriented carbon nanotube under the action of moving load," *Appl Math Model*, vol. 36, p. 1371-94, 2012.
- [247] C.-L. TuckerIII and E. Liang, "Stiffness predictions for unidirectional short-fiber composites: Review and evaluation," *Compos Sci Technol*, vol. 59, p. 655-71, 1999.
- [248] T. Chen, G.-j. Dvorak and Y. Benveniste, "Mori-Tanaka estimates of the overall elastic moduli of certain composite materials," *J Appl Mech*, vol. 59, p. 539-46, 1992.
- [249] J. Wang and R. Pyrz, "Prediction of the overall moduli of layered silicate-reinforced nanocomposites-part I: Basic theory and formulas," *Compos Sci Technol*, 2004.
- [250] J.-D. Eshelby, "The determination of the elastic field of an ellipsoidal inclusion, and related problems," *Proc R Soc London Ser A Math Phys Sci*, vol. 241, p. 376-96, 1957.
- [251] T. Mura, *Micromechanics of defects in solids*, Springer Science & Business Media, 1982.
- [252] D.-L. Shi, X.-Q. Feng, K.-C. Y.-Y. Huang and H. Gao, "The Effect of Nanotube Waviness and Agglomeration on the Elastic Property of Carbon Nanotube-Reinforced Composites," *J Eng Mater Technol*, vol. 126, p. 250-7, 2004.
- [253] J.-N. Reddy, *Mechanics of laminated composite plates and shells: theory and analysis*, CRC press, 2003.
- [254] M. Ferrari and G.-C. Johnson, "Effective elasticities of short-fiber composites with arbitrary orientation distribution," *Mech Mater*, vol. 8, p. 67-73, 1989.
- [255] G. Marom and A. Weinberg, "The effect of the fibre critical length on the thermal expansion of composite materials," *J Mater Sci*, vol. 10, p. 1005-10, 1975.
- [256] C.-W. Bert and R.-A. Kline, "Composite-material mechanics: Properties of planar-random fiber composites," *Polym Compos*, vol. 6, p. 133-41, 1985.
- [257] N. H. Alamusi, B. Jia, M. Arai, C. Yan, J. Li and e. al, "Prediction of thermal expansion properties of carbon nanotubes using molecular dynamics simulations," *Comput Mater Sci*, vol. 54, p. 249-54, 2012.
- [258] Y.-K. Kwon, S. Berber and D. Tománek, "Thermal Contraction of Carbon Fullerenes and Nanotubes," *Phys. Rev. Lett.*, vol. 92, no. 1, p. 15901, 2004.
- [259] S.-I. Kundalwal and M.-C. Ray, "Effect of carbon nanotube waviness on the effective thermoelastic properties of a novel continuous fuzzy fiber reinforced composite," *Compos Part B Eng*, vol. 57, p. 199-209, 2014.
- [260] A.-C. Ugural and S.-K. Fenster, *Advanced strength and applied elasticity*, Pearson education, 2003.

- [261] M.-Y. Quek and C.-Y. Yue, "Axisymmetric stress distribution in the single filament pull-out test," *Mater Sci Eng A*, vol. 189, p. 105–16, 1994.
- [262] D.-Y. Song, N. Takeda and S. Ogihara, "A method of stress analysis for interfacial property evaluation in thermoplastic composites," *Mater Sci Eng A*, vol. 278, p. 242–6, 2000.
- [263] Maplesoft, *Maple User Manual*, a division of Waterloo, 1996-2021.
- [264] S. Dutton, D. Kelly and A. Baker, *Composite materials for aircraft structures*, American Institute of Aeronautics and Astronautics, 2004.
- [265] X. Ren, J. Burton, G.-D. Seidel and K. Lafdi, "Computational multiscale modeling and characterization of piezoresistivity in fuzzy fiber reinforced polymer composites," *Int J Solids Struct*, vol. 54, p. 121–34, 2015.
- [266] M.-A. Shazed, A.-R. Suraya, S. Rahmanian and M.-A. M. Salleh.
- [267] R. Malekimoghadam and M. Gherlone, "Bending Analysis of CNT Coated–Fiber Multi-Scale Composite Beams Using the Refined Zigzag Theory," *Composite Structures*, vol. is being submitted, 2022.
- [268] D. Qian, E. Dickey, R. Andrews and T. Rantel, "Load transfer and deformation mechanisms in carbon nanotube-polystyrene composites," *Appl Phys Lett*, vol. 76, p. 2868–70, 2000.
- [269] L.-S. Schadler, S.-C. Giannaris and P.-M. Ajayan, "Load transfer in carbon nanotube epoxy composites," *Appl Phys Lett*, vol. 73, p. 3842–4, 1998.
- [270] N. Subramanian, B. Koo, K. R. Venkatesan and A. Chattopadhyay, "Interface mechanics of carbon fibers with radially-grown carbon nanotubes," *Carbon*, vol. 134, pp. 123-133, 2018.
- [271] P. Lv, Y.-y. Feng, P. Zhang, H.-m. Chen, N. Zhao and W. Feng, "Increasing the interfacial strength in carbon fiber/epoxy composites by controlling the orientation and length of carbon nanotubes grown on the fibers," *Carbon*, vol. 49, no. 14, p. 4665–4673, 2011.
- [272] R. Rafiee and A. Ghorbanhosseini, "Stochastic multi-scale modeling of randomly grown CNTs on carbon fiber," *Mechanics of Materials*, vol. 106, pp. 1-7, 2017.
- [273] N. Lachman, E. Wiesel, R. -G. d. Villoria, B.-L. Wardle and H.-D. Wagner, "Interfacial load transfer in carbon nanotube/ceramic microfiber hybrid polymer composites," *Compos Sci Technol*, vol. 72, p. 1416–22, 2012.
- [274] E.-J. Garcia, B.-L. Wardle, A. J. Hart and N. Yamamoto, "Fabrication and multifunctional properties of a hybrid laminate with aligned carbon nanotubes grown In Situ," *Compos Sci Technol*, vol. 68, p. 2034–41, 2008.
- [275] M.-S. Radue and G.-M. Odegard, "Multiscale modeling of carbon fiber/carbon nanotube/epoxy hybrid composites: Comparison of epoxy matrices," *Compos Sci Technol*, vol. 166, p. 20–6, 2018.
- [276] X. Ma, F. Scarpa, H.-X. Peng, G. Allegri, J. Yuan and R. Ciobanu, "Design of a hybrid carbon fibre/carbon nanotube composite for enhanced lightning strike resistance," *Aerosp Sci Technol*, vol. 47, p. 367–77, 2015.
- [277] G. Pal and S. Kumar, "Multiscale modeling of effective electrical conductivity of short carbon fiber-carbon nanotube-polymer matrix hybrid composites," *Mater Des*, vol. 89, p. 129–36, 201.

- [278] Y. Rao, J. Ban, S. Yao, K. Wang, N. Wei, Y. Lu and S. Ahzi, "A hierarchical prediction scheme for effective properties of fuzzy fiber reinforced composites with two-scale interphases: Based on three-phase bridging model," *Mechanics of Materials*, vol. 152, p. 103653, 2021.
- [279] G. Chatzigeorgiou, Y. Efendiev and D.-C. Lagoudas, "Homogenization of aligned "fuzzy fiber" composites," *International Journal of Solids and Structures*, vol. 48, no. 19, pp. 2668-2680, 2011.
- [280] Q. Chen, G. Chatzigeorgiou and F. Meraghni, "Hybrid hierarchical homogenization theory for unidirectional CNTs-coated fuzzy fiber composites undergoing inelastic deformations," *Composites Science and Technology*, vol. 215, p. 109012, 2021.
- [281] S.-I. Kundalwal and S.-A. Meguid, "Micromechanics modelling of the effective thermoelastic response of nano-tailored composites," *Eur J Mech - A/Solids*, vol. 53, p. 241–253, 2015.
- [282] A. Tessler, M. D. Sciuva and M. Gherlone, "A Refined Zigzag Beam Theory for Composite and Sandwich Beams," *Journal of Composite Materials*, vol. 43, no. 9, pp. 1051-1081, 2009.
- [283] A. Tessler, M. D. Sciuva and M. Gherlone, "Refinement of Timoshenko Beam Theory for Composite and Sandwich Beams Using Zigzag Kinematics," NASA-TP-2007-215086, National Aeronautics and Space Administration, Washington, D.C, 2007.
- [284] L. Iurlaro, M. Gherlone, M. D. Sciuva and A. Tessler, "Assessment of the Refined Zigzag Theory for bending, vibration, and buckling of sandwich plates: a comparative study of different theories," *Composite Structures*, vol. 106, pp. 777-792, 2013.
- [285] M. Gherlone, "Tria and quad plate finite elements based on RZT(m) for the analysis of multilayered sandwich structure," *Composite Structures*, vol. 220, pp. 510-520, 2019.
- [286] L. Iurlaro, M. Gherlone and M. D. Sciuva, "A comparison of zigzag functions for the bending, vibration and buckling analysis of multilayered composite and sandwich plates," in *XI World Congress on Computational Mechanics*.
- [287] A. Ascione, M. Gherlone and A.-C. Orifici, "Nonlinear static analysis of composite beams with piezoelectric actuator patches using the Refined Zigzag Theory," *Composite Structures*, vol. 282, p. 115018, 2022.
- [288] G. Zhang, Z. Rasheva, J. Karger-Kocsis and T. Burkhart, "Synergetic role of nanoparticles and micro-scale short carbon fibers on the mechanical profiles of epoxy resin," *Express Polym. Lett*, vol. 5, p. 859–872, 2011.
- [289] J. Gao and X. G. Y. He, "Effect of electric field induced alignment and dispersion of functionalized carbon nanotubes on properties of natural rubber," *Results in Physics*, vol. 9, pp. 493-499, 2018.
- [290] U. o. Delaware, "Carbon Nanotube-Based Sensing Composites; A Novel Distributed Sensing Approach for Structural Health Monitoring," 2013. [Online]. Available: <https://sites.udel.edu/nsf-cmmi-cnt-shm/the-basics/>.
- [291] C. Lan, M. Guo, C. Li, Y. Qiu, Y. Ma and J. Sun, "Axial Alignment of Carbon Nanotubes on Fibers To Enable Highly Conductive Fabrics for Electromagnetic

- Interference Shielding," *ACS Applied Materials & Interfaces*, vol. 12, no. 6, pp. 7477-7485, 2020.
- [292] G.-M. Odegard, T.-S. Gates, K.-E. Wise, C. Park and E.-J. Siochi, "Constitutive modeling of nanotube-reinforced polymer composites," *Composites Science and Technology*, vol. 63, no. 11, pp. 1671-1687, 2003.
- [293] F. Tornabene, M. Baccocchi, N. Fantuzzi and J. Reddy, "Multiscale approach for three-phase CNT/polymer/fiber laminated nanocomposite structures," *Polym. Compos.*, vol. 40, pp. 102-126, 2019.
- [294] Z. Hashin, "Analysis of Properties of Fiber Composites With Anisotropic Constituents," *Journal of Applied Mechanics*, vol. 46, no. 3, p. 543-550, 1979.
- [295] Z. Hashin, "Analysis of Composite Materials—A Survey," *Journal of Applied Mechanics*, vol. 50, pp. 481-505, 1983.
- [296] E. R. 862, "Hexion," [Online]. Available: <https://www.hexion.com/en-US/product/epikote-resin-862..>
- [297] S. Sockalingam, M. Dey, J.-W. Gillespie and M. Keefe, "Finite element analysis of the microdroplet test method using cohesive zone model of the fiber/matrix interface," *Composites Part A: Applied Science and Manufacturing*, vol. 56, pp. 239-247, 2014.
- [298] J.-C. Halpin, "Effect of environmental factors on composite materials," Air Force Technical Report AFML-TR 67-423, Dayton, OH, 1967.
- [299] J.-C. H. Halpin and J.-L. Kardos, "The Halpin-Tsai equations: A review," *Polym Eng Sci*, vol. 16, pp. 344-352, 1976.
- [300] Z. Zhao, L. Ci, H.-M. Cheng and J. Bai, "The growth of multi-walled carbon nanotubes with different morphologies on carbon fibers," *Carbon*, vol. 43, p. 663-5, 2005.
- [301] M.-A. Shazed, A.-R. Suraya, S. Rahmanian and M.-A. M. Salleh, "Effect of fibre coating and geometry on the tensile properties of hybrid carbon nanotube coated carbon fibre reinforced composite," *Materials & Design*, vol. 54, pp. 660-669, 2014.
- [302] R.-B. Mathur, S. Chatterjee and B.-P. Singh, "Growth of carbon nanotubes on carbon fibre substrates to produce hybrid/phenolic composites with improved mechanical properties," *Composites Science and Technology*, vol. 68, no. 7-8, pp. 1608-1615, 2008.
- [303] M. Sorrenti, M. D. Sciuva, J. Majak and e. al, "Static Response and Buckling Loads of Multilayered Composite Beams Using the Refined Zigzag Theory and Higher-Order Haar Wavelet Method," *Mech Compos Mater*, vol. 57, p. 1-18, 2021.
- [304] M. D. Sciuva, M. Gherlone and L. Librescu, "Implications of damaged interfaces and of other non-classical effects on the load carrying capacity of multilayered composite shallow shells," *International Journal of Non-Linear Mechanics*, vol. 37, no. 4-5, pp. 851-867, 2002.
- [305] G.-M. Cook and A. Tessler, "A {3,2}-order bending theory for laminated composite and sandwich beams," *Composites Part B: Engineering*, vol. 29, no. 5, pp. 565-576, 1998.
- [306] E. Madenci and I. Guven, *The finite element method and applications in engineering using ANSYS®*, Boston, MA: Springer, 2015.

- [307] G.-. M. Cook and A. Tessler, "A {3,2}-order bending theory for laminated composite and sandwich beams," *Composites Part B: Engineering*, vol. 29, no. 5, pp. 565-576, 1998.

Appendix A

The Eshelby tensor elements $[S_r]$ for cylindrical reinforcement [224]:

$$S_{1111} = 0, \quad S_{2222} = S_{3333} = \frac{5-4\nu_m}{8(1-\nu_m)},$$

$$S_{2233} = S_{3322} = \frac{4\nu_m-1}{8(1-\nu_m)},$$

$$S_{1122} = S_{1133} = 0, \quad S_{2211} = S_{3311} = \frac{\nu_m}{2(1-\nu_m)},$$

$$S_{1212} = S_{1313} = \frac{1}{4}, \quad S_{2323} = \frac{3-4\nu_m}{8(1-\nu_m)},$$

Where ν_m is Poisson's ratio of matrix.

Appendix B

The A tensor parameters are given as below [248] :

$$a_1 = (-1 + 2\nu_m) [E_m + 2k_{ENF}(1 + \nu_m)]$$

$$a_2 = E_m + 2m_{ENF}(3 - \nu_m - 4\nu_m^2)$$

$$a_3 = E_m(1 - \nu_m) \{E_m(3 - 4\nu_m) + 2(1 + \nu_m)[m_{ENF}(3 - 4\nu_m) + k_{ENF}(2 - 4\nu_m)]\}$$

$$a_4 = E_m(1 - \nu_m) \{E_m(1 - 4\nu_m) + 2(1 + \nu_m)[m_{ENF}(3 - 4\nu_m) + k_{ENF}(2 - 4\nu_m)]\}$$

Appendix C

The Hill's constants of reinforcement phase are obtained using below equations [222]:

$$\alpha_{ENF} = \frac{3 (K_m + G_m) + k_{ENF} - l_{ENF}}{3 (G_m + k_{ENF})}$$

$$\beta_{ENF} = \frac{1}{5} \left\{ \frac{4 G_m + 2 k_{ENF} + l_{ENF}}{3 (G_m + k_{ENF})} + \frac{4 G_m}{G_m + p_{ENF}} + \frac{2 [G_m (3 K_m + G_m) + G_m (3 K_m + 7 G_m)]}{G_m (3 K_m + G_m) + m_{ENF} (3 K_m + 7 G_m)} \right\}$$

$$\delta_{ENF} = \frac{1}{3} \left[n_{ENF} + 2 l_{ENF} + \frac{(2 k_{ENF} + l_{ENF})(3 K_m + 2 G_m - l_{ENF})}{G_m + k_{ENF}} \right]$$

$$\eta_{ENF} = \frac{1}{5} \left[\frac{2}{3} (n_{ENF} - l_{ENF}) + \frac{8 G_m p_{ENF}}{G_m + p_{ENF}} + \frac{8 m_{ENF} G_m (3 K_m + 4 G_m)}{3 K_m (m_{ENF} + G_m) + G_m (7 m_{ENF} + G_m)} + \frac{2 (k_{ENF} - l_{ENF})(2 G_m + l_{ENF})}{3 (G_m + k_{ENF})} \right]$$

Appendix D

Regarding CNT-coating interphase (CCR), the integrations of normal, shear and radial stresses at this region are calculated as following. Thus, considering the term regarding axial stress in CCR:

$$\begin{aligned} \frac{1}{2} \sigma_{ACCR}^{zz} \epsilon_{ACCR}^{zz} &= \frac{1}{2} \sigma_{ACCR}^{zz} \left[\frac{1}{E_{ACCR}^z} (\sigma_{ACCR}^{zz} - 2 \nu_{ACCR}^z \sigma_{ACCR}^{rr}) + \alpha_{ACCR}^z \Delta T \right] \\ &= \frac{1}{2 E_{ACCR}^z} (\sigma_{ACCR}^{zz})^2 - \frac{\nu_{ACCR}^z}{E_{ACCR}^z} \sigma_{ACCR}^{zz} \sigma_{ACCR}^{rr} + \frac{1}{2} \sigma_{ACCR}^{zz} \alpha_{ACCR}^z \Delta T \end{aligned} \quad (E.1)$$

Hence, by substituting the stresses in terms of $g_1(z)$ and $g_2(z)$ obtained by Eq (6.37) & (6.45) into (E.1), the integral related to axial stress is expressed as:

$$\begin{aligned}
& \iiint_V \left(\frac{1}{2} \sigma_{ACCR}^{zz} \varepsilon_{ACCR}^{zz} \right) r dr d\theta dz \\
&= \iiint_V \left[\frac{B_2^2}{2E_{ACCR}^z} g_2(z)^2 - \frac{\nu_{ACCR}^z}{E_{ACCR}^z} B_2 g_2(z) \left\{ -\frac{B_1}{4} \frac{d^2 g_1(z)}{dz^2} \left(2R_f^2 \ln R_m - (R_m^2 - 2R_{CCR}^2 \ln R_m) \frac{V_f}{V_m} + (R_{CCR}^2 - \right. \right. \right. \\
& \left. \left. 2R_{CCR}^2 \ln R_{CCR} \right) \frac{V_f}{V_m} - 2R_f^2 \ln r \right\} - \frac{B_2}{4} \frac{d^2 g_2(z)}{dz^2} \left(2(R_{CCR}^2 - R_f^2) \ln R_m - (R_m^2 - 2R_{CCR}^2 \ln R_m) \frac{V_{CCR}}{V_m} - 2 \right. \\
& \left. (R_{CCR}^2 - R_f^2) \ln R_{CCR} + (R_{CCR}^2 - 2R_{CCR}^2 \ln R_{CCR}) \frac{V_{CCR}}{V_m} - 2R_f^2 \ln R_{CCR} + R_{CCR}^2 + 2R_f^2 \ln r - r^2 \right) \left. \right\} + \\
& \left. \frac{1}{2} B_2 g_2(z) \alpha_{ACCR}^z \Delta T \right] r dr d\theta dz
\end{aligned} \tag{E.2}$$

The integration with respect to r from R_f to R_{CCR} is performed as below:

$$\begin{aligned}
& \int_{R_f}^{R_{CCR}} \left(\frac{1}{2} \sigma_{ACCR}^{zz} \varepsilon_{ACCR}^{zz} \right) r dr \\
&= \frac{1}{4E_{CCR}^z (-1 + V_f)} \left(\left(- \left(- (R_f + R_{CCR})(R_f - R_{CCR}) ((V_{CCR} - V_f + 1) R_{CCR}^2 + R_f^2 (-1 + V_f)) \ln(R_m) - 2R_{CCR}^2 \left(-\frac{V_f}{2} + \frac{V_{CCR}}{2} + \frac{1}{2} \right) R_{CCR}^2 \right. \right. \right. \\
& \left. \left. + R_f^2 \left(V_f - \frac{V_{CCR}}{2} - 1 \right) \ln(R_{CCR}) + R_f^4 (-1 + V_f) \ln(R_f) - \frac{3}{4} (R_f + R_{CCR})(R_f - R_{CCR}) \left(-\frac{V_f}{3} + \left(\frac{2V_{CCR}}{3} + \frac{1}{3} \right) R_{CCR}^2 + R_f^2 (-1 + V_f) - \right. \right. \right. \\
& \left. \left. \left(\frac{2}{3} R_m^2 V_o \right) \right) \nu_{CCR} B_2 \left(\frac{d^2}{dz^2} g_2(z) \right) + \left(- (R_f + R_{CCR})(R_f - R_{CCR}) (-R_{CCR}^2 V_f + R_f^2 (-1 + V_f)) \ln(R_m) + (R_{CCR}^4 V_f - 2R_f^2 (V_f - \frac{1}{2}) \right. \right. \\
& \left. \left. R_{CCR}^2 \ln(R_{CCR}) + R_f^4 (-1 + V_f) \ln(R_f) - \frac{1}{2} (-R_{CCR}^2 V_f + R_f^2 (-1 + V_f) + R_m^2 V_f (R_f + R_{CCR})(R_f - R_{CCR})) \right) \nu_{CCR} B_1 \left(\frac{d^2}{dz^2} g_1(z) \right) - \right. \\
& \left. (R_f - R_{CCR})(R_f + R_{CCR})(-1 + V_f) (\alpha_{CCR}^z \Delta T E_{CCR}^z + B_2 g_2(z)) \right) B_2 g_2(z) \Big)
\end{aligned} \tag{E.3}$$

From Eq (6.58), the term related to shear stress in Eq (6.60) is stated as:

$$\tau_{ACCR}^{rz} \varepsilon_{ACCR}^{rz} = \frac{1}{2G_{ACCR}} (\tau_{ACCR}^{rz})^2, \quad G_{ACCR}^z = \frac{E_{ACCR}^z}{2(1 + \nu_{ACCR}^z)}$$

Then : (E.4)

$$\tau_{ACCR}^{rz} \varepsilon_{ACCR}^{rz} = \frac{1 + \nu_{ACCR}^z}{E_{ACCR}^z} (\tau_{ACCR}^{rz})^2$$

Thus, by substituting the CCR's shear stress in terms of g₁(z) and g₂(z) obtained by Eq (6.44) into (E.4):

$$\begin{aligned}
\iiint_v (\tau_{ACCR}^{rz} \varepsilon_{ACCR}^{rz}) r dr d\theta dz &= \iiint_v \left[\frac{1 + \nu_{ACCR}^z}{E_{ACCR}^z} (\tau_{ACCR}^{rz})^2 \right] r dr d\theta dz \\
&= \iiint_v \left[\frac{1 + \nu_{ACCR}^z}{E_{ACCR}^z} \left(\frac{1}{4r^2} \left\{ B_1 R_f^2 \frac{dg_1(z)}{dz} + B_2 (r^2 - R_f^2) \frac{dg_2(z)}{dz} \right\}^2 \right) \right] r dr d\theta dz
\end{aligned} \tag{E.5}$$

The integration with respect to r from RCCR to R_m is accomplished accordingly:

$$\begin{aligned}
&\int_{R_f}^{R_{CCR}} (\tau_{ACCR}^{rz} \varepsilon_{ACCR}^{rz}) r dr \\
&= -\frac{1 + \nu_{CCR}^z}{4 E_{CCR}^z} \left(\left(\ln(R_f) R_f^4 - \ln(R_{CCR}) R_f^4 - \frac{3R_f^4}{4} + R_{CCR}^2 R_f^2 - \frac{R_{CCR}^4}{4} \right) B_2^2 \left(\frac{d}{dz} g_2(z) \right)^2 - \right. \\
&\quad \left. 2R_f^2 B_1 \left(R_f^2 \ln(R_f) - R_f^2 \ln(R_{CCR}) - \frac{R_f^2}{2} + \frac{R_{CCR}^2}{2} \right) B_2 \left(\frac{d}{dz} g_1(z) \right) \left(\frac{d}{dz} g_2(z) \right) + \right. \\
&\quad \left. B_1^2 \left(\frac{d}{dz} g_1(z) \right)^2 R_f^4 (\ln(R_f) - \ln(R_{CCR})) \right)
\end{aligned} \tag{E.6}$$

With the same procedure for shear and axial stresses, the radial stress of CCR is acquired as following:

$$\begin{aligned}
\frac{1}{2} \sigma_{ACCR}^{rr} \varepsilon_{ACCR}^{rr} &= \frac{1}{2} \sigma_{ACCR}^{rr} \left[\frac{1}{E_{ACCR}^r} (\sigma_{ACCR}^{rr} - \nu_{ACCR}^r (\sigma_{ACCR}^{zz} - \sigma_{ACCR}^{\theta\theta})) + \alpha_{ACCR}^r \Delta T \right] \\
&= \frac{1}{2 E_{ACCR}^r} (\sigma_{ACCR}^{rr})^2 - \frac{\nu_{ACCR}^r}{2 E_{ACCR}^r} \sigma_{ACCR}^{rr} \sigma_{ACCR}^{zz} - \frac{\nu_{ACCR}^r}{2 E_{ACCR}^r} \sigma_{ACCR}^{rr} \sigma_{ACCR}^{\theta\theta} \\
&\quad + \frac{1}{2} \sigma_{ACCR}^{rr} \alpha_{ACCR}^r \Delta T
\end{aligned} \tag{E.7}$$

Thus, as the last term of total energy formula of CCR, the integral including radial stress is calculated using Maple:

$$\int_{R_f}^{R_{CCR}} \left(\frac{1}{2} \sigma_{ACCR}^{rr} \varepsilon_{ACCR}^{rr} \right) r dr \quad (E.8)$$

$$\begin{aligned}
&= \frac{1}{384 E_{ccrr} (V_f - 1)^2} (24 (\nu_{ccrr} -) ((R_f + R_{ccr})(R_f - R_{ccr})) ((V_{ccr} - V_f + 1) R_{ccr}^2 + R_f^2 (-1 + V_f))^2 \ln(R_m)^2 \\
&\quad - 2(-2 R_{ccr}^2 ((-\frac{V_f}{2} + \frac{V_{ccr}}{2} + \frac{1}{2}) R_{ccr}^2 + R_f^2 (V_f - \frac{V_{ccr}}{2} - 1)) \ln(R_{ccr}) + R_f^4 (-1 + V_f) \ln(R_f) - \frac{3}{4} (R_f + R_{ccr}) \\
&\quad (R_f - R_{ccr}) ((-\frac{V_f}{3} + \frac{2V_{ccr}}{3} + \frac{1}{3}) R_{ccr}^2 + R_f^2 (-1 + V_f) - (\frac{2R_m^2 V_{ccr}}{3})) ((V_{ccr} - V_f + 1) R_{ccr}^2 + R_f^2 (-1 + V_f)) \\
&\quad \ln(R_m) - ((V_{ccr} - V_f + 1) R_{ccr}^2 - R_f (V_f - V_{ccr} - 1) R_{ccr} - R_f^2 (-1 + V_f)) R_{ccr}^2 ((V_{ccr} - V_f + 1) R_{ccr}^2 - R_f (V_f \\
&\quad - V_{ccr} - 1) R_{ccr} + R_f^2 (-1 + V_f)) \ln(R_{ccr})^2 - 2 R_{ccr}^2 (R_f^4 (-1 + V_f) (V_f - V_{ccr} - 1) \ln(R_f) - \frac{1}{4} (V_f - V_{ccr} - 1) (V_f \\
&\quad - 2V_{ccr} - 1) R_{ccr}^4 + ((\frac{5}{4} V_f^2 + (\frac{-5}{2} - 2V_{ccr}) V_f + 2V_{ccr} + \frac{5}{4} + \frac{V_{ccr}^2}{2}) R_f^2 - \frac{1}{2} R_m^2 V_{ccr} (V_f - V_{ccr} - 1)) R_{ccr}^2 - \frac{5}{4} \\
&\quad R_f^2 ((-1 + V_f) (V_f - \frac{3V_{ccr}}{5} - 1) R_f^2 - \frac{4}{5} (V_f - \frac{V_{ccr}}{2} - 1) V_{ccr} R_m^2)) \ln(R_{ccr}) + R_f^6 (-1 + V_f)^2 \ln(R_f)^2 - \frac{3}{2} R_f^4 \\
&\quad ((-\frac{2}{3} V_f + \frac{2}{3} V_{ccr} + \frac{2}{3}) R_{ccr}^2 + R_f^2 (-1 + V_f) - \frac{2R_m^2 V_{ccr}}{3}) (-1 + V_f) \ln(R_f) \frac{1}{24} ((2V_f^2 + (-6V_{ccr} - 4) V_f + \\
&\quad 6V_{ccr}^2 + 6V_{ccr} + 2) R_{ccr}^4 + (-13(-1 + V_f) (V_f - (\frac{18V_{ccr}}{13} - 1) R_f^2 + 6R_m^2 V_{ccr} (V_f - 2V_{ccr} - 1)) R_{ccr}^2 + 17(-1 \\
&\quad + V_f)^2 R_f^4 - 18R_m^2 V_{ccr} (-1 + V_f) R_f^2 + (6R_m^4 V_{ccr}^2) (R_f + R_{ccr}) (R_f - R_{ccr})) B_2^2 \left(\frac{d^2}{dz^2} g_1(z) \right)^2 - 48(\nu_{ccrr} \\
&\quad - 1) ((R_f + R_{ccr}) (R_f - R_{ccr}) ((V_{ccr} - V_f + 1) R_{ccr}^2 + R_f^2 (-1 + V_f)) (-R_{ccr}^2 V_f + R_f^2 (-1 + V_f)) \ln(R_m)^2 + \\
&\quad (4R_{ccr}^2 (\frac{1}{2} V_f (V_f - V_{ccr} - 1) R_{ccr}^4 - \frac{3}{2} R_f^2 (V_f^2 + (-\frac{2V_{ccr}}{3} - \frac{4}{3}) V_f + \frac{V_{ccr}}{3} + \frac{1}{3}) R_{ccr}^2) + R_f^4 (-1 + V_f) (V_f \\
&\quad - \frac{V_{ccr}}{4} - \frac{3}{4})) \ln(R_{ccr}) - 2R_f^4 (-1 + V_f) ((-V_f + \frac{V_{ccr}}{2} + \frac{1}{2}) R_{ccr}^2 + R_f^2 (-1 + V_f)) \ln(R_f) + (\frac{5}{4} (\frac{3}{5} V_f (V_f \\
&\quad - \frac{4V_{ccr}}{3} - 1) R_{ccr}^4) + (-\frac{8}{5} (-1 + V_f) (V_f - \frac{V_{ccr}}{2} - \frac{3}{8}) R_f^2) - (\frac{2}{5} R_m^2 V_f (V_f - 2V_{ccr} - 1)) R_{ccr}^2 + R_f^2 (R_f^2 (-1 \\
&\quad + V_f) + \frac{2R_m^2 (V_f - V_{ccr})}{5}) (-1 + V_f) (R_f + R_{ccr}) (R_f - R_{ccr})) \ln(R_m) - R_{ccr}^2 (V_f (V_f - V_{ccr} - 1) R_{ccr}^4 - 3R_f^2 \\
&\quad (V_f^2 + (-\frac{2}{3} V_{ccr} - \frac{4}{3}) V_f + \frac{V_{ccr}}{3} + \frac{1}{3}) R_{ccr}^2 + (-1 + V_f)^2 R_f^4) \ln(R_{ccr})^2 - 2R_{ccr}^2 (R_f^4 (-1 + V_f) (V_f - \frac{V_{ccr}}{2} - \\
&\quad \frac{1}{2}) \ln(R_f) - \frac{3}{8} V_f (V_f - \frac{4V_{ccr}}{3} - 1) R_{ccr}^4) + ((\frac{11}{8} V_f^2 + (-\frac{7}{4} - V_{ccr}) V_f + \frac{V_{ccr}}{2} + \frac{3}{8}) R_f^2 + \frac{1}{4} R_m^2 V_f (V_f - 2V_{ccr} \\
&\quad - 1)) R_{ccr}^2 - \frac{9}{8} R_f^2 ((V_f - \frac{2V_{ccr}}{9} - \frac{2}{3}) (-1 + V_f) R_f^2 + \frac{4}{9} R_m^2 (V_f^2 + (-\frac{3V_{ccr}}{2} - 1) V_f + \frac{V_{ccr}}{2})) \ln(R_{ccr}) + R_f^6 \\
&\quad (-1 + V_f)^2 \ln(R_f)^2 - \frac{5}{4} R_f^4 (-1 + V_f) ((-\frac{4}{5} V_f + \frac{2V_{ccr}}{5} + \frac{2}{5}) R_{ccr}^2 + R_f^2 (-1 + V_f) + \frac{2}{5} R_m^2 (V_f - V_{ccr})) \\
&\quad \ln(R_f) + \frac{9}{16} (\frac{2V_f}{9} (V_f - 2V_{ccr} - 1) R_{ccr}^4) + (-(-1 + V_f) (V_f - \frac{4V_{ccr}}{9} - \frac{1}{3}) R_f^2
\end{aligned}$$

Continue of (E.8)

$$\begin{aligned}
& -\left(\frac{2}{9}R_m^2V_f(V_f-4V_{ccr}-1))R_{ccr}^2+(-1+V_f)^2R_f^4+\frac{2}{3}(-1+V_f)R_m^2(V_f-\frac{2}{3}V_{ccr})R_f^2-\frac{4R_m^4V_fV_{ccr}}{9}\right)(R_f+ \\
& R_{ccr})(R_f-R_{ccr})\mathcal{B}_1\left(\frac{d^2}{dz^2}\mathbf{g}_1(z)\right)-(-(R_f+R_{ccr})(R_f-R_{ccr})(V_{ccr}-V_f+1)R_{ccr}^2+R_f^2(-1+V_f))\ln(R_m) \\
& -2R_{ccr}^2\left(-\frac{V_f}{2}+\frac{V_{ccr}}{2}+\frac{1}{2}\right)R_{ccr}^2+R_f^2(V_f-\frac{V_{ccr}}{2}-1))\ln(R_{ccr})+R_f^4(-1+V_f)\ln(R_f)-\frac{3}{4}(R_f+R_{ccr}) \\
& (R_f-R_{ccr})\left(-\frac{V_f}{3}+\frac{2V_{ccr}}{3}+\frac{1}{3}\right)R_{ccr}^2+R_f^2(-1+V_f)-\left(\frac{2R_m^2V_{ccr}}{3}\right)(-1+V_f)(E_{ccrr}\alpha_{ccrr}\Delta T-\nu_{ccrr}B_2 \\
& g_2(z))\mathcal{B}_2\left(\frac{d^2}{dz^2}\mathbf{g}_2(z)\right)+24\left(\frac{d^2}{dz^2}\mathbf{g}_1(z)\right)(\nu_{ccrr}-1)((R_f+R_{ccr})(R_f-R_{ccr})(-R_{ccr}^2V_f+R_f^2(-1+V_f))^2 \\
& \ln(R_m)^2-2((R_{ccr}^4V_f-2R_f^2(V_f-\frac{1}{2})R_{ccr}^2)\ln(R_{ccr})+R_f^4(-1+V_f)\ln(R_f)-\frac{1}{2}(-R_{ccr}^2V_f+R_f^2(-1+V_f) \\
& +R_m^2V_f)(R_f+R_{ccr})(R_f-R_{ccr})(-R_{ccr}^2V_f+R_f^2(-1+V_f))\ln(R_m)+\frac{1}{2}(\frac{R_{ccr}^4V_f^2}{2}+((-V_f^2+V_f)R_f^2- \\
& R_m^2V_f^2)R_{ccr}^2+(-1+V_f)^2R_f^4+R_m^2V_f(-1+V_f)R_f^2+\frac{R_m^4V_f^2}{2})(R_f+R_{ccr})(R_f-R_{ccr}))\mathcal{B}_1\left(\frac{d^2}{dz^2}\mathbf{g}_1(z)\right) \\
& -2(-(R_f+R_{ccr})(R_f-R_{ccr})(-R_{ccr}^2V_f+R_f^2(-1+V_f))\ln(R_m)+(R_{ccr}^4V_f-2R_f^2(V_f-\frac{1}{2})R_{ccr}^2)\ln(R_{ccr}) \\
& +R_f^4(-1+V_f)\ln(R_f)-\frac{1}{2}(-R_{ccr}^2V_f+R_f^2(-1+V_f)+R_m^2V_f)(R_f+R_{ccr})(R_f-R_{ccr}))(-1+V_f) \\
& (E_{ccrr}\alpha_{ccrr}\Delta T-\nu_{ccrr}B_2g_2(z)))\mathcal{B}_1)
\end{aligned}$$

Appendix E

By solving Eq. (7.58) through Maple software, the four kinematic variables of the RZT for CFMC beam are expressed as following:

$$U_{CFMC} = \frac{-q_0 L^3 \left[\left((B_{CFMC} D_{CFMC}^\phi - A_{CFMC}^\phi B_{CFMC}^\phi) \pi^2 + L^2 B_{CFMC} \mu_{CFMC} \right) (Q_{CFMC} + \mu_{CFMC}) - \left((B_{CFMC} B_{CFMC}^\phi - A_{CFMC}^\phi D_{CFMC}) \pi^2 + L^2 (-\mu_{CFMC}) B_{CFMC} \right) (-\mu_{CFMC}) \right]}{\left[\left(\left(-D_{CFMC}^\phi (B_{CFMC})^2 + 2 A_{CFMC}^\phi B_{CFMC}^\phi B_{CFMC} + \left(A_{CFMC} D_{CFMC}^\phi - (A_{CFMC}^\phi)^2 \right) D_{CFMC} - A_{CFMC} (B_{CFMC}^\phi)^2 \right) \pi^2 + L^2 \mu_{CFMC} (A_{CFMC} D_{CFMC} - (B_{CFMC})^2) \right) (Q_{CFMC} + \mu_{CFMC}) - L^2 (-\mu_{CFMC})^2 (A_{CFMC} D_{CFMC} - (B_{CFMC})^2) \right] \pi^3}$$

$$\Theta_{CFMC} = \frac{-q_0 L^3 \left[\left(\left(A_{CFMC} D_{CFMC}^\phi - (A_{CFMC}^\phi)^2 \right) \pi^2 + L^2 \mu_{CFMC} A_{CFMC} \right) (Q_{CFMC} + \mu_{CFMC}) - (-\mu_{CFMC}) \left((B_{CFMC}^\phi A_{CFMC} - B_{CFMC} A_{CFMC}^\phi) \pi^2 + L^2 (-\mu_{CFMC}) A_{CFMC} \right) \right]}{\left[\left(\left(D_{CFMC} D_{CFMC}^\phi - (B_{CFMC}^\phi)^2 \right) A_{CFMC} - (B_{CFMC}^\phi)^2 D_{CFMC}^\phi + \right) \pi^2 + L^2 \mu_{CFMC} \left(A_{CFMC} D_{CFMC} - (B_{CFMC}^\phi)^2 \right) \right] (Q_{CFMC} + \mu_{CFMC}) - \left[\begin{array}{l} \left(2 A_{CFMC}^\phi B_{CFMC}^\phi B_{CFMC} - (A_{CFMC}^\phi)^2 D_{CFMC} \right. \\ \left. L^2 (-\mu_{CFMC})^2 (A_{CFMC} D_{CFMC} - (B_{CFMC}^\phi)^2) \right) \end{array} \right] \pi^3}$$

$$\Psi_{CFMC} = \frac{q_0 L^3 \left[(B_{CFMC}^\phi A_{CFMC} - B_{CFMC} A_{CFMC}^\phi) (Q_{CFMC} + \mu_{CFMC}) - (-\mu_{CFMC}) (A_{CFMC} D_{CFMC} - (B_{CFMC}^\phi)^2) \right]}{\left[\left(\left(D_{CFMC} D_{CFMC}^\phi - (B_{CFMC}^\phi)^2 \right) \pi^2 + L^2 \mu_{CFMC} D_{CFMC} \right) A_{CFMC} + \right. \\ \left. (-D_{CFMC}^\phi \pi^2 - L^2 \mu_{CFMC}) (B_{CFMC}^\phi)^2 + 2 \pi^2 A_{CFMC}^\phi B_{CFMC}^\phi B_{CFMC} - (Q_{CFMC} + \mu_{CFMC}) - L^2 (-\mu_{CFMC})^2 (A_{CFMC} D_{CFMC} - (B_{CFMC}^\phi)^2) \right] \pi \\ \left. \pi^2 (A_{CFMC}^\phi)^2 D_{CFMC} \right]}$$

$$W_{CFMC} = \frac{q_0 L^2 \left[\left(\left(D_{CFMC} D_{CFMC}^\phi - (B_{CFMC}^\phi)^2 \right) A_{CFMC} - (B_{CFMC}^\phi)^2 D_{CFMC}^\phi + 2 A_{CFMC}^\phi B_{CFMC}^\phi B_{CFMC} - (A_{CFMC}^\phi)^2 D_{CFMC} \right) \pi^4 + \right. \\ \left(D_{CFMC} \mu_{CFMC} - 2 B_{CFMC}^\phi (-\mu_{CFMC}) + D_{CFMC}^\phi (Q_{CFMC} + \mu_{CFMC}) \right) A_{CFMC} - (Q_{CFMC} + \mu_{CFMC}) (A_{CFMC}^\phi)^2 + \left. \left(2 (-\mu_{CFMC}) B_{CFMC}^\phi A_{CFMC}^\phi - \mu_{CFMC} (B_{CFMC}^\phi)^2 \right) \right] L^2 \pi^2 \\ \left. + L^4 A_{CFMC} \left((Q_{CFMC} + \mu_{CFMC}) \mu_{CFMC} - (-\mu_{CFMC})^2 \right) \right]}{\left[(Q_{CFMC} + \mu_{CFMC}) \left(\left(D_{CFMC} D_{CFMC}^\phi - (B_{CFMC}^\phi)^2 \right) A_{CFMC} - (B_{CFMC}^\phi)^2 D_{CFMC}^\phi + 2 A_{CFMC}^\phi B_{CFMC}^\phi B_{CFMC} - (A_{CFMC}^\phi)^2 D_{CFMC} \right) \pi^2 + \right. \\ \left. L^2 (A_{CFMC} D_{CFMC} - (B_{CFMC}^\phi)^2) \left((Q_{CFMC} + \mu_{CFMC}) \mu_{CFMC} - (-\mu_{CFMC})^2 \right) \right] \pi^4}$$